Theoretical and Experimental Studies on Charge Deformation Densities and Hydrogen Bridges in Borane Anions and Related Species

Gary F Mitchell

Doctor of Philosophy
University of Edinburgh
1988

Declaration

I declare that the work described in this thesis has not been submitted for any other degree, and is the original work of the author, except where acknowledgement is made by reference. The work was carried out in the Chemistry Department of the University of Edinburgh between October 1983 and September 1986 under the supervision of Dr. A.J.Welch.

Acknowledgement

I would like to thank the Science and Engineering Research Council for the grant which funded this research and the Edinburgh Regional Computing Centre for the provision of computing services essential to the research. Thanks are also due to the ERCC advisory staff who were helpful in solving the more obscure problems.

In the course of my research at Edinburgh I was fortunate to have good friends and colleagues around me. Their knowledge and experience were as important a source of information as any library and for taking time to share it with me I thank them all. I would like to especially thank four people: Dr R.O.Gould for preparing a computer program necessary for the graphical presentation of the Fourier Maps, Dr Paul Taylor for his cooperation and advice on diverse computing problems and Dr A.J.Blake for being a good sport and enabling me to conclude the latter part of my work at Edinburgh. Finally, I would like to thank my supervisor, Dr Alan Welch for his enthusiasm for the research, advice, encouragement and patience.

Dedication

This work is dedicated to my parents Charles and Margaret. I will always be grateful to them for supporting me through those extra years at University.

"Read not to contradict and confute, nor to believe and take for granted, nor to find talk and discourse, but to weigh and consider."

Francis Bacon 1561–1626
Essays, 50, 'Of Studies'

Errata

UNIVERSITY OF EDINBURGH

ABSTRACT OF THESIS (Regulation 7.9)

The thesis is primarily concerned with the use of *X*-ray diffraction measurements of extraordinary precision and quantity to characterise the electron density distribution in three selected compounds. These compounds (CaB_6, salts of the ions $[B_{12}H_{12}]^{2-}$ and $[B_3H_8]^-$) were selected because their structures can only be rationalised by chemical bonding called 'delocalised'. The experimental results are compared and contrasted with results from theoretical calculations. This leads to important conclusions about suggested improvements in the method of experimental measurement and about the significant deficiencies in the theoretical simulation of the electron density distribution of some these structures.

The results from work on the polymeric semiconductor CaB_6 give a description of the electron density distribution in good agreement with theoretical models and, uniquely, in good agreement with the Electric Field Gradient Tensor which had previously been established by NQR spectroscopy.

The study of a salt containing the icosahedral di-anion $[B_{12}H_{12}]^{2-}$ shows(via the deformation electron density) that the radial binding component is negligable relative to binding over the polyhedral surface. This corrects some misconceptions about the importance of chemical bonding between non-adjacent atoms in this and similar clusters. This particular experiment further reveals a weakness in the popular two-stage measurement of diffraction data and suitable precautions are suggested.

The principal conclusion from the work on the benzyltrimethylammonium salt of the octahydrotriborate anion ($[B_3H_8]^-$) is that the theoretical simulation of the electron distribution, and even of the geometry of the ion, is anomalously poor. The experimental results cast doubt on the established topological explanation of the rare feature of this anion: the B-B bonds of the B_3 triangle which are bridged by hydrogens are *short* relative to the unbridged one. A molecular orbital based approach to hydrogen bridging is described which not only explains the anomalous structure of $[B_3H_8]^-$ but also explains the usual lengthening of H-bridged connectivities. The utility of the Laplacian function in the estimation of the ease with which molecular electron densities can be measured by *X*-ray diffraction is also introduced.

Finally, an algorithm is presented which estimates with a high degree of success the positions of hydrogen atoms given the geometry of the non-hydrogen atoms in, for example, transition metal clusters. This new method replaces a previously established program which had severe limitations originating from it's foundation on simple empirical rules. The new method reproduces observed asymmetry in the M-H bond lengths of hydrogen-bridged metal-metal bonds for all compounds for which the method was tested.

Introduction

This thesis is primarily concerned with the use of *X*-ray diffraction measurements of extraordinary precision and quantity to characterise the electron density distribution in selected compounds. These 'electron-deficient' compounds (CaB_6, salts of $[B_{12}H_{12}]^{2-}$ and $[B_3H_8]^-$) have been selected because their structures can only be rationalised by a type of chemical bonding called 'delocalised'. The experimental results are compared and contrasted with results from theoretical calculations. This leads to important conclusions about suggested improvements in the method of experimental measurement and about the significant deficiencies in the theoretical simulation of the electron density distribution of some these structures.

The first chapter gives an introduction to the concepts of deformation density studies which are presented in subsequent chapters and a short description of the development of this field of research which began in earnest in the late 1970's.

The second chapter describes work on the polymeric semiconductor CaB_6. This refractory compound afforded excellent measurements which gave a description of the electron density distribution in good agreement with theoretical models and, uniquely, in good agreement with the Electric Field Gradient Tensor which had previously been established by NQR spectroscopy.

The third chapter describes work on a salt containing the icosahedral di-anion $[B_{12}H_{12}]^{2-}$. The deformation density, (defined as the difference between the molecular electron density and that from the simple superimposition of atomic electron densities) of this anion has now been successfully characterised - even though it is extremely small. These results, backed by new theoretical calculations, correct some misconceptions about the importance of chemical bonding between non-adjacent atoms in these clusters. The radial bonding component is demonstrated to be negligeable relative to the binding over the polyhedral surface. This particular experiment further revealed a weakness in the popular two-stage measurement of diffraction data and suitable precautions are suggested.

The fourth chapter describes work on $[B_3H_8]^-$. The principle conclusion is that the theoretical simulation of the electron distribution, and even of the geometry of the ion, is anomalously poor. The experimental results cast doubt on the established topological explanation of the rare feature of this anion: the B-B bonds of the B_3 triangle which are bridged by hydrogens are SHORT relative to the unbridged one. An alternative explanation of this feature and the more usual opposite effect on bond lengths is propounded in the sixth chapter. The utility of the Laplacian function in the estimation of the ease with which molecular electron densities can be measured by *X*-ray diffraction is also introduced.

The fifth chapter describes a project which was initialised by the study of the bridging H-positions in $[B_3H_8]^-$. A pilot computer program was developed which estimates with a high degree of success the positions of hydrogen atoms given the geometry of the non-hydrogen atoms in, for example, transition metal clusters. This new method replaces a previously established program which had severe limitations originating from it's foundation on simple empirical rules. The justification of the development of this new program lies in its capability to be combined with *X*-ray diffraction results to give information (the hydrogen positions) which are chemically important but which hitherto have only been attainable by making vastly more expensive and difficult neutron diffraction measurements.

The sixth and final chapter describes an approach to hydrogen bridging which not only explains the usual lengthening of H-bridged connectivities but also explains the anomalous structure of $[B_3H_8]^-$ which was re-affirmed in the thorough study described above.

TABLE OF CONTENTS

1 Charge Deformation Density : Concepts and History

2 Charge Deformation Density in CaB$_6$

3 Charge Deformation Density in $[Et_3NH]^+{}_2[B_{12}H_{12}]^{2-}$

4 Charge Deformation Density of Benzyltrimethylammonium Octahydrotriborate

5 The Effect of Edge-bridging Hydrogen Atoms on the Lengths of B-B and Metal-Metal Bonds in Cluster Compounds

6 Hydride Location in Transition Metal Clusters

Chapter 1

Charge Deformation Density : Concepts and History

1.1. Synopsis

A detailed description of the methods used to measure, and terms to describe, deformation electron density, together with a catalogue of previous experimental results in this field is beyond the scope of this chapter. Therefore this chapter, together with the glossary, can only provide an outline of the development of this recent branch of crystallography and some of its concepts. There exist several good introductory articles [4,5,6] as well as some comprehensive texts [1,2,3] for those more familiar with XRD. Reviews of progress in the field have also appeared [7]. Papers relating to deformation density are now published regularly, particularly in *Acta Crystallographica*. The quality of published work has improved with advances in the refinement of deformation density but no work has been subsequently been refuted. There has however been criticism [9] of overly-optimistic interpretations of some results [8].

1.2. *X*-ray Structure Factors and Fourier Transforms

The intensities of the diffracted beams (I_{hkl}) in an *X*-ray diffraction experiment are proportional to the square of structure factors F_{hkl} (or more precisely FF^* where F^* is the complex conjugate of F). These structure factors are therefore in proportion to the amplitude of the diffracted beam and are related to the electron density ρ(r) by a Fourier Transform (FT) :

$$F_{calc}=(1/V)\int \rho(r)\exp(2\pi iH.r)dr$$

where V is the volume of the unit cell, ρ(r) is the electron density (= - charge density) at coordinate **r** (x,y,z), **H** is the integer triplet h,k,l for the diffracting plane and **H.r** is the dot product of vectors **H** and **r** equal to (hx + ky + lz).

For a molecular crystal ρ(r) is very low in most of the unit cell except in the vicinity of nuclear positions. Since one of the properties of FTs is that the FT of a sum of functions is equal to the sum of the FTs of the individual functions then ρ(r) can be approximated by a sum of isolated atomic densities. Such spherically symmetric atomic densities are simple functions with simple FTs which depend on the magnitude of H but not its orientation. These FTs of atomic density are called free-atom scattering factors (or curves) f and they can be computed from quantum-mechanical calculations on isolated atoms and then tabulated or fitted by functions [10]. The calculation of F_c is then simplified to a summation of scattering factors over each atom with consideration of the relative phases introduced by the spread of atomic coordinates in the unit cell.

$$F_c = \sum f_n(\mathbf{H})\exp(2\pi i\mathbf{H}.\mathbf{r}_n)$$

where $\mathbf{r}_n$ is the fractional coordinate of the n^{th} atom of scattering factor f_n. This approximation is used without problems in the routine solution and refinement of crystal structures. The approximation holds well because the perturbation of an atom's electron density upon molecule formation, the deformation density, is very small. Quantitative estimates of the magnitude of the deformation density could only be made with the advent of molecular *ab-initio* quantum mechanical calculations These calculations confirmed that the molecular electron density was only slightly different from the superimposed atomic densities (promolecular density) just as the total energy of a molecule is only slightly different from the summed electronic energy of each atom. In early experimental work the errors in the measurement of intensities and in corrections for absorption and extinction led to errors in observed structure factors F_{obs} that were large compared to those in F_c by virtue of the free atom model. Where the compound was assumed ionic the scattering factors of free ions such as Na^+ or Cl^- were substituted. Furthermore the scattering factor for hydrogen was frequently replaced by a sharpened one by scaling the profile to that for a nuclear charge of +1.2. This last substitution was to account for the observation that the electron density around hydrogen positions was frequently found to be more compact than for an isolated hydrogen atom. To this point these scattering factors were simply substituted and never refined. Serious consideration of the possibility of using still more complicated scattering factors only began when automated 4-circle diffractometers (for the accurate measurement of large data sets) and fast computers (capable of processing the extra calculations associated with the more complex aspherical scattering factors) became available.

1.3. Simple Modification of Scattering Curves

Among the earlier attempts to adapt the scattering factors of atoms to their chemical environment was the inclusion of spherically symmetric functions - effectively modelling a change in the atom's radial electron density distribution curve. Since such modifying functions were even and therefore had non-vanishing integrals their refinement was also a refinement of the atom's charge. This approach was taken by Coppens [12] with the qualification that since the core electron density is unperturbed it is sufficient for only the valence electron density to be modified ie :

$$\rho(r)=\rho_{core}(r)+P_{val}\rho_{val}(\kappa,r)$$

where P_{val} is a population parameter for the valence density function $\rho_{val}(\kappa,r)$ and κ is an expansion-contraction parameter. The refinements of P and K was known as "Kappa refinement" or more loosely as a "radial refinement"; moreover, since the work was largely confined to atoms with 2s/2p valence orbitals the technique was sometimes described as the "l-shell projection" method [11]. When the highly correlated position, thermal and extinction parameters were simultaneously refined it then became known as the "extended l-shell" method [13,14]. These initial results were very encouraging, for although there was no information on the change in angular distribution of electron density the results showed that for a single atom type in a series of compounds a set of charges could be obtained that were in broad agreement with chemical assumptions about oxidation state and the relative electronegativity of bound groups [12]. Furthermore the relationship between charge and size - contracted cations and expanded anions - was in agreement with the theoretical estimates of Slater [15].

These early refinements still could not model an important change in the atomic density upon molecule formation. This was the shift of the centroid of electron density away from the nuclear position. This asphericity shift is particularly large for hydrogen but it is still observable for other atoms. Without due allowance for this aspherical distortion the refinement of atomic positions gives coordinates which are biased towards the centroid of electron density. When this "free-atom bias" is towards the bond the calculated bond lengths are usually too short compared with those from the more accurate (if often less precise) neutron diffraction measurements. The thermal parameters - probability distribution functions of atomic position - may also refine to values which attempt to compensate for the aspherical deformation density. The direction of the centroid shift is not always into a bond but is in some instances is in the opposite direction if, for example, there is a pronounced lone pair.

1.4. X–N and X–X Maps

These were the first crude attempts to get a 3-dimensional representation of the deformation density. The XRD experiment can give the molecular electron density but not the unbiased atomic coordinates necessary to construct the reference or "promolecular" density. The neutron diffraction experiment does give the nuclear coordinates and their thermal motion free from any bias due to electron distribution. Subtraction of the promolecular density from the molecular density gives the deformation density or to use FTs:

$$\Delta\rho(\mathbf{r})=(1/V)\int[\,F_{obs}(\mathbf{H})/k\ -F_{c,free-atom}(\mathbf{H})]\exp(-2\pi i\mathbf{H}.\mathbf{r})$$

Where F_c has been prepared using the neutron diffraction results for positional and thermal parameters and k is a scale factor which *cannot* be that from the neutron diffraction experiment (there are necessarily two experiments) but is ideally estimated such that the integration of the deformation density over the unit cell is zero.

These experimental X–N maps showed clearly for the first time zones of excess electron density between chemically bonded atoms and peaks attributable to lone pairs.

Neutron diffraction is not readily available and the requirement for two experiments on two crystals on different machines using different detection techniques resulted in serious problems with systematic errors in at least one data set. The possibility of extracting unbiased atomic positions using *X*-ray data alone exists because the valence electron density is diffuse, and in the nature of FTs, diffuse functions have compact FTs. Therefore the exclusion or down-weighting of "low-angle" diffraction data leads to atomic coordinates where the free-atom bias is minimal. The limit for "low-angle" data was initially estimated at $2\sin\theta/\lambda$ 1.3Å^{-1} because quantum mechanical calculations (on free atoms) suggested that this was the point where the contribution of valence electrons to scattering was only a few percent. This limit was increased over the years towards 1.7Å^{-1}. Substitution of high order (HO) parameters for neutron diffraction derived ones gives " $X\text{-}X_{HO}$" or simply "X-X" maps. The scale factor should be that from the HO refinement but systematic errors frequently alter k and instead it is often re-refined using some or all of the data. Such maps of course show the *dynamic* deformation density since the XRD experiment gives the time averaged electron distribution. This is not immediately comparable with the results from *ab-initio* calculations which are for an instantaneous nuclear configuration. There are still other difficulties with X-X maps (see Chapter 2 : the limitations of X-X maps).

1.5. Multipolar Methods

The next advance was therefore the refinement of odd functions on the atoms to model the asphericity shift . This was investigated by Stewart [16], by Dawson [17], and by Hirshfeld [18]. The functions now had a third term with an angular dependence :

$$\rho(r)=\rho_{core}(r)+P_{valence}\rho_{valence}(\kappa,r)+\sum_l\sum_m P_{l,m}Y_{l,m}(\theta,\phi)R_l(r)$$

where $P_{l,m}$ is the population coefficient of an aspherical function of radial dependence $R_l(r)$ and angular dependence $Y_{l,m}(\theta,\phi)$. These extra aspherical functions (describing electron density) were analagous to the p, d, f, g hydrogen atomic orbital functions (which describe the wavefunction). Spherical harmonic functions are by definition mutually orthogonal but while this is an advantage in some applications of least-squares refinement it is *not* a necessary condition. Hirshfeld developed a similar approach using simpler non-orthogonal functions [18] of the form :

$$\rho_{def'n}=R_n(r)\cos^n\theta_k \quad (n= 0,1,2,3,4)$$

where $R_n(r)$ is a radial distribution function and θ_k is the angle from some specified polar axis, 3 axes for n=1 and 15 axes for n=4. The programs of Coppens and of Hirshfeld which were developed to apply these functions in the refinement of the molecular electron density became widely available from 1979. Since the deformation density was now neatly parameterised the static deformation density could also then be evaluated and plotted. Multipolar models represented a significant improvement over X-X methods. The maps now had the noise due to random errors in F_{obs} filtered out and were, for the first time, maps capable of being compared to theoretical results.

1.6. *Ab-initio* Calculations

The comparison of experimental deformation density studies with results from theoretical calculations of various levels of sophistication showed that the experimental deformation could only be reproduced by *ab-initio* calculations of at least split valence level (4-31G, 3-21G), with some subtle features reproduced only after expansion of the basis sets to include polarisation functions. This was to be expected since it is only at this level of calculation that theoretical deformation densities converge to within approximately 0.05 $e\text{Å}^{-3}$ in the interatomic region [19]. The effect of electron correlation on the electron density is fortunately an order of magnitude smaller than the deformation density and is therefore negligible when making comparisons within experimental results. Nevertheless the size of the basis sets required indicates that for larger molecules /polymers the deformation density may be more accessable from *X*-ray diffraction than by molecular orbital or band calculations.

In the early development of multipole refinement the close analogy between the molecular density defined as a series of short range overlapping functions and the density matrix $P_{\mu,\nu}$ of the LCAO molecular orbital method was exploited [20]. The goal of measuring the *X*-ray diffraction pattern so accurately that the wavefunction density matrix could be refined (rather than calculated by *ab-initio* means), and hence all properties predicted by application of the appropriate operator is still remote, but a system of computer programs to acheive this has been tested successfully on lithium and beryllium, admittedly using calculated structure factors [21].

Chapter 2

Charge Deformation Density in CaB_6

2.1. Why Study CaB_6?

Calcium hexaboride was first prepared in 1897 [22] and is one of a series of isostructural MB_6 borides where M is a group IIa metal. Other hexaborides are known such as rare-earth hexaborides and KB_6, SiB_6 etc. These hexaborides are worthy of an accurate *X*-ray diffraction study because of the unusual binding of the boron framework. The structure consists of B_6 octahedra and metal atoms arranged in 8:8 (i.e. CsCl) cubic packing. The B_6 octahedra are sufficiently close for the contacts to be interpreted as bonds. An illustration of part of the polymeric structure is sketched in Fig 1.1.

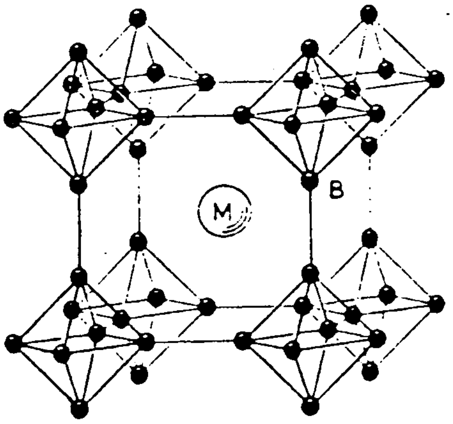

FIGURE 2.1

Structure of CaB_6

Thus the number of connectivities for each boron atom is 4 intra-octahedral and 1 inter-octahedral, which even assuming the transfer of 2 electrons from the Ca to the B_6 unit allows only 2/3 electrons for each connectivity. This leads to an interpretation of the bonding as involving 2-electron 2-centre bonds only between the octahedra with delocalised bonds within the octahedra.

The latter are of greater interest since their delocalisation makes their "observation" via XRD a challenge. Furthermore, boron polyhedra are a class of compounds on which relatively few charge deformation density studies have been done.

The bonding pattern of the B_6 octahedra of CaB_6 is entirely analagous to that in the hexaborate di-anion $[B_6H_6]^{2-}$ [23]. This can be prepared [24] and crystallised as its $[N(Me)_4]^+$ salt [25]. The latter salt could instead be studied with the same objective and would be more suitable for a charge deformation density study as indicated by its higher Coppens suitability factor [26].

$$S_c = V/\sum n^2$$

where V is the unit cell volume and n is the number of core electrons, the summation is over all atoms in the unit cell. For $[NMe_4]_2[B_6H_6]$ $S_c = 6.48$ (cf. CaB_6 0.20). Another advantage of $[NMe_4]_2[B_6H_6]$ over CaB_6 is a smaller absorption coefficient: $\mu(\text{Mo-K}_\alpha) = 0.49$, $\mu(\text{Ag-K}_\alpha) = 0.33\ \text{cm}^{-1}$ (cf. $\mu(\text{Mo-K}_\alpha)$ 17.8, $\mu(\text{Ag-K}_\alpha) = 9.1\ \text{cm}^{-1}$). The $[B_6H_6]^{2-}$ ion would also be more immediately comparable with studies in other hydroborate anions (such as $[B_{12}H_{12}]^{2-}$) of which there is a greater variety in polyhedral geometry than in the borides. The disadvantages of the tetramethylammonium salt are that tetramethyl ions show some disorder and/or rotation of methyl hydrogens and the synthesis of $[B_6H_6]^{2-}$ is potentially hazardous. Moreover the use of alkali metal salts of $[B_6H_6]^{2-}$ would result in the absence of a 2-electron 2-centre bond (other than the unsatisfactory B-H bond), to act as a check on the quality of the data before interpreting the delocalised deformation density in the B_6 fragment. The synthesis of CaB_6 demands extreme conditions but fortunately it is available commercially at little expense. The remaining disadvantages of CaB_6 are the low suitablity factor (see above) and the extended polymeric lattice. The latter presents difficulties when calculating the theoretical deformation density. However, the same polymeric lattice confers extreme crystallinity and reduces drastically the thermal vibrations of the boron atoms allowing measurement of Bragg reflections to extraordinary values of $\sin\theta/\lambda$ at room temperature. Finally the unit cell (4.14Å cubic P) is smaller (cf. $[NMe_4]_2[B_6H_6]$ 11.84Å cubic F) and therefore fewer reflections need to be measured to achieve the same resolution.

2.2. Experimental

Two data sets were collected using the same crystal but different *X*-ray wavelengths. The experimetal details are summarised below.

2.2.1. Data Collection

2.2.1.1. Collection 'RTMO' (Room Temperature Mo-K_α)

CaB_6 was obtained from ALFA (99.5 %). Black, opaque cuboid block 0.050x0.048x0.035 cm. Space group (Pm3m) and preliminary cell dimensions by Weisenberg photography ; accurate cell parameters using CAD-4 diffractometer, 293K, 25 centred reflections ($12° < \theta < 56°$), graphite monochromated Mo-K_α (λ_{av} 0.71069Å), for data collection $\theta max = 76°$, $\omega-2\theta$ scans in 96 steps (each reflection scanned twice using 48 alternate steps, profile compared and if not statistically similar twice more, if still dissimilar measurement flagged), ω-scan width $0.45+0.35\tan\theta$, medium speed prescan after which reflections of $I \geq 3\sigma I$ re-measured such that final net intensity had $I > 33\sigma I$ subject to a maximum measuring time of 90s. Full sphere of 6239 data measured over 67 *X*-ray hours. No detectable crystal decay or movement.

2.2.1.2. Collection 'RTAG' (Room Temperature Ag-K_α)

Same crystal used, collection as per RTMO except cell based on 24 centred reflections ($9° < \theta < 48°$), graphite monochromated Ag-K_α (λ_{av} 0.56160Å) for data collection θ max=60°, ω-scan width 0.5+0.45 tanθ, medium speed prescan after which reflections of $I \geq 0.67\sigma I$ re-measured such that final net intensity had $I > 33\sigma I$ subject to a maximum measuring time of 120s. Full sphere of 11144 data measured over 260 *X*-ray hours.

2.2.2. Data Reduction

2.2.2.1. RTMO

115 reflections with $I<0$ discarded together with reflections flagged as

- overloading the detector counter
- having an irreproducible profile
- being weak with a peak offset from the expected position
- having an uneven background

Total deletions amounted to no more than 10% of data collected. Data corrected for Lorentz and polarisation factors (including terms for monochromator polarisation). Analytical absorption correction using SHELX76[27] on six measured 001-type faces, μ(Mo-K_α) 18.31cm^{-1}. T_{max} 0.581, T_{min} 0.444. Data then merged to give 187 unique data (R_{merg} 0.040), reflections with $\Delta/\sigma>3$ deleted. The two lowest-θ reflections persistently had Fo < Fc ; this was attributed to extinction and these two reflections (001 and 002) were deleted to give a final list of 176 Fobs.

2.2.2.2. RTAG

- as per RTMO except: 757 reflections with $I<0$ discarded, μ(Ag-K_α)=9.10cm^{-1}, T_{max} 0.746, T_{min} 0.646. Data merged to give 314 unique data (R_{merg} 0.025). Reflections with $F < 5\sigma F$ omitted together with 001 (Fo<<Fc: attributed to extinction), to give a final list of 297 Fobs.

Summary

CaB_6, Mr=104.94, ρ_x 2.45gcm^{-3}, cubic, space group Pm3m (No. 221), a=4.1422(5)Å(averaged), V=71.07(2)Å^3, Z=1, μ(Mo-K_α)=18.31cm^{-1}, μ(Ag-K_α)=9.10cm^{-1}, F_{000}=50, T=293K.

2.3. Refinement of Standard Parameters

The starting point of the refinement was the long established but imprecise positional parameters of Stackelberg and von Neumann [28] but with an arbitary origin shift such that B is at (x,0,0) and Ca is at (1/2,1/2,1/2). Thermal parameters were initially (over)estimated at 0.05.

There are only 5 standard crystallographic variables of which only one is a positional variable. These were refined using weights of $1/\sigma^2F$, minimising the function $\Delta_1=\Sigma|Fo-kFc|^2$. These are listed below in Table 2.3 together with their esd's, in columns (a) and (b) for RTMO and RTAG.

TABLE 2.3

	a	b	c
$\sin\theta/\lambda$	1.37	1.54	1.37
λ	0.71069	0.5616	0.5616
N_{obs}	176	297	191
Ca u11	.01254(4)	.01237(6)	.01238(7)
B x	0.29832(9)	0.29856(14)	0.29858(18)
B u11	0.00444(8)	0.00458(13)	0.00466(18)
B u22	0.00624(6)	0.00621(9)	0.00625(12)

These two solutions are *not* significantly different with the possible exception of Ca u11 where the difference is between 2 and 3σ. Excluding data from RTAG of resolution greater than than obtained with Mo-Kα measurements, ie using only data of $\sin\theta/\lambda$ < 1.37Å^{-1}, gives the set of parameter in column c. These are broadly similar but with larger esd's.

2.4. Experimental Charge Deformation Density

There are several functions which can be employed to display the charge deformation density determined from *X*-ray diffraction experiments, as described in the previous chapter. Here X-X maps are presented.

2.4.1. X-X Maps

In preparing an X-X map it is neccessary to divide the data into low and high angle sets and refine a model using only the latter. This model is then fixed and used in conjunction with the low angle set to prepare a difference map which is the deformation density map. The scale factor alone may be or may not be further refined but fixing it at the high order value is preferred.

The division in $S = 2\sin\theta/\lambda$ is however somewhat arbitary because the limit in S at which the contribution of the atom's valence deformation becomes negligible will depend not only on the unit cell composition but also on each atom type. This dependence is demonstrated by refining the CaB_6 model with various values of S_{min}. The results for data set RTAG are tabulated below in Table 2.4.1.

TABLE 2.4.1

S_{min}	0.0	0.8	1.2	1.6	2.0	2.4	2.8
N_{obs}	297	288	274	248	210	161	90
Ca u11*	1237(6)	1243(5)	1255(4)	1222(3)	1238(4)	1250(6)	1247(18)
B u11	444(8)	457(9)	431(6)	422(5)	429(4)	430(6)	448(18)
B u22	624(6)	627(6)	611(5)	609(4)	617(9)	621(5)	640(18)
k-1	.328(2)	.333(3)	.314(3)	.308(4)	.328(5)	.341(10)	.39(4)

* thermal parameters $\times 10^5 \text{Å}^{-2}$

From Table 2.4.1 it is apparent that the boron parameters plateau at $S_{min} >$

2.0Å^{-1} while the calcium parameters continue to shift as S_{min} is raised to 2.4Å^{-1}. All parameters shift as S_{min} is raised to 2.8Å^{-1} but this is attributable to the severe correlation of scale and thermal parameters (due to the narrow θ range) and the severely diminished number of reflections. These factors result in increased esd's, the particularly high esd on the scale factor (3%) makes it unusable for X-X maps.

The limit in S of Fobs contributing to the difference (X-X) map need not be the same as that dividing the data into low and high order reflections. The inclusion of reflections from higher angle increases the resolution but the noise becomes worse as shown by Figs 2.4.1(a) and 2.4.1(b) where the parameters are from S >= 1.2 but S_{max} of the final ΔF synthesis is respectively 1.0 (16 unique reflections) and 1.4 (35 reflections). The features of these maps are discussed in section 2.7.

2.4.2. The limitations of X-X Maps

X-X maps are unsatisfactory for several reasons:

- The contribution of (Fo-Fc) to the map is not dependent on the statistical uncertainty associated with Fo. Hence large ΔF terms can have a profound influence on the map even though some may have an appreciable error.

- The formulation of X-X maps is imprecise, ie there is *not* a universally applicable limit of S for dividing the data into low and high order.

- The scale factor is usually associated with a large esd and correspondingly the absolute sign of much of the map is uncertain. Where it is re-refined prior to preparing the ΔF map various methods have been employed. The ideal of a scale factor such that the integration over the difference map is zero is rarely achieved.

- In non-centrosymmetric structures the ΔF magnitude and phase are particularly sensitive to small changes in Fcalc.

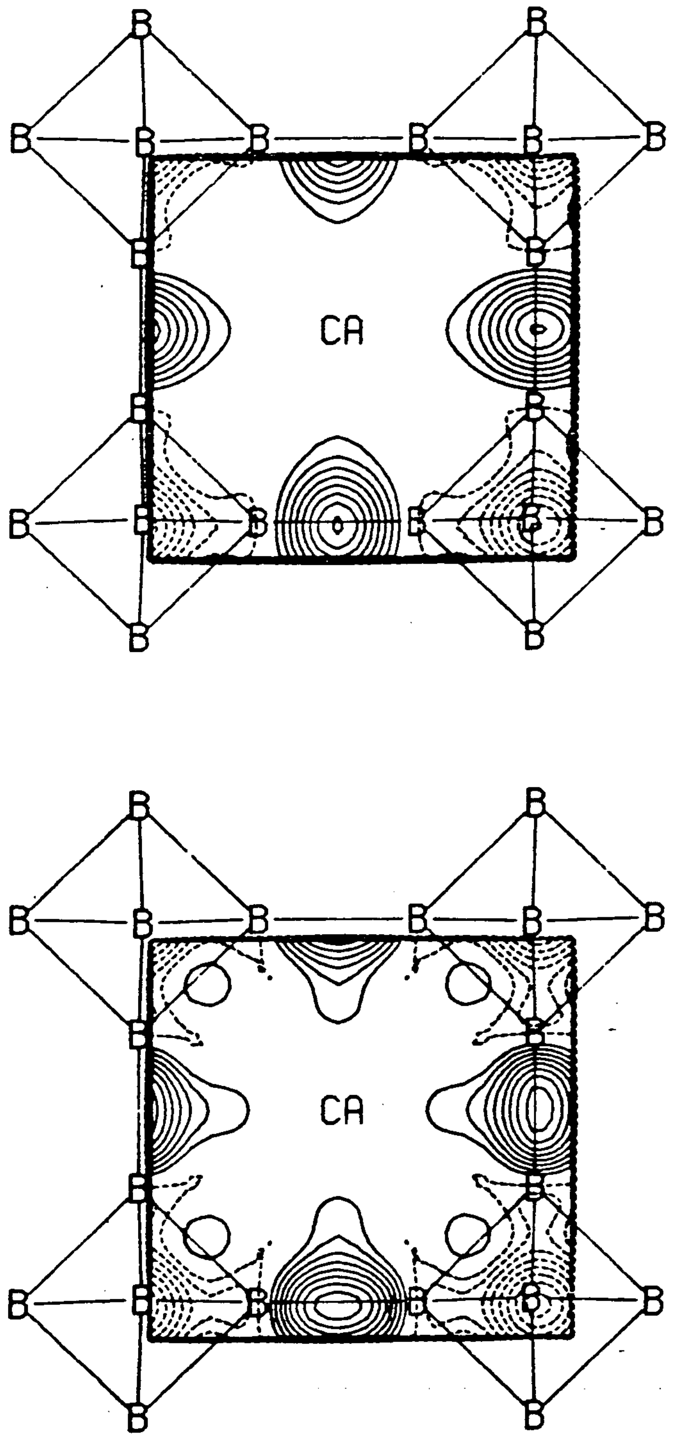

FIGURE 2.4.1

X–X map for a plane containing
the centres and four edges of B_6 octahedra.
(a) $S \leq 1.0\text{Å}^{-1}$
(b) $S \leq 1.4\text{Å}^{-1}$

- The more higher angle terms included in the ΔF synthesis then the worse the errors associated with features on the map. High resolution and good signal to noise ratio are therefore conflicting requirements.

2.5. Multipolar Refinement

This section describes the refinement of the deformation density of CaB_6 using the program LSEXP developed by Hirshfeld. The refinement reported is for the data set RTAG only and all subsequent discussion is confined to this collection. (The other data set RTMO was also refined and gave similar results subject to a smaller data/variable ratio and stronger absorption.)

2.5.1. The Multipolar Model

Several programs have been used by various authors for multipole refinement. Some use functions to describe all of the atomic density, others assume a core density profile and describe by functions only the valence density, and finally others assume an atomic density corresponding to a free isolated atom and describe the distortion of the valence density by functions. These functions can be spherical harmonics which are orthogonal but can also be simpler angular functions (which are non-orthogonal), linear combinations of which are spherical harmonics. The radial dependence can be either Slater type ($e^{-\alpha r}$) or Gaussian ($e^{-\gamma rr}$). The multipole refinement reported here (and those in other chapters) was carried out using the program LSEXP developed by F.L.Hirshfeld [29] which modifies the atomic electron density profile (implied by input standard free atom scattering curves) by electron density terms of the form:

$$\rho_{\alpha,l}(r) = \rho_n(r_\alpha, \theta_k)$$

$$= N_n r^n \exp(-\alpha r_\alpha) \cos^n \theta_k$$

where r_α is the distance from the atomic centre α, θ_k is the angle between radius vector r_α and a specified polar axis k, n is an integer ranging between 0 and 4 and α is the exponent which governs the radial range of the deformation functions. N_n is a normalising factor. The 35 functions transform to 3 monopoles, 6 dipoles, 10 quadrupoles, 7 octapoles and 9 hexadecapoles and as such define a highly flexible basis.

2.5.2. Multipolar refinement of CaB_6

Symmetry constraints originating from the crystallographic point symmetry (Ca: O_h, B: C_{4v}) drastically reduce the number of independent deformation coefficients from 35 each to 4 for Ca and 10 for B. The finite expansion of the deformation functions to fourth order results in effective constraint on the Ca deformation basis to spherical point symmetry ; however, the cumulative interaction of neighbouring atom's deformation functions means that spherical point symmetry is not reflected in deformation maps at the Ca position. Initial estimates of the deformation coefficients were zero while the exponents were estimated at 5Å^{-1} for Ca and for B. These exponents were initially fixed. The deformation coefficients and standard parameters were refined by full matrix least squares with initial heavy damping. The function minimised was $\Delta_2 = \Sigma w_2(|Fo^2-k^2Fc^2|)^2$ rather than $\Delta_1 = \Sigma w_1|Fo-kFc|^2$ in line with current thought on the relative merit of Δ_1 and Δ_2 minimisation [30].

For data set RTAG the initial weighted R-factor R_w for 5 converged standard parameters was 4.108%. The introduction of 14 deformation coefficients and 1 constraint ($F_{(000)} = 50$) reduced R_w to 1.842%. Despite more than trebling the number of variables this is still a significant decrease in the R_w factor according to Hamilton's test [31]. The contribution of the 'cusp' or 'spherical' functions (n=0) in reducing R_w is small, 0.5%. Refinement of the exponents (in a separate block) slowly reduces R_w still further to 1.706% (again significantly) but the exponent on B becomes unreasonably low (3.42Å^{-1}), and consequently the model violates the convolution approximation which requires deformation density to undergo the thermal motion of its nearest neighbour nucleus. (This problem probably only arises because a large component of the deformation density is between symmetry related boron atoms with parallel thermal ellipsoids.) The results with exponents fixed at 5Å^{-1} were therefore retained. These are set out below in table 2.5.2.

TABLE 2.5.2

Standard parameters

	x	y	z	u11	u22=u33
B	0.29834(7)	0	0	0.00420(6)	0.00619(7)
Ca	1/2	1/2	1/2	0.01226(4)	

Deformation Parameters

Atom	Order	Axis	Coefficient (esd)
B	0	-	-0.028(38)
	1	100	0.088(32)
		{010,001}	0
	2	{110,1-10,101 10-1}	0.169(44)
		{011,01-1}	-0.367(46)
	3	{110,1-10,101, 10-1}	0.556(54)
		{111,1-1-1,-(-11-1), -(-1-11)}	-0.713(56)
		{011,01-1}	0
	4	100	-0.297(58)
		{010,001}	0.049(28)
		{a11,-a11,a-11,a-11}	0.011(17)
		{1a1,11a,1-a1,11-a, 1a-1,-11a,-1a1,1-1a}	0.058(15)
Ca	0	-	0.375(207)
	2	{110,1-10,101,10-1, 011,01-1}	-0.064(55)
	4	{100,010,001}	-0.408(156)
		{a11,1a1,11a,-a11, 1-a1,11-a,a-11,1a-1,	

-lla,al-l,-lal,l-la} -0.009(49)

R-factor R 0.0134, weighted R-factor R_w 0.0184.
$a = \sqrt{2} - 1$

2.5.2.1. Verification of Thermal Deconvolution

A map of the electron density in a unit cell, such as prepared by direct Fourier synthesis, shows atoms as local concentrations of electron density. These are in general *not* spherical for two reasons. These are 1) the atoms undergo thermal motion which is usually anisotropic and 2) the electron density of the atom does not remain spherical if the atom forms chemical bonds. These two factors are applied to the free atom scattering, $f_{hkl,0}$, in the structure factor calculation by the temperature factor u (strictly a second rank symmetric tensor) and a small F term, f_m, which is the transform of the deformation multipoles.

$$f_{hkl}=(f_{hkl,0}+f_{hkl,m})\exp[-2\pi^2(u_{11}h^2a^{*2}+u_{22}k^2b^{*2}+u_{33}l^2c^{*2}+2u_{12}hka^*b^*+2u_{13}hla^*c^*+2u_{23}klb^*c^*)]$$

These terms are correlated, since each describes an aspherical electron density, but the correlation is imperfect because their modifications of f_{hkl} as a function of $\sin\theta/\lambda$ have different profiles [32]. Given data covering a large range of S therefore, these contributions can be resolved. This process of thermal deconvolution *must* be successful if the deformation density determined is to be meaningful.

Verification of thermal deconvolution is done by confirming that the resulting thermal parameters are chemically sensible or agree with independent measurements such as neutron diffraction. Chemically sensible means that the bonds should be nearly rigid since it is well established that the force constants for bond compression/extension are much larger than for bond angle deformation. This leads to the conclusion that for two bonded atoms the components of the thermal motion parallel to the bond should be very nearly equal[32]. For rigid groups such as phenyl rings this idea can be extended [33] to the statement that all pairs of atoms in a rigid group (bonded or not) should have near equal amplitudes of vibration along the vector between them. The limit 'near equal' is usually interpreted as an difference in the components of thermal parameters below 0.0001Å^2. Where thermal parameters are refined without multipole deformations and especially if the data span only a small range of S, such as for routine structure solution, the thermal parameters do *not* pass a rigid bond test and almost certainly mask deformation density features. The recent realisation of this means most of the thermal parameters published in the last few decades are not quantitative and perhaps explains the current trend to exclude thermal parameters from the publication of routine structure solutions.

Examination of the thermal parameters to prove thermal deconvolution in CaB_6 is complicated by the fact that the borons at either end of the inter-octahedral connectivity have symmetry equivalent thermal parameters parallel to the bond (u_{11}). The intra-octahedral components parallel to the octahedral edges similarly are symmetry equivalent. For the purpose of demonstrating successful thermal deconvolution more subtle methods are needed. Table 2.5.2.1 lists u_{11} and u_{22} for B after refinement with and without deformation functions.

TABLE 2.5.2.1

Boron & Calcium Thermal Parameters

deformation functions:	B u_{11}	B u_{22}	Ca u_{11}
excluded	0.00454(11)	0.00619(16)	0.01228(4)

included	0.00420(6)	0.00619(7)	0.01226(4)

Other than a general reduction in the esd's the only difference is that the anisotropy becomes more pronounced. The Raman spectrum of several MB_6 compounds, including CaB_6, has been measured [34] and assigned. Three bands corresponding to vibrational modes of the B_6 octahedron of symmetry A_{1g}, E_g and F_{2g} occur at successively lower frequencies (1300, 1150, 780 cm^{-1} approximately from Fig.2 of reference 34). This suggests that the largest amplitude of vibration should be of F_{2g} type. This mode corresponds to scissoring around the four-fold axis of the octahedron. Given the threefold degeneracy the thermal motion of the rigid octahedron should be large tangential to the inter-octahedral bond and smaller parallel to the bond. This is indeed reproduced in the thermal parameters and is more pronounced after inclusion of valence deformation multipoles. The thermal motion of the Ca atom is less clearly resolved, there being no significant change.

2.5.3. Static Deformation Maps

Fig 2.5.3(a) shows the static deformation density using the parameters from the RTAG refinement with evaluation over a grid of 51x51 points of approximately 0.1Å divisions. Contours are in intervals of $0.05e\text{Å}^{-3}$. The zero contour is omitted. The plane is perpendicular to the 001 direction and contains the centre of an octahedron.

Fig 2.5.3(b) - as above but for a parallel plane passing through the centre of an octahedral face.

Fig 2.5.3(c) - as above, passing through a B position.

Fig 2.5.3(d) shows the esd of the static deformation density evaluated for a

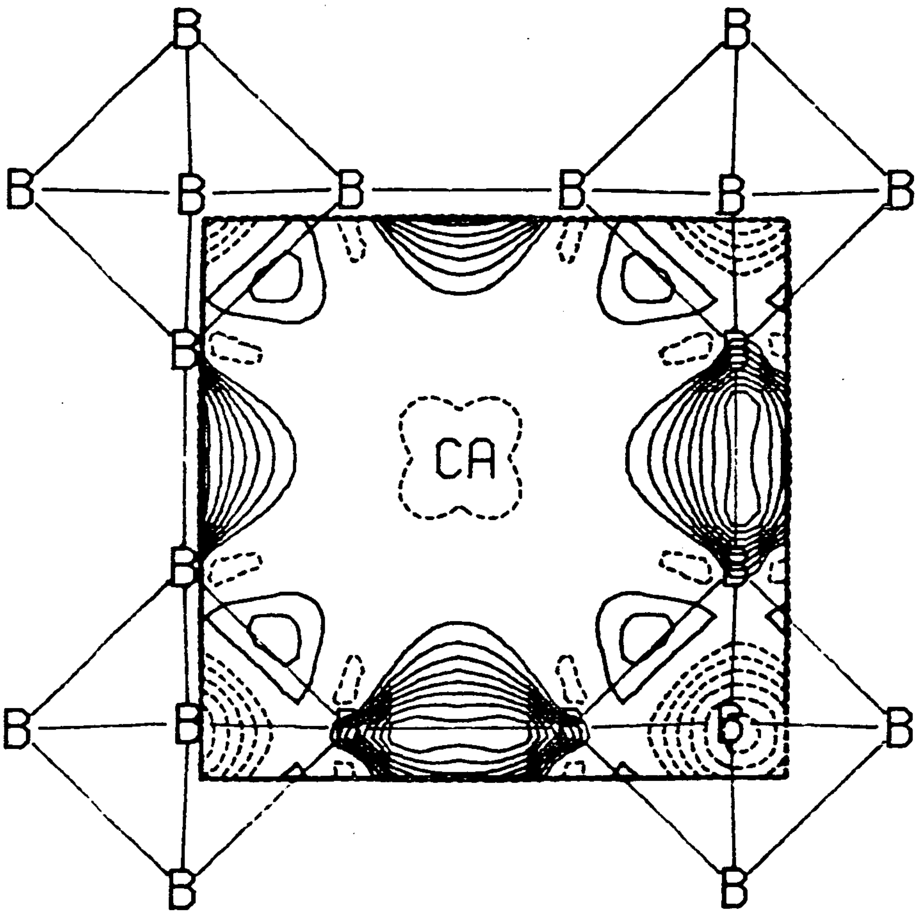

FIGURE 2.5.3(A)

Static Deformation Density
for a plane perpendicular to 001 and containing
an octahedral centre .

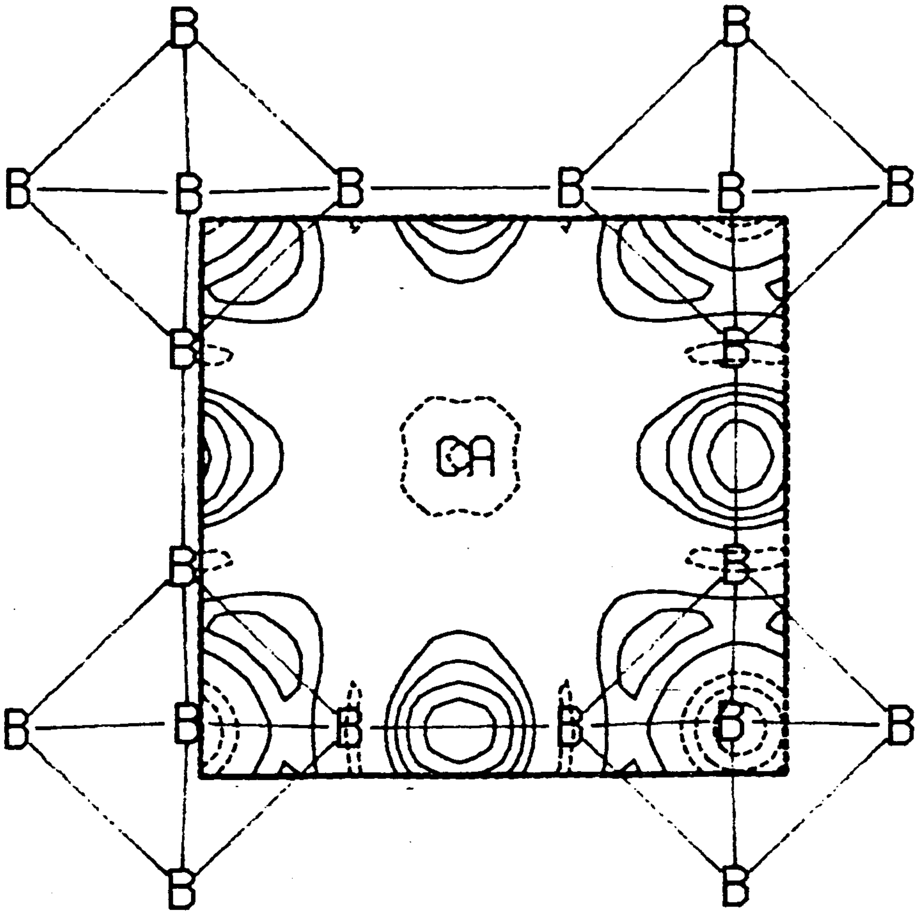

FIGURE 2.5.3(B)

Static Deformation Density
for a plane perpendicular to 001 and passing
through the centre of an octahedral face.

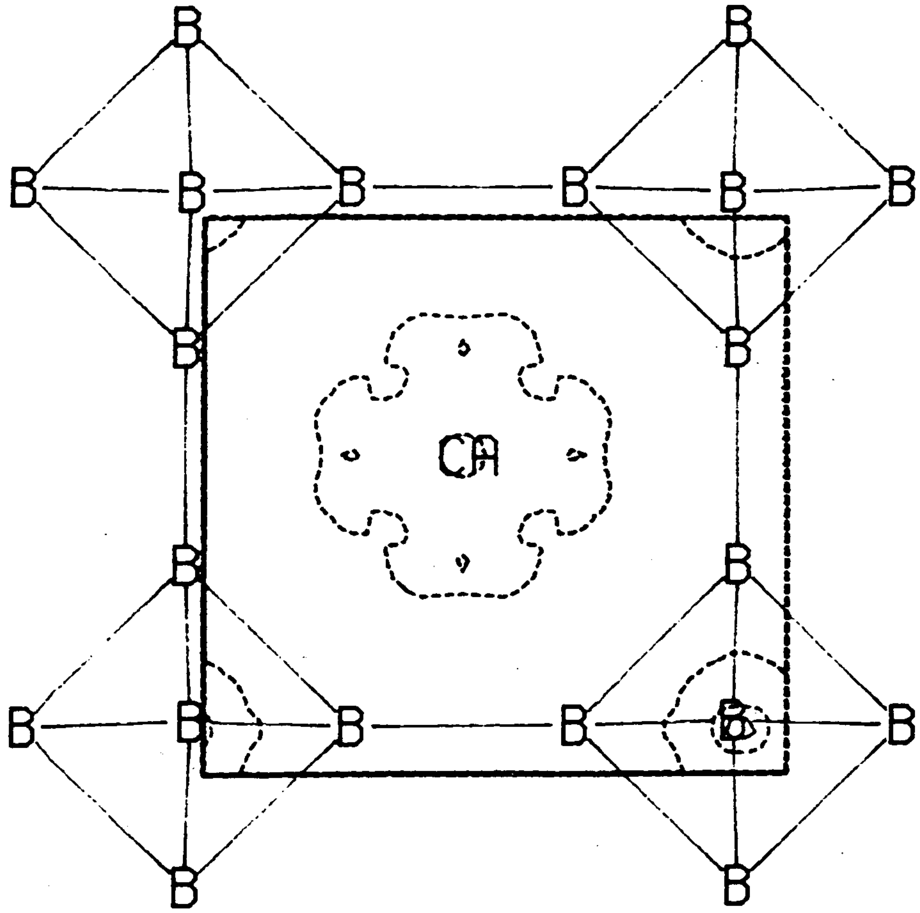

FIGURE 2.5.3(C)

Static Deformation Density
for a plane perpendicular to 001 and passing
through a B position on 00z.

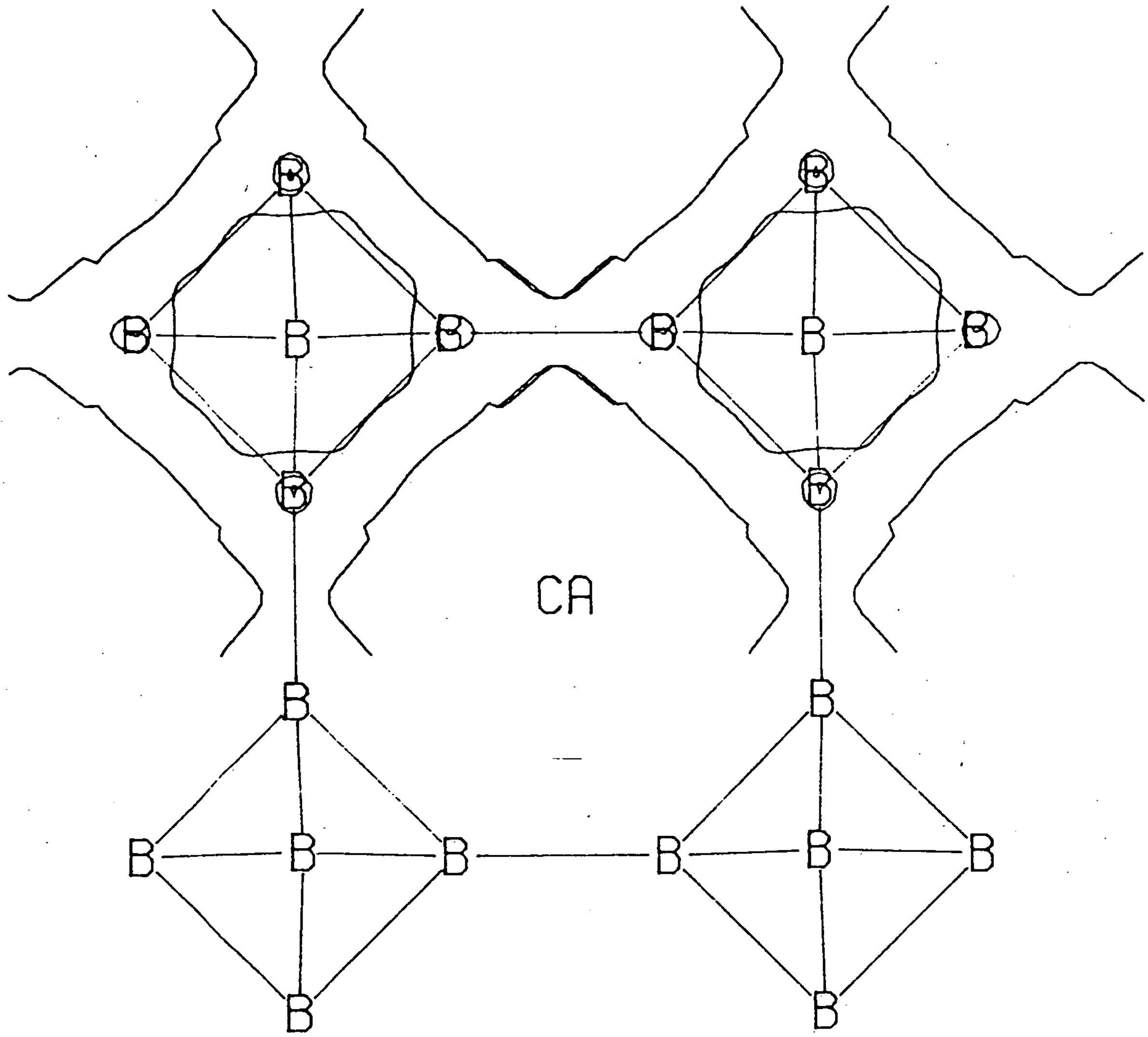

FIGURE 2.5.3(D)

ESD of Static Deformation Density
for the plane in 2.5.3(a).

portion of figure 2.5.3(a) using the least squares covariance matrix and the program DEFEX by Hirshfeld [29].

2.5.4. Dynamic Deformation Density Maps

These were prepared using Fourier transforms (rather than the tedious convolution of numerically summed deformation functions with the thermal parameters), and are essentially difference maps of two Fcalc's.

$$\Delta\rho_{dyn}=1/V\ \Sigma(F_1-F_2)\exp(-2\pi iH.r)$$

where F_1 = Fcalc from a model with full deformation functions and F_2=F'calc using structural parameters taken from the multipole model refinement and only free atom scattering factors. Summation was over all indices (observed or not observed in the experiment) to an adequate resolution for the grid employed.

Figs 2.5.4(a) to (c) show sections analagous to Figs 2.5.3(a) to (c). Contour intervals are unchanged. The thermal amplitudes are so small that the decrease in peak heights is very slight.

2.5.5. Residual Density Maps

Substitution of Fobs for F_1 (see Section 2.5.4) gives (dynamic density + residual density). Subtraction of the dynamic density grid previously calculated (using only Fc for which an Fobs was measured) leaves the residual density.

Figs 2.5.5(a) to (c) shows the residual density in some of the sections in Figs 2.5.3(a) to (d).

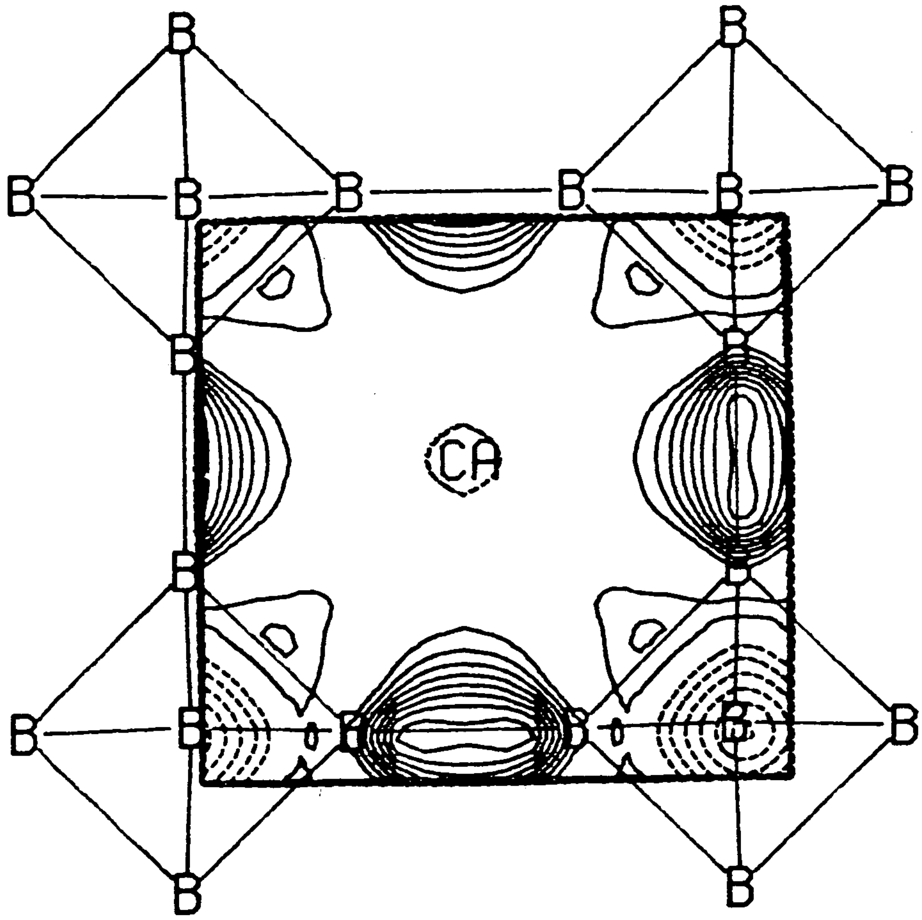

FIGURE 2.5.4(A)

Dynamic Deformation Density
for a plane perpendicular to 001 and containing
an octahedral centre .

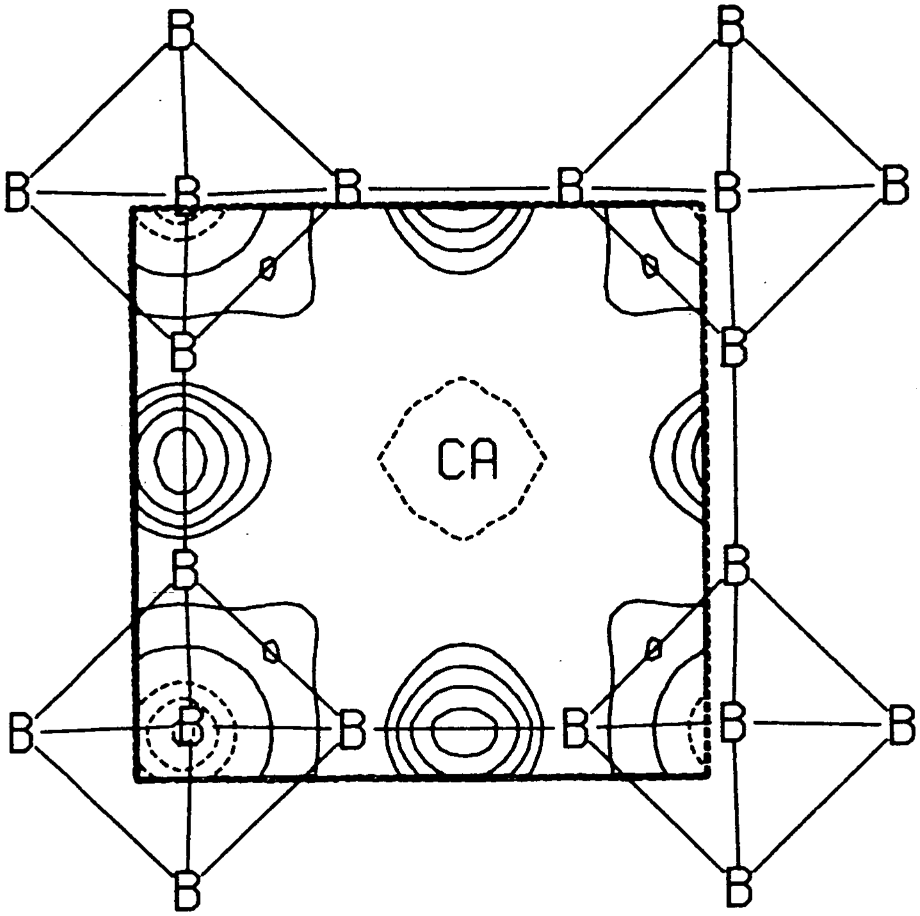

FIGURE 2.5.4(B)

Dynamic Deformation Density
for a plane perpendicular to 001 and passing
through the centre of an octahedral face.

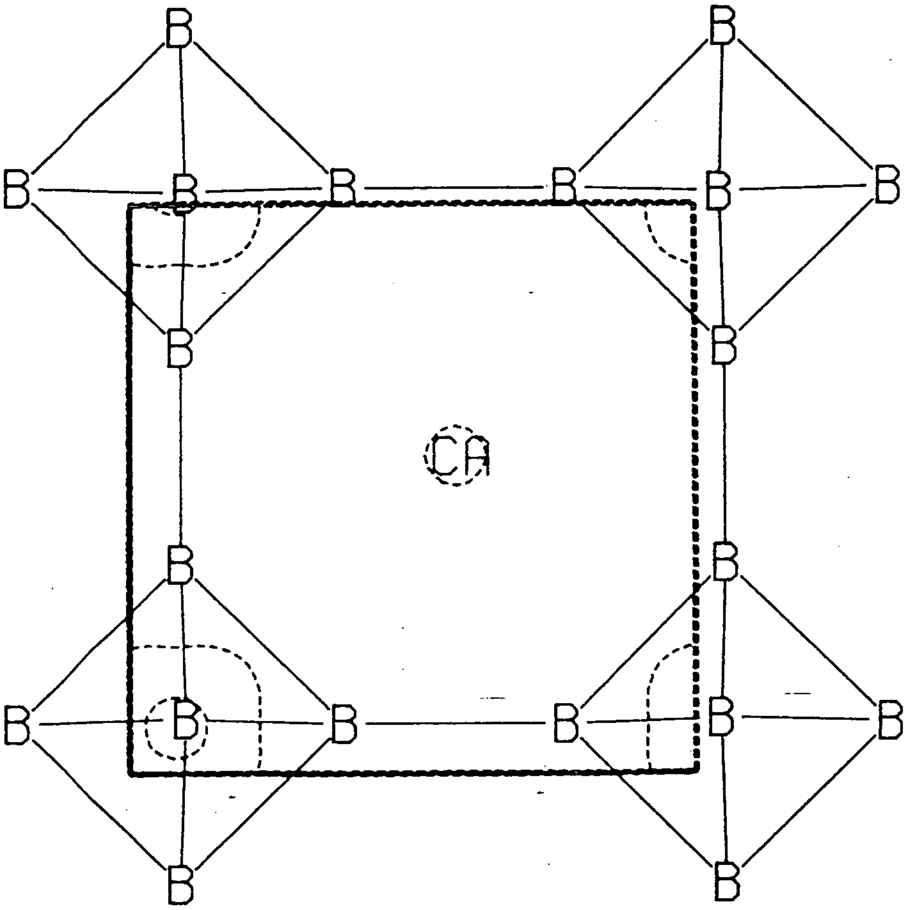

FIGURE 2.5.4(C)

Dynamic Deformation Density
for a plane perpendicular to 001 and passing
through a B position on 00z.

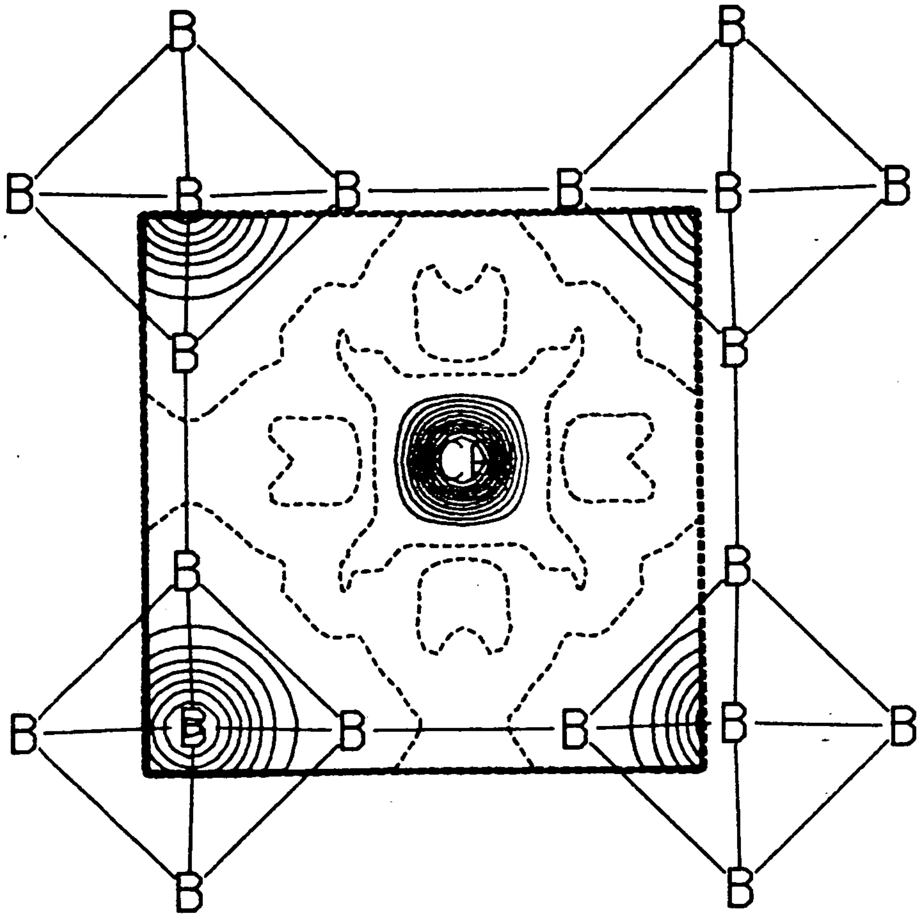

FIGURE 2.5.4(D)

Dynamic Deformation Density
for a plane perpendicular to 001 and passing
through the Ca position.

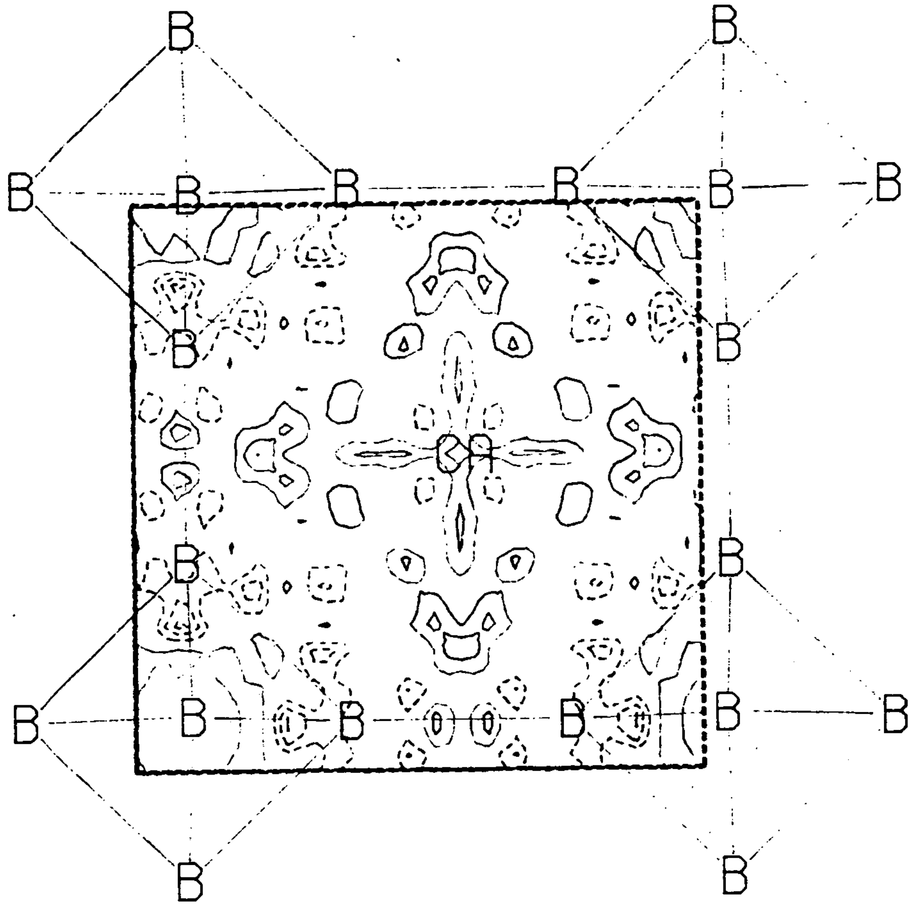

FIGURE 2.5.5(A)

Residual Density
for a plane perpendicular to 001 and containing
an octahedral centre .

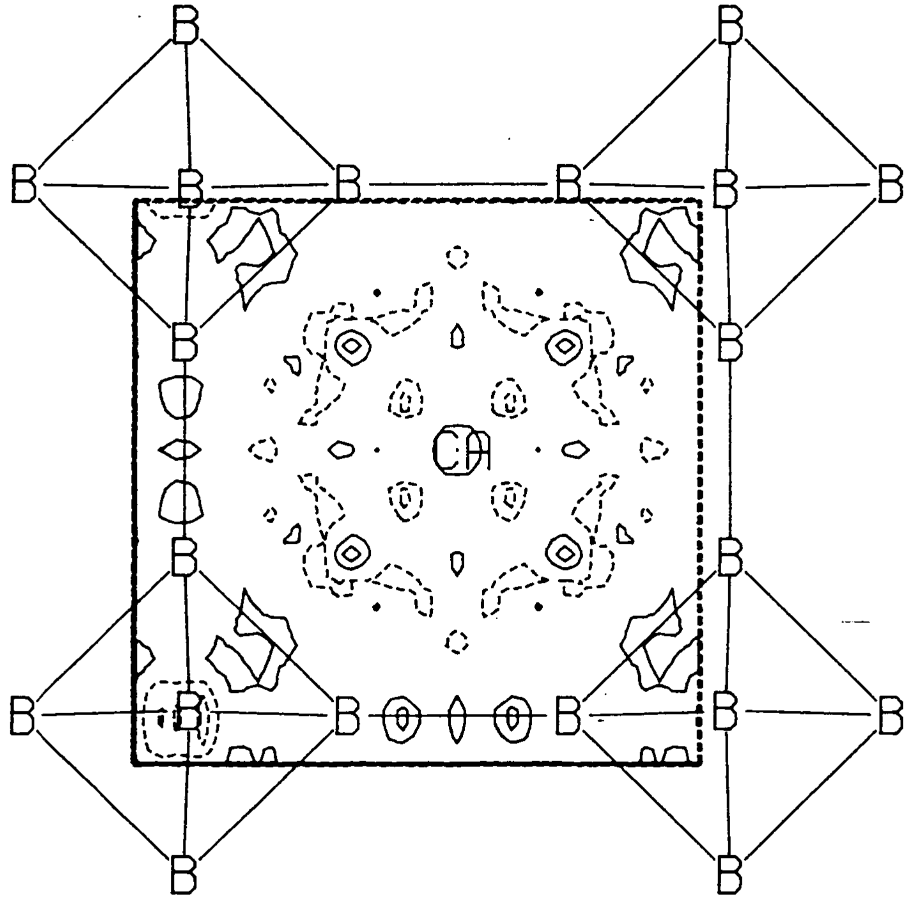

FIGURE 2.5.5(B)

Residual Density
for a plane perpendicular to 001 and passing
through a B position on 00z.

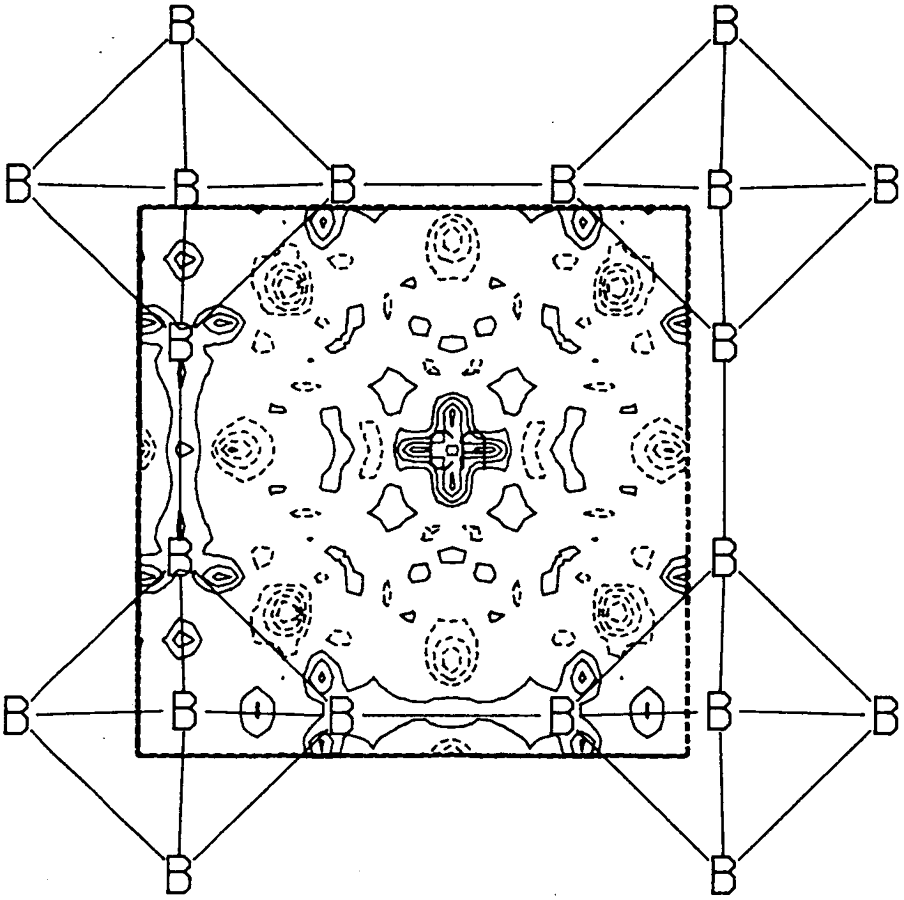

FIGURE 2.5.5(c)

Residual Density
for a plane perpendicular to 001 and passing
through the Ca position.

In the plane of the octahedral core (Fig 2.5.5(a)) the largest peaks are only 0.1eÅ^{-3} and while symmetrical are not significant. By contrast the residual at the Ca position (Fig 2.5.5(d)) is sharp but short range. This form cannot be rationalised by an inadequacy of deformation functions - the peaks are much too close to the core. However this form of residual can be interpreted as due to an inadequacy in the temperature factor for the Ca atom. The temperature factor is not inadequate because it is isotropic (that is a point symmetry requirement for a second rank tensor description) but because the displacement potential is anharmonic and needs to be modelled by a more complicated thermal parameter (ie third or higher rank symmetric tensor). This anharmonic behaviour is confirmed by the work of Paderno *et al* [35] which showed a non-linear dependence of the cell constant on temperature. Furthermore results of Paderno showed a non-linear increase of u_{bar}^2, the rms dynamic displacement. Figs 3 and 4 of reference 35 show that u_{bar}^2 as a function of temperature for the Ca atom is more curved than the corresponding one for the B_6 component. This agrees with the relative magnitudes of the residual density at the Ca and B positions.

2.5.6. The Limitations of Multipolar Maps

An analysis of the error in deformation density maps concludes that the errors are at their most serious in the vicinity of nuclear positions (< 0.03Å distant) and to a lesser extent in proximity to symmetry operators [36]. The esd of the static deformation density can be evaluated from the covariance matrix (see Section 2.5.3) for an example) but the integrations required for the esd of the dynamic density are considerably more time consuming and this is rarely attempted.

Excessive constraints applied to multipoles or the use of a deformation basis of inadequate flexibity will be revealed by the non random residual density in positions other than those of the atomic positions.

Where the static or dynamic deformation density is prepared by using structure factors there is a series termination error and a limit on the resolution obtained determined by the highest value of S used for the Fcalc's employed. The omission of reflections will introduce errors in proportion to their magnitude. These errors can be eliminated by using all reflections to such a high value of S that the resolution is limited by the grid over which the deformation density is evaluated and contoured. While this approach is obvious the manipulation of large structure factor lists, especially in low-symmetry Laue classes, slows computation.

For CaB_6 the distortions due to structure factor list truncation were therefore evaluated for planes corresponding to Fig 2.5.3(a) using 1) $S < 2.0Å^{-1}$ only (Fig 2.5.6(a)) 2) $S < 2.0Å^{-1}$ and $|F| > 1.5$ (Fig 2.5.6(b)). From these the distortion attributable to the exclusion of reflections of extreme high order is negligible but the exclusion of weak F's is serious (and unpredictable).

2.5.7. Moments and Charges

The refinement of multipolar functions on atoms includes even functions which are therefore associated with charge accumulation or depletion on the atom. For the RTAG refinement these are B −0.22(1) and Ca 1.34(1). These charges are not usually reliable because the diffuse functions on atoms may maximise between bonded atoms. The deformation density of such functions should therefore be partitioned. An established method is to evaluate the deformation density over divisions of the molecular volume and distribute the

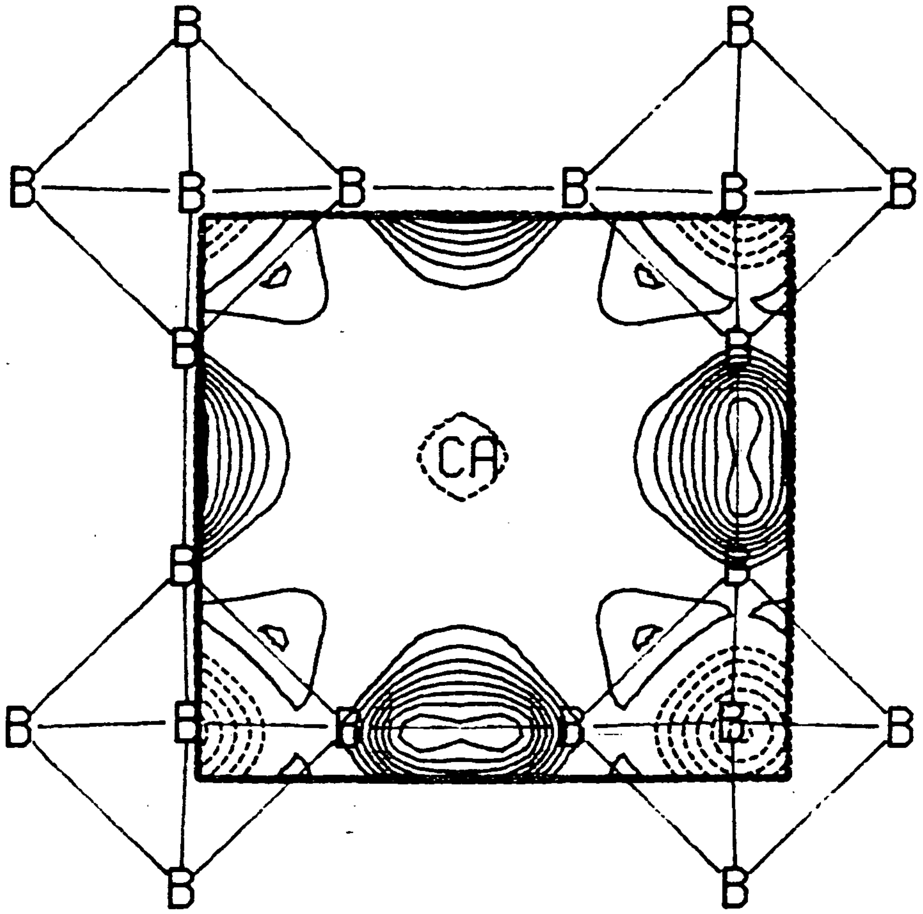

FIGURE 2.5.6(A)

[illegible] Static Deformation Density for the plane in 2.5.3(a). $S < 2.0 Å^{-1}$

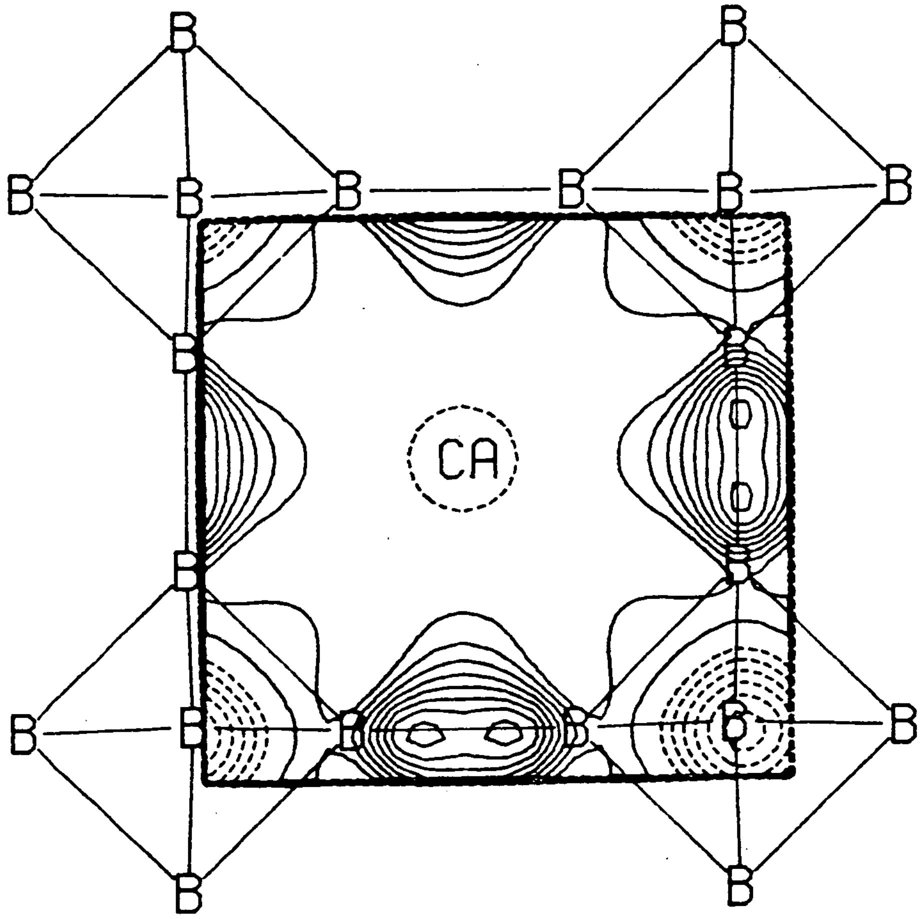

FIGURE 2.5.6(B)

[illegible] Static Deformation Density for the plane in 2.5.3(a). $S < 2.0 \text{Å}^{-1}$ *and* $|F| > 1.5$

deformation density within each division to each atom in proportion to the relative radial density of the neutral spherical atom at that distance. This formula[37, 39] has the advantage that when applied to the pro-molecule density the atomic charges are all zero. Application of the stockholder partitioning recipe, in this case, gives a similar charge distribution of B -0.20, Ca 1.20. These charges are of course not the classical charges $Ca^{2+}(B_6)^{2-}$ which might simplistically be expected for a calcium compound. They are however in good agreement with the result obtained using Pauling's electronegativity scale in conjunction with the electro-neutrality principle[38] with some corrections to the original theory (see Section 2.7.5). The charges according to Pauling's method are Ca +1.08 and B -0.18.

The moments can be deduced directly from the magnitude of the multipolar terms on each atom alone but these are excessive since deformation functions on neighbouring atoms could cancel. Multipoles from partitioned deformation density are therefore minimum values. Unique values are given below in Table 2.5.7 with respect to the local molecular axes. First and second moments are given in units of eÅ and eÅ^2 respectively. The integrations were carried out over a cube of edge 5.2Å centred on each atom type with divisions of 0.2Å.

TABLE 2.5.7

Moments and Charges

Atom	Charge	First Moment		Second Moment			
	Q	L	M,N	LL	(MM,NN)	(LM,LN)	MN
B	-0.20	0.023	0.005	-0.084	0.022	0	
Ca	1.49	0	-	14.035	-	0	-

Second moments

From these moments the quadrupolar moments can be deduced (but not vice versa) $\theta_{NN}=\mu_{NN} - 0.5\ (\mu_{LL} + \mu_{MM})$,$\theta_{MN}= (3/2)\ \mu_{MN}$ etc.

The quadrupolar moment for Ca is zero by symmetry while for B θ_{LL} = -0.106, θ_{NN}= -0.053. The interpretation of these values is that B gains electrons (negative q) which are distributed remarkably anisotropically ($\mu_{LL} << \mu_{MM} = \mu_{NN}$ or θ_{LL} not equal to 0) The negative μ_{LL} suggests excess electronic charge is concentrated on the 4-fold symmetry axis while the positive μ_{MM}, μ_{NN} confirm the depletion of electronic charge in perpendicular directions.

First Moments

The observation of μ_L as positive at first sight conflicts with the expected negative sign for negative charge on the +L axis (into the inter-octahedral bond) as shown in the multipole and X-X maps. The positive value indicates that the combined components on intra-octahedral bonding more than cancel the dipole moment from the more obvious inter-octahedral bonding.

2.5.8. Electric Field Gradient Tensor

The EFG tensor is a second rank tensor of zero trace [40], and can be estimated if the multipolar method is used to examine the deformation density as shown by Schwarzenbach and Thong [41](S&T). These computed values are important because they can be compared not only with *ab-initio* calculated values but with the magnitudes (and occasionally signs) of the eigenvalues interpreted from Nuclear Quadrupole Resonance (NQR) spectroscopy. Stewart [42] concluded that the EFG of light atoms, despite being a property dependent on inner moments, should be within the resolution of XRD measurements and called for cooperative efforts to confirm this.

However S&T investigated the (non-centrosymmetric) low quartz structure of aluminium phosphate [43], $AlPO_4$, and found that the electron distribution obtained by a standard multipole charge density refinement could not reproduce the correct EFG for the Al site (NQR -3.8, +2.4, +1.4, +0.5 ; XRD -0.4, +1.5, -1.1, -4.1 for ∇E_{11}, ∇E_{22}, ∇E_{33} and ∇E_{23} respectively, units of 10^{14}esu ; 1au = 3.2414×10^{15}esu cm^{-3}). This very poor result led to employing the NQR results as observations in the least-squares and hence the stabilisation of a difficult refinement. Thereafter a similar experiment was attempted on lithium nitride [44] where the modulus of the field gradient of *both* nuclei had been measured by NQR, but the agreement was again poor and frequently the esd's on the derived values for the EFG were similar to their magnitude. Their conclusion was that XRD observations could only infer some of the signs of the EFG eigenvalues and that the EFG, being a function of inner moments, was essentially complementary to XRD which effectively defines outer moments.

There have been several NQR studies of CaB_6 [45, 46, 47]. The site symmetry of the boron (4mm) means that the EFG tensor is adequately described by just one term (∇E_{11}) along the symmetry axis ($\nabla E_{22} = \nabla E_{33} = -0.5\nabla E_{11}$, $\nabla E_{12} = \nabla E_{13} = \nabla E_{23} = 0$) which is therefore simply called eq. Values for eq are not known precisely since the quadrupolar interaction coupling constant $|e^2qQ|$ is related by the nuclear quadrupole moment eQ which is usually only known to low precision eg ^{11}B eQ = 0.03×10^{24} cm^2 [48].

The probable value for $|eq|$ from NQR measurements is between 1.16 and 1.20 $e\text{Å}^{-3}$. The value for the deformation density refinement was calculated as follows. The observed eq can be considered as the sum of two terms. The first is due to the penetration of a nucleus into the spherical electron density of a neighbouring atom. This term is small and dominated by contributions from near neighbours (< 3Å). The second term is due to the deformation density of all atoms. In considering the large second term some assumptions have to be made about the degree of correlation of the thermal motions of the nucleus and the neighbouring atoms - information absent from elastic *X*-ray scattering. The second term is best calculated in reciprocal space ie using the structure factors of the deformation density alone in equation 11 of S&T.

The first approximation is that all atoms ride on the nucleus of interest, and the evaluation of structure factors is therefore done with the atom at the site static. For all rigidly bonded atoms, (together with those equivalent by translation) the thermal motion is corrected by subtracting out that of the EFG nucleus. Such an approximation reduces the space group rotational symmetry to that of the EFG site. For CaB_6 and EFG at the B nucleus the space group for structure factor evaluation then reduces to P4/mmm with two independent borons. Unfortunately this standard procedure is complicated by the fact that, for the boron atom which is not the EFG site, the corrected thermal parameter can not be positive definite.

The calculation of the EFG was therefore carried out making the further assumption that all thermal motion is due to lattice vibrational motion. The EFG tensor was calculated from deformation density structure factors and the computer program 'TENSOR'[49]. The result is fully defined by an eq of +2.09 $eÅ^{-3}$. The dependence on thermal parameter subtraction was investigated by allowing Ca to have a thermal motion relative to the EFG site equivalent to $u = 0.008063Å^2$. This model gave an eq of 2.01 $eÅ^{-3}$. Before comparing either of these with the NQR values, a term has to be added due to the promolecular density of neighbours. This was evaluated using the program 'TENSNEB'[50] to be eq = −0.53 eÅ^{-3}. The EFG is therefore calculated to be 1.56 eÅ^{-3}. The experimental (NQR) value of 1.20 eÅ^{-3} is in good agreement with those calculated from the multipole refinement. The value of 1.56eÅ^{-3} (entirely static) is a maximum value; allowing Ca to have an imperfectly correlated motion gives 1.48eÅ^{-3}. Such differences are slight in comparison with the esd of the EFG which (using another version of the multipole program on the same data) is calculated to be ca. 0.2 eÅ^{-3}. The sign and magnitude of the EFG from NQR and XRD measurements is supported by *ab-initio* calculations on $[B_6H_6]^{2-}$ (in a crystal field) where the EFG is estimated at 1.18 eÅ^{-3}. That this necessarily static value of 1.18eÅ^3 is close to the NQR experimental value is plausible because of the low amplitude of vibration of the atoms in this refractory solid.

2.6. Theoretical Deformation Density

2.6.1. The Method of Calculation

Calculations on isolated molecules can be made to greater accuracy than for periodic systems although substantial progress has been made in work on the latter [51]. The current optimal approach to *ab-initio* calculations on periodic systems such as CaB_6 is to identify the unit cell and divide the neighbouring atoms into three types. For those within the asymmetric unit integrations are explicit (as for molecular calculations), those at intermediate range are modelled by a linear combination of multipoles, the order of which is allowed to decrease with increasing range until the final range where point charges are used. Unfortunately the means for such a calculation were not available.

The approximation employed made use of the available package GAMESS (General Atomic & Molecular Electronic Structure System) where CaB_6 was successively modelled by

$[B_6H_6]^{2-}$

$[[(B_6H_5)_2]^{4-}(X^{2+})_4]^{4+}$

$[[(B_6H_5)_2]^{4-}(X^{2+})_{24}(Y^{2-})_{22}]^0$

where X and Y are point integer charges devoid of basis functions.

Values for parameters such as prefactor tolerance for integrals and SCF convergence criterion are listed in Appendix III.

2.6.2. Models for CaB_6

The models could not be larger than 2 octahedra for even with recognition of symmetry equivalent integrals the calculations become prohibitively time consuming. While the $[B_6H_6]^{2-}$ ion and B_6^{2-} octahedra are electronically similar their geometry is slightly different. The B-B distance in $[B_6H_6]^{2-}$ is 1.69(1)Å, while that in CaB_6 is larger at 1.748(1)Å. While CaB_6 was a superior material for an XRD study and was chosen to model $[B_6H_6]^{2-}$ the calculations use $[B_6H_6]^{2-}$ and the dimer $[(B_6H_5)_2]^{4-}$ *not* to model $[B_6H_6]^{2-}$ but to provide theoretical results for comparison with experimental work. The models are therefore built using the bond distance from preliminary diffraction results on CaB_6. Finally, the wavefunctions for $[B_6H_6]^{2-}$ were recalculated using a B-B distance of 1.69Å to demonstrate any changes in deformation density associated with a change in the absolute size of the octahedron. Parameters are given below. Coordinates are in Appendix IV.

Model I

$[(B_6H_5)_2]^{4-}(X^{2+})_4$: D_{4h} intra-octahedral B-B 1.748Å, inter-octahedral B-B 1.673Å, B-H 1.167Å.

Model II

$[(B_6H_5)_2]^{4-}(X^{2+})_{24}(Y^{2-})_{22}$: D_{2h} Bond lengths as per model I.

Model III

$[B_6H_6]^{2-}(X^{2+})_{24}(Y^{2-})_{23}$: C_{2h} Bond lengths as per model I.

Model IV

$[B_6H_6]^{2-}(X^{2+})_{24}(Y^{2-})_{23}$: C_{2h} intra-octahedral B-B 1.690Å, B-H 1.167Å.

2.6.3. Theoretical Static Deformation Maps

The static deformation density was calculated and plotted using the program MOSCOW [52]. Reference atomic densities were derived from calculations, using the same basis on A_2 systems with d(A-A) = 17au (9Å) with averaging of atomic states where appropriate.

The maps were calculated using grids of 51x51 points using symmetry where applicable. The absence of an external field in calculations on $[B_6H_6]^{2-}$ (or the dimer) gave unbound valence molecular orbitals. The use of only 4 point charges of +2, in positions corresponding to Ca in CaB_6 gave a solution where all occupied orbitals of $[(B_6H_5)_2]^{4-}$ were bound. However, the deformation density map showed substantial distortion of the valence density of each of the B_6 octahedra (Fig 2.6.3(a)). The use of an extended array of 46 point charges gave a map where the density in the vicinity of the octahedron

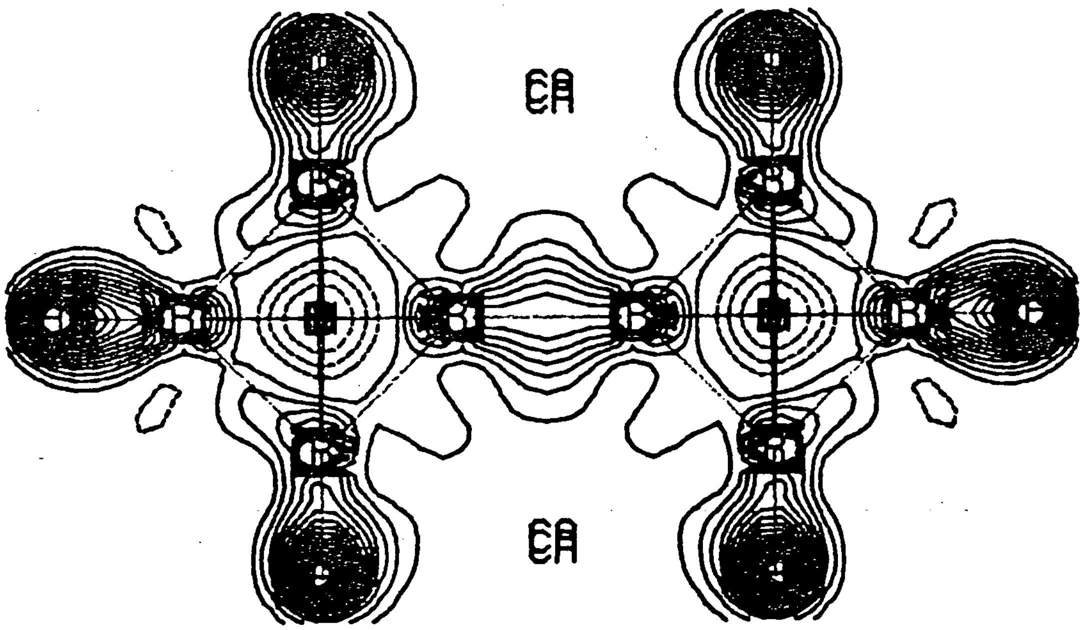

FIGURE 2.6.3(A)

Theoretical Deformation Density
in $[(B_6H_5)_2]^{4-}(X^{2+})_4$

further approached octahedral point symmetry (Fig 2.6.3(b)). The latter point charges were in a D_{2h} point symmetry - lower than the molecular point symmetry of D_{4h} - to test the degree of convergence. Examination of similar planes showed no important differences.

The electrostatic potential of the 46 point charges through a symmetry plane of $[(B_6H_5)_2]^{4-}$ is shown in Fig 2.6.3(c). Contours are in intervals of 0.05 au. This is similar to the more precise potential of 48 2+ charges and 132 charges of −1/3 at the neighbouring Ca and B positions respectively (Fig 2.6.3(d)). The potentials agree well for B positions if not the H positions of $[(B_6H_5)_2]^{4-}$. The use of integer point charges is therefore adequate (the use of non-integer point charges is not permitted within the *ab-initio* program GAMESS). The validity of using only 46 point charges is not so easily demonstrated for although the Coulombic potential is easily calculated the series, as a function of distance from the origin, is poorly convergent.

Examination of the map passing through the 8 octahedral edges and both centres shows the following features (Fig 2.6.3(b))

- large accumulation of density on the inter-octahedral connectivity peaking at 0.35-0.40eÅ^{-3}. The density broadens considerably at the midpoint.
- Weak, diffuse surplus electron density along the octahedral edges of 0.05-0.10eÅ^{-3}. The density is mostly outside the edge.
- Medium deficiency of electron density at the core of each octahedron. The minimum is approximately -0.15eÅ^{-3}.

A second map, Fig 2.6.3(e), based on the same calculation for a plane rotated 45° from the first about the symmetry axis further reveals :

- Weak, diffuse surplus density over the octahedral faces of 0.10-0.15eÅ^{-3}.

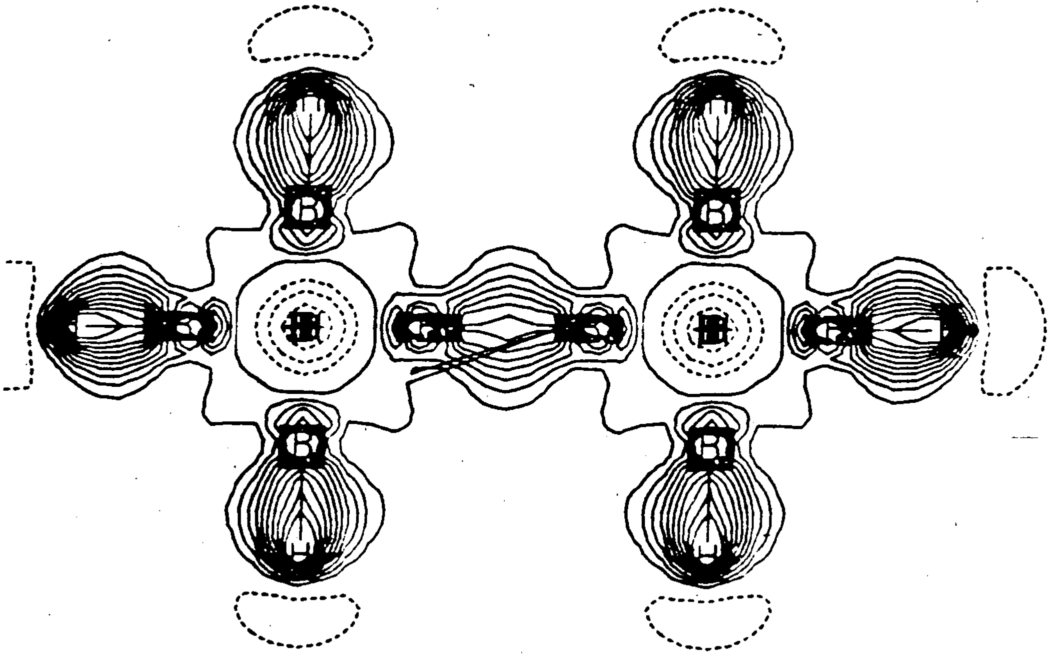

FIGURE 2.6.3(B)

Theoretical Deformation Density in $[(B_6H_5)_2]^{4-}(X^{2+})_{24}(Y^{2-})_{22}$

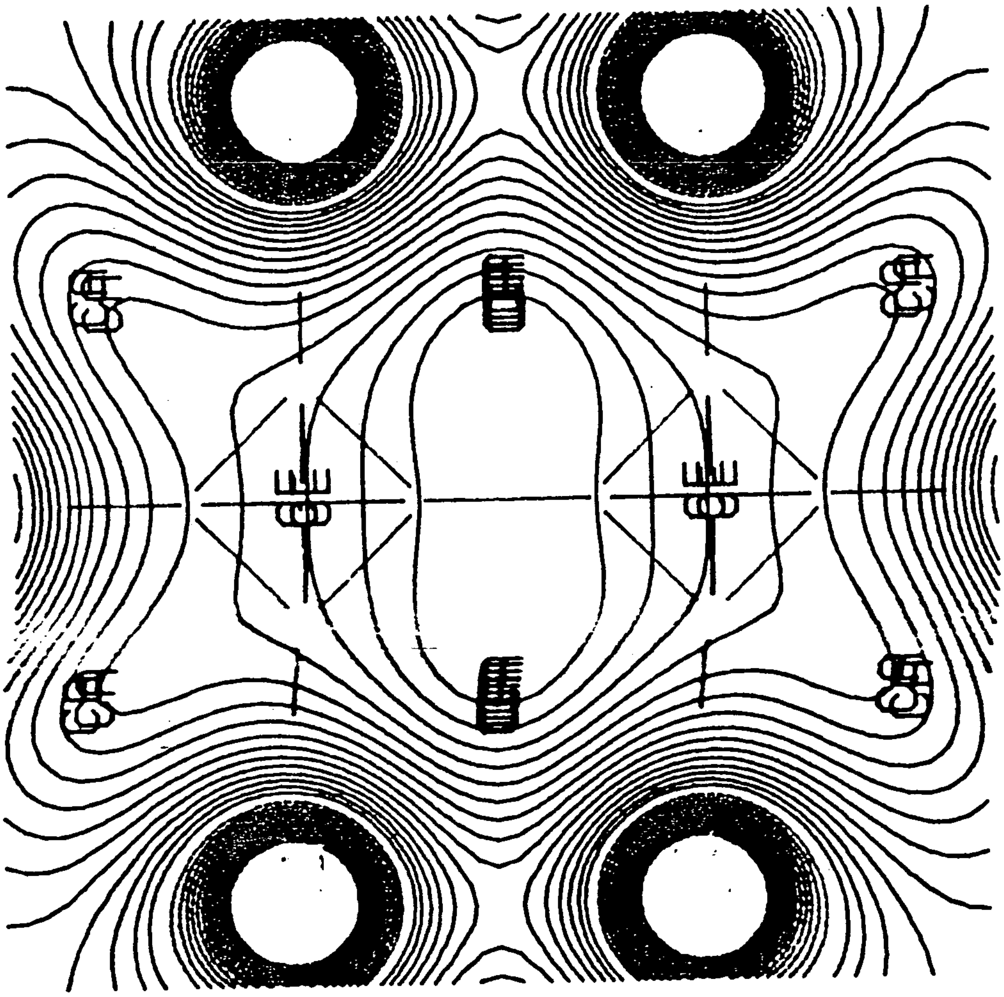

FIGURE 2.6.3(C)

External Electrostatic Potential
for $(X^{2+})_{24}(Y^{2-})_{22}$

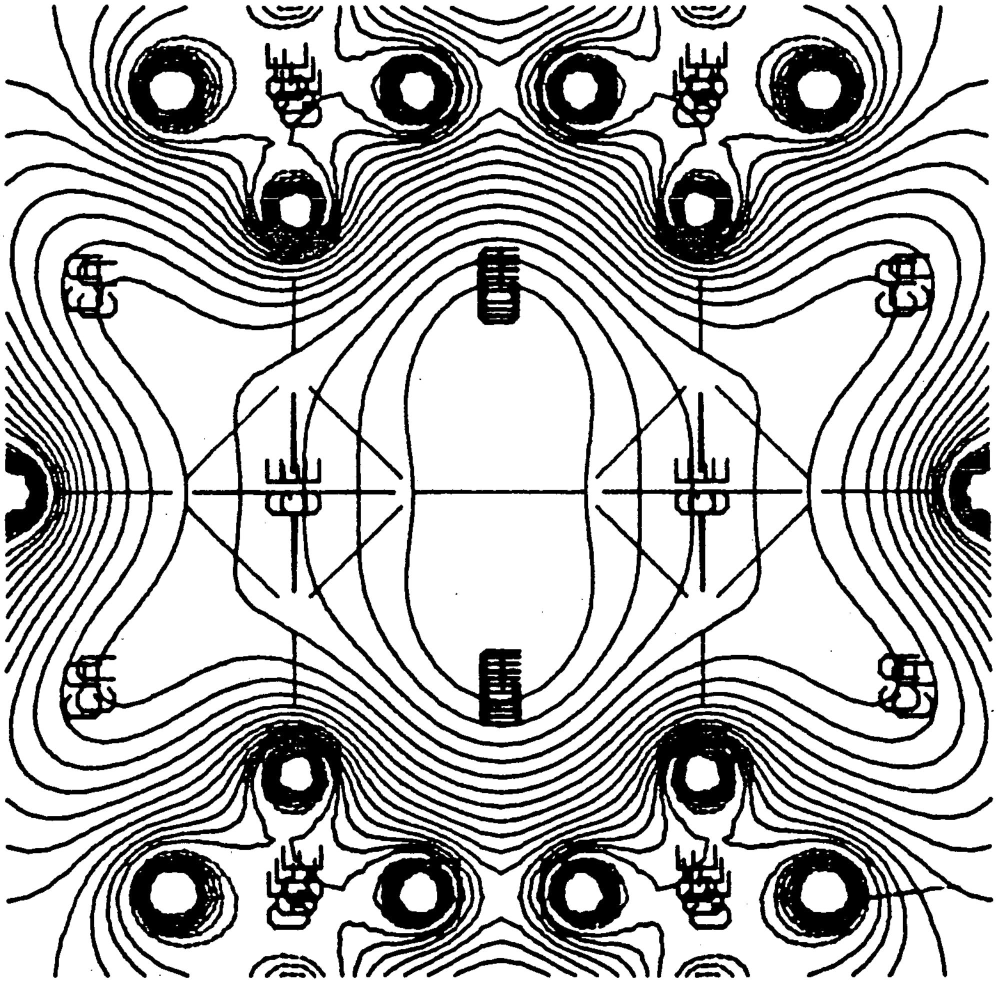

FIGURE 2.6.3(D)

External Electrostatic Potential for $(X^{2+})_{48}(Y^{-1/3})_{132}$

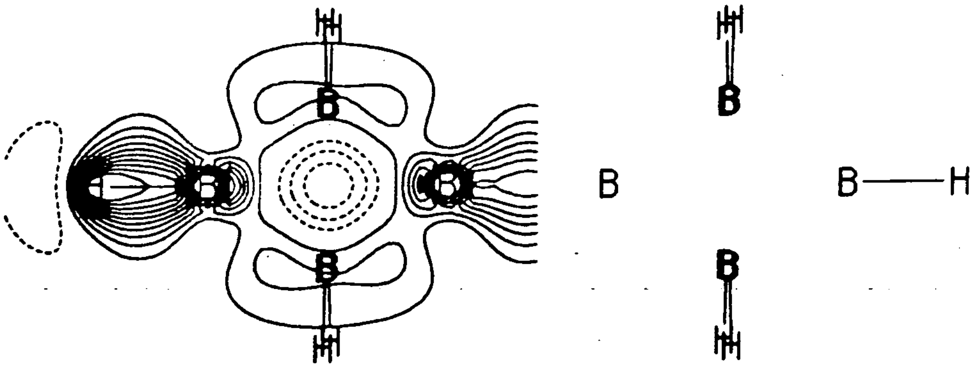

FIGURE 2.6.3(E)

Theoretical Deformation Density
in $[(B_6H_5)_2]^{4-}(X^{2+})_{24}(Y^{2-})_{22}$

The overall shape of the surplus deformation density over the octahedra is shown in perspective for the iso-density surface at 0.10eÅ^{-3} (Fig 2.6.3(f)) and shows clearly how most of the intra-octahedral density is positioned over the faces (rather than the edges) in the form of triangular pyramids in a conformation staggered with respect to the triangular faces.

The negative of the Laplacian function (ie $-\nabla^2\rho = - d^2\rho/dx^2 - d^2\rho/dy^2 - d^2\rho/dz^2$) gives extra insight into the electron density distribution. The Laplacian of the molecular electron density is presented in Figs 2.6.3(g),(h). Contours levels are in a geometric series (0.01,0.02 ... 0.64au) These figures show inter-octahedral = -0.32au (intense localisation), intra B-B edge = -0.08au (weak localisation) and at the face of an octahedron = -0.04au (very weak localisation). In describing the intra-octahedral density the term 'localisation' should be applied to the octahedral edge and not the face even though the edge density has a smaller deformation density maximum.

2.7. Discussion: Theory and Experiment

2.7.1. Which Maps Should be Compared

In comparing the results of theory and experiment there can be two approaches.

The first is to compare the static theoretical density with the static experimental density. The latter density can be calculated only if the experimental diffraction data is fitted using a multipolar model

The second approach is to compare dynamic deformation densities for which the experimental density is prepared by a Fourier transform of the deformation density structure factors (which have been multiplied by a

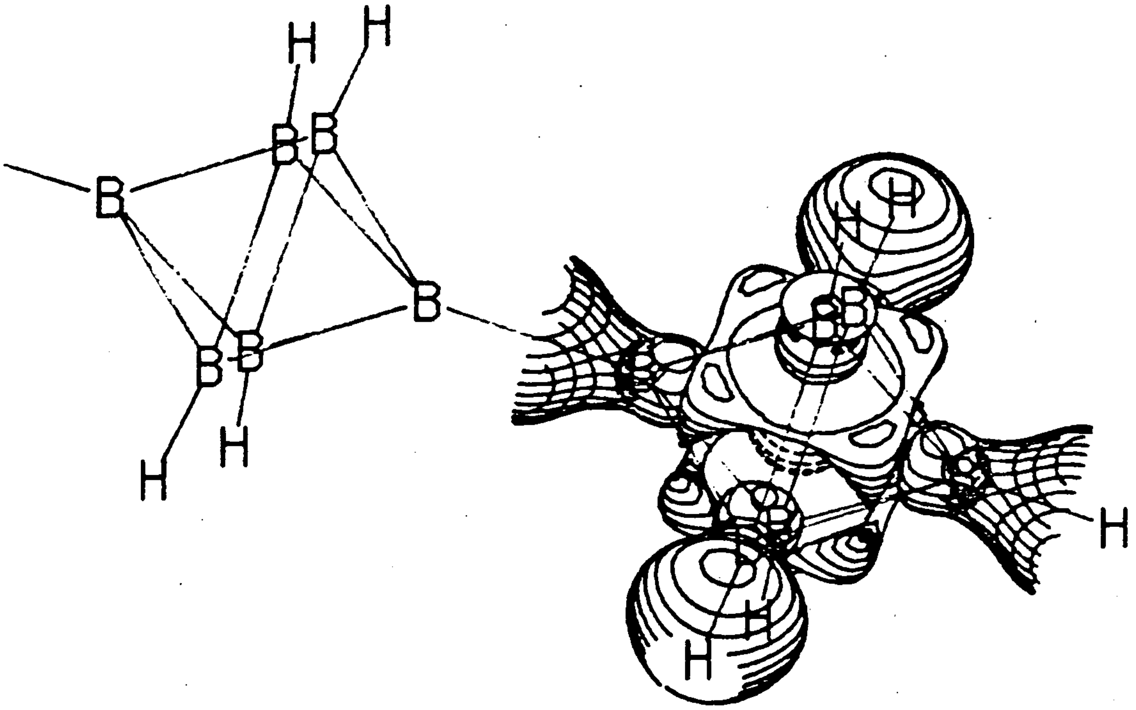

FIGURE 2.6.3(F)

Theoretical Deformation Density:
Iso-deformation density Surface for $[(B_6H_5)_2]^{4-}(X^{2+})_{24}(Y^{2-})_{22}$

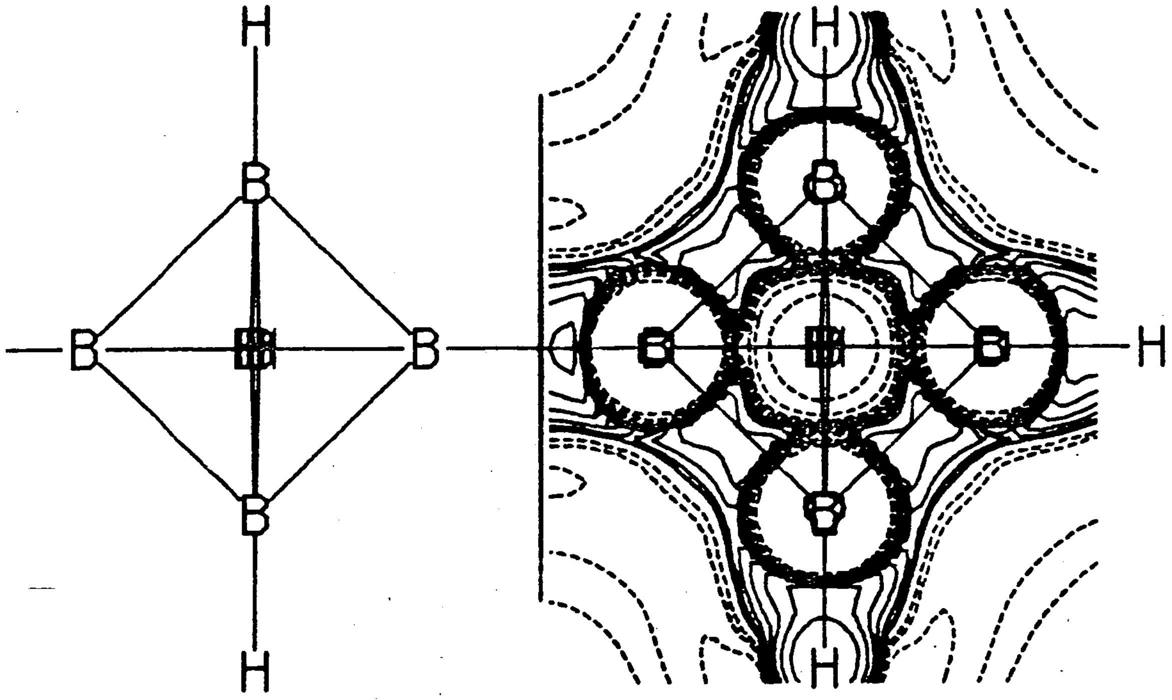

FIGURE 2.6.3(G)

Negative Laplacian of Electron Density
for $[(B_6H_5)_2]^{4-}(X^{2+})_{24}(Y^{2-})_{22}$
for the plane in 2.5.3(a).

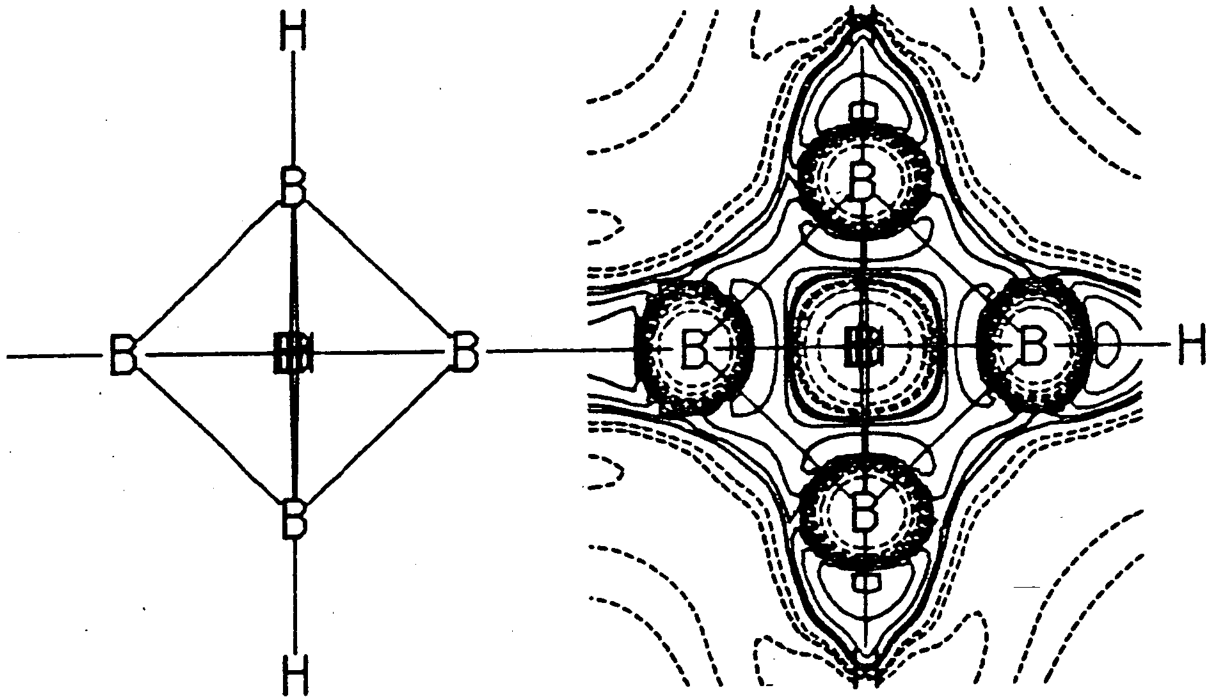

FIGURE 2.6.3(H)

Negative Laplacian of Electron Density
for $[(B_6H_5)_2]^{4-}(X^{2+})_{24}(Y^{2-})_{22}$
for the plane in 2.5.3(b).

temperature factor.) The theoretical dynamic density is prepared by using the XRD determined thermal parameters and an algorithm for partitioning the electron density before application of the thermal parameters of the various atoms. This process is well documented but not trivial [53,54]. The electron density can be represented by a density matrix. Diagonal terms are clearly associated with just one atom as are the products of basis orbitals sited on the same atom. The remaining off-diagonal or overlap density must be partitioned between the pair of atoms and the respective atomic thermal parameters applied to each. This partitioning need not simply be division into halves.

The more critical comparison, and more readily executed, is between static deformation densities. If these agree before thermal convolution then they will continue to do so after convolution. Note, however, that differences visible before convolution may be blurred or undetectable afterwards. Also, the static experimental map is a display of information which is not strictly inherent in the data and features in it are dependent on the model being reasonable. The use of subtly different multipolar refinement programs with the same data has been shown to yield almost identical dynamic deformation density maps [1] but slightly different static maps. Calcium hexaboride and other polymeric solids or minerals have such low amplitudes of vibration that the distinction is less important.

Comparison of the static maps (Figs 2.5.3(a), 2.6.3(b)) shows them to be remarkably similar with the sign and magnitude of the deformation density agreeing over a wide area. Deformation densities at selected points are compared below in Table 2.7.1.

TABLE 2.7.1

A Comparison of Deformation Densities

Point	$\Delta\rho/e\text{Å}^{-3}$ multipole XRD	4-31G
B_6 core	-0.30(2)	-0.15(2)
B_6 face	0.10(5)	0.10(2)
B_6 edge	0.10(5)	0.05(2)
inter B_6	0.40(5)	0.35(2)

The only point where the values are substantially different is the core of the B_6 octahedron where the *X*-ray determined deformation is almost twice that calculated using a 4-31G basis and model II. This difference can only be attributed to an error in an a_{1g} (with respect to the octahedron) type wavefunction. This symmetry is also one of those possible by linear combination of calcium s-orbitals which are of course absent.

To investigate whether the calculated core deformation could change drastically if the basis functions were extended a further calculation was carried out on model III with split valence s-basis functions (equivalent to those on H in the 4-31G basis) at the core. The deficit remained unchanged and the energy decreased by only 0.04au. Repeating the calculation with 8 basis centres, each at the centre of an octahedral face reduced the energy much more (0.28au) but still did not alter the core deformation.

Whether the true core electron deformation density is -0.30 or $-0.15e\text{Å}^{-3}$ is debatable but the sign is certainly negative. The sign is important because there is a popular misconception that in boron polyhedra there is strong intramolecular bonding between non-adjacent boron atoms across the core. This has been reflected in the choice of algorithm for an empirical method, the 'bi-reciprocal potential' to estimate the relative stability of various n-vertex polyhedra for a given value of n [55]. This method has been criticised [56] for encouraging users of the method to believe that the cross-polyhedral binding component is important although the proponents of the method have re-affirmed [57] that while the application gives weight to these components the method is empirical and that it was never intended that the energies for model compounds could be meaningfully sub-divided. Other authors [59,58] have calculated the total electron density for a hexaboride and mis-interpreted the accumulation of total electron density within the polyhedron as an indication of cross-polyhedral bonding. In fact the mere overlap of six spherical atoms in an octahedral arrangement would alone give higher electron density values within the polyhedron. When the spherical atom (promolecular) density is subtracted (to give the deformation density) the stress on cross-polyhedral bonding is demonstrated to be unfounded.

2.7.2. External Comparisons

Once the experimental electron density distribution has been determined it might be hoped that electrostatic and other properties could be calculated and compared with values deduced from other experimental techniques. Examples of properties would be molecular dipole moments, force constants, and electric field gradients. Comparison of molecular dipole moments using Hirshfeld-type multipole refinements with those determined by experiment or *ab-initio* calculation are fair [60] but are dependent on accurately partitioning the deformation density between a molecule and its neighbours in the lattice.

The calculation of force constants is by application of the Hellmann-Feynmann theorem and classical electrostatic arguments.

$$-F_{\alpha,x} = dE/dx_{\alpha} = \int dV_{ne}(r)/dx.\rho(r)dr$$

where V_{ne} is the electron - nuclear interaction term, dE is the energy change when nucleus α is moved along the x-direction and $\rho(r)$ describes all the electronic and neighbouring nuclear charge density. Unfortunately this is usually flawed by the fact that calculation of the electric field vector at the nuclear position frequently finds it to be non-zero, in which case the nucleus cannot be at its equilibrium position and dE/dx may be negative. It is for the same reason that *ab-initio* methods cannot give force constants unless the molecule has first been geometry optimised. This flaw can be overcome by using the certainty that the electric field vector is zero at equilibrium as an observation and, through its dependence on the deformation density and hence the structure factors, be used in the least squares refinement of deformation multipoles. The inclusion of this extra observation has been shown to give little extra information on the deformation density - the zero-field condition is easily fulfilled by a short range deformation function which decays before it reaches the reliable region of bonds.

Molecular dipole moments are not appropriate to CaB_6 and atomic moments are not observables ie while molecular dipole moments can be deduced from some spectroscopic techniques *atomic* moments can not.

Finally there is the electric field gradient (EFG) tensor which is calculable (usually at the site of a nucleus) according to:

$$\nabla E_{mn} = \frac{\int 3x_m x_n - \delta_{mn} |r|^2 \rho(r) d^3r}{4\pi\epsilon_0 |r|^5}$$

where ∇E is a symmetric tensor of rank two and has zero trace (trace = $\nabla E_{11} + \nabla E_{22} + \nabla E_{33}$), x_m is the coordinate in the m-direction of volume element d^3r. The charge density in the volume element is given by $\rho(r)$ and includes nuclei and electrons (except the nuclear charge of the nucleus for which ∇E is evaluated). EFG terms have proper SI units of $JC^{-1}m^{-2}$ or equivalently Volt m^{-2}. Frequently these are, however, calculated excluding the vacuum permitivity constant $4\pi\epsilon_0$ and therefore reported in Cm^{-3} or em^{-3} or some other expression of charge concentration. For nuclear isotopes of spin not equal to 1/2 then the Nuclear Quadrupole Resonance (NQR) spectra of the solid can give up to 5 quantities [62] viz the quadrupole coupling constant $|eQ.\nabla E_{zz}/h|$ (where eQ is the nuclear quadrupole moment - a constant for a given nucleus - and h is Plank's constant), the asymmetry parameter $\eta = (\nabla E_{xx}-\nabla E_{yy})/\nabla E_{zz}$ where $0 \leq \eta \leq 1$), and finally up to three orientation parameters of the eigenvectors x,y,z with respect to the unitary crystal coordinate system. The two isotopes of boron ^{10}B, ^{11}B have spins of 3 and 3/2 and abundances of 19.6 and 80.4% respectively.

The NQR spectrum of CaB_6 and related compounds have been reported several times [46,45]. For CaB_6 the quadrupolar coupling constant has been found to be 1.26(2)MHz (Sears,1982) and 1.22(1)MHz (Aono,Kawai,1979). This difference does not necessarily mean that the esd's are underestimated or the values imprecise. The lattice parameter of A&K's (from their Figure 3) was 4.150(5)Å, while that of Sear's sample was not stated. This lattice parameter is clearly different from the results of this work (a=4.1422(5)Å). The QCC value has been demonstrated by A&K to decrease with increasing lattice parameter and so a value of 1.26Mhz for a=4.14Å would still fit on A&K's experimental curve (their Figure 3). This large uncertainty in the QCC translates to an estimation of $|eq|$ for B of between 1.20 and 1.15eÅ^{-3}. The value calculated from a deformation multipole refinement is 1.56eÅ^{-3}. (See Section 2.5.8 for the method of calculation). The match of the magnitude is good but furthermore the sign is definitely positive in agreement with that computed by

A&K using Bloch functions [45] which gave eq= $+1.25e\text{Å}^{-3}$. The 4-31G *ab-initio* calculation (model III) gives eq = $+1.18e\text{Å}^{-3}$ which confirms the correctness of the positive sign and the limited utility of Huckel-type band calculations in estimating electric field gradients.

2.7.3. Bonding in CaB_6

The interesting inability to assign simple 2-electron 2-centre bonds to all B-B connectivities in MB_6, even assuming charge transfer from electropositive metals, led to an investigation by Longuet-Higgins and Roberts (L-H&R) which used an LCAO Huckel type approximation in a band calculation with only a B 2s2p basis. The results were not on an absolute energy scale, nevertheless this simple calculation showed the structure could be interpreted as linked closed shell $[B_6]^{2-}$ octahedra. L-H&R concluded that $M^{2+}B_6{}^{2-}$ should be either insulators or semi-conductors while $M^{3+}B_6{}^{3-}$ should be metallic conductors. The experimental conductivities were at that time still in some doubt and L-H&R interpreted the reported weak conductivity of bivalent metal hexaborides as attributable to impurities but accepted the reported conductivity of trivalent metal hexaborides as genuine and attributable to the incompletely occupied energy band they had calculated.

The point symmetry of the boron atom suggested to Flodmark that d-orbitals on the boron atom should play an important role in determining the electronic properties. In 1959 Flodmark therefore presented elaborate and detailed work [64] where 3s3p3d (ie M-shell functions) were included on boron. Unfortunately the inclusion of these M functions with their long-range overlaps gave rise to new bands which were of lower energy than occupied bands in the L-shell approximation. The results therefore gave metallic conductivity in MB_6 for divalent and trivalent atoms. Flodmark interpreted the then current experimental conductivities for divalent metal hexaborides to be true.

Subsequent investigation by Etourneau et al [65] on magnetic susceptibility, thermoelectric power and specific heat measurements led to the conclusion that ThB_6 and LaB_6 were trivalent metallic conductors and that Ca/Sr/YbB_6 were semiconductors in agreement with L-H&R. This view now prevails.

All the above at least agreed that the boron acted as an electron acceptor but this opinion was not universal and the use of *X*-ray Photoelectron spectroscopy (XPS or ESCA) by Aleshin, Serebryakova *et al* [66] was helpful in classifying borides with B as either an acceptor or donor. The only hexaboride tested was CaB_6 for which B was an electron acceptor with the binding energy of the 1s boron electrons (187.5eV) less than that for rhombohedral boron (187.8eV).

Another ESCA study [67] had a B 1s binding energy nearer 187.0 eV perhaps indicating the importance of avoiding surface oxidation. This study confirmed, via the ESCA profile, the weak covalent bonding between the boron and metal atoms in hexaborides. The profile fitted well that estimated from the model of L-H&R and did not agree with the alternative model of Yamazaki [68] where metal-boron overlaps were included in an LCAO method calculation.

2.7.4. Bonding in $[B_6H_6]^{2-}$

The size of the B_6 octahedron is smaller in $[B_6H_6]^{2-}$ than in CaB_6 with B-B = 1.69Å rather than 1.75Å. It might therefore be expected that the inward pointing sp hybrids on B-H fragments should have a greater overlap and consequently the core deformation density to be less deficient than that observed in CaB_6 or calculated in the $[B_6H_6]^{2-}$ or $[(B_6H_5)_2]^{4-}$ used to model CaB_6.

This expectation is not confirmed by calculations on $[B_6H_6]^{2-}$ with B-B =1.69Å (Fig 2.7.4(a)) and B-B = 1.75Å (Fig2.7.4(b)) where the core deformation density remains $-0.15e\text{Å}^{-3}$ but in the former the edge bonding increases to $0.10e\text{Å}^{-3}$. The general topology of the deformation density nevertheless remains unchanged.

2.7.5. Pauling's Electroneutrality Principle: Does $Ca^{2+}(B_6)^{2-}$ Exist?

The charges calculated by stockholder-type partitioning of the deformation density do not correspond to $Ca^{2+}(B_6)^{2-}$ as might simplistically be expected for a calcium compound. This section seeks

- to correct the popular misconception of near-integer charges in the solid state of salts.
- to re-interpret Pauling's electroneutrality principle especially in its application to the charges in solid state salts.
- to explain why the more moderate charges of $Ca^{1.20}(B_6)^{-1.20}$ were found and show how application of a corrected version of Pauling's electroneutrality principle can be used to estimate charges where there has been no deformation density study.

The evidence against the integer ionic charges such as are usually written in formulae such as Na^+Cl^-, $Mg^{2+}O^{2-}$, $(Al^{3+})_2(O^{2-})_3$ is the high second and third ionisation potentials (IP's) of metals. For Al the second IP is approximately double the energy released upon oxidation of the metal and the third IP still higher. Evidence for large charges in compounds includes measurements on aqueous solutions which clearly support the existence of $Al^{3+}_{(aq)}$. However Pauling recognised that there was no evidence for large charges on atoms in

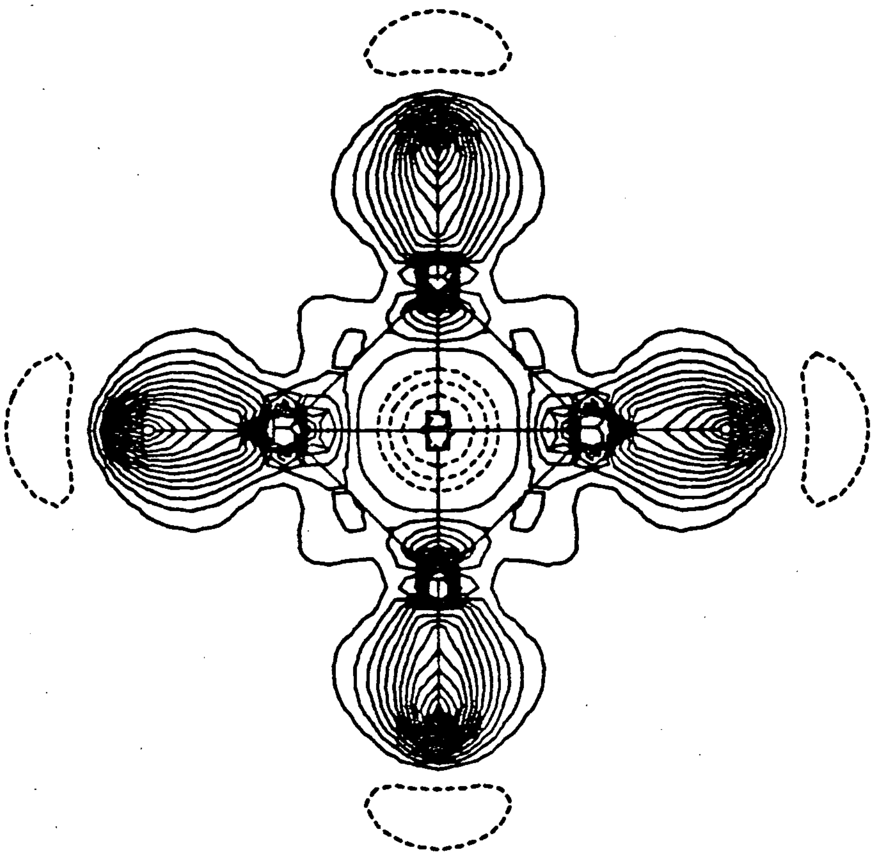

FIGURE 2.7.4(A)

Theoretical Deformation Density
in $[B_6H_6]^{2-}(X^{2+})_{24}(Y^{2-})_{23}$,
B–B 1.69Å.

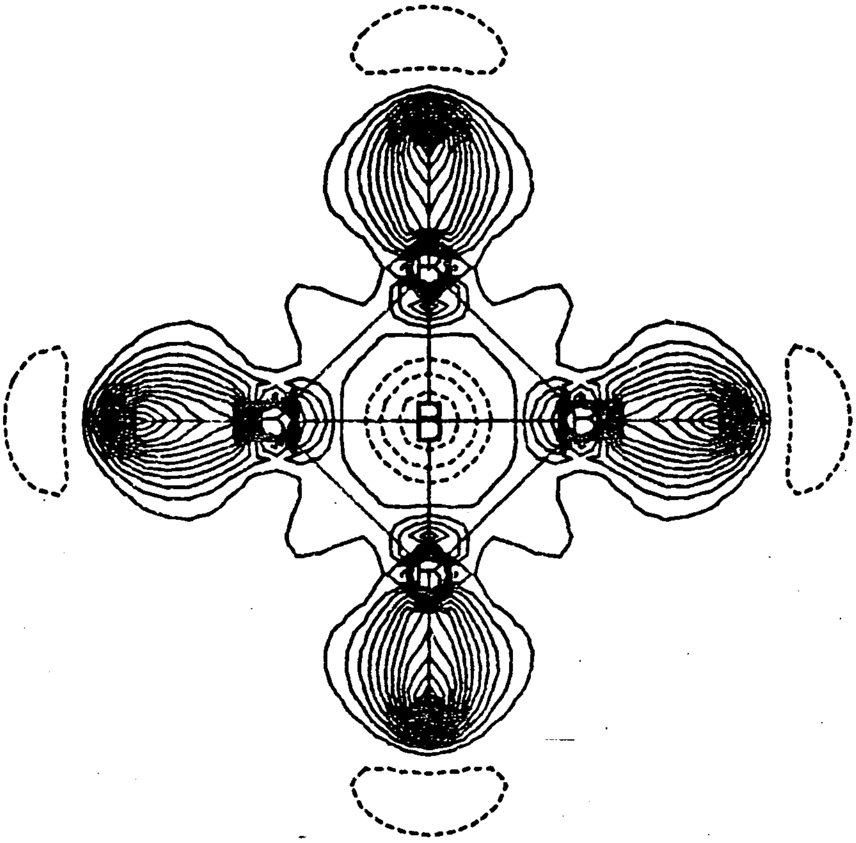

FIGURE 2.7.4(B)

Theoretical Deformation Density
in $[B_6H_6]^{2-}(X^{2+})_{24}(Y^{2-})_{23}$,
B-B 1.75Å.

chemically bonded molecules. The conductance measurements only confirmed the existence of $[Al(H_2O)_6)]^{3+}$. In 1948 Pauling formulated his *postulate of the essential electrical neutrality of atoms.* This is fundamental to the following discussion and is reproduced below.

> ... the electronic structure of substances is such as to cause each atom to have essentially zero resultant electrical charge, the amount of leeway being not greater than about ±1/2, and these resultant charges are possessed mainly by the most electropositive and electronegative atoms ,and are distributed in such a way as to correspond to electrostatic stability.

Pauling carefully assigned an electronegativity number, x ranging from 0.7 (Cs) to 4.0 (F) and related these to the percentage ionic character of a bond according to:

$$\%_{ionic}=16\,|x_a-x_b|+3.5\,|x_a-x_b|^2$$

Application of this formula gives small atomic charges eg $[Al^{0.24}(H^{0.32}{}_2O^{-0.18})_6]$. Does this help explain the XRD determined charges in CaB_6? To some extent it does. Pauling states that charges will not be " greater than about ±1/2 " so Ca^{2+} is not to be expected. However a charge of +1.20 for Ca is still larger than 1/2. The foundation for Pauling's '1/2' limit appears in the same paper.

> The difference in electronegativity, 3.3, of caesium and fluorine permits the amount of covalent character to be estimated as 9%. It is only to this degree of approximation, then, that the bond in the caesium fluoride molecule can be described as an ionic bond. In the caesium fluoride crystal each caesium atom is surrounded octahedrally by six fluorine atoms. If each of these bonds had 9% covalent character, the total covalency of caesium and of fluorine would be 0.54, and the crystal could be described as involving , for each atom, a single bond, about 50% covalent and 50% ionic, resonating among the six positions connecting the atom with it's six ligates.
>
> This description would assign to the caesium atom in the caesium fluoride crystal a resultant charge +1/2 and to the

> fluorine atom a charge −1/2. It has seemed to me likely that in general all of the atoms in the complexes that constitute stable chemical substances have resultant electrical charges smaller than those shown by these most electropositive and electronegative atoms in their compounds with one another, and I have accordingly formulated the *postulate of the essential electrical neutrality of atoms: namely that the electronic structure....*

This calculation on CsF is flawed. Pauling argues that in a CsF molecule the charge is proportional to the difference in the electronegativities and therefore in proportion to the percentage ionic character. In the CsF crystal he argues that the charge (0.54) is now proportional to the degree of *covalent* character (0.09) and the coordination (6). This flaw is made obvious by applying the same arguments to CsCl. The electronegativity difference of $|0.7-3.0|=2.3$ permits the amount of covalent character to be estimated as 46%. Each Cs atom is surrounded by eight chlorides. If each of the eight bonds had 46% covalent character the total covalency would be 3.28 and this description would assign charges of $Cs^{3.3}Cl^{-3.3}$! The error lies in including coordination number (if CsCl were isostructural with NaCl would the degree of electron transfer change?) and similarly in asserting that the extent of electron transfer is different from that in an isolated molecule. The electroneutrality principle is, however, not worthless. Ignoring the coordination number and reverting to the plausable idea that charge is proportional to the percentage ionic character gives for CsF (solid or molecule) $Cs^{0.81}Cl^{-0.81}$ and for caesium chloride $Cs^{0.54}Cl^{-0.54}$. The electroneutrality principle should therefore be modified to require charges not greater than about ±0.8. This should be further qualified as the limit in 1:1 ie MX compounds. For other ratios the limit may be still higher. For CaB_6 the electronegativity difference of $|1.0-2.0|=1.0$ equates to 18% ionic character. Therefore for each Ca−B 'bond' Ca acquires a charge of 0.18. For a ratio of six borons to one calcium the result is $Ca^{1.08}B_6^{-1.08}$. This is in good agreement with the XRD results: simple multipole charges Ca +1.5, B −0.2, stockholder-partitioned charges Ca +1.2 B −0.2.

Does the evidence for calcium atoms in compounds being nearer to Ca^{+} rather than Ca^{++} matter for routine structural crystallography? The difference is small and will not seriously impede structure determination. More serious is the tabulation of scattering factors for 'chemically significant ions' such as Fe^{3+}, U^{+6} in 'International Tables for Crystallography'. This is an invitation to use scattering factors quite inappropriate for any crystallographic study.

Chapter 3

Charge Deformation Density in $[Et_3NH]^+_2[B_{12}H_{12}]^{2-}$

3.1. Why Study $[Et_3NH]^+_2[B_{12}H_{12}]^{2-}$?

The objective of the work presented here was to investigate the charge deformation density in a member of the series of *closo-* $[B_nH_n]^{2-}$ anions such that the extent of electron delocalisation and the relative importance of tangential vs radial (intrapolyhedral) bonding could be assessed.

The $[B_{12}H_{12}]^{2-}$ anion is an important member of the series being highly symmetrical (I_h). Each boron atom has five equivalent boron connectivities and one B-H bond. This anion is therefore interesting to compare with $[B_6H_6]^{2-}$, (and its analogue CaB_6), which is also highly symmetrical with each boron atom having four equivalent boron connectivities and one B-H bond. The ratio of valence electrons binding the icosahedron (26) to the number of faces (20) and edges (30) is much lower than in CaB_6 (14 electrons, 6 faces, 12 edges) and consequently observation by *X*-ray diffraction of any electron density accumulation over the faces/edges is a greater challenge.

The structure of the $[Et_3NH]^+$ salt of $[B_{12}H_{12}]^{2-}$ had been previously established [69] to have high crystallographic symmetry (R-3, z=1). This enables the measurement of sets of equivalent reflections which reduce random or systematic (such as absorption, anisotropic extinction) errors in the data. Moreover, the point symmetries imposed on the anion (-3, S_6) and cation (3, C_3) reduces the number of variables in the refinement.

Other salts such as $(M^+)_2[B_{12}H_{12}]^{2-}.xH_2O$, M= Na, K, Cs and Rb [70,71] x=4,0,0,0, have even higher crystallographic symmetry (space group Fm3, z=4) but the M^+ ion is , compared to $[Et_3NH]^+$, more capable of polarising the $[B_{12}H_{12}]^{2-}$ ion and distorting it from icosahedral geometry. This problem is shown to be still worse in the structures of $Ca[B_{12}H_{12}].8H_2O$ [72] and $Sr[B_{12}H_{12}].7H_2O$ [73]. There are further obstacles to using these salts in a deformation density study when the metals are heavy and have larger absorption coefficients. Absorption is the principle reason for dismissing $[Ni(en)_3]^{2+}[B_{12}H_{12}]^{2-}$ (en= ethylendiamine), which has also been characterised by *X*-ray diffraction [74] and the mixed salt $(K)_3[B_{12}H_{12}](Br)$ [75].

The $[Et_3NH]^+$ counterion is itself useful. Information on the form and magnitude of simple 2-centre 2-electron bonds has accumulated. Consistency of features in the deformation density of the $[Et_3NH]^+$ cation with this body of data serves as an indicator of the quality of the data. Such an indicator is important in interpreting features in the more important $[B_{12}H_{12}]^{2-}$ anion where there are relatively fewer studies on similar compounds. An alkyl ammonium cation is also used in the study of $B_3H_8^-$ (see Chapter 4) .

3.2. Experimental

3.2.1. Data Collection

Preparation of $[Et_3NH]_2[B_{12}H_{12}]$ was by a published synthetic route [80] using decaborane ($B_{10}H_{14}$) and triethylamine-borane adduct. The high boiling point solvent "ultrasene" (a kerosene fraction bp 190°C) proposed was unavailable and instead the inert hydrocarbon decalin was used. This required a reduction in reflux temperature and subsequently this reduction in temperature was identified as the reason for the co-formation of the N-adduct compound $[Et_3NB_{12}H_{11}]^-[Et_3NH]^+$. This was isolated after conversion to the $[NMe_4]^+$ salt. The zwitterionic by-product was characterised by *X*-ray diffraction [82,Appendix VI]. The use of the triethylamine borane adduct in the synthesis of $[B_{12}H_{12}]^{2-}$ is deliberate in its intention to minimise formation of the by-product. Much higher yields of the corresponding N-trimethyl adduct can be obtained by the use of trimethylamine borane.

Large colourless crystalline blocks of $[Et_3NH]_2[B_{12}H_{12}]$ were obtained by slow evaporation of an acetonitrile solution. The selected crystal was sphericalised to a diameter of 0.4mm. Preliminary Weisenberg photography confirmed that the crystal had remained singular and was free from powder.

It was considered impractical to collect all independent reflections (1/6 of the sphere eg all -h +k +l and also +h +k +l (h $\geq$k$\geq$l)) to the required resolution of $S = 2\sin\theta/\lambda = 2.60Å^{-1}$. Such a large number of data would take too long to collect and long low temperature collections are vulnerable to ice-formation on the crystal. Furthermore a large proportion of the high angle reflections was expected to be too weak to be measured reliably. Instead, previous refinements on data measured at low temperature were used to predict structure factors Fc and normalised structure factors Ec to $S= 2.6Å^{-1}$. These were sorted into decreasing Fc and the lowest 10% discarded. The 4000 highest E values together with all Fc's greater than 10 gave an initial list of 4037 unique reflections. This list was subsequently shortened to the top 2000 by F. It is more important that the selected indices are evenly distributed in reciprocal space (hence the use of E and F) rather than that they are accurately selected. A simple check on the distribution showed that the +h +k +l indices accounted for 22% of indices selected (ideal 25%).

The successful use of such a shortened list in deformation density studies has been demonstrated several times [76-79]. While this approach invalidates an X-X map as a means of examining the deformation density (because of the necessary omission of low-angle non-zero structure factors), the multipole approach is unaffected.

Accurate cell parameters were obtained using a CAD-4 diffractometer at 115K, 25 centred reflections (15°$<\theta<$ 31°), graphite monochromated Mo-K_α

(λ_{av} = 0.71069Å). For data collection θ_{max}=67.5°, ω−2θ scans in 96 steps, scan width (ω) = 0.80 + 0.35tanθ. Moderate prescan and for I/σI > 0.5 this was followed by a slow scan such that the final I/σI ratio was better than 33 subject to a time constraint of 100s. Over 228 hours 7107 data were measured. No detectable crystal decay or movement.

Summary

$H_{44}B_{12}C_{12}N_2$, Mr = 346.22, ρ_x=0.983g cm^{-3}, Rhombohedral R-3 (No 148), a=8.8242(16)Å, α=69.803(15)° (averaged) V= 584.94Å^3, [Hexagonal cell a=10.098(18), c= 19.872(36)Å], V= 1754.9Å^3, μMoK_α = 0.46 cm^{-1}, F_{000} = 190, T = 115K.

3.2.2. Data Reduction

Data which had 1) net I < 0 or 2) were flagged as overloading counter or 3) were flagged as weak with a peak offset from the expected position or 4) had an uneven background were deleted to give 5003 data. The data were then corrected for Lorentz and polarisation factors (including terms for monochromator polarisation). The low value of μr (0.009) and the use of a near spherical crystal obviated the need for an absorption correction . The data were merged to give 1854 unique reflections (R_{merg} 0.030), all of which had F/σF better than 2.0.

3.3. Standard Refinement

The starting point of the refinement was a set of coordinates previously published. These were refined using weights for the observations of $1/\sigma^2F$, minimising the function $\Delta_1 = \Sigma|Fo-kFc|^2$. Allowing anisotropic thermal motion for non-H atoms and isotropic motion for the H atoms gave a final R factor of 0.043 (R_w 0.070). These results are *not* presented here since they were subsequently shown to have clear asphericity shifts and modified thermal parameters. For the standard parameters from the multipole refinement see Section 3.4.2.

The global structure is based on a distortion of the cubic anti-fluorite structure (8:4 coordination; cubic and tetrahedral environments eg $K_2B_{12}H_{12}$) along the cubic 111 vector. The resulting array of anions and cations is usually described as the 'anti-$CdCl_2$' lattice and is substantially rarer than the $CdCl_2$ lattice. This structural analogy is however strained since although the hexagonal c-axis and independent z-coordinate are similar (ie the layers perpendicular to the hexagonal c-axis are similarly separated) the rhombohedral α angle in $CdCl_2$ is small (33.6°) ie the atoms within the layers are much more closely packed. A closer structural analogy is $TbFe_2$ with α=59.6° [83].

The utility of recognising similar anion/cation packing is that when polarisation due to packing is invoked then they should be applicable to all such similar compounds. (See the discussion of charge distribution in in $[Et_3NH]^+$ and the reported polarisation of the Cs^+ ion in the anti-$CdCl_2$ structure Cs_2O, section 3.6.1.) Another structure with similar packing is $[MeNH_3]_2^+[SnCl_6]^{2-}$ [84] in which α is 50.3°.

3.4. Experimental Charge Deformation Density

3.4.1. Multipole Model and Refinement

The program LSEXP was used (see Chapter 2, section 2.5.1). Crystallographic point symmetry reduces only the number of deformation functions for N and HN (See Fig 3.4.1a for labelling). This alone would still

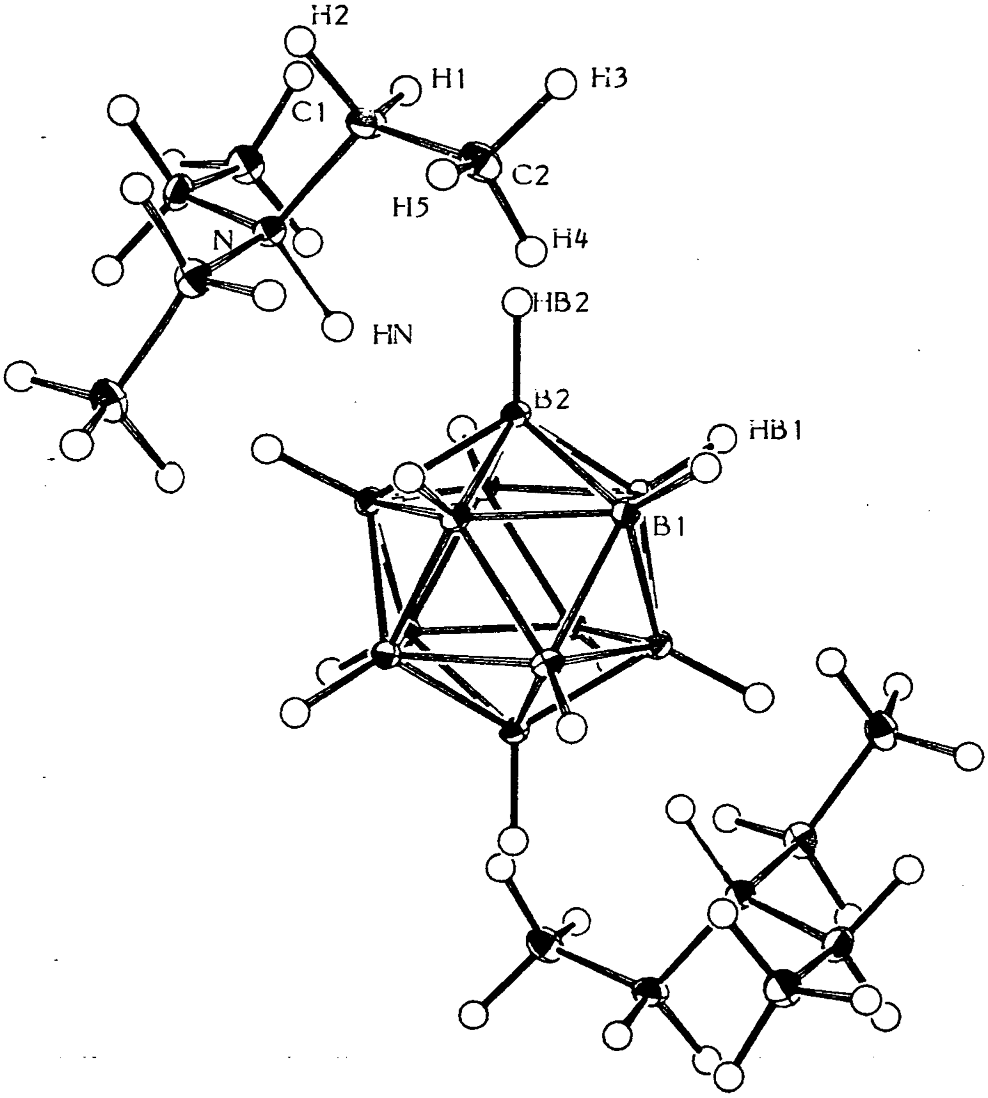

Figure 3.4.1(a)

ORTEP drawing of the structure showing labelling scheme

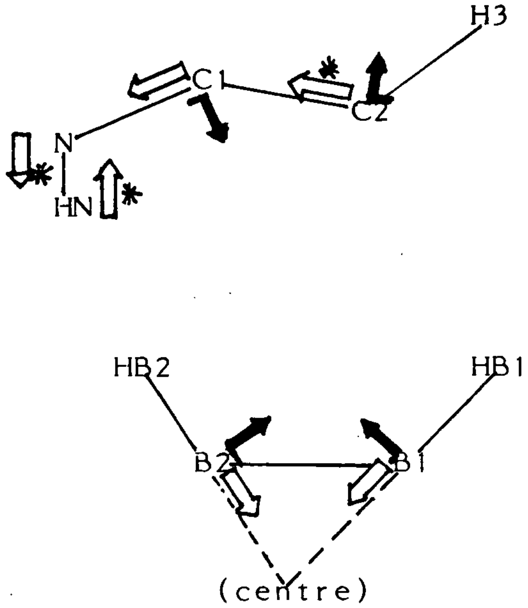

Fig 3.4.1(b)

labelling and local axes for deformation functions

⇨ L vector

➡ M vector

* ⇨ L' = (L+M+N)/3 for an atom of local 3-fold symmetry

N vector given by LxM

leave too large a number of deformation parameters for a practical full-matrix refinement. Therefore non-crystallographic point symmetry was imposed. These constraints were :

- All hydrogen atoms axially symmetric with respect to their bonded neighbour.
- Only 3 types of hydrogen : HC, HB and HN according to the element type of the bonded atom.
- Atom C2 of point symmetry C_{3v} with respect to the C1-C2 vector.
- Atom C1 of point symmetry C_s with respect to the N-C1-C2 plane.
- Atoms B1 and B2 have equivalent deformation functions and each of C_{5v} point symmetry with respect to the B-(0,0,0) vector.

The full range in the order of the deformation multipoles was used for C, B and N atoms (ie n=0,1,2,3,4) but for H atoms no fourth order multipoles were refined.

The positions of HB1, HB2, and HN refined to give unreasonably short bond lengths and were highly correlated with H-based deformation functions. This was not unexpected since the 'frozen cusp' model is least appropriate for hydrogen. In the absence of any neutron diffraction data it was necessary to fix the HB hydrogens at positions (initially) calculated to be 1.185Å from the B position and radial from the polyhedral centre. All deformation density in the B-H bonds is therefore only approximated in the refinement.

The local axes for the non-hydrogen atoms are indicated in Figure 3.4.1. The axes for N and C2 were chosen to have the 3-fold axis equal to the body diagonal of the orthogonal L,M,N axes.

The exponents were initially fixed at reasonable values (N 5.3; C1,C2 5.28; B

4.47; HC,HB,HN 5.45Å^{-1}) . Cusp functions (n=0) were refined in a separate block. Refinement of 64 standard parameters and 76 deformation parameters with one constraint (F_{000}=190) gave a final R factor of 0.0258 (R_w 0.0259). The inclusion of the four exponents (in the smaller block) reduced the R factor to 0.0254 (R_w 0.0251) but the deformation maps are largely unchanged more than 0.4Å from atom positions and, considering the esd maps, are insignificantly changed more than 0.3Å from atomic positions.

3.4.2. Multipole Refinement Results

The standard parameters together with their esd's are listed in Table 3.4.2a. Derived bonds and angles are listed in Table 3.4.2b. The deformation coefficients are listed in Table 3.4.2c.

In these tables X-Y@n refers to Y under symmetry operation n. The symmetry operators are defined to be in the order x,y,z/y,z,x/z,x,y and their inversion related equivalents.

TABLE 3.4.2(A)

Fractional Coordinates of Atoms with Standard Deviations

	x	y	z
N	0.23506(20)	0.23506(0)	0.23506(0)
C1	0.10565(8)	0.28101(7)	0.38708(8)
C2	-0.05995(8)	0.39287(6)	0.35314(4)
B1	0.17245(5)	-0.13686(5)	-0.08380(4)
B2	0.18345(5)	-0.00703(4)	0.02544(3)
H1	0.0908(12)	0.162(3)	0.479(3)
H2	0.1700(20)	0.3344(18)	0.4358(18)
H3	-0.154(3)	0.3908(12)	0.475(3)
H4	-0.1061(19)	0.3394(19)	0.2882(22)
H5	-0.0497(13)	0.519(3)	0.2839(22)
Hb2	0.31161(0)	-0.01354(0)	0.04617(0)
Hb1	0.29335(0)	-0.23012(0)	-0.14434(0)
Hn1	0.171(5)	0.171(0)	0.171(0)

Thermal Parameters xÅ^2

	u11	u22	u33	u12	u23	u13
N	.01103(25)		-.00323(23)			
C1	.01608(14)	.01588(14)	.01157(13)	-.00257(11)	-.00556(10)	-.00346(11)
H1	.027(3)					
H2	.043(4)					
C2	.01552(13)	.01494(11)	.01510(12)	-.00087(11)	-.00506(9)	-.00144(10)
H3	.035(3)					
H4	.050(4)					
H5	.038(3)					
B1	.00936(11)	.01025(10)	.01116(10)	-.00209(8)	-.00413(8)	-.00260(8)
B2	.00905(11)	.01059(10)	.01075(10)	-.00301(7)	-.00351(7)	-.00320(7)
HB2	.0251(15)					
HB1	.0305(18)					
HN1	.032(8)					

TABLE 3.4.2(B)

Bond Lengths(Å) with standard deviations

N - C(1)	1.5054(12)	C(1) - C(2)	1.5170(9)
N -Hn(1)	1.27(3)	C(2) - H(3)	1.110(23)
C(1) - H(1)	1.098(22)	C(2) - H(4)	1.094(18)
C(1) - H(2)	1.106(17)	C(2) - H(5)	1.091(22)

Angles(degrees) with standard deviations

C(1) - N -Hn(1)	107.6(12)	C(1) - C(2) - H(3)	107.7(12)
N - C(1) - H(1)	106.1(11)	C(1) - C(2) - H(4)	110.6(9)
N - C(1) - H(2)	103.4(9)	C(1) - C(2) - H(5)	111.1(11)
N - C(1) - C(2)	114.03(6)	H(3) - C(2) - H(4)	103.8(15)
H(1) - C(1) - H(2)	105.6(14)	H(3) - C(2) - H(5)	111.7(16)
H(1) - C(1) - C(2)	111.6(11)	H(4) - C(2) - H(5)	111.6(15)
H(2) - C(1) - C(2)	115.3(9)		

Torsion angles(degrees) with standard deviations

Hn(1)- N - C(1) -H(1)	68.7(17)	H(1)- C(1) - C(2) -H(3)	44.8(17)
Hn(1)- N - C(1) -H(2)	179.6(15)	H(1)- C(1) - C(2) -H(4)	-68.0(16)
Hn(1)- N - C(1) -C(2)	-54.5(12)	H(1)- C(1) - C(2) -H(5)	167.4(17)
N - C(1) - C(2) -H(3)	165.0(13)	H(2)- C(1) - C(2) -H(3)	-75.6(16)
N - C(1) - C(2) -H(4)	52.2(10)	H(2)- C(1) - C(2) -H(4)	171.5(14)
N - C(1) - C(2) -H(5)	-72.4(12)	H(2)- C(1) - C(2) -H(5)	47.0(15)

Bond Lengths(Å) with standard deviations

B(1) - B(2)	1.7763(6)	B(2) - B(2)@2	1.7823(6)
B(1) - B(1)@-2	1.7882(6)	B(2) - B(2)@-2	1.7802(6)
B(1) - B(2)@-3	1.7784(6)	B(2) -Hb(2)	1.1859(4)
B(1) -Hb(1)	1.1851(5)		

Angles(degrees) with standard deviations

B(2) - B(1) -Hb(1)	121.75(3)	B(1) - B(2) -Hb(2)	121.52(3)

TABLE 3.4.2(C)

Deformation Coefficients and esd's

N EXPON	5.108(29)	N SPHER	-0.126(13)	N LINR1	0.34(25)
N QUDR1	0.05(24)	N QUDR2	-0.41(12)	N CUBI1	-2.12(37)
N CUBI2	0.00(5)	N CUBI7	0.96(114)	N CUBI8	0.10(12)
N QUR 1	0.36(17)	N QUR 4	-0.99(31)	N QUR 7	1.19(24)
N QUR10	-0.19(21)	N QUR12	-1.20(20)	C1EXPON	5.44(6)
C1SPHER	-0.070(7)	C1LINR1	-0.15(5)	C1LINR2	-0.18(7)
C1QUDR1	-0.09(7)	C1QUDR2	-0.04(7)	C1QUDR3	0.03(6)
C1QUDR6	0.42(6)	C1CUBI1	1.70(21)	C1CUBI2	0.16(22)
C1CUBI3	0.93(13)	C1CUBI5	0.47(14)	C1CUBI7	-1.72(19)
C1CUBI8	-0.37(14)	C1QUR 1	0.20(11)	C1QUR 2	0.29(10)
C1QUR 3	-0.07(9)	C1QUR 4	-0.11(10)	C1QUR 5	0.36(11)
C1QUR 6	-0.15(5)	C1QUR 7	-0.24(9)	C1QUR 8	-0.33(10)
C1QUR12	0.10(8)	C2EXPON	5.25(7)	C2SPHER	-0.039(7)
C2LINR1	0.04(3)	C2QUDR1	0.10(4)	C2QUDR2	0.19(4)
C2CUBI1	-0.40(10)	C2CUBI2	-0.02(4)	C2CUBI7	1.05(12)
C2CUBI8	0.15(6)	C2QUR 1	-0.23(5)	C2QUR 4	0.00(7)
C2QUR 7	0.07(6)	C2QUR10	-0.28(10)	C2QUR12	0.13(10)
B EXPON	5.04(4)	B SPHER	0.118(4)	B LINR1	0.00(3)
B QUDR1	0.023(28)	B QUDR5	0.01(3)	B CUBI1	-0.67(15)
B CUBI7	0.93(13)	B QURT1	-0.01(7)	B QURT4	0.061(15)
B QURT5	-0.035(14)	HCEXPON	5.26(5)	HCSPHER	0.0054(25)
HCLINR1	0.37(10)	HCQUDR1	0.01(4)	HCQUDR5	-0.07(5)
HCCUBI1	0.04(6)	HCCUBI7	0.01(5)	HBEXPON	5.21(7)
HBSPHER	-0.018(6)	HBLINR1	0.172(28)	HBQUDR1	0.07(4)
HBQUDR5	0.066(24)	HBCUBI1	0.20(10)	HBCUBI7	-0.20(9)
HNEXPON	5.44(6)	HNSPHER	-0.015(21)	HNLINR1	2.29(43)
HNQUDR1	0.72(35)	HNQUDR2	-0.18(28)	HNCUBI1	-0.85(92)
HNCUBI7	1.19(94)	B QURT2	-0.15(3)		

Orienatations of the polar axes follow the sequence :

linear terms	100	010	001			
quadratic terms	110	1-10	101	10-1	011	01-1
cubic terms	110	1-10	101	10-1	011	01-1
	111	1-1-1	-11-1	-1-11		
quartic terms	100	010	001	A11	1A1	11A
	-A11	1-A1	11-A	A-11	1A-1	-11A
	A1-1	-1A1	1-1A			

The parameter 'A' is the constant SQRT(2) - 1 .

A search on the Cambridge Crystallographic Database gave 54 previous records of structure determination on this cation. Of these 24 structures had coordinates of all non-hydrogen atoms and HN deposited. The mean values for the bond lengths are HN-N 0.96(10), N-C1 1.506(32), C1-C2 1.486(49)Å.

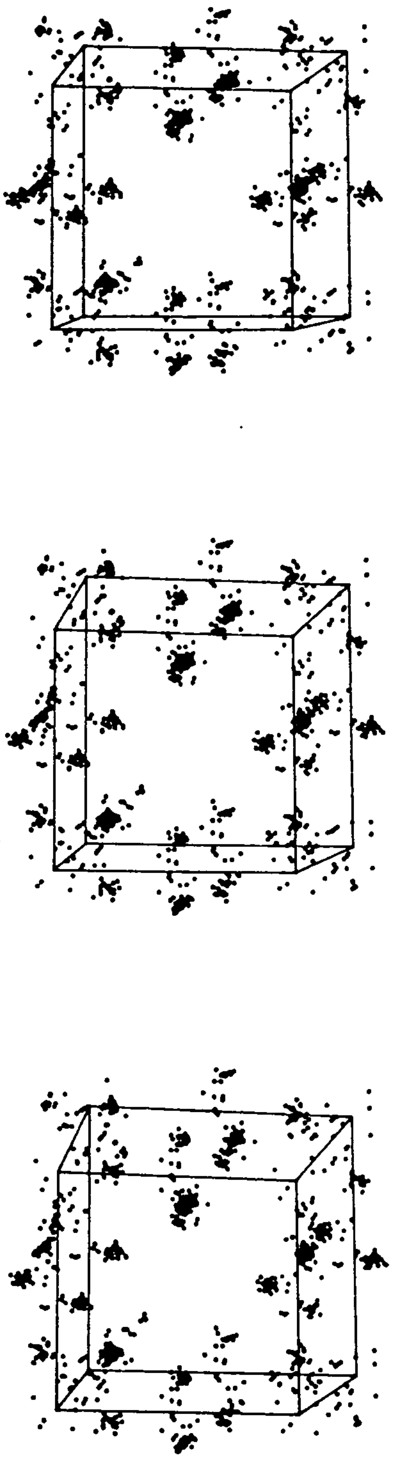

FIGURE 3.4.2(A)

Conformational Distribution
of $[Et_3NH]^+$. Data from
Cambridge Crystallographic Database. Presented in
the Space Group R32.

Two Stereo Pairs

One low temperature neutron study has been done but unfortunately the cation was disordered over two orientations.

The conformation of the $[Et_3NH]^+$ cation in the $[B_{12}H_{12}]^{2-}$ salt is characterised by the torsion HN-N-C1-C2 (-54.5(12)°), and 3-fold symmetry. This (α,α,α) conformation is rare. It accounts for only 8% of database entries. The principal conformations are (180°,60°,-60°) (37%), and its mirror image (180,60,-60) (also 37%). The distribution is simply illustrated using a unit cell of edge 360° and the space group R32. Figure 3.4.2(a) presents a stereo pair of this 3-D distribution. A large (20%) number of database entries indicated some disorder of the cation. The distribution is clearly clustered and this could be put to use in fitting restrained models to the electron density in disordered sites.

The $[B_{12}H_{12}]^{2-}$ ion has a mean B-B bond length of 1.781(5)Å. This is close to the mean in the K^+ salt (1.775(7)Å), the $[Ni(en)_3]^{2+}$ salt (1.786Å) and also the earlier structure determination of the $[Et_3NH]^+$ salt (1.781(2)Å). The slight variation in the bond lengths in Table 3.4.2b is due to a slight compression of the icosahedron parallel to the crystallographic 3-fold (centre-B2) 1.688(1), centre-B1 1.701(1)Å). The crystallographic point symmetry is S_6 but there is no perceptable distortion from D_{3d}.

3.4.3. Static Deformation Density Maps

These maps were prepared by direct summation using multipole functions rather than by Fourier summation. Consequently only contributions from one unit cell are presented.

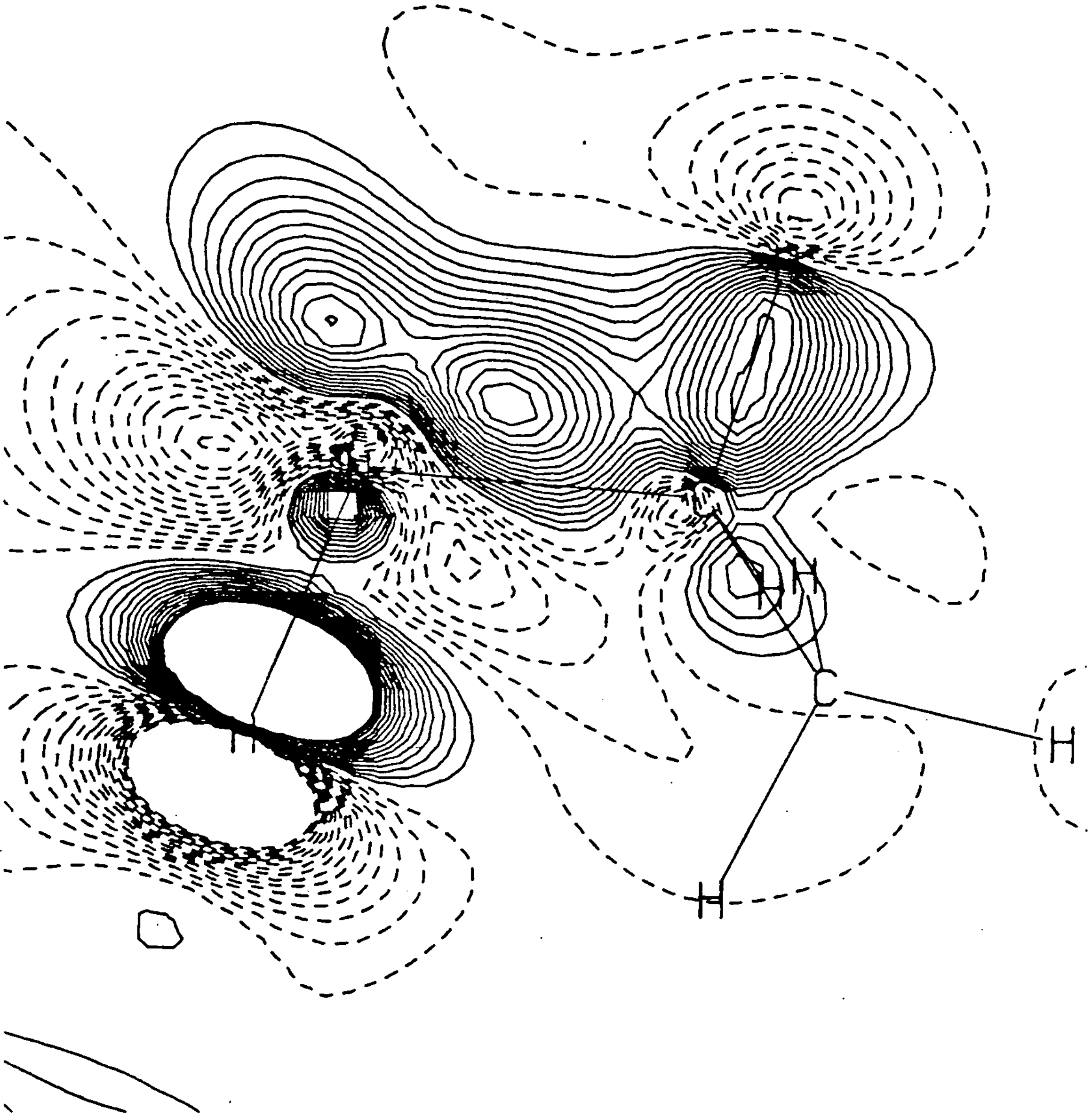

FIGURE 3.4.3.1(A)

Static Deformation Density
in the HN-N-C1 plane.

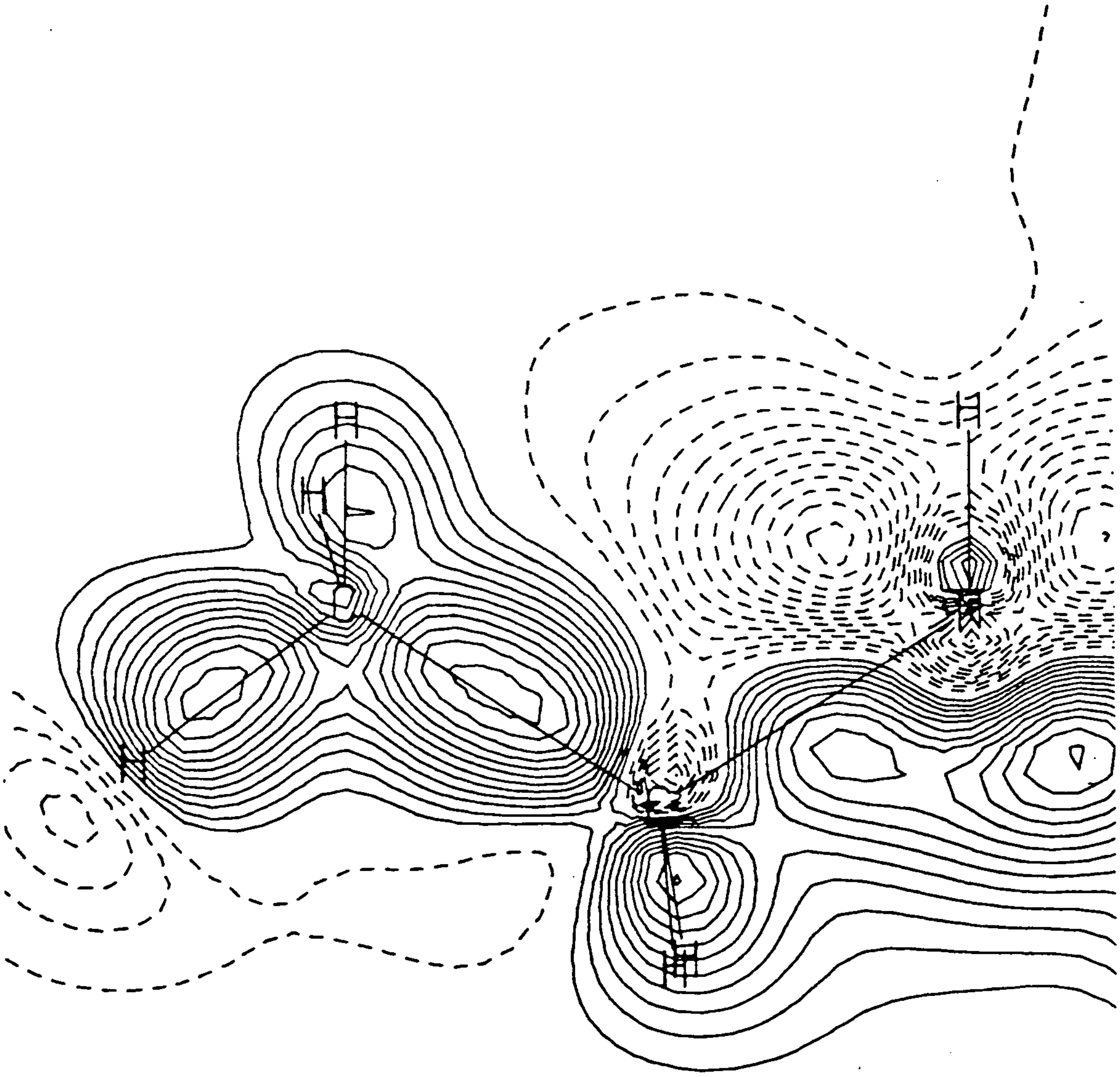

FIGURE 3.4.3.1(B)

Static Deformation Density
in the N-C1-C2 plane.

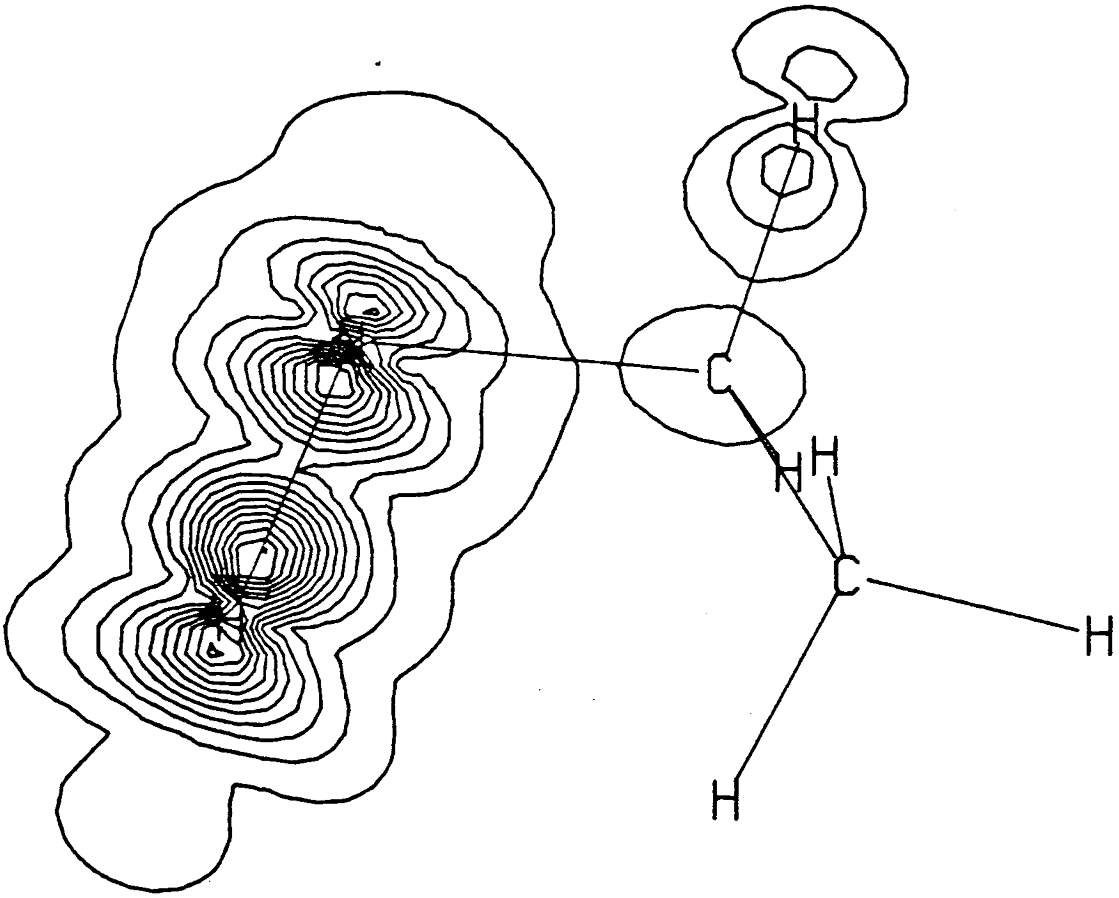

FIGURE 3.4.3.1(C)

ESD of Static Deformation Density
in the HN-N-C1 plane.

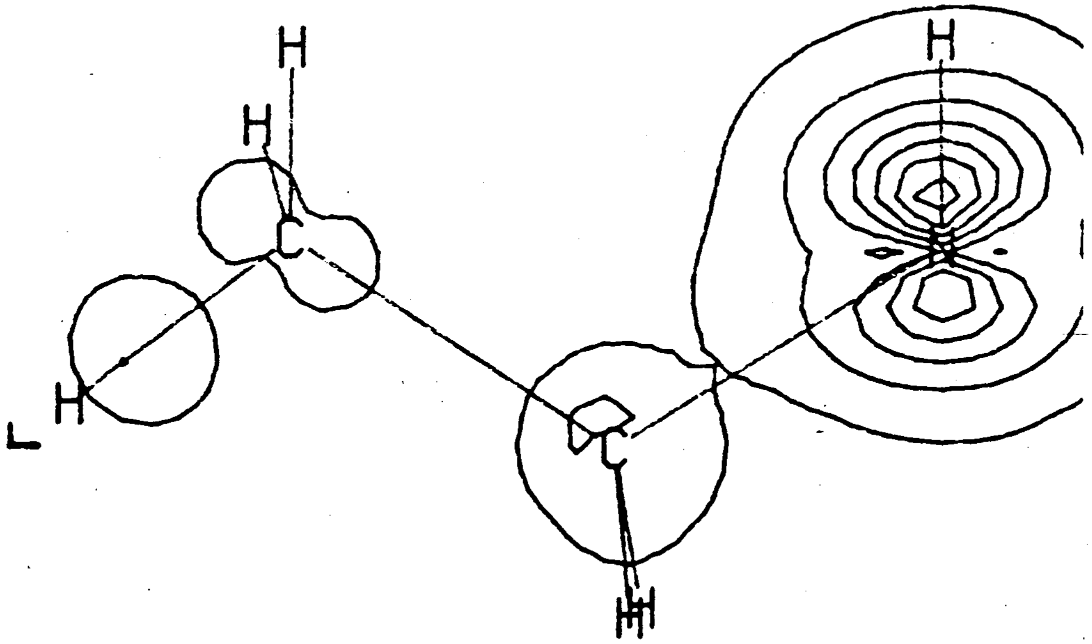

FIGURE 3.4.3.1(D)

ESD of Static Deformation Density
in the N-C1-C2 plane.

3.4.3.1. The Triethylammonium Cation

Figures 3.4.3.1(a) and (b) show the deformation density in the plane of the atoms HN-N-C1 and N-C1-C2 respectively. Contours are in intervals of 0.05eÅ^{-3}. The esd for the static deformation density in these planes is plotted in Figures 3.4.3.1(c) and (d) respectively. Contours are in intervals of 0.02eÅ^{-3}. Peaks in these maps not between labelled atoms are from other portions of the ion or counterion. The deformation in the C-H or N-H bonds should *not* be given serious interpretation because the H coordinates are almost certainly not those that would be determined by a neutron diffraction experiment.

The deformation peak heights are N-C1 (0.70(5)eÅ^{-3}) and C1-C2 (0.60(2)eÅ^{-3}). The C1-C2 bond peak is typical of the deformation density between two sp^3 carbons but the peak for the N-C1 bond, while of reasonable magnitude is curiously off the N-C1 vector. The direction of the shift is away from HN. These maps should be compared with *ab-initio* simulations in Section 3.5.2. For a discussion see Section 3.6.1.

3.4.3.2. The *closo*-$[B_{12}H_{12}]^{2-}$ Ion

The high point symmetry of this anion and the constraint on the deformation functions refined on the boron atoms enables the deformation density to be described extensively by only one plot. Figure 3.4.3.2(a) shows the deformation density in a plane through an edge and the inversion centre; contours are in intervals of 0.05eÅ^{-3}. This map is required to have approximate mm symmetry and conveniently shows the deformation density for an edge, for a perpendicular bisector to an edge and also for a section perpendicular to a triangular face. Four B-H bonds are also in this plane.

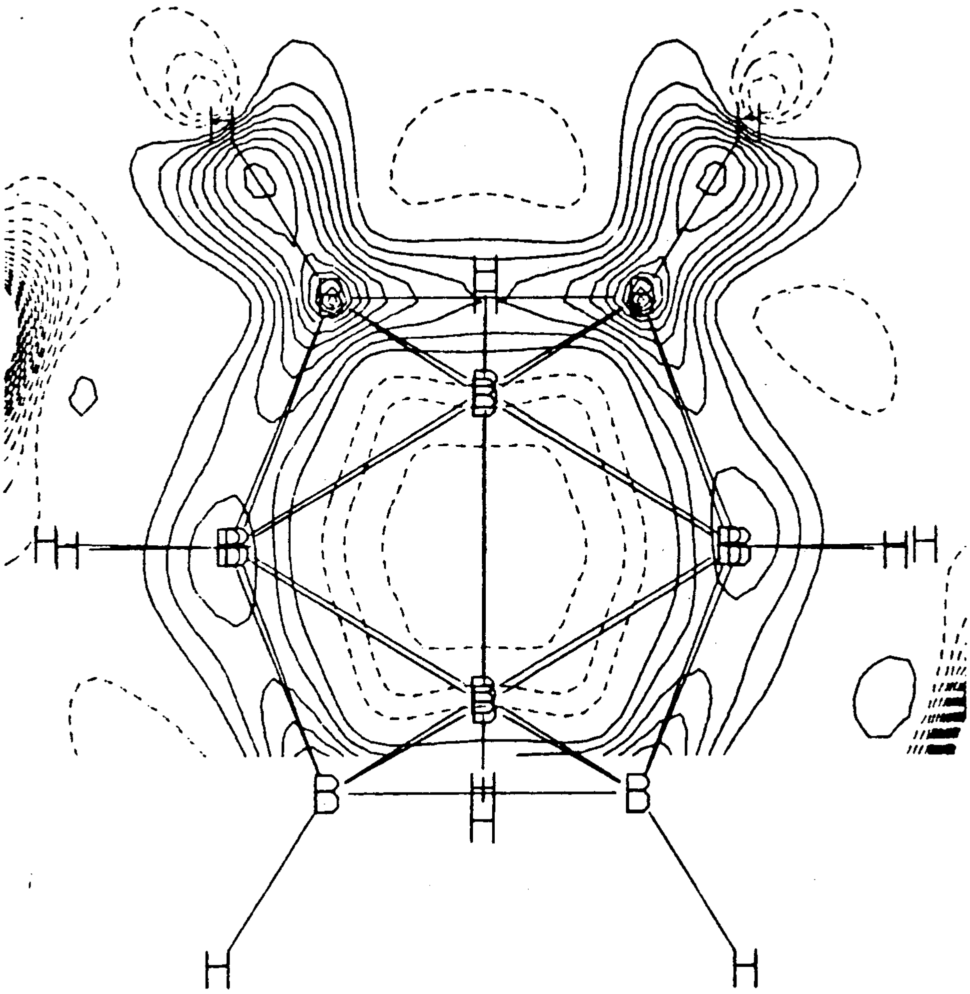

FIGURE 3.4.3.2(A)

Static Deformation Density
in a plane containing an edge and an inversion centre.

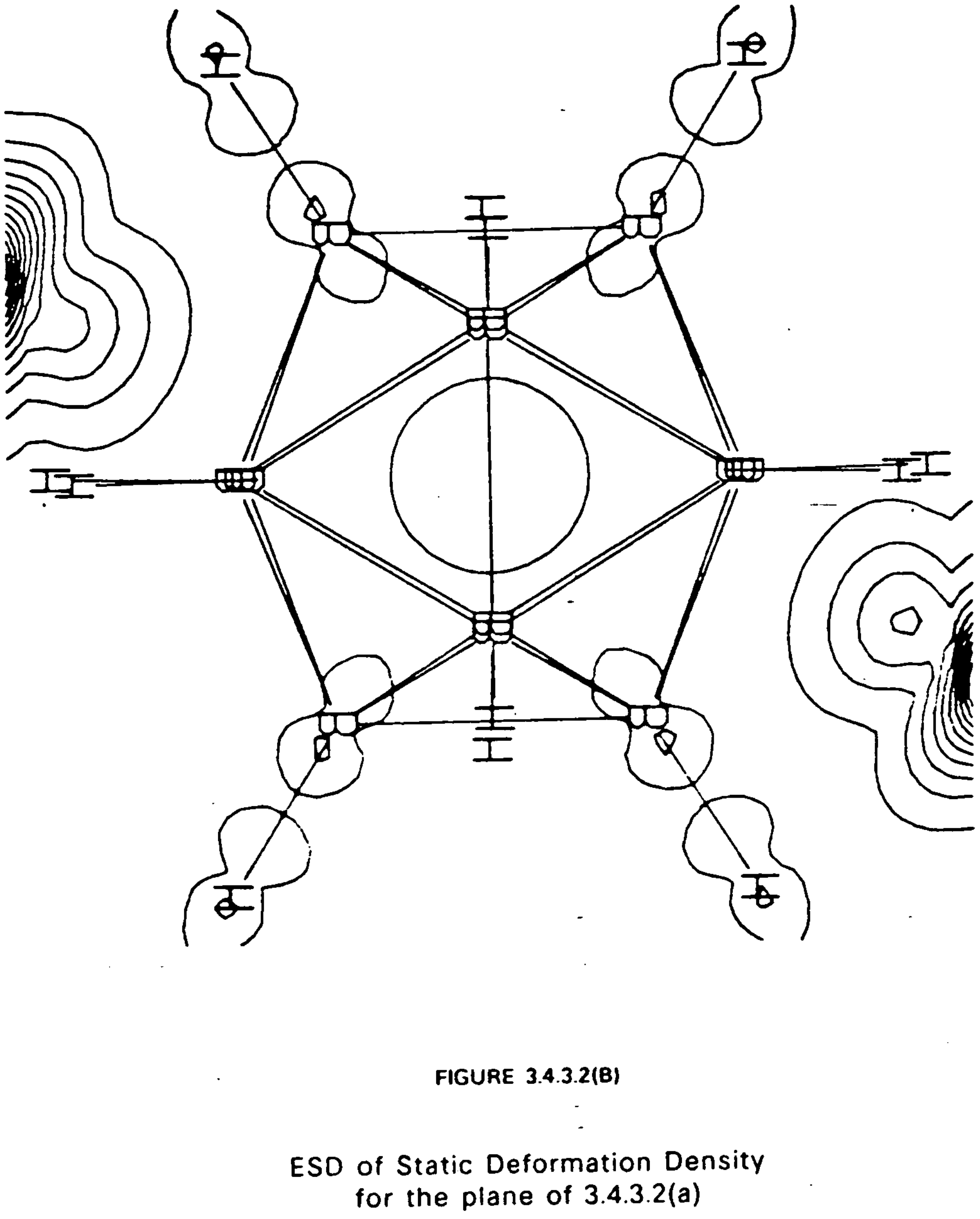

FIGURE 3.4.3.2(B)

ESD of Static Deformation Density
for the plane of 3.4.3.2(a)

Figure 3.4.3.2(b) shows the associated esd; contours are in intervals of 0.02eÅ^{-3}.

There is a clear electron defficiency at the polyhedral core of -0.15eÅ^{-3}. The deformation density is diffuse and nearly spherical maximising (0.15eÅ^{-3}) at a radial distance corresponding to that from the polyhedral centre to the midpoint of the B-B edges. This necessarily requires the deformation density to maximise just outside the polyhedral faces.

For a theoretical comparison see Section 3.5.3, for a discussion see Section 3.6.2.

3.4.4. Dynamic Deformation Density Maps

These were prepared using Fourier transform methods and calculated structure factors. Because of the large number of reflections S_{max} was limited to 2.0Å^{-1} (3277 structure factors). Figures 3.4.4(a) and (b) are analagous to the static maps (Fig 3.4.3.1(a) and (b)) for the triethylammonium cation. Figure 3.4.4(c) is analagous to the static map for the anion (Fig 3.4.3.2(a)).

3.4.5. Residual Density Maps

The residual electron density for the planes H-N-C1, N-C1-C2 and B1-centre-B2 are shown in Figures 3.4.5(a), (b) and (c) respectively. These are based on 1854 observed and calculated structure factors. Contours are in intervals of 0.02eÅ^{-3}.

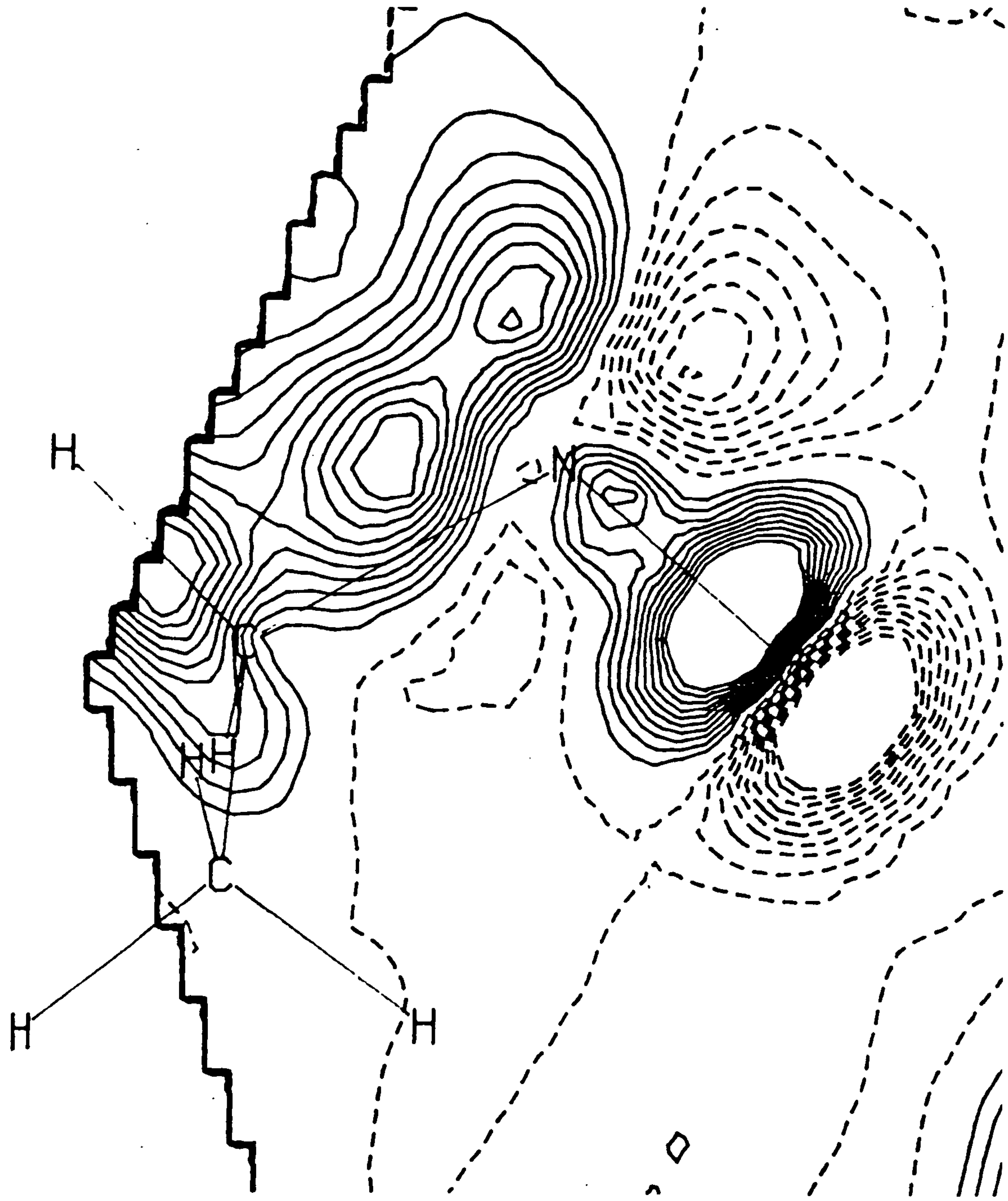

FIGURE 3.4.4(A)

Dynamic Deformation Density
in the HN-N-C1 plane.

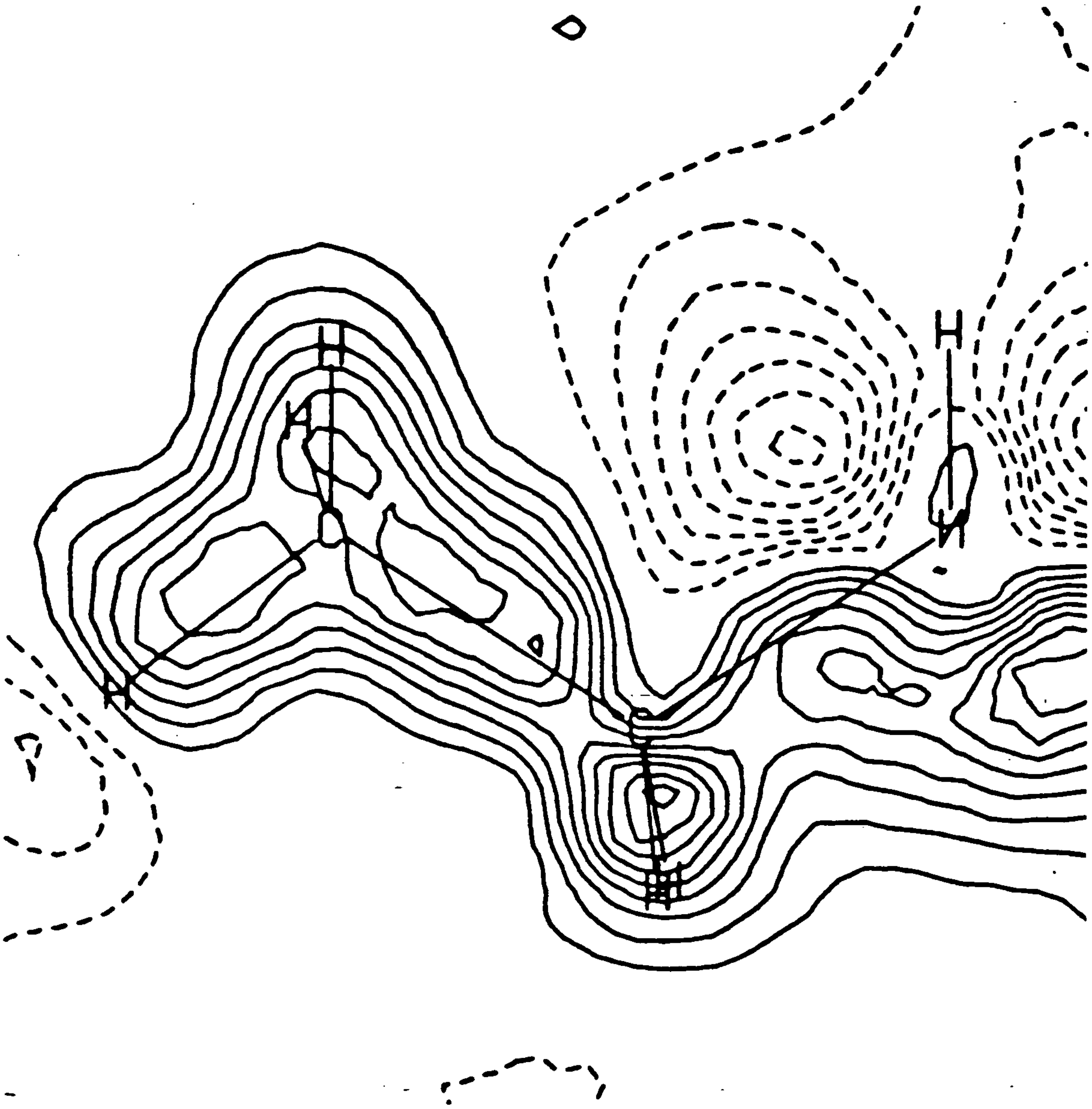

FIGURE 3.4.4(B)

Dynamic Deformation Density
in the N-C1-C2 plane.

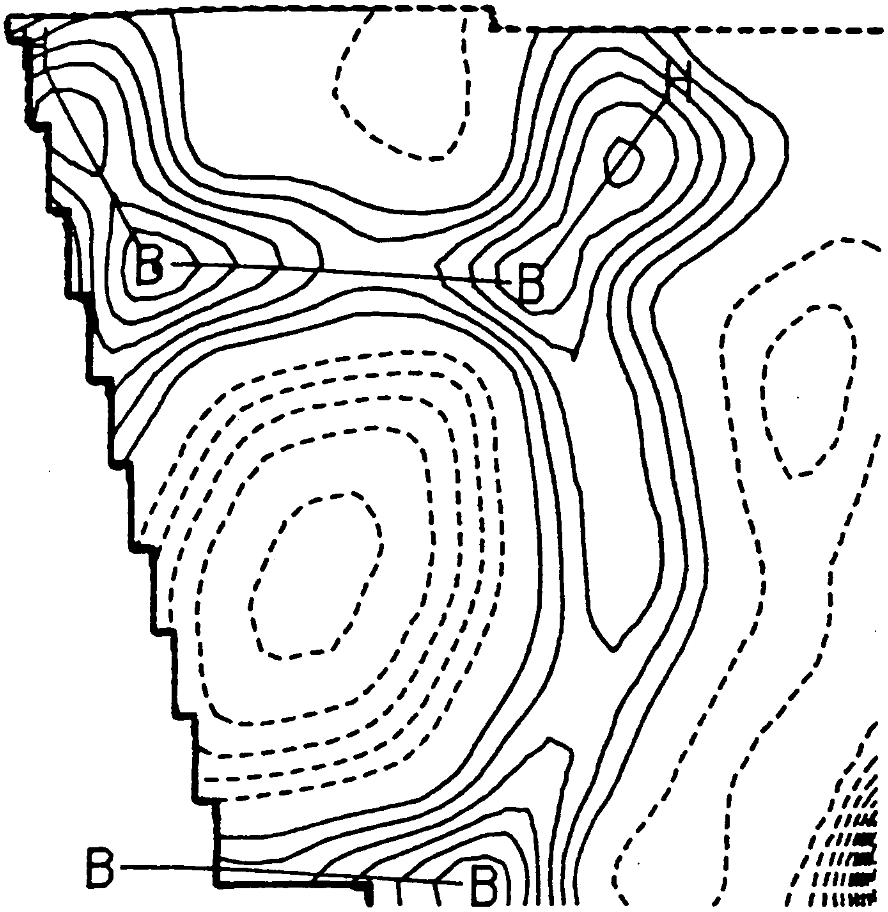

FIGURE 3.4 1(C)

Dynamic Deformation Density
in the B1-centre-B2 plane.

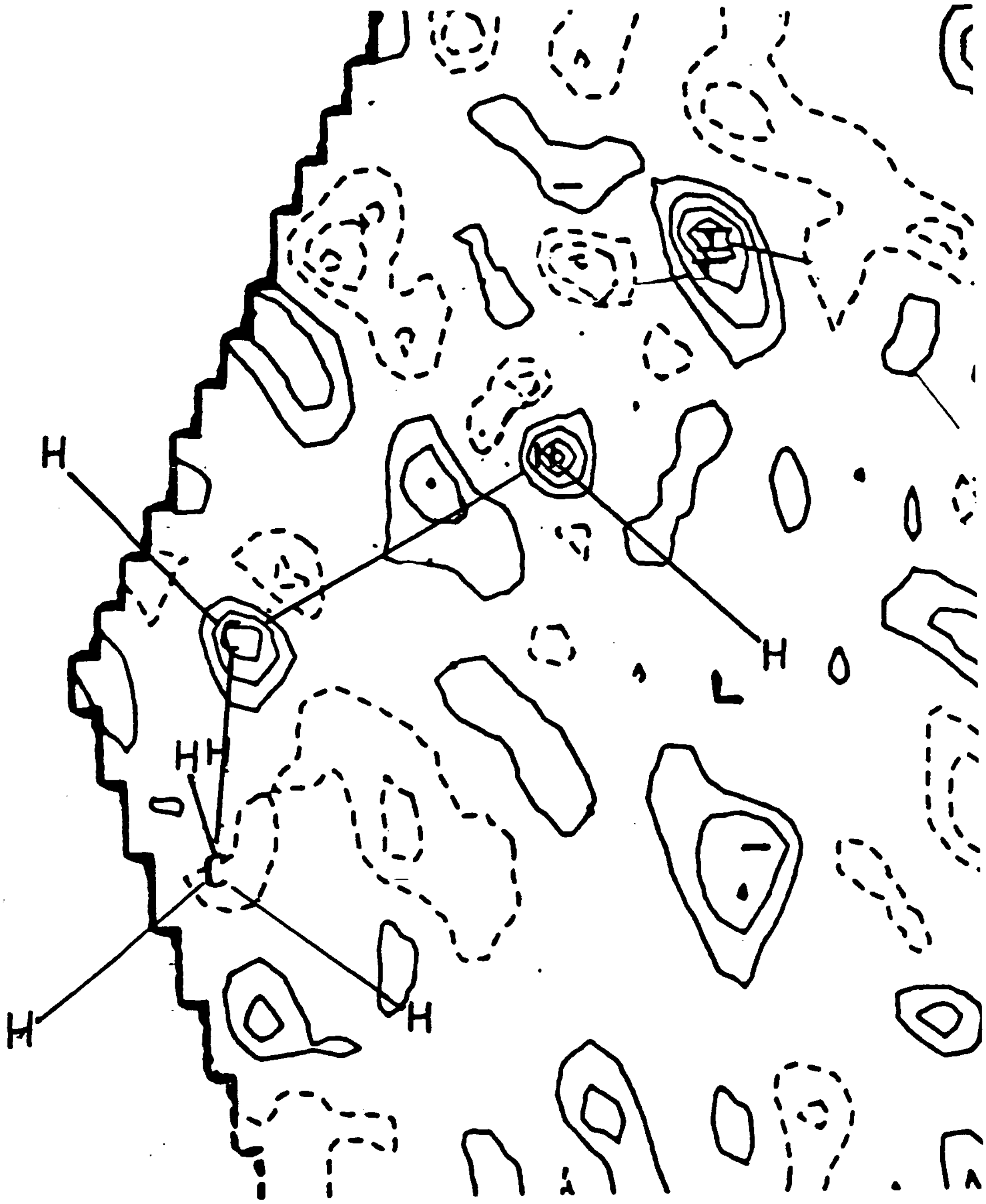

FIGURE 3.4.5(A)

Residual Density
in the HN-N-C1 plane.

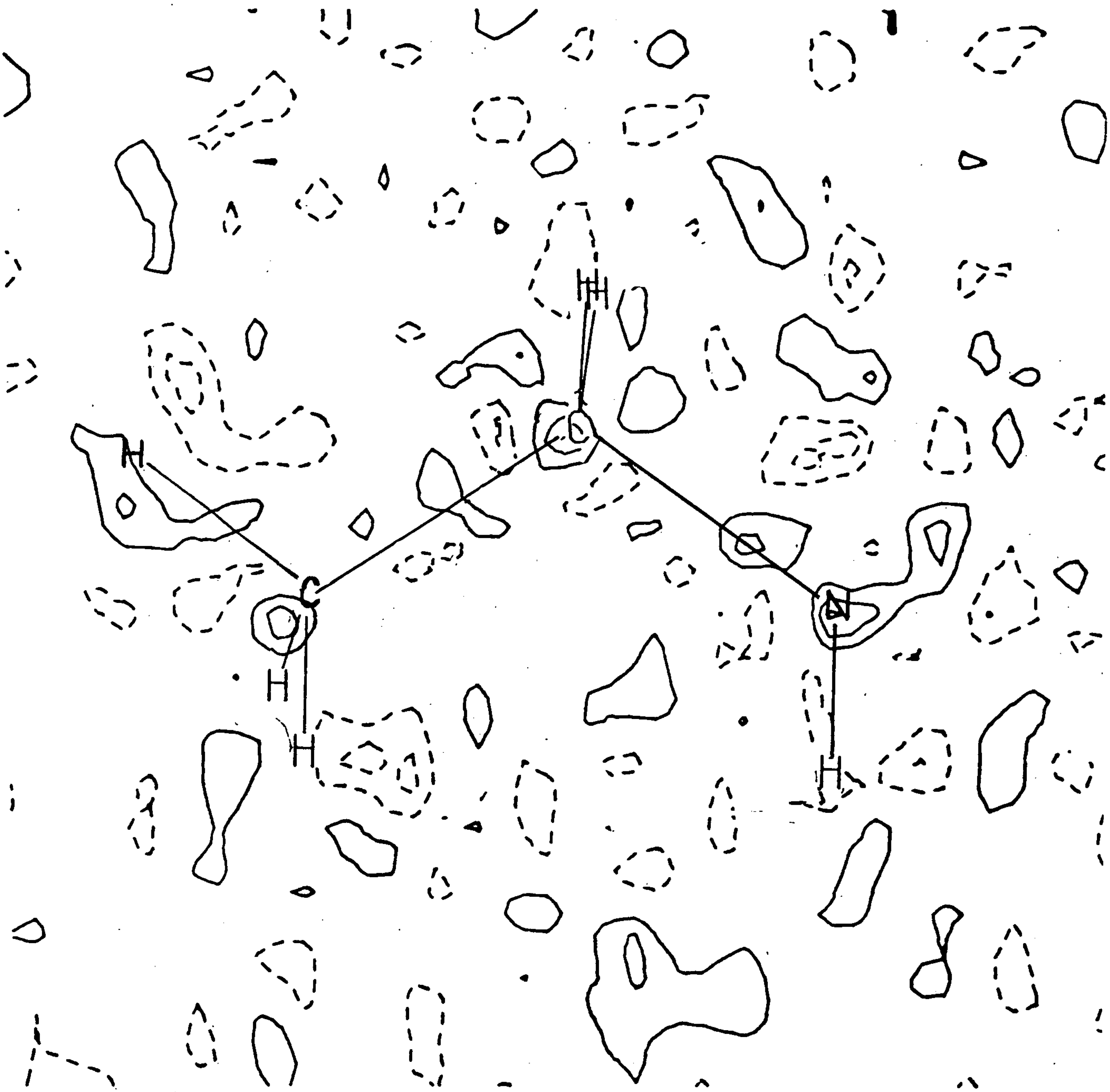

FIGURE 3.4.5(B)

Residual Density
in the N-C1-C2 plane.

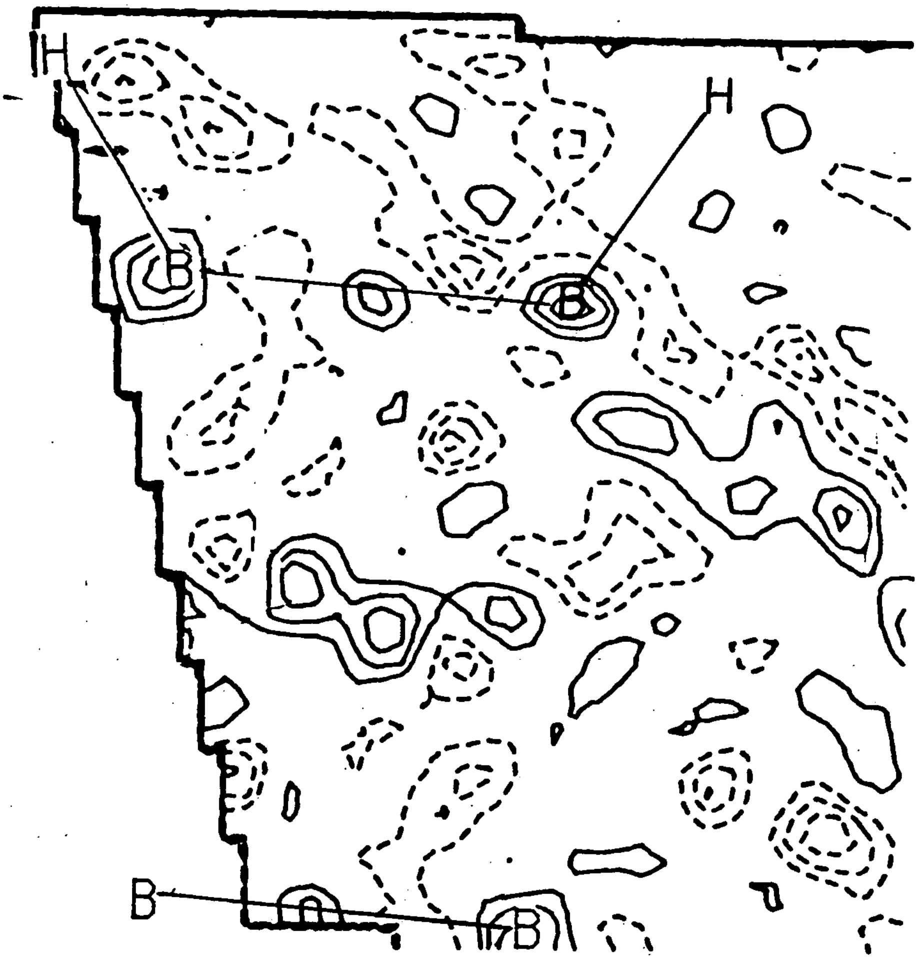

FIGURE 3.4.5(C)

Residual Density
in the B1-centre-B2 plane.

3.4.6. Charges and Moments

Average charges for deformation types obtained by direct interpretation of the refined coefficients of even deformation functions are given in column 1 of Table 3.4.6. Charges obtained by numerical integration and partitioning according to the stockholder recipe are given in column 2. The integration was carried out over a cube of edge 5.2Å centred on the atom and in divisions of edge 0.2Å. The second moment off-diagonal terms are omitted. For all deformation types these terms had an esd (estimated from the averaging of chemically similar atoms of the same deformation type) similar to their magnitude.

TABLE 3.4.6

Moments and Charges

Atom	Charges		First Moment			Second Moment		
	(1)	(2)	L	M	N	LL	MM	NN
N	3.7	.33(-)	.20(4)	*	*	.82(7)	*	*
C1	-.38	-.15(-)	-.025(-)	.194(-)	-.116(-)	.614(-)	.569(-)	.689(-)
C2	.07	-.17(-)	.025(-)	.037(-)	-.039(-)	.573(-)	.476(-)	.853(-)
HC	.09	.087(17)	.003(14)	.01(14)	.003(21)	.15(4)	.125(18)	.19(3)
HN	-2.5	.071(-)	-.021(-)	£	£	.031(-)	.135(-)	*
B	.13	-.152(17)	-.138(6)	.040(8)	.007(12)	.223(22)	.089(22)	.155(7)
HB	-.40	.059(10)	-.050(7)	-.018(10)	.007(5)	.112(3)	.14(3)	.109(10)

Note : * denotes dependent
£ denote zero by site symmetry
Esd's for N based on range on integrated values due to rounding error

The charges from the deformation coefficients, as expected, have an excessive ionic character (the charge on N and HN clearly shows this) but still identifies the anion and cation. The charges from numerical integration are, however, chemically sensible. For example both carbon atoms C1 and C2 have a small negative charge. The difference between the charges in the first and second column is attributable to the excessive assignment of multipolar functions (and hence charge) to hydrogens in the multipolar refinement. The charge distribution is discussed further in section 3.6.

3.4.7. Electric Field Gradient Tensor

To date there has been no Nuclear Quadrupole Resonance (NQR) study of any $[B_{12}H_{12}]^{2-}$ salt. Nevertheless, the EFG tensor is worth calculating to enable a comparison with the EFG for boron sites in decaborane ($B_{10}H_{14}$) and the the "icosahedral" carborane $C_2B_{10}H_{12}$.

The NQR study [85] of decaborane gave an e^2qQ/h value of 1.21(5) MHz for ^{11}B (2.52(5)MHz for ^{10}B) with the asymmetry parameter $\eta = 0$ by approximate site symmetry (C_{5v}). Furthermore this study was able to determine the sign of ∇E_{zz} to be negative. Therefore eq is estimated at $-1.16e\text{Å}^{-3}$. The sign was attributed by the authors to "more electron density in the boron-hydrogen bond (z-direction of EFG) than in boron-boron bonds which is consistent with the electron-deficient character of < polyhedral > B-B bonds". This statement conflicts with the theoretical ($[B_6H_6]^{2-}$) and experimental (CaB_6) results (see Chapter 2) where ∇E_{zz} has a definite positive sign even though these polyhedral B-B bonds are also electron deficient. In these B_6 octahedron based compounds the borons make 4 polyhedral connectivities and the BBH ($BB\text{-}B_{exo}$) bond angles are 135° rather than 120.4(2)° in decaborane as determined by a neutron diffraction study [86].

The second NQR study [87] on *closo*-$C_2B_{10}H_{12}$ (which has three isomers), gave no signs for the quadrupolar coupling constants, only magnitudes which were (after taking averages) 1.08, 0.92 and 0.80 MHz for ^{11}B in the 1,2- 1,7- and 1,12- isomers respectively. Here the geometry, as established by electron diffraction [88,89,90] is even closer to that of the isoelectronic $[B_{12}H_{12}]^{2-}$

icosahedron. The B-B bond length for local C_{5v} symmetry sites is 1.79(1)Å. For these sites the quadrupolar coupling constant is somewhat lower, between 0.71 and 0.92 MHz. This equates to $|\nabla E_{zz}|$ of approximately 0.69 to 0.88 eÅ^{-3}.

Application of published formulae for the calculation of ∇E from the deformation density and assuming only lattice vibrations gives an eq of -0.18 and -0.17eÅ^{-3} respectively. Correction for the contribution from the promolecular density (eq -0.19 η 0.05) gives eq +0.15 and -0.18 with η 0.77 and 0.24. No esd on these values is available from the refinement program employed but the poor agreement between B1 and B2, even though the deformation functions on each were constrained to be identical, suggests the precision is so poor as to invalidate any interpretation of these eq and η values. The very large difference between the ∇E tensors for the B1 and B2 sites is not plausable. The contribution of the large (but unjustified - see Section 3.6) deformation on the H-N bond of the cation is probably responsible.

3.5. Theoretical Deformation Density Maps

3.5.1. Models for $[Et_3NH]^+$ and $[B_{12}H_{12}]^{2-}$

These calculations were carried out using a 4-31G basis and the *ab-initio* program GAMESS. The $[B_{12}H_{12}]^{2-}$ ion cannot be calculated in isolation because the large negative charge causes some occupied orbitals to be unbound, at least in the early SCF calculation. Furthermore the GAMESS program, while recognising symmetry elements to minimise integral evaluation, is unable to utilise I_h point symmetry. Two point charges reduced the point symmetry to D_{3d}. The position of the two point charges cannot be precisely determined from the crystal structure since this would demand certain preconceptions about the distribution of the positive charge within the triethylammonium ion. The charges were therefore located on a threefold axis each 12Å from the polyhedral centre. The deformation density was thus calculated without detailed modelling of the solid state electric field. This is not a serious disadvantage since in the experimental refinement of the deformation density the two crystallographically independent boron atoms were equivalenced and assigned ideal point symmetry. This is strictly invalidated by the solid state environment. The theory and experiment are both therefore comparable. The model used a B-B distance of 1.817Å and B-H bond length of 1.166Å.

The calculation on the triethylammonium ion was carried out without any point charges. The geometry was taken from preliminary *X*-ray diffraction results which are not substantially different from those after convergence of the multipole refinement.

To explore the charge distribution relative to the free base the same coordinates were used to examine Et_3N.

3.5.2. The $[Et_3NH]^+$ Cation

Figures 3.5.2(a) and (b) show the deformation density calculated for the H-N-C1 and N-C1-C2 planes respectively. Contours are again in intervals of $0.05eÅ^{-3}$. The N-C bond is particularly unusual with no peak midway along the vector but instead a steady decline from an initial large surplus electron density near the N atom to a deficit near the carbon position. The C1-C2 bond is also unusual with a similar gradient in the deformation density from large at C1 to small at C2.

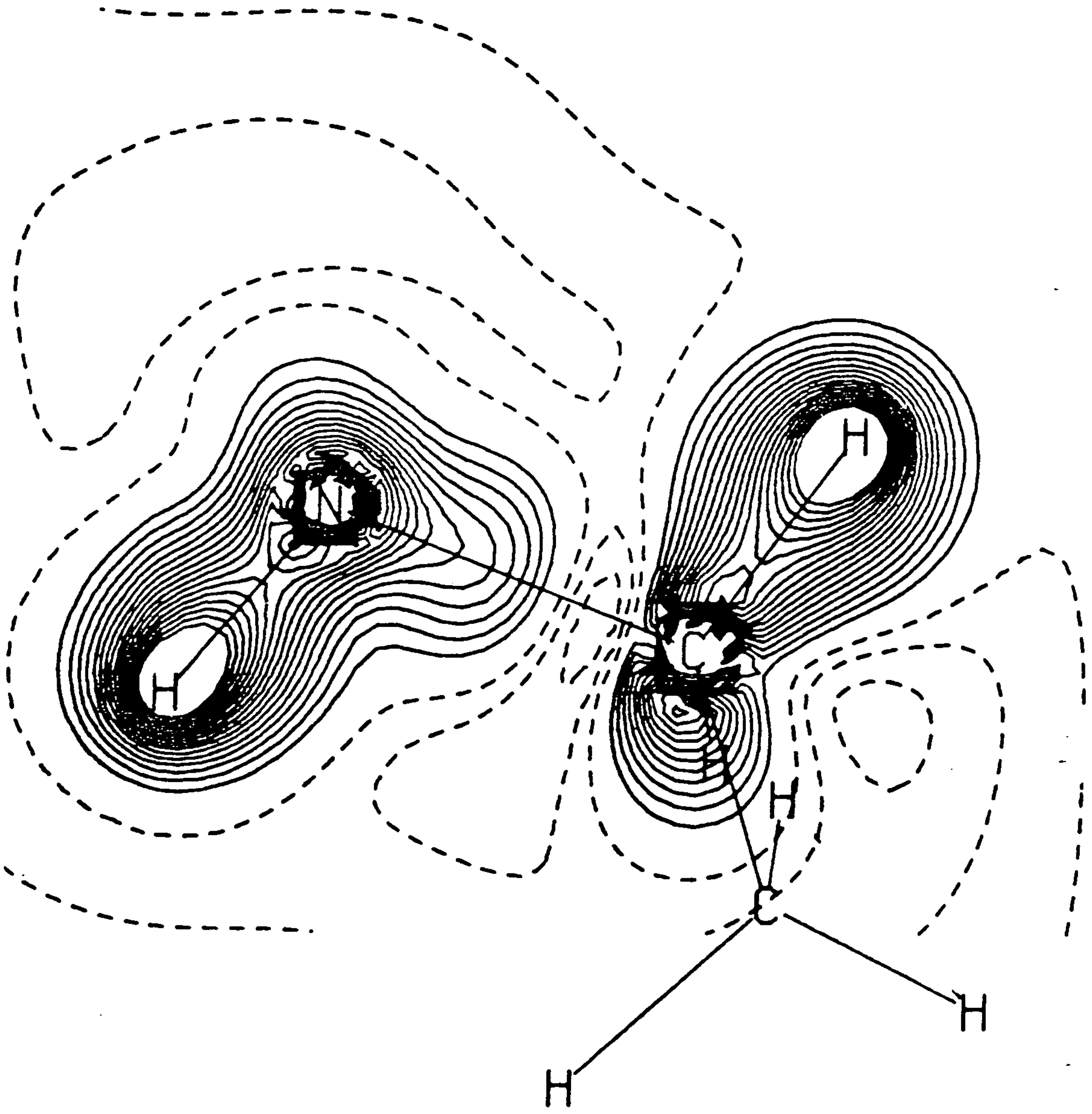

FIGURE 3.5.2(A)

Theoretical Deformation Density
in H-N-C1 plane.

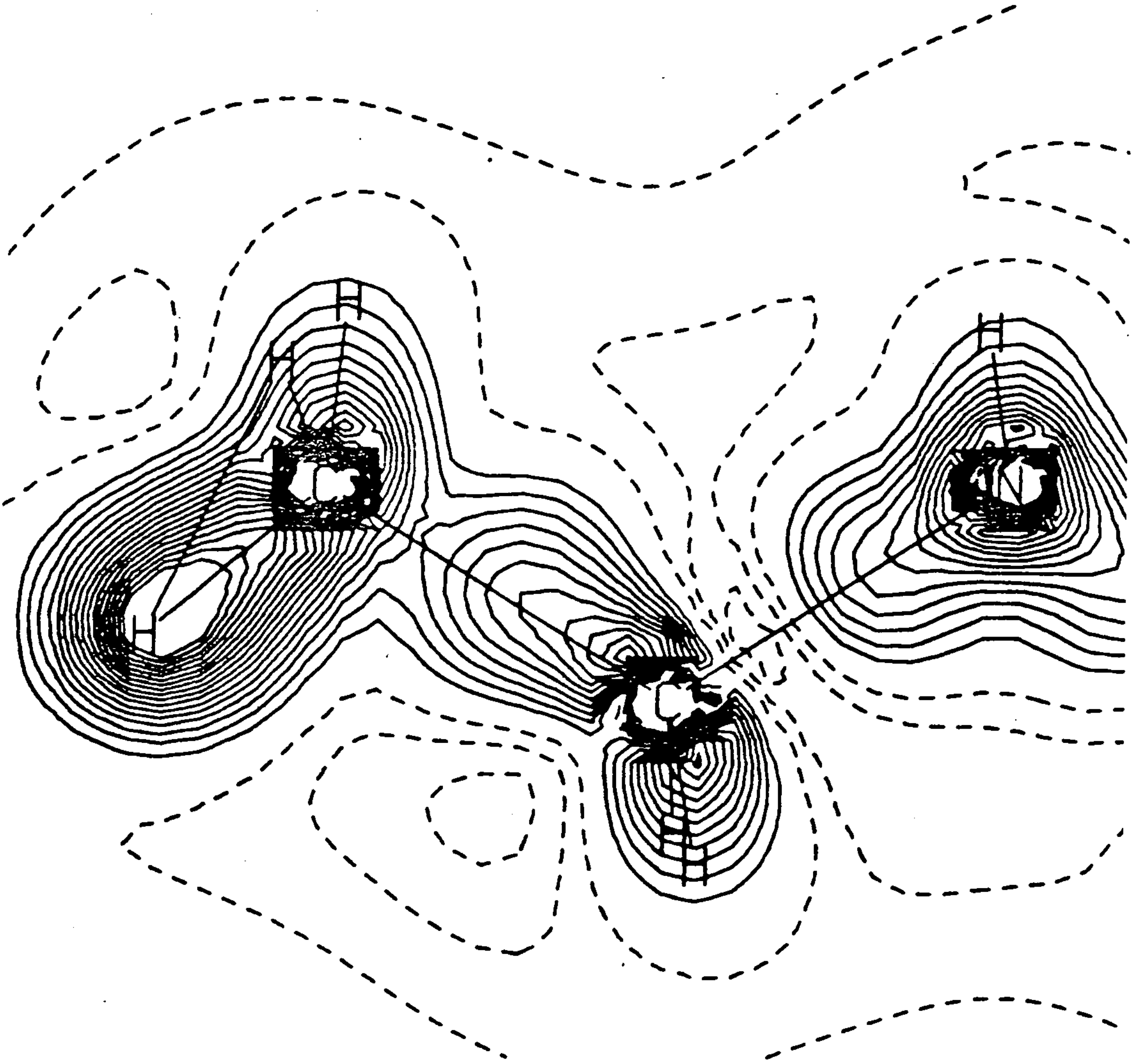

FIGURE 3.5.2(B)

Theoretical Deformation Density
in N-C1-C2 plane.

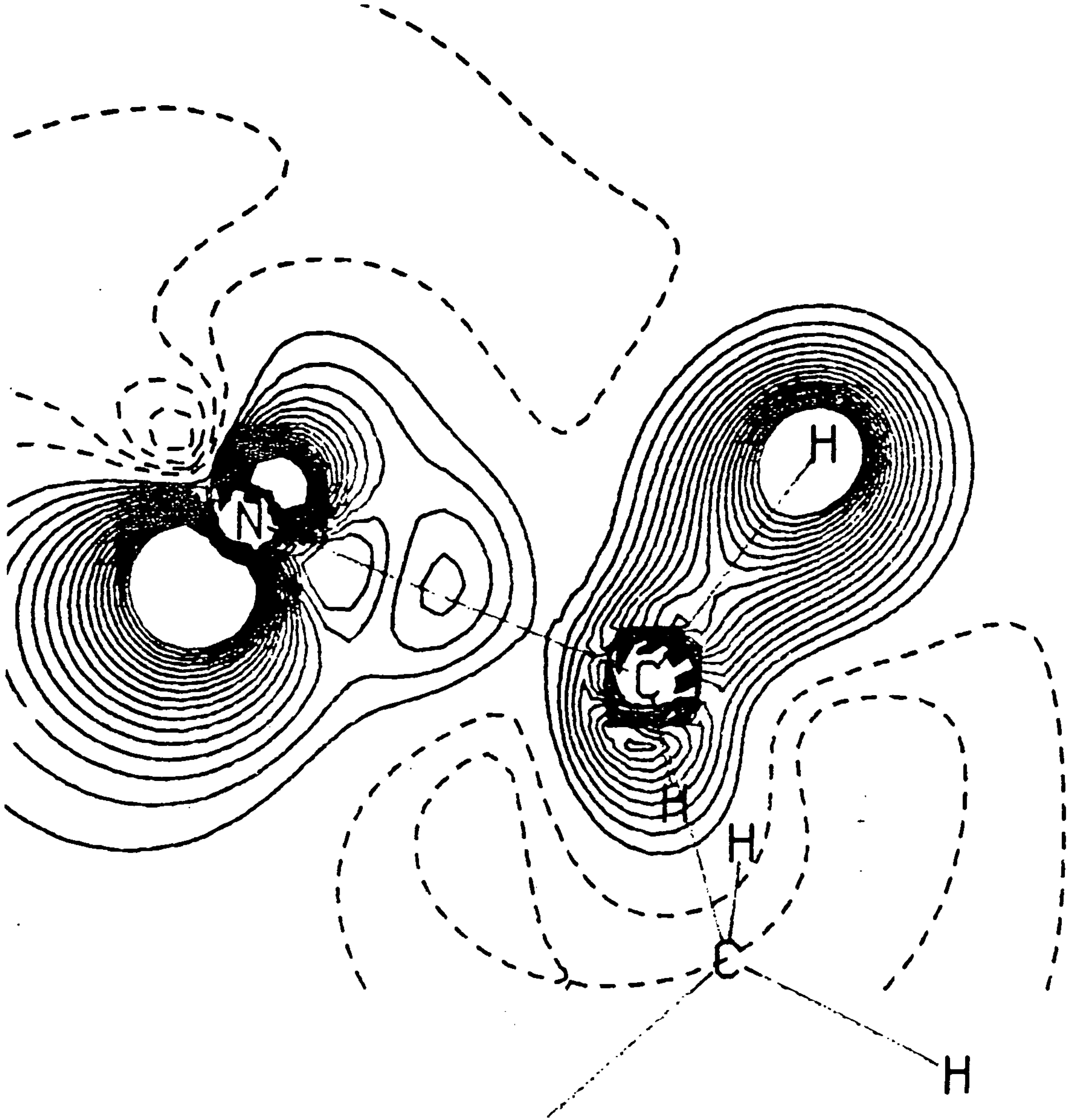

FIGURE 3.5.2(C)

Theoretical Deformation Density
for NEt_3, plane as for 3.5.2(a)

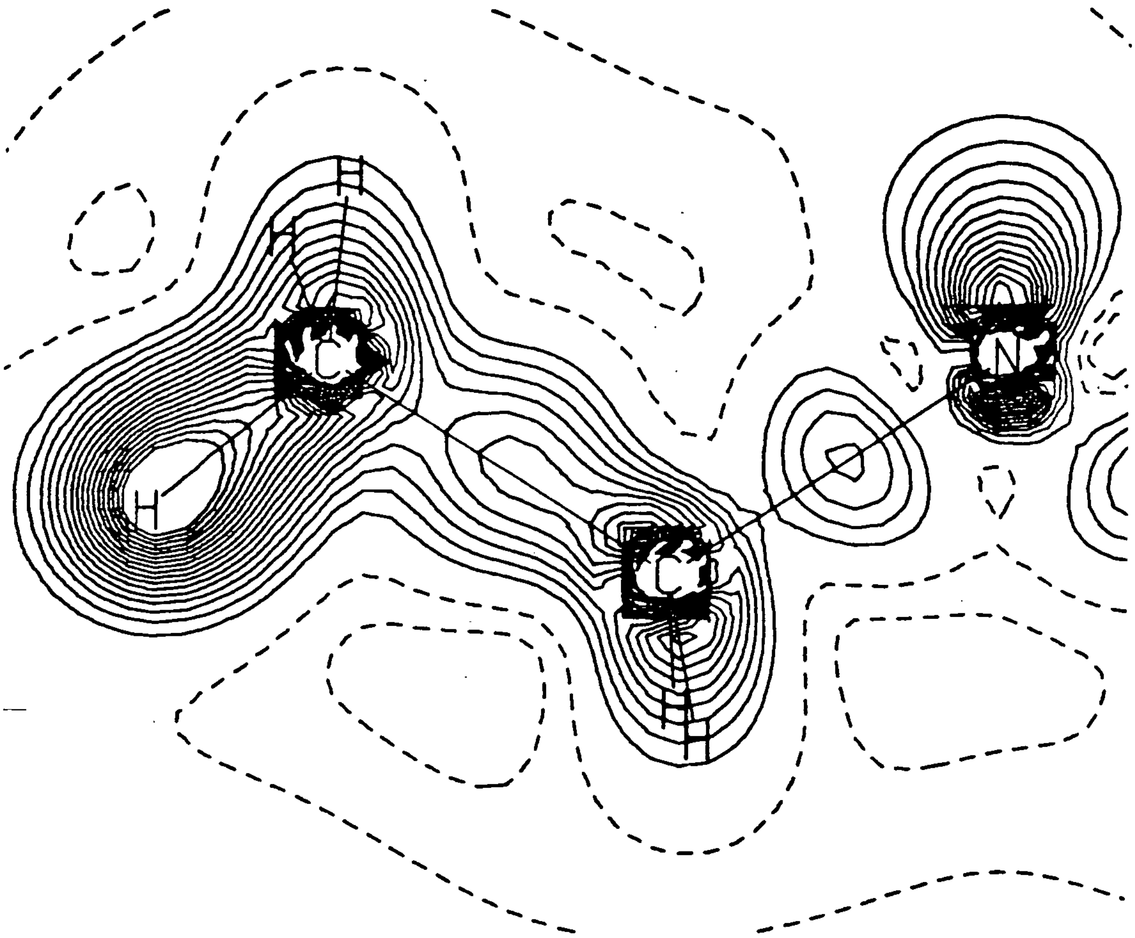

FIGURE 3.5.2(D)

Theoretical Deformation Density
for NEt_3, plane as for 3.5.2(b)

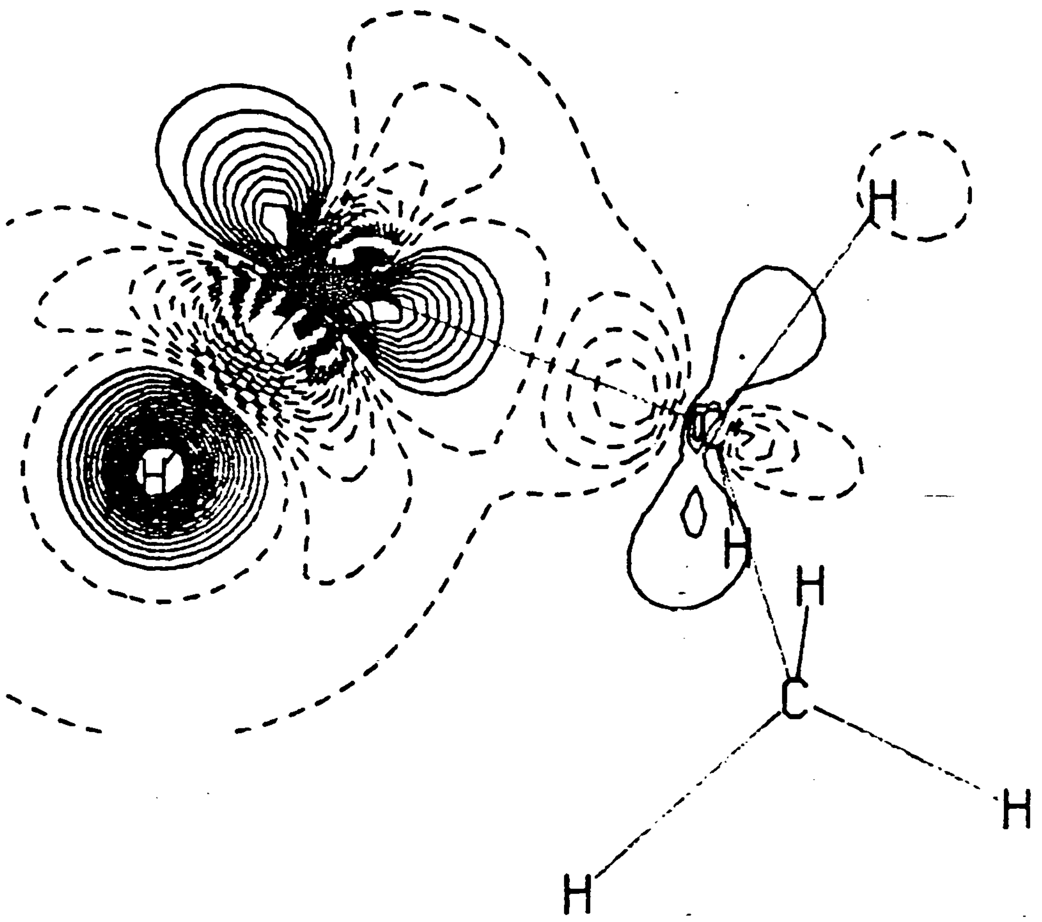

FIGURE 3.5.2(D)

Fragment Deformation Density
= (a)-(c).

Figures 3.5.2(c) and (d) are analagous to (a) and (b) but for the free base Et_3N. These show the more usual bond peaks midway along the interatomic vectors. Figure 3.5.2(d) shows the difference density (a)-(c) (a fragment deformation density) which demonstrates how protonation of the base draws electron density from the lone pair on nitrogen which in turn draws electron density along the σ-bonded alkyl chains.

The theoretical results in Figures 3.5.2(a) and (b) should be compared with experimental results displayed in Figures 3.4.3.1(a), (b). They are discussed in Section 3.6.1.

3.5.3. The $[B_{12}H_{12}]^{2-}$ Anion

The theoretical deformation density for a plane containing an edge and the inversion centre is presented in Figure 3.5.3. This should be compared with the experimental result in Section 3.4.3.2. The features are discussed in Section 3.6.2.

3.6. Discussion : Theory and Experiment

3.6.1. Charge Distribution in $[Et_3NH]^+$

The positive charge in alkylammonium ions is *not* simply localised on the nitrogen atom, nor, in the case of $[Et_3NH]^+$, is it localised on the unique hydrogen. A Mulliken population analysis shows a charge distribution more close to H +0.41, N −0.83, CH_2 +0.32, CH_3 +0.15. However even a Mulliken population analysis is flawed by the simplistic division of overlap density between atoms. This is of course more serious for pairs of atoms of different electronegativity eg C and H. The stockholder recipe (which can be applied to the electron density from an *ab-initio* calculation) when applied to the

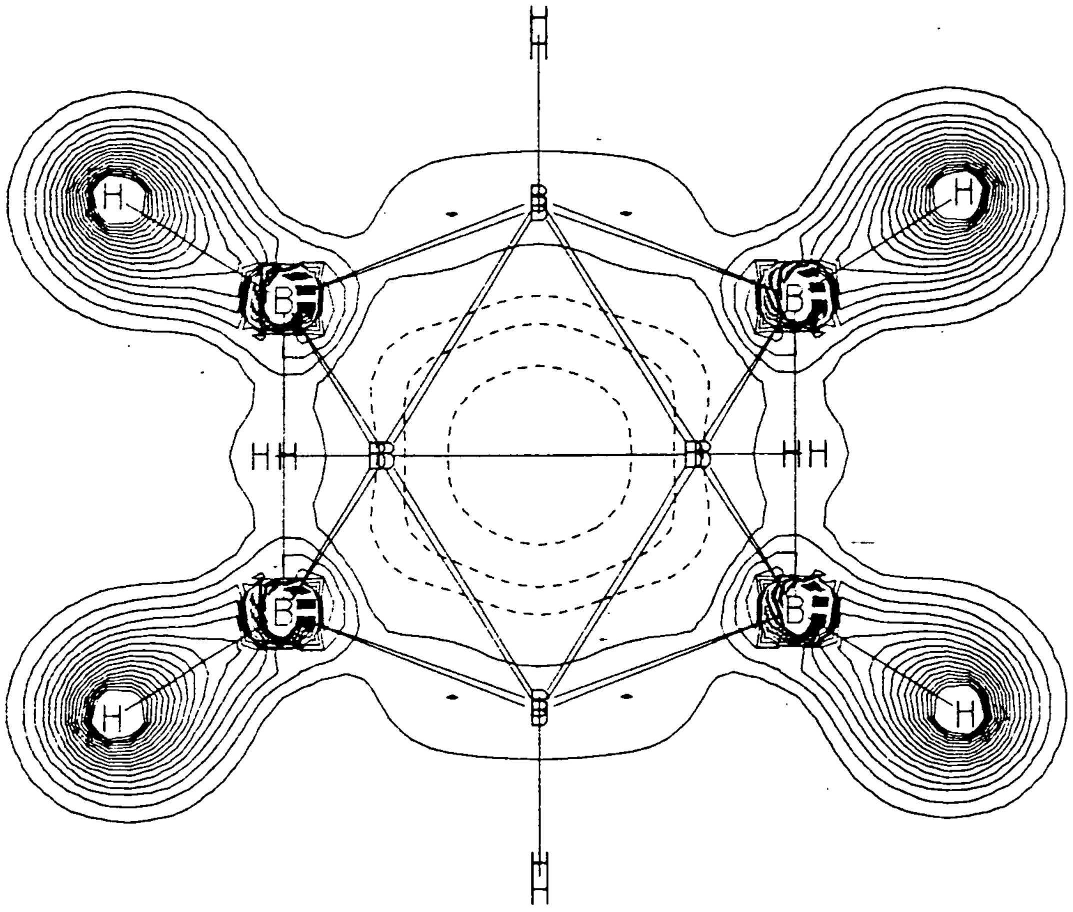

FIGURE 3.5.3

Theoretical Deformation Density
for $[B_{12}H_{12}]^{2-}$, plane as for 3.4.3.2(a)

experimental charge distribution gives H 0.07, N 0.33, CH_2 0.03 and CH_3 0.10, (sum for Et_3NH +0.79). All these results and the fragment deformation density (see Section 3.5.2) show that the positive charge is not localised. This is in agreement with Pauling's electroneutrality principle[38].

The agreement of the deformation density maps with simulations from *ab-initio* calculations is not good. The N-C bond peak is clearly shifted off the N-C vector in the experimental map but not in the calculated one. Furthermore the profile is markedly different. Comparison of the N-C1-C2 planes is better although again the C-C bond deformation density is calculated to be asymmetrical but is 'observed' in the multipole refinement to be approximately symmetrical. Possible sources of discrepancies are

- The basis functions for the multipole refinement are too limited to describe the deformation density
- Errors in the observed structure factors.
- The deformation density for the ion in an ionic solid is genuinely different from that for the isolated ion.
- The basis functions for the *ab-initio* calculation are inadequate.

The contribution of the first source can be estimated by examining the residual density maps and looking for non-random features. Figures 3.4.5(a) and (b) do not show any such features.

The contribution from the second source can be estimated by examining the esd of the deformation density to determine if the discrepancy is statistically significant. The esd maps (Figs 3.4.3.1(c), (d)) show a very large esd near the symmetry axis which rapidly decays. This suggests that the discrepancy is significant.

The third source could be tested by re-calculating the *ab-initio* deformation density for the ion in some external electric potential which modelled the potential inside the ionic crystal. This test is demanding. Each neighbouring $[B_{12}H_{12}]^{2-}$ anion could be effectively modelled by a point charge since for all points outside a spherically symmetric charge distribution the electric field is identical to that generated by the net charge of the distribution at the centre. The anion is sufficiently symmetric for this approximation. The $[Et_3NH]^+$ is not highly symmetric and can be modelled by integer charges only very crudely. The packing of anions and cations in the unit cell is a complex layer structure - $[(A\gamma B)(C\beta A)(B\alpha C)]_n$ in the conventional notation[1] - with each anion having 8 neighbouring cations (6 in a trigonal antiprism at 6.15Å, 2 on the threefold axis at 4.67Å) and each cation having 4 neighbouring anions (in a distorted tetrahedron : one at 4.67Å, three at 6.15Å) and 6 neighbouring cations (in a distorted trigonal antiprism, three at 6.43Å, three at 7.02Å). A calculation using a 4-31G basis and a $[Me_3NH]^+$ model both with and without an environment of integer charges $((X^+)_{53}(Y^{2-})_{27})$ showed no significant distortion of the deformation density due to the point charges.

The above result is in contrast to the effect reported in an *X*-ray diffraction study of Cs_2O [91] (Space group R-3m, a=6.9790Å, α=35.93°) where there is an apparent elongation of the charge distribution along the hexagonal c-axis. The elongation is asymmetric with electrons on the Cs^+ ion drawn towards the adjacent layer of Cs^+ ions. While expounding that the Cs ions "must be highly polarised in the layer crystal of Cs_2O" the authors also invoke anisotropic extinction attributable to layer -shearing disorder perpendicular to the c-axis. Such disorder has a more severe effect on the alignment of hexagonal (h, k, 0) planes than the (0, 0, l) planes. This is a notorious feature of $CdCl_2$ lattices where polytypes can be generated such as the 2H, 4H, 6H, 6R, 12H and 12R (R

---

[1] A.R.Verma and P.Krishna, "Polymorphism in Crystals", Wiley, New York,(1966)

- rhombohedral, H - hexagonal). An example would be the 12R modification with the layer structure $[(A\gamma B)(C\alpha B)(C\beta A)(B\gamma A)(B\alpha C)(A\beta C)]_n$. Where the layer structure flips frequently, disordered structures result. This structural relationship between $[Et_3NH]_2[B_{12}H_{12}]$ and Cs_2O is not exact enough for the polarisation (if true) to justify deformation density distortion in the $[Et_3NH]^+$ cation but if proven in Cs_2O some contribution should be expected in $[Et_3NH]_2[B_{12}H_{12}]$, $TbFe_2$ and $[Me_3NH]_2[SnCl_6]$. It would therefore be interesting to determine the deformation density in another anti-$CdCl_2$ lattice structure.

The polarisation of the Cs^+ ion in Cs_2O was modelled by $Cs^+(X^+)_{66}(Y^{2-})_{28}$ using an extensive basis set for Cs [92] augmented with two independent polarisation functions. The difference density Cs^+ - $[Cs^+(X^+)_{66}(Y^{2-})_{28}]$ for a plane containing the hexagonal c-axis was found to be negligible. The magnitude of the distortion from spherical symmetry was much smaller than the distortion observed in the residual density from the *X*-ray diffraction experiment. The rationalisation of the difference maps by simple polarisation arguments is therefore not supported. However, expansion of the model to include one oxygen atom (TZVP on O) does alter the calculated result with some deformation density on the internuclear axis. This last calculation, although having only two centres for basis functions, was the largest that could be tackled. This theoretical result supports the residual density features of the *X*-ray diffraction work but clearly the calculation is grossly inadequate. An analogy with Cs_2O cannot yet be used to rationalise the shifted N-C bond peak in $[Et_3NH]^+$.

The fourth possibility - that the 4-31G basis used is inadequate could only be demonstrated by repeating the calculation with a larger basis set (ideally including polarisation functions). The triethylammonium ion is too large for this purpose. A smaller model $[Me_3NH]^+$ is still too large but $[H_3NMe]^+$ can be used. The MOSCOW graphical analysis program previously used to display the results from the *ab-initio* GAMESS program is not capable of using basis sets other than 'STO-nG' or 'n-(n-1)1G' therefore the calculations including the evaluation of the deformation density were carried out using the ATMOL program package. Figures 3.6.1(a) and (b) show the calculated deformation density for an isolated $[H_3NMe]^+$ ion using the 4-31G and TZV (triple zeta valence) basis sets respectively. The differences are very slight and the 4-31G basis set is concluded to be adequate for the purpose.

The failure to reproduce or explain the the shift of the N-C bond deformation off the inter-nuclear axis prompted a more critical analysis of this feature. The dynamic deformation density map using all Fc to a sufficient resolution again shows the anomalous feature. The whole map is, as expected, similar to the static map but with smaller peaks due to thermal smearing. If instead only those Fc corresponding to structure factors *which were measured* (and used in the refinement) are included in the Fourier summation then Figure 3.6.1(c) is obtained. This map is substantially different and is in much better agreement with the theoretical result. In particular an electron surplus surrounds the N-C vector and the asymmetry in the profile (along the interatomic vector) is qualitatively reproduced - subject to the inadequacy of comparing a dynamic and static (theoretical) map. Re-calculation of the static experimental map, again using only Fc calculated in the refinement, gives the result displayed in Figure 3.6.1(d) which should be compared to Figure 3.5.2(a) and contrasted with Fig.3.4.3.1(a).

The important question is how can the experimental maps produced using all Fc's and those using necessarily refined Fc's give such different results?

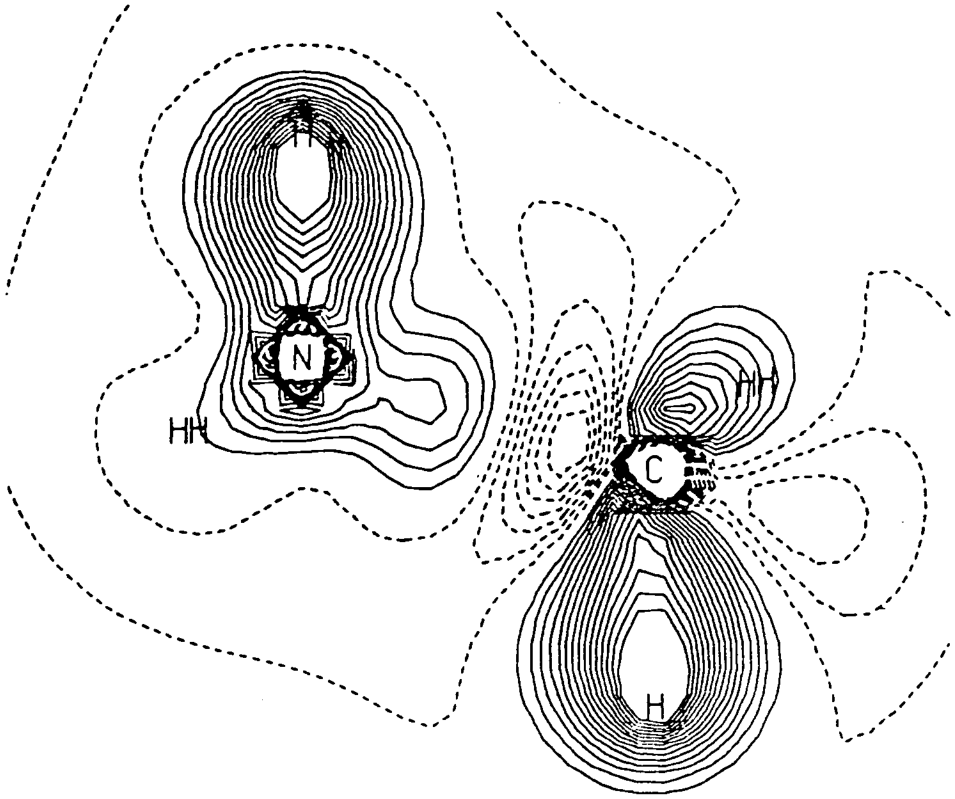

FIGURE 3.6.1(A)

Theoretical Deformation Density
for $[MeNH_3]^+$, 4-31G basis, mirror plane.

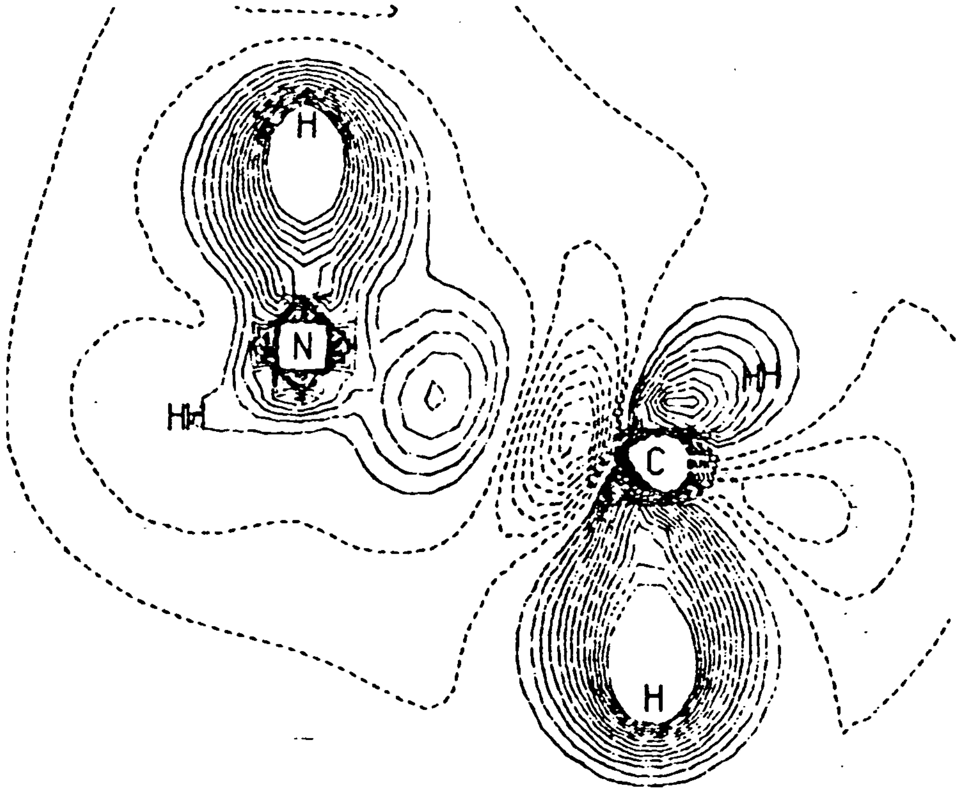

FIGURE 3.6.1(B)

Theoretical Deformation Density
for $[MeNH_3]^+$, TZV basis, mirror plane.

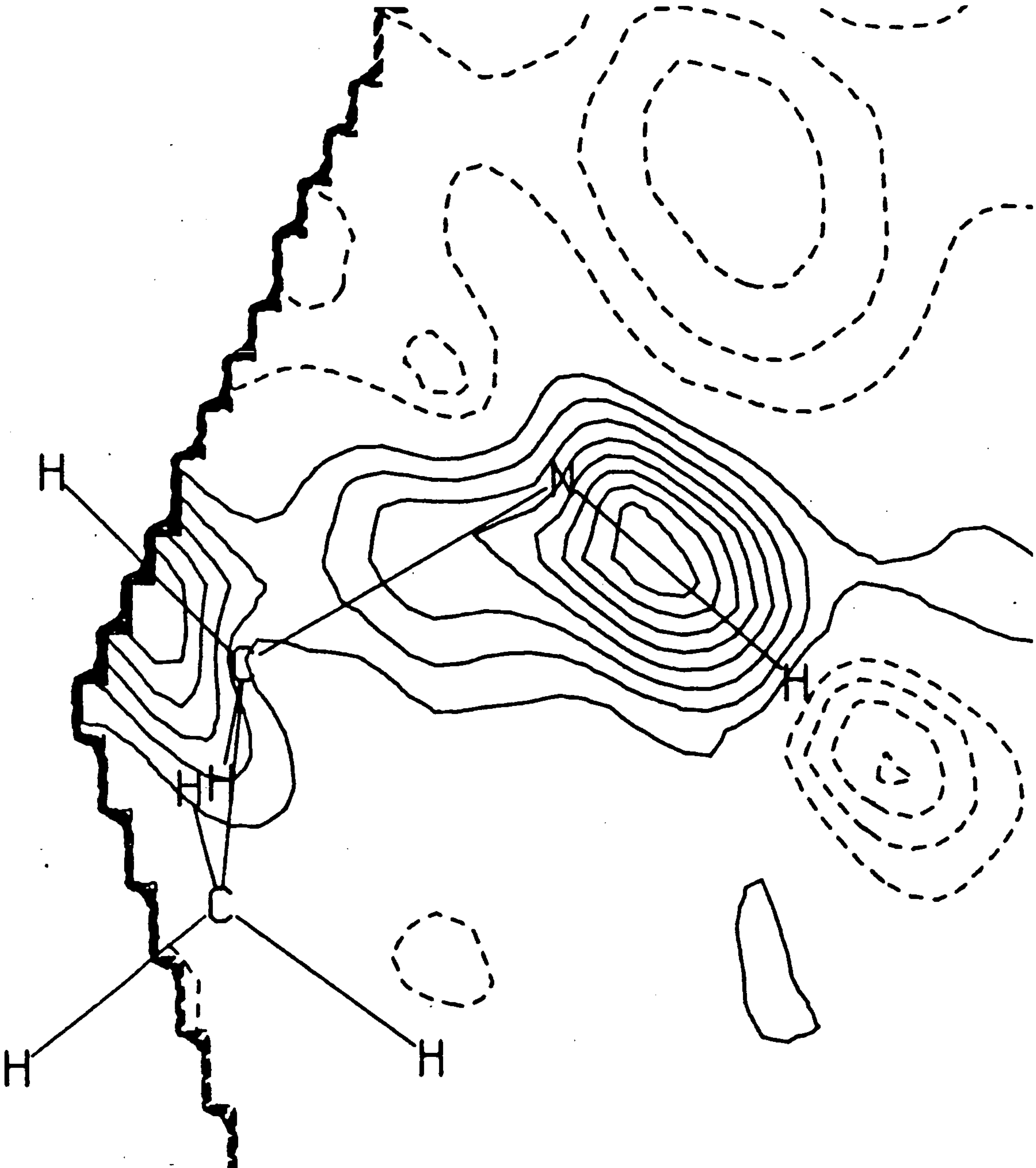

FIGURE 3.6.1(C)

Dynamic Deformation Density
in $[Et_3NH]^+$, limited Fc terms –see text.

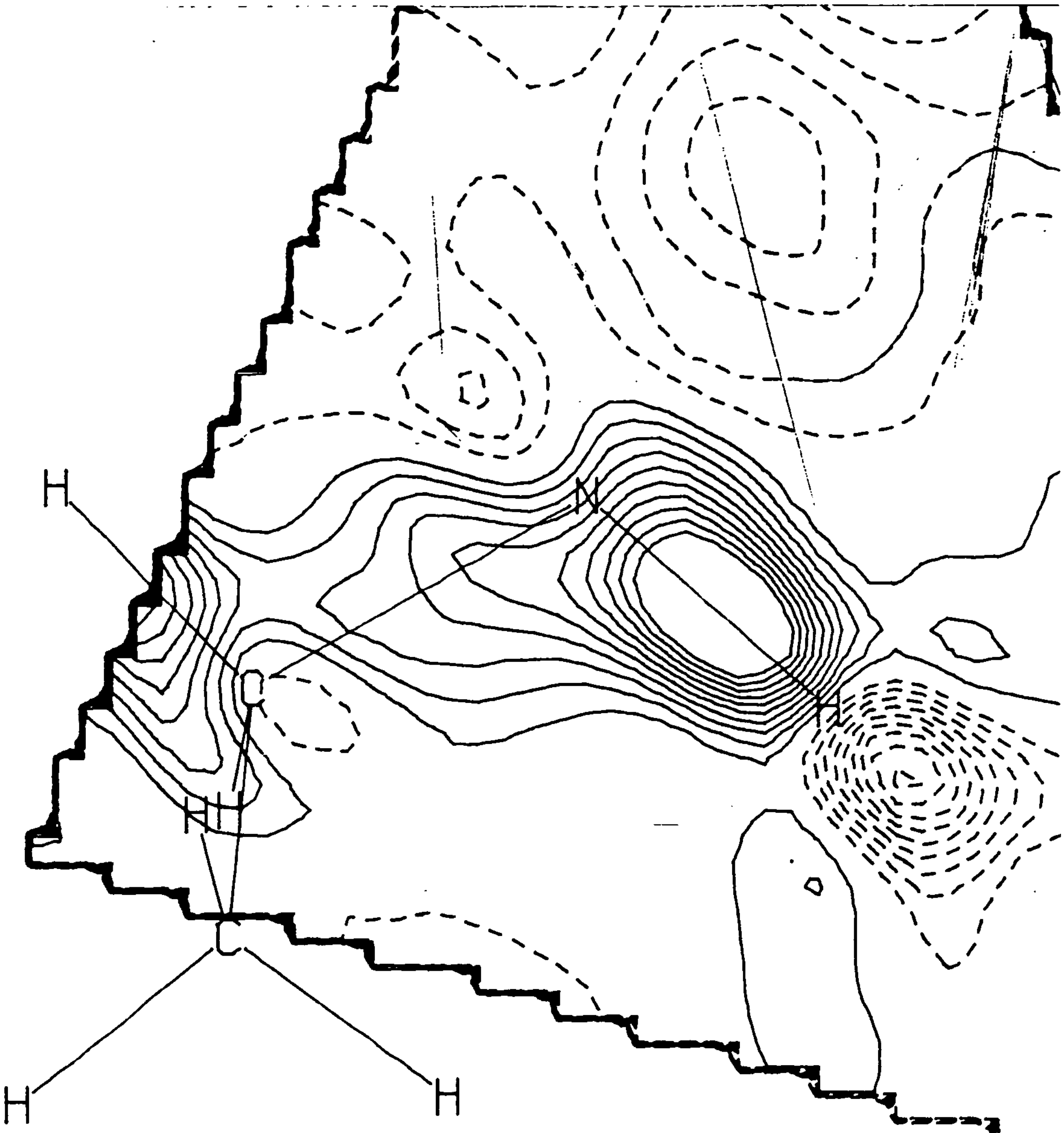

FIGURE 3.6.1(D)

Static Deformation Density
in $[Et_3NH]^+$, limited Fc terms -see text.

Furthermore does this difference invalidate the technique of collecting only a limited portion of the data and using multipolar methods to refine and display it?

The answer to the first question is simple - neither map is inconsistent with the observed data. However, the difference in the maps originates from inclusion of Fc's for which no matching observation was made. Consequently there is in effect no explicit restraint on their value. Another way of explaining the difference, in direct space, is that the model fits the observed density as efficiently as possible but, like any other model, can give a poor fit for interpolated or extrapolated points.

The answer to the second question is clearly important but is not so simple. The two-stage measurement technique is dependent on selected data points being distributed in such a way that all density features are equally well characterised. Consequently it is important that there is an even distribution of data points in reciprocal space. For practical reasons data points with large (estimated) values of F_{hkl} are selected for measurement. The additional use of E_{hkl} in the selection process improves the radial distribution in reciprocal space. However, the angular distribution in reciprocal space is not usually checked before the selected indices are used in data collection. This omission can result in weak characterisation of the deformation density in certain planes. This defect will *not* be detected in an esd map which only identifies zones where the fit to the observed data is poor.

How might the data distribution in reciprocal space be checked? One method would be to plot each data point (h, k, l) (and those equivalent by symmetry) using the reciprocal cell coordinate axes and examine either a stereo pair or several projections. The resulting plot should be nearly spherically (circularly) symmetric. This procedure is practical only for small unit cells and/or low resolution data. An alternative method would be to calculate the moments of inertia of the set of selected reciprocal lattice points (and their equivalents). The three moments should be nearly equal for an evenly distributed data set. This test could be applied to shells of lattice points. This 'moments' test will of course not work for cubic unit cells and is of limited use in the uniaxial spacegroups.

The application of such tests may discredit some data set selections but the same tests are difficult to incorporate in an algorithm for the determination of a data set satisfactorily distributed in reciprocal space. The ideal method would be to use the data already collected to refine a multipolar model which would predict which, as yet uncollected data, are most acutely dependent on the deformation density. These data would then be acquired and the iterative process repeated.

Returning to the problem of the shifted N-C bond peak, the flaw in the data set which permitted this problem is displayed in Figure 3.6.1(e) - a stereo pair illustration of the distribution of the 97 unique lowest angle data (and their symmetry equivalents). The reciprocal cell is also illustrated but on a different scale. This figure shows a lack of data near the 3-fold axis. Such a deficiency means the N-C bond component along the hexagonal c-axis is ill-characterised. This is the direction of the spurious bond peak shift.

This imbalance in data point distribution becomes less important when the same multipolar basis is used to describe the deformation density for several chemically equivalent (but crystallographically independent) atoms. In such cases refinement of the multipoles is dependent on a larger, more widely distributed set of data. For example, a dipole function orientated at different

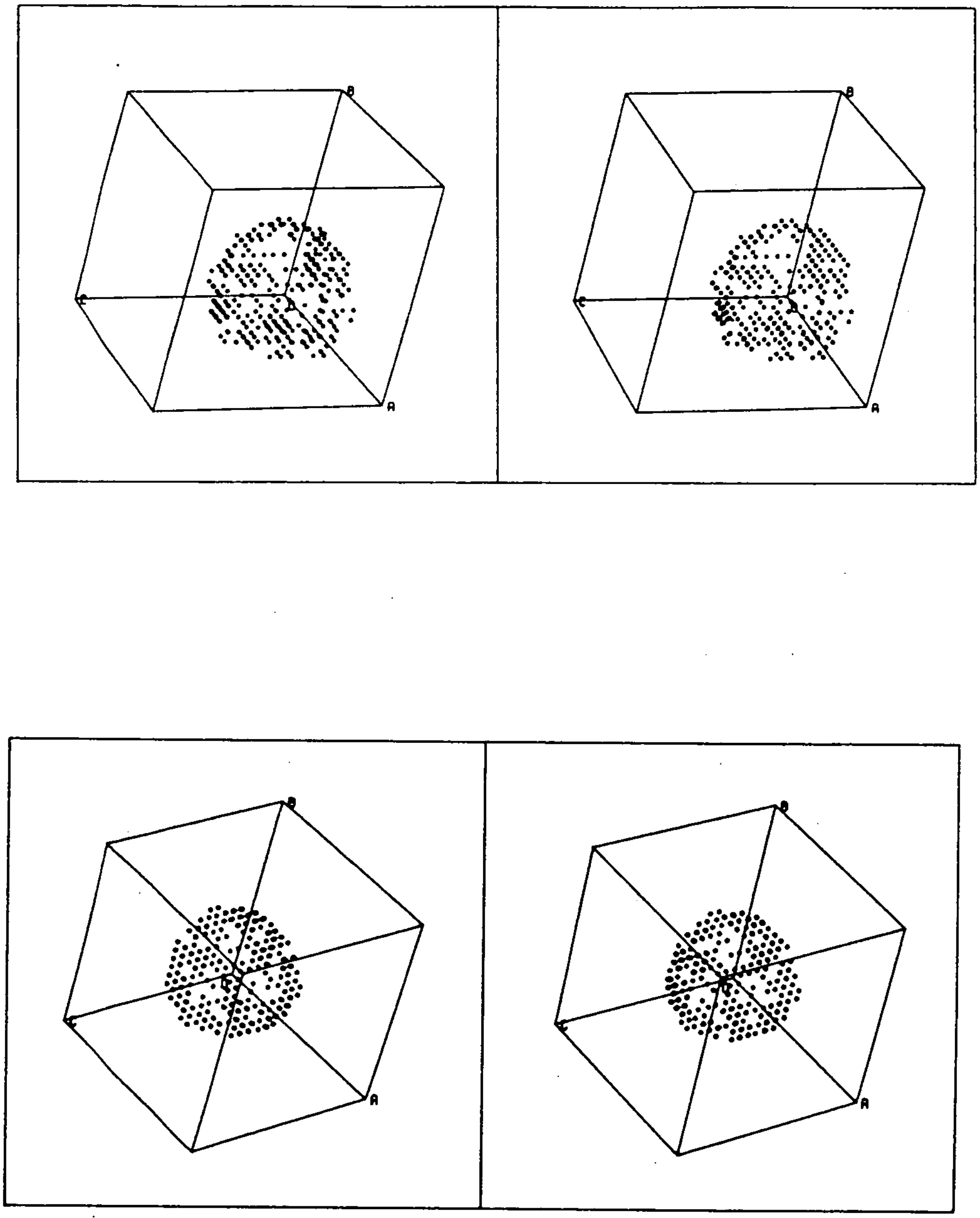

FIGURE 3.6.1(E)

Distribution of Data in Reciprocal Space.

angles on two atoms is heavily dependent on data in two directions of the reciprocal lattice. Consequently only if both these directions are relatively deficient in data will there be a divergence of deformation maps using Fc for observed structure factors and direct summation using the multipolar expansion.

3.6.2. Charge Distribution in the $[B_{12}H_{12}]^{2-}$ Ion

A comparison of the theoretical deformation density (Figure 3.5.3) with the experimental static deformation density (Figure 3.4.3.2(a)) shows good qualitative agreement : electron deficiency inside the polyhedron and a continuous surplus at a fixed radius (ie on edges but over faces). Close inspection, however, reveals differences (other than in the B-H bond where the experimental technique is of limited validity).

The surplus electron density in the theoretical map is diffuse and almost constant over the polyhedral surface at between 0.05 and (briefly) 0.10eÅ^{-3}, except in close proximity (< 0.4Å) to the borons. The largest contour to define a continuous iso-density surface is calculated to be 0.06eÅ^{-3}. In contrast the experimental map shows peaks as high as 0.15eÅ^{-3} on the midpoint of the B-B connectivities and a continuous iso-density surface of approximately 0.12eÅ^{-3}.

This difference is significant because the discrepancy (0.10eÅ^{-3} on the midpoint of the B-B vector) is much more than the esd (0.01eÅ^{-3}; Figure 3.4.3.2(b)) or the residual density (0.03eÅ^{-3}; Figure 3.4.5(c)). *Ab-initio* calculations at the 4-31G level are not necessarily the 'correct' result. There was a significant change in the deformation density when the basis was improved from 3-21G and it is quite probable that further changes would occur if the basis set was increased again (for example by the inclusion of bond-centre functions and/or polarisation functions). Like $[Et_3NH]^+$ the $[B_{12}H_{12}]^{2-}$ ion is too large for an *ab-initio* calculation using an extended basis but unlike the cation there is not a smaller model of the anion to demonstrate the limit of the deformation density. A crude approximation would be the 5-fold sites in *closo*-$[B_7H_7]^{2-}$ (D_{5h}) which is the smallest of the $[B_nH_n]^{2-}$ series to have a six (five B, one H) connected boron. This small model is unsatisfactory because of the short B-B distance on the five fold axis. This would result in a quite different electron distribution inside the polyhedron. (The structure of $[B_7H_7]^{2-}$ has *not* been determined by *X*-ray diffraction but carborane analogues have been characterised by microwave spectroscopy[93] and electron diffraction[94].)

3.6.3. Related Deformation Density Studies

Other boron polyhedra which have been studied are $LiAlB_{14}$ [95] and α-AlB_{12} [96] each of which contains a B_{12} icosahedron. Although these examinations were recent (1983 and 1979 respectively) they used only the primitive X-X method to display the deformation density (although charges were refined using the extended L-shell method). In $LiAlB_{14}$ the B_{12} icosahedra are substantially distorted and while each B has an external B contact these contacts are not all chemically similar (some are contacts with neighbouring icosahedra, others are with boron atoms which are in turn coordinated to Li and Al). Not all the deformation density maps for crystallographically independent planes were published for $LiAlB_{14}$ but the following features were observed :

- Electron deficiency at the core of $-0.20e\text{Å}^{-3}$.

- Large peaks ($0.15e\text{Å}^{-3}$) bordering the midpoint of B-B connectivities.
- Diffuse electron surplus ($0.10e\text{Å}^{-3}$) external to the faces.

The fact that the latter peaks are external to the faces is not stressed by the authors and a second figure presents the deformation density for a plane containing a triangular face rather than one over it . The authors do stress that there were " accumulation of charges at the centres of the faces which is characteristic feature of delocalised 3 centre bonds." All these features are in good agreement with those in $[Et_3NH]_2[B_{12}H_{12}]$ but are woefully ill-characterised in X-X maps. The structure factors for $LiAlB_{14}$ should be utilised in a multipolar-expansion program to increase the resolution and filter out the random noise. Only this would allow a proper comparison - and perhaps enable the interpretation of any differences in terms of the short range polarisation.

The α-AlB_{12} structure contains B_{12} and B_{19} units (two icosahedra fused face to face and each icosahedron missing one vertex) as well as single borons. This work was not a deliberate study of the deformation density but a careful examination of the non-random residual density from a conventional structure solution data set. The data extended to only $S = 1.56\ e\text{Å}^{-1}$ (θ=34° for Mo-K_α) but the successful mapping of the deformation density using the weak X-X technique was made possible by averaging the 120 original residual densities for the B_{12} triangular face and 60 original densities for the bisecting plane through two opposite edges.

The results were impressive with a clear deficiency at the core ($-0.18e\text{Å}^{-3}$), and surplus density maximised over the faces ($0.10e\text{Å}^{-3}$) which decreased towards the B-B edges ($0.05e\text{Å}^{-3}$) with a local maximum slightly inside the B-B connectivity. The relatively massive peaks on the exo-polyhedral B-B contacts (0.20eÅ^{-3}) were interpreted by the authors as evidence of two-centre two-electron bonds. The authors therefore recognised the close similarity in the electronic structure of the icosahedral unit in α-AlB$_{12}$ with the $[B_{12}H_{12}]^{2-}$ molecular ion. Their calculation of the deformation density using CNDO/2 bears little more than a simple qualitative resemblance to that calculated at the 4-31G level or experimental results on $[B_{12}H_{12}]^{2-}$ or their own results on α-AlB$_{12}$. Such a map serves only to confirm the inadequacy of the semi-empirical MO methods in providing a comparison for *X*-ray diffraction deformation density studies. Again the information which could be obtained from the α-AlB$_{12}$ structure factors would be greatly improved if multipolar refinement methods were employed.

The last related compound which has been the subject of a deformation density study is decaborane ($B_{10}H_{14}$). This is the only other hydroborate to have been studied. The first study [97] in 1971 used *X*-ray and neutron data in a crude refinement of the deformation density using fractions of hydrogen atoms with variable temperature factors. This model was expanded [98] in 1978 to refine some 55 independent deformation parameters. Typical surplus electron deformation densities in the plane of independent B_3 triangles are 0.15eÅ^{-3}. This is slightly larger than those in $[Et_3NH]^+{}_2[B_{12}H_{12}]^{2-}$. These crude results also agree in the form of the surplus deformation density being triangular pyramids staggered with respect to the B_3 coordinates and positioned slightly outside the polyhedral surface (elevations 0.12(4), 0.01(3) and 0.05(3)Å cf $[B_{12}H_{12}]^{2-}$ 0.10(2)Å). The question of edge vs face localisation is not resolved since this option was not permitted for all independent faces and edges. In the same paper comparisons were made with the theoretical result for $B_{10}H_{14}$ using a minimal basis set [99]. These maps bear scant resemblance to the experimental results for $B_{10}H_{14}$ or to the experimental or calculated maps for $[B_{12}H_{12}]^{2-}$. This again demonstrates how the minimal basis sets are useless for even qualitative estimation of the deformation density.

3.7. $[B_{12}H_{12}]^{2-}$ and $[B_6H_6]^{2-}$: Similarities and Contrasts

The icosahedral $[B_{12}H_{12}]^{2-}$ ion and the octahedral $[B_6H_6]^{2-}$ ion are both examples of ions which have more connectivities than pairs of electrons. Initially these geometries were rationalised by introducing bond types other than the familiar two-electron two-centre bonds. These were the 3-centre 2-electron bonds such as BBB and (for the rationalisation of other hydroborates) BHB. For $[B_6H_6]^{2-}$, which has 12 connectivities and is bound by 7 pairs of electrons, one topologically allowed description would be 3 BBB bonds and 4 BB bonds. However, just one such description would not give octahedral symmetry and therefore averaging over symmetry related resonance forms needs to be invoked. There are still other topologies of 3 BBB/4 BB bonds and even others with different ratios of two- and three-centre bonds. For $[B_{12}H_{12}]^{2-}$ the number of symmetry independent resonance forms is very large and can only be generated with the aid of a computer. Such topological arguments were superceded by Wade's Rules which relate the geometry of polyhedra to the number of electron pairs needed to bind the polyhedral skeleton (PSEP's). The foundation of Wade's Rules was MO theory which had established that for closed triangulated polyhedra with n-vertices, with each atom having s and p-orbitals, there are exactly (n+1) bonding molecular orbitals. Only numerical calculation can finally determine the number of bound orbitals.

Both the above ions belong to the *closo*-class in Wade's classification and the B_n frameworks are therefore bound by (n+1) pairs of electrons. The 4-31G calculations on these ions (Figs 2.7.4(a) and 3.5.3) reveal the same qualitative features : electron deficiency at the core and surplus electron density extending from just inside the polyhedral surface outwards. The largest deformation density feature is always associated with the *exo*-polyhedral σ-type bond (ie B-H). Any bonding through the core of the polyhedron should be a maximum for $[B_6H_6]^{2-}$ which has the shorter B-(core)-B distance (2.39Å). However, the deformation density at the core is calculated to be negative ($-0.15eÅ^{-3}$), exactly the same as for $[B_{12}H_{12}]^{2-}$. Therefore the stress on the importance of electron density accumulation inside the B_6 octahedron of CaB_6 [59,58] (analagous to $[B_6H_6]^{2-}$ - see Chapter 2) is unfounded. Similarly the empirical bi-reciprocal relationship[55-57] between B-B distances and potential energy, (which for $[B_{12}H_{12}]^{2-}$ assigns 53% of the energy to internal interactions and for $[B_6H_6]^{2-}$ 19%) over emphasises the importance of cross-polyhedral interactions. (See chapter 2 - section 2.7.1)

The 3-dimensional shape of the deformation density in $[B_6H_6]^{2-}$ is in the form of triangular pyramids extending from the triangular faces but staggered with respect to these faces. That calculated for $[B_{12}H_{12}]^{2-}$ is much more diffuse. Figure 3.7 presents a stereo pair of an iso-density surface ($\rho=0.05eÅ^{-3}$) evaluated for a thick slice through the icosahedron.

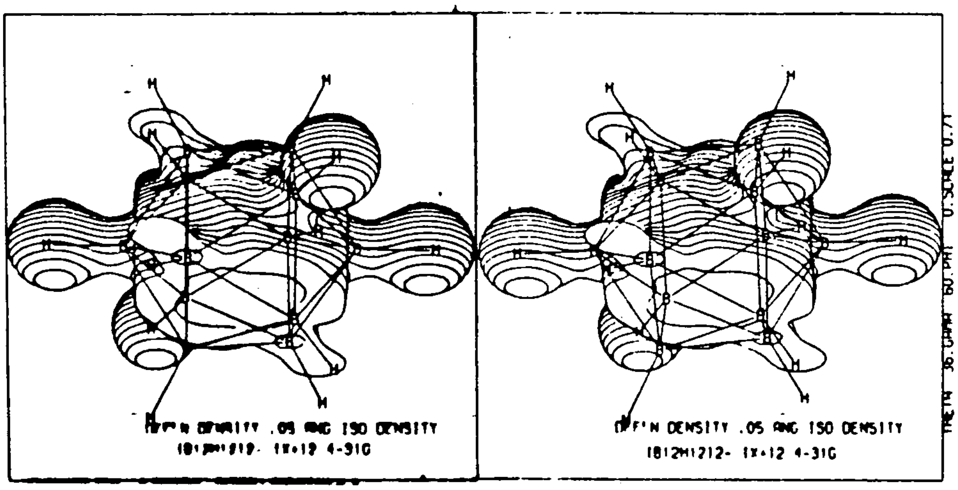

FIGURE 3.7

Theoretical Deformation Density:
Iso-deformation density Surface for $[B_{12}H_{12}]^{2-}$.

From this figure the topology is seen to be different to that of $[B_6H_6]^{2-}$ and is better described as a set of 12 fused toroids with 12 projecting cones on the B–H vectors. The face and edge deformation densities are not sufficiently different for them to be meaningfully ordered.

3.8. Chemical Reactivity and Deformation Density

It ought to be possible to correlate the topology of the deformation density with the chemical reactivity of a substance, in particular electrophilic or nucleophilic reactivity. The protonation of $[B_6H_6]^{2-}$ to give $[B_6H_7]^-$ is one reaction which has recently been studied. Application of the Huckel method suggested an edged-bridged structure [100] for $[B_6H_7]^-$. Application of MNDO and *ab-initio* techniques [101] in which the core of the boron cluster was not constrained predicted the disruption of the octahedron on protonation and the loss of any defineable cluster geometry. Still more work using MNDO with an octahedral constraint on the boron framework gave a μ_3 (face bridging) geometry [102] which was rationalised using localised 2- and 3-centre bond descriptions. The structure of the $[B_6H_7]^-$ anion was recently determined by *X*-ray diffraction [103] and the protonation site was found to be over a face. The topology of the deformation density in CaB_6 with electron density accumulation over the faces – rather than the edges – is in agreement with the structural study in identifying the face as the most probable site for electrophilic attack. Furthermore the extremely diffuse topology of the deformation density in $[B_{12}H_{12}]^{2-}$ may explain the stability of the acid in contrast to $[B_6H_6]^{2-}$ which is steadily degraded in acid conditions.

Chapter 4

Charge Deformation Density of Benzyltrimethylammonium Octahydrotriborate

4.1. Why Study $[C_6H_5CH_2NMe_3]^+$ $[B_3H_8]^-$?

The $[B_3H_8]^-$ ion is, after diborane and $[BH_4]^-$, the smallest and simplest borohydride known. The structure was first determined by *X*-ray diffraction in 1960 [104] although the positions of the bridging hydrogens (or any other atoms) were not published but assigned to peaks in an illustration of a superimposed electron density map. Another structure of an un-coordinated $[B_3H_8]^-$ ion was determined more recently [105]. The structure is another example where the number of connectivities (13) exceeds the number of pairs of valence electrons (9). The topology can be explained in terms of two-centre two-electron (2c-2e) bonds and two-electron three-centre bonds (2c-3e) as shown in Figure 4.1(I).

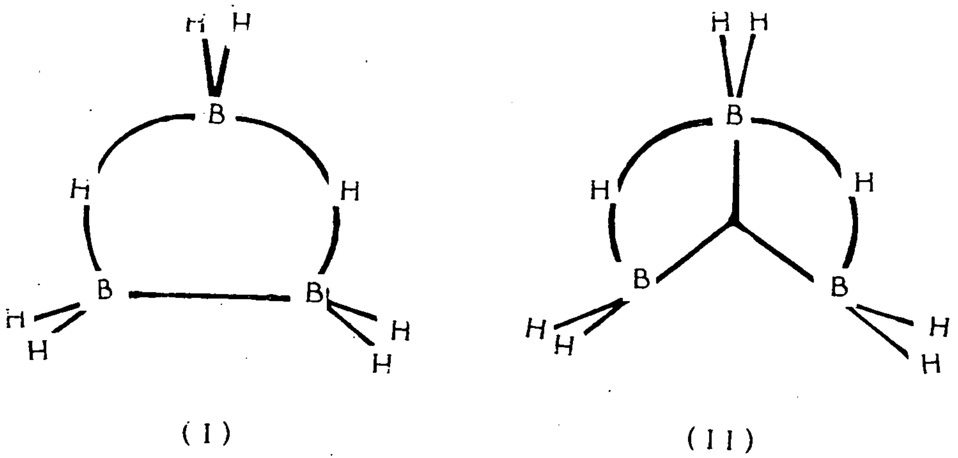

(I) (I I)

FIGURE 4.1

Topological Forms for $[B_3H_8]^-$.

Other bonds descriptions can be written eg (II) but only (I) is topologically allowed with each B participating in exactly 4 bonds and each H only 1. There are as many bonds as pairs of valence electrons.

The special interest in $[B_3H_8]^-$ is the possibility that the topologically forbidden form (II) may make a substantial contribution. This has been suggested by Lipscomb [106] in order to explain the asymmetric hydrogen bridges and the shorter lengths of the bridged B-B connectivities. The previously forbidden 5-coordinate boron has been rationalised by invoking fractionality [107]. Form (II) explains the B-B shortening because the the bridged borons are bound twice by a 3c-2e BHB bond and a 3c-2e BBB bond. If the latter really does make an important contribution then this should be observable in a charge deformation density refinement.

Calculation of the deformation density alone is not a solution to the question of the contribution of (II) to the electronic structure because *ab-initio* calculations, at least at the 4-31G or 6-31G level can not reproduce a geometry optimised structure with bonds and angles near those that have been determined crystallographically - certainly not values as accurate as geometry optimised values for compounds with only 2c-2e bonds. This defect is also worth investigating. The deformation density in B-H bonds (bridged or terminal) remains inaccessable and while the deformation density in these bonds has been refined the results in this portion of the anion are not reliable.

$[B_3H_8]^-$ presents a challenge because of the large ratio of hydrogen to boron and the large amplitude of vibration of these hydrogens. In the solution state there is strong evidence that the molecule is fluxional. The importance of low temperatures in the *X*-ray diffraction study of substituted triboranes $[B_3H_7L]^{1-}$, L=NCS, NCSe, has been demonstrated [108].

The benzyltrimethylammonium ion (BTMA) was selected because an ion of poor polarising power was needed if the deformation density in the $[B_3H_8]^-$ ion was not to be perturbed. The choice of cation was further limited because the

$[B_3H_8]^-$ ion can act as a ligand as shown by the *X*-ray determined structures of $Be(B_3H_8)_2$ [109] and $[(CO)_4CrB_3H_8]^-$ [110]. When $[B_3H_8]^-$ acts as a ligand the geometry is perturbed. Several other salts were prepared (PNP^+, NPr_4^+,NEt_4^+) but these produced crystals of sub-standard diffraction quality or, on preliminary structure determination, showed some disorder in the alkyl groups or $[B_3H_8]^-$ ion. The BTMA ion is large but has some symmetry and could therefore be refined with a modest number of deformation functions. The deformation density in BTMA is easily measured and refined because of the rigid C-skeleton of the $C_6H_5CH_2$ group and the inherent nature of the curvature of the electron density (ie Laplacian electron density) in aromatic rings.

Finally, as is always important when investigating new bond deformation types, BTMA is useful as an internal standard to check the quality of the data. The phenyl group has been a component in other deformation density studies [111,112].

4.2. Experimental

4.2.1. Preparation of the Crystal

$[BTMA]^+][B_3H_8]^-$ was prepared by the quantitative reaction of $Tl^+[B_3H_8]^-$ and $BTMA^+Br^-$. The thallium salt was in turn prepared from commercially supplied $[NMe_4][B_3H_8]$ via a published synthetic route [113]. The $[BTMA][B_3H_8]$ was finally crystallised by slow evaporation of a CH_2Cl_2 solution. A colourless regular block was sphericalised (diameter 0.40(4)mm) and examined by oscillation photography to confirm that the crystal had remained singular and free from powder.

4.2.2. Data Collection

A preliminary *X*-ray diffraction experiment gave a model structure which was used to prepare a list of structure factors F and normalised structure factors E extending to $S = 2\sin\theta/\lambda = 2.6Å^{-1}$. From this a reduced list of indices estimated worthy for collection (ie with above average E values and reasonably large F values) was prepared. The first asymmetric unit was collected (ASU1), the results used to further refine the model and prepare a slightly revised list of indices for collection in a second asymmetric unit (ASU2). This second collection was prematurely terminated after approximately 60% of selected indices had been collected when the crystal was damaged. The details of each collection are summarised below.

ASU1

Accurate cell parameters were obtained using a CAD-4 diffractometer at 113 K using 25 centred reflections ($9° < \theta < 32°$), graphite monochromated Mo K_α (λ_{av} 0.71069Å). For data collection $\theta_{max} = 70°$, ω-2θ scan in 96 steps. Each scan done twice using 48 alternate steps and profiles compared. If the profiles were not statistically similar then the reflection scanned twice more, if still dissimilar reflection flagged for subsequent deletion. Scan width (ω) $= 0.80 + 0.35 \tan\theta$. Moderate prescan and for $I/\sigma I > 1$ this was followed by a slow scan such that the final $I/\sigma I$ ratio was better than 33 subject to a maximum time constraint of 120s. Over 197 hours 6586 acceptable data were measured. No detectable crystal decay or movement.

ASU2

- as per ASU1 except cell calculated from 25 centred reflections ($9° < \theta < 34°$). 4170 data measured over 164 hours.

Summary

$H_{24}B_3C_{10}N_1$, Mr=190.74, Monoclinic $P2_1/c$ (No 14), Z=4, ρ_x=0.979gcm^{-3}, averaged cell a=11.293(5), b=9.384(4), c=13.118(5)Å, β=111.46(2)°, V=1293.8Å^3, μMoK_α=0.49cm^{-1}, $F_{(000)}$=424, T=−162°C (111 K)

4.2.3. Data Reduction

Data which had 1) net I<0, or 2) were flagged as overloading counter or 3) were flagged as weak with a peak centre offset from the expected position or 4) had an uneven background were deleted to leave 5637 (ASU1) and 4045 (ASU2) data. These were corrected for Lorentz and polarisation factors (including monochromator polarisation). The low value of μ and the use of a near spherical crystal eliminated the need for an absorption correction. The data were merged to give 5990 unique reflections (R_{merg} 0.0510, batch scale factor 1.000) of which 5717 had F> 3σF. A further two reflections (110 and 102) repeatedly had Fo<<Fc in the subsequent standard refinements (which was attributed to extinction) and were deleted. A final list of 5715 Fobs was used in the deformation density refinement program.

4.3. Standard Parameter Refinement

The starting point for the refinement was a set of coordinates established from an earlier *X*-ray diffraction experiment which in turn had been solved by direct methods (B, C, N) and iterative least-squares and ΔF syntheses (H). These refined rapidly to convergence. The function minimised was $\Delta_1=\sum|Fo-kFc|^2$ with weights for the observations of $1/\sigma^2F$. Thermal parameters were anisotropic for B, C and N atoms but isotropic for H atoms. No constraint was imposed on the phenyl group. Refinement of 224 standard parameters (5715 observations) gave a final R factor of 0.0803 (R_w 0.0845). These results are *not* listed because they are superceded by values from the

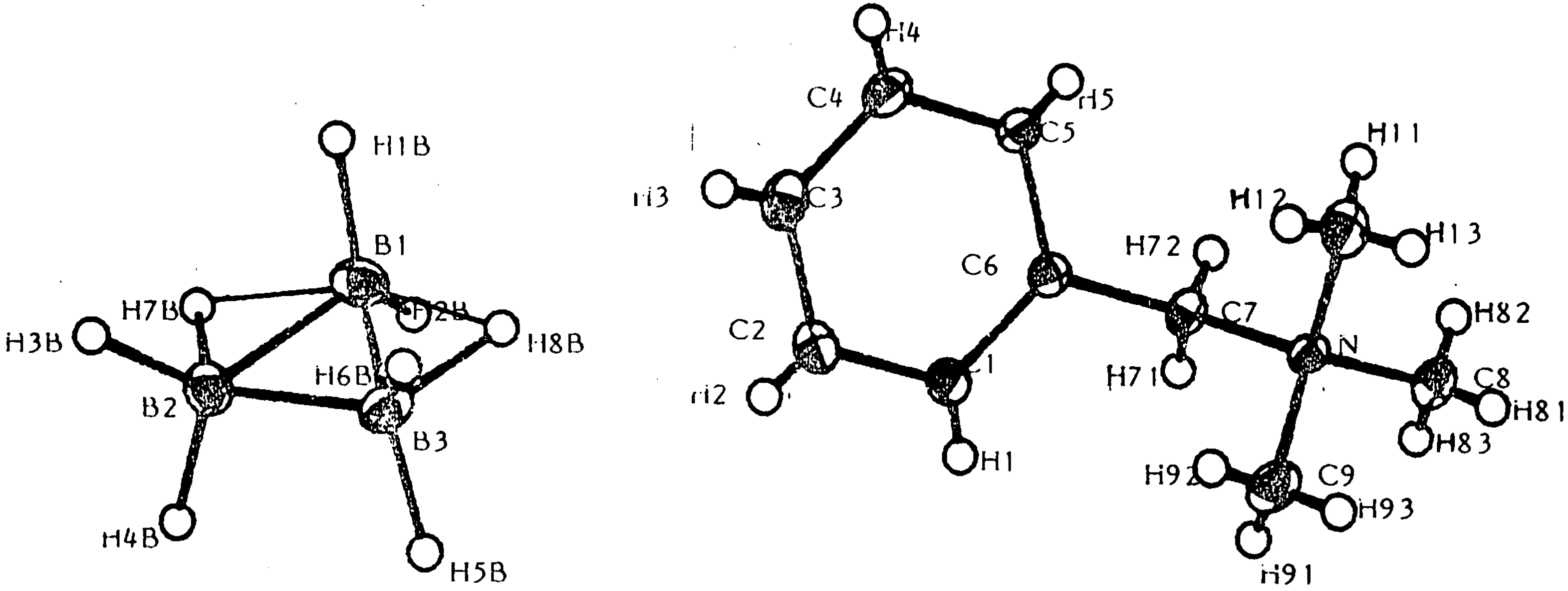

FIGURE 4.3(A)

Ortep drawing

refinement including multipole functions (see section 4.4.2 for tables).

Figure 4.3(a) shows an ORTEP drawing of the anion and cation respectively and the labelling scheme adopted. The parameters used in the preparation of Figure 4.3(a) are those from the converged multipole result.

4.4. Experimental Charge Deformation Density

4.4.1. Multipole Model and Refinement

The program LSEXP was used (see Chapter 2 section 2.5.1). There are no crystallographic symmetry constraints on any part of the anion or cation. To bring the number of refined parameters down to a size which enabled a least-squares refinement cycle to be achieved with a reasonable demand on computer resources, non crystallographic local point symmetry was imposed. This alone still gave an excessive number of independent deformation coefficients and therefore further, chemically plausible, equivalences were made. The final constraints were

- Only 9 atomic deformation types N {N}, C_{methyl} {C8, C9, C10}, $C_{aromatic}${C1-C6 inclusive}, B_{unique} {B1}, B_{basal} {B2, B3}, C_{benzyl} {C7}, H_c {all H bonded to C}, H_B {6 H terminally bonded to B}, H_μ {both bridging H-atoms in $[B_3H_8]^-$}.
- Point symmetries for the atomic deformation types : N (C_{3v}), C_{methyl} (C_{3v}), $C_{aromatic}$(C_{2v}) B_{unique}(C_{2v}), B_{basal}(C_s), C_{benzyl}(C_s), H_C($C_{\infty v}$), H_μ(C_s).
- Basis functions : spherical (n=0) to quartic (n=4) for non-H, spherical to cubic (n=3) for H atoms.
- Exponents fixed at plausible values N 5.3Å^{-1}; C_{Me}, C_{arom}, C_{benzyl} 5.28 Å^{-1}; B_{un}, B_{bas} 4.47Å^{-1}; all H 5.45Å^{-1}.
- F_{000} restrained to 424.

Refinement was in three blocks : cation parameters, anion parameters and spherical deformation coefficients (228, 110 and 9 parameters respectively).

The function minimised was $\Delta_2 = \Sigma|Fo^2-(kFc)^2|^2$. Over 20 cycles the R factor was reduced (standard parameters only) to R 0.05504 (R_w 0.05142) (with deformation multipoles). The R-factor decrease per cycle was then only 0.00007. Examination of the deformation density maps showed no significant changes over the last few cycles and refinement was therefore terminated.

4.4.2. Multipole refinement results

The standard parameters together with their esd's are listed in Table 4.4.2(a). Derived bonds and angles are listed in Table 4.4.2(b). The deformation coefficients are listed in Table 4.4.2(c)

TABLE 4.4.2(A)

Fractional Coordinates of Atoms with Standard Deviations

	x	y	z
N	0.80964(16)	0.16728(18)	0.52232(13)
C(1)	0.59327(20)	0.20216(23)	0.64303(18)
C(2)	0.51036(23)	0.13593(24)	0.68544(19)
C(3)	0.55331(23)	0.02188(24)	0.75814(19)
C(4)	0.67783(22)	-0.0258(3)	0.78787(18)
C(5)	0.76061(24)	0.04063(22)	0.74564(17)
C(6)	0.71906(18)	0.15484(20)	0.67309(14)
C(7)	0.80882(21)	0.22754(23)	0.62956(16)
C(8)	0.90549(25)	0.2503(3)	0.49182(21)
C(9)	0.68259(24)	0.1824(4)	0.43376(19)
C(10)	0.8475(3)	0.01386(24)	0.53572(23)
B(1)	0.29715(24)	0.1321(3)	0.89834(21)
B(2)	0.13007(23)	0.1421(3)	0.86472(20)
B(3)	0.1946(3)	0.0942(3)	0.76123(19)

Fractional Coordinates of Hydrogen Atoms

	x	y	z
H(1)	0.567(4)	0.260(4)	0.605(3)
H(2)	0.452(4)	0.160(4)	0.674(3)
H(3)	0.511(5)	-0.005(5)	0.776(3)
H(4)	0.696(4)	-0.084(5)	0.820(3)
H(5)	0.819(4)	0.020(4)	0.760(3)
H(71)	0.796(3)	0.305(4)	0.621(3)
H(72)	0.877(3)	0.229(4)	0.671(3)
H(81)	0.904(4)	0.226(5)	0.440(4)
H(82)	0.970(4)	0.238(4)	0.534(3)
H(83)	0.888(3)	0.323(5)	0.486(3)
H(91)	0.667(4)	0.257(5)	0.433(3)
H(92)	0.637(3)	0.138(4)	0.449(3)
H(93)	0.690(4)	0.166(5)	0.384(4)
H(11)	0.913(4)	0.011(5)	0.584(4)
H(12)	0.801(4)	-0.017(4)	0.544(3)
H(13)	0.853(3)	-0.012(4)	0.485(3)
H(1B)	0.345(5)	0.018(5)	0.965(4)
H(2B)	0.360(5)	0.253(6)	0.919(4)
H(3B)	0.054(6)	0.027(6)	0.885(5)
H(4B)	0.067(4)	0.279(5)	0.837(4)
H(5B)	0.152(4)	0.200(5)	0.684(4)
H(6B)	0.172(6)	-0.044(6)	0.714(5)
H(7B)	0.212(8)	0.195(9)	0.970(7)
H(8B)	0.319(6)	0.084(8)	0.783(6)

Thermal Parameters xÅ^{-2}

	u11	u22	u33	u12	u23	u13
N	.0191(7)	.0142(7)	.0118(6)	.0005(6)	.0003(5)	.0062(5)
C(1)	.0198(10)	.0167(9)	.0197(9)	.0013(7)	-.0003(7)	.0084(8)
C(2)	.0194(10)	.0203(9)	.0271(10)	-.0003(8)	-.0017(8)	.0115(8)
C(3)	.0265(11)	.0191(9)	.0244(10)	-.0051(8)	-.0021(8)	.0135(9)
C(4)	.0290(11)	.0180(9)	.0196(9)	.0005(8)	.0029(8)	.0116(8)
C(5)	.0207(10)	.0193(9)	.0153(8)	.0022(8)	.0023(7)	.0070(7)
C(6)	.0186(9)	.0144(8)	.0134(7)	.0002(7)	-.0018(6)	.0060(7)
H(1)	.041(10)					
H(2)	.046(10)					
H(3)	.051(11)					
H(4)	.047(11)					
H(5)	.035(10)					
C(7)	.0190(9)	.0151(8)	.0135(8)	-.0031(7)	-.0026(6)	.0069(7)
H(71)	.030(8)					
H(72)	.035(9)					
C(8)	.0246(11)	.0236(11)	.0217(10)	-.0025(9)	.0034(9)	.0124(9)
H(81)	.054(12)					
H(82)	.048(11)					
H(83)	.039(10)					
C(9)	.0229(11)	.0367(15)	.0130(8)	-.0038(10)	.0013(9)	.0025(7)
H(91)	.048(12)					
H(92)	.036(9)					
H(93)	.058(11)					
C(10)	.0377(14)	.0138(9)	.0291(11)	.0031(9)	-.0006(8)	.0210(11)
H(11)	.052(12)					
H(12)	.045(11)					
H(13)	.041(9)					
B(1)	.0202(10)	.0250(12)	.0234(10)	-.0004(9)	.0015(9)	.0025(9)
B(2)	.0230(11)	.0212(11)	.0249(10)	.0019(9)	-.0015(9)	.0107(9)
B(3)	.0308(13)	.0218(11)	.0167(9)	.0026(9)	.0017(8)	.0093(9)
H(1)	.078(14)					
H(2)	.086(15)					
H(3)	.097(17)					
H(4)	.077(14)					
H(5)	.067(13)					
H(6)	.108(20)					
H(7)	.149(29)					
H(8)	.119(22)					

TABLE 4.4.2(B)

Cation Bond Lengths(Å) with standard deviations

N - C(7)	1.519(3)	C(5) - H(5)	0.65(4)
N - C(8)	1.502(3)	C(6) - C(7)	1.498(3)
N - C(9)	1.486(3)	C(7) -H(71)	0.74(3)
N -C(10)	1.494(4)	C(7) -H(72)	0.76(4)
C(1) - C(2)	1.398(3)	C(8) -H(81)	0.71(5)
C(1) - C(6)	1.400(3)	C(8) -H(82)	0.75(4)
C(1) - H(1)	0.72(4)	C(8) -H(83)	0.70(4)
C(2) - C(3)	1.397(4)	C(9) -H(91)	0.72(4)
C(2) - H(2)	0.66(4)	C(9) -H(92)	0.74(4)
C(3) - C(4)	1.389(3)	C(9) -H(93)	0.71(5)
C(3) - H(3)	0.65(4)	C(10) -H(11)	0.78(4)
C(4) - C(5)	1.396(3)	C(10) -H(12)	0.64(4)
C(4) - H(4)	0.67(4)	C(10) -H(13)	0.73(4)
C(5) - C(6)	1.396(3)		

Cation Bond Angles(°) with standard deviations

C(7) - N - C(8)	107.61(17)	N - C(7) - C(6)	114.69(17)
C(7) - N - C(9)	110.92(17)	N - C(7) -H(71)	106.7(26)
C(7) - N -C(10)	110.38(18)	N - C(7) -H(72)	109.0(27)
C(8) - N - C(9)	109.01(18)	C(6) - C(7) -H(71)	112.5(26)
C(8) - N -C(10)	109.15(19)	C(6) - C(7) -H(72)	112.3(27)
C(9) - N -C(10)	109.71(19)	H(71) - C(7) -H(72)	100.6(37)
C(2) - C(1) - C(6)	120.34(20)	N - C(8) -H(81)	108.7(37)
C(2) - C(1) - H(1)	116.5(30)	N - C(8) -H(82)	108.9(32)
C(6) - C(1) - H(1)	123.2(30)	N - C(8) -H(83)	108.7(32)
C(1) - C(2) - C(3)	119.77(22)	H(81) - C(8) -H(82)	109.5(49)
C(1) - C(2) - H(2)	121.3(34)	H(81) - C(8) -H(83)	108.0(49)
C(3) - C(2) - H(2)	118.8(34)	H(82) - C(8) -H(83)	112.9(45)
C(2) - C(3) - C(4)	120.11(22)	N - C(9) -H(91)	105.4(34)
C(2) - C(3) - H(3)	114.8(38)	N - C(9) -H(92)	107.1(27)
C(4) - C(3) - H(3)	125.1(38)	N - C(9) -H(93)	107.5(37)
C(3) - C(4) - C(5)	120.06(22)	H(91) - C(9) -H(92)	111.7(44)
C(3) - C(4) - H(4)	118.3(35)	H(91) - C(9) -H(93)	108.1(51)
C(5) - C(4) - H(4)	121.5(35)	H(92) - C(9) -H(93)	116.4(46)
C(4) - C(5) - C(6)	120.45(21)	N -C(10) -H(11)	106.0(32)
C(4) - C(5) - H(5)	121.0(33)	N -C(10) -H(12)	103.9(36)
C(6) - C(5) - H(5)	118.6(33)	N -C(10) -H(13)	109.0(30)
C(1) - C(6) - C(5)	119.27(19)	H(11) -C(10) -H(12)	115.4(48)
C(1) - C(6) - C(7)	120.44(18)	H(11) -C(10) -H(13)	111.3(44)
C(5) - C(6) - C(7)	120.28(18)	H(12) -C(10) -H(13)	110.6(46)

Cation Torsion angles(°) with standard deviations

C(8)- N - C(7) - C(6)	-179.12(18)	C(9)- N -C(10) -H(11)	-177.5(34)

C(8)- N - C(7) -H(71)	55.6(27)	C(9)- N -C(10) -H(12)	-55.5(37)
C(8)- N - C(7) -H(72)	-52.2(28)	C(9)- N -C(10) -H(13)	62.5(32)
C(9)- N - C(7) - C(6)	61.73(23)	C(6)- C(1) - C(2) - C(3)	0.0(3)
C(9)- N - C(7) -H(71)	-63.5(27)	C(6)- C(1) - C(2) - H(2)	175.7(39)
C(9)- N - C(7) -H(72)	-171.4(28)	H(1)- C(1) - C(2) - C(3)	179.2(34)
C(10)- N - C(7) - C(6)	-60.10(24)	H(1)- C(1) - C(2) - H(2)	-5.0(52)
C(10)- N - C(7) -H(71)	174.6(27)	C(2)- C(1) - C(6) - C(5)	0.2(3)
C(10)- N - C(7) -H(72)	66.8(28)	C(2)- C(1) - C(6) - C(7)	-178.74(20)
C(7)- N - C(8) -H(81)	-176.8(39)	H(1)- C(1) - C(6) - C(5)	-179.1(36)
C(7)- N - C(8) -H(82)	64.4(33)	H(1)- C(1) - C(6) - C(7)	2.0(36)
C(7)- N - C(8) -H(83)	-59.4(34)	C(1)- C(2) - C(3) - C(4)	-0.2(4)
C(9)- N - C(8) -H(81)	-56.4(39)	C(1)- C(2) - C(3) - H(3)	179.8(42)
C(9)- N - C(8) -H(82)	-175.6(33)	H(2)- C(2) - C(3) - C(4)	-176.1(38)
C(9)- N - C(8) -H(83)	61.0(34)	H(2)- C(2) - C(3) - H(3)	3.9(57)
C(10)- N - C(8) -H(81)	63.4(39)	C(2)- C(3) - C(4) - C(5)	0.4(4)
C(10)- N - C(8) -H(82)	-55.8(33)	C(2)- C(3) - C(4) - H(4)	-175.8(40)
C(10)- N - C(8) -H(83)	-179.2(34)	H(3)- C(3) - C(4) - C(5)	-179.6(47)
C(7)- N - C(9) -H(91)	54.5(35)	H(3)- C(3) - C(4) - H(4)	4.2(62)
C(7)- N - C(9) -H(92)	-64.6(29)	C(3)- C(4) - C(5) - C(6)	-0.2(3)
C(7)- N - C(9) -H(93)	169.6(39)	C(3)- C(4) - C(5) - H(5)	178.5(38)
C(8)- N - C(9) -H(91)	-63.8(35)	H(4)- C(4) - C(5) - C(6)	175.8(41)
C(8)- N - C(9) -H(92)	177.1(29)	H(4)- C(4) - C(5) - H(5)	-5.4(56)
C(8)- N - C(9) -H(93)	51.3(39)	C(4)- C(5) - C(6) - C(1)	0.0(3)
C(10)- N - C(9) -H(91)	176.7(35)	C(4)- C(5) - C(6) - C(7)	178.88(20)
C(10)- N - C(9) -H(92)	57.6(29)	H(5)- C(5) - C(6) - C(1)	-178.8(37)
C(10)- N - C(9) -H(93)	-68.2(39)	H(5)- C(5) - C(6) - C(7)	0.1(37)
C(7)- N -C(10) -H(11)	-55.-(34)	C(1)- C(6) - C(7) - N	-89.62(23)
C(7)- N -C(10) -H(12)	67.0(37)	C(1)- C(6) - C(7) -H(71)	32.6(28)
C(7)- N -C(10) -H(13)	-175.0(32)	C(1)- C(6) - C(7) -H(72)	145.2(29)
C(8)- N -C(10) -H(11)	63.1(34)	C(5)- C(6) - C(7) - N	91.51(23)
C(8)- N -C(10) -H(12)	-174.9(37)	C(5)- C(6) - C(7) -H(71)	-146.3(28)
C(8)- N -C(10) -H(13)	-56.9(32)	C(5)- C(6) - C(7) -H(72)	-33.7(29)

Anion Bond Lengths(Å) with standard deviations

B(1) - B(2)	1.776(4)	B(2) -H(3B)	1.47(6)
B(1) - B(3)	1.783(4)	B(2) -H(4B)	1.45(5)
B(1) -H(1B)	1.36(5)	B(2) -H(7B)	1.44(9)
B(1) -H(2B)	1.31(5)	B(3) -H(5B)	1.37(5)
B(1) -H(7B)	1.68(9)	B(3) -H(6B)	1.42(6)
B(1) -H(8B)	1.68(7)	B(3) -H(8B)	1.33(7)
B(2) - B(3)	1.817(4)		

Anion Bond Angles(°) with standard deviations

B(2) - B(1) - B(3)	61.38(15)	B(3) - B(2) -H(7B)	120.5(34)
B(2) - B(1) -H(1B)	109.5(21)	H(3B) - B(2) -H(4B)	115.7(31)
B(2) - B(1) -H(2B)	116.9(24)	H(3B) - B(2) -H(7B)	106.8(42)
B(2) - B(1) -H(7B)	49.3(29)	H(4B) - B(2) -H(7B)	91.4(39)
B(2) - B(1) -H(8B)	106.5(25)	B(1) - B(3) - B(2)	59.12(15)

B(3) - B(1) -H(1B)	116.7(21)	B(1) - B(3) -H(5B)	121.6(19)
B(3) - B(1) -H(2B)	119.0(24)	B(1) - B(3) -H(6B)	124.7(26)
B(3) - B(1) -H(7B)	110.1(29)	B(1) - B(3) -H(8B)	63.2(31)
B(3) - B(1) -H(8B)	45.1(25)	B(2) - B(3) -H(5B)	104.3(19)
H(1B) - B(1) -H(2B)	119.1(32)	B(2) - B(3) -H(6B)	119.5(26)
B(1) - B(2) - B(3)	59.49(15)	B(2) - B(3) -H(8B)	122.4(31)
B(1) - B(2) -H(3B)	123.8(24)	H(5B) - B(3) -H(6B)	112.2(33)
B(1) - B(2) -H(4B)	119.2(20)	H(5B) - B(3) -H(8B)	105.5(37)
B(1) - B(2) -H(7B)	61.7(34)	H(6B) - B(3) -H(8B)	92.4(41)
B(3) - B(2) -H(3B)	112.3(24)	B(1) -H(7B) - B(2)	69.0(36)
B(3) - B(2) -H(4B)	108.9(20)	B(1) -H(8B) - B(3)	71.7(33)

Anion Torsion angles(°) with standard deviations

H(1B)- B(1) - B(2) - B(3)	-110.5(23)	H(2B)- B(1) - B(3) -H(6B)	146.9(42)
H(2B)- B(1) - B(2) - B(3)	110.1(27)	H(2B)- B(1) - B(3) -H(8B)	73.9(44)
H(8B)- B(1) - B(2) - B(3)	-0.5(26)	B(3)- B(1) -H(7B) - B(2)	9.1(36)
B(3)- B(1) - B(2) -H(3B)	97.8(29)	B(2)- B(1) -H(8B) - B(3)	0.6(32)
B(3)- B(1) - B(2) -H(4B)	-95.8(23)	H(3B)- B(2) - B(3) - B(1)	-117.2(26)
B(3)- B(1) - B(2) -H(7B)	-170.3(39)	H(4B)- B(2) - B(3) - B(1)	113.4(21)
H(1B)- B(1) - B(2) -H(3B)	-12.7(37)	H(7B)- B(2) - B(3) - B(1)	10.0(40)
H(1B)- B(1) - B(2) -H(4B)	153.7(32)	B(1)- B(2) - B(3) -H(5B)	-118.5(20)
H(1B)- B(1) - B(2) -H(7B)	79.3(45)	B(1)- B(2) - B(3) -H(6B)	115.1(30)
H(2B)- B(1) - B(2) -H(3B)	-152.2(39)	B(1)- B(2) - B(3) -H(8B)	0.6(37)
H(2B)- B(1) - B(2) -H(4B)	14.2(35)	H(3B)- B(2) - B(3) -H(5B)	124.3(33)
H(2B)- B(1) - B(2) -H(7B)	-60.2(47)	H(3B)- B(2) - B(3) -H(6B)	-2.0(40)
H(1B)- B(1) - B(3) - B(2)	98.7(24)	H(3B)- B(2) - B(3) -H(8B)	-116.5(45)
H(2B)- B(1) - B(3) - B(2)	-106.7(27)	H(4B)- B(2) - B(3) -H(5B)	-5.1(29)
H(7B)- B(1) - B(3) - B(2)	-7.9(31)	H(4B)- B(2) - B(3) -H(6B)	-131.5(37)
B(2)- B(1) - B(3) -H(5B)	88.3(23)	H(4B)- B(2) - B(3) -H(8B)	114.0(43)
B(2)- B(1) - B(3) -H(6B)	-106.5(32)	H(7B)- B(2) - B(3) -H(5B)	-108.5(44)
B(2)- B(1) - B(3) -H(8B)	-179.4(35)	H(7B)- B(2) - B(3) -H(6B)	125.1(50)
H(1B)- B(1) - B(3) -H(5B)	-173.0(33)	H(7B)- B(2) - B(3) -H(8B)	10.6(54)
H(1B)- B(1) - B(3) -H(6B)	-7.7(40)	B(3)- B(2) -H(7B) - B(1)	-9.7(38)
H(1B)- B(1) - B(3) -H(8B)	-80.7(42)	B(2)- B(3) -H(8B) - B(1)	-0.6(36)
H(2B)- B(1) - B(3) -H(5B)	-18.4(35)		

TABLE 4.4.2(C)

Deformation Coefficients and esd's

N EXPON	5.108(29)	N SPHER	-0.126(13)	N LINR1	0.34(25)
N EXPON	5.30(-)	N SPHER	0.0200(-)	N LINR1	0.19(3)
N QUDR1	0.20(5)	N QUDR2	0.05(5)	N CUBI1	-2.30(31)
N CUBI2	0.09(3)	N CUBI7	2.91(43)	N CUBI8	-1.19(16)
N QUR 1	0.02(9)	N QUR 4	-0.58(8)	N QUR 7	0.04(9)
N QUR10	0.09(12)	N QUR12	0.28(11)	CMEXPOC	5.28(-)
CMSPHER	0.007(-)	CMLINR1	0.010(21)	CMQUDR1	0.09(3)
CMQUDR2	-0.06(3)	CMCUBI1	-0.56(9)	CMCUBI2	-0.094(20)
CMCUBI7	0.93(15)	CMCUBI8	-0.12(5)	CMQUR 1	-0.45(4)
CMQUR 4	-0.10(5)	CMQUR 7	-0.20(5)	CMQUR10	0.12(7)
CMQUR12	-0.11(7)	CAEXPOC	5.28(-)	CASPHER	0.0184(-)
CALINR1	0.063(24)	CAQUDR1	0.23(3)	CAQUDR3	-0.13(3)
CAQUDR5	-0.18(3)	CACUBI1	-0.12(5)	CACUBI3	-0.91(5)
CACUBI7	0.78(5)	CAQUR 1	-0.15(3)	CAQUR 2	0.26(7)
CAQUR 3	0.092(29)	CAQUR 4	-0.048(13)	CAQUR 5	-0.131(14)
CAQUR 6	0.048(27)	BuEXPOC	4.470(-)	BuSPHER	0.1624(-)
BuLINR1	-0.25(7)	BuQUDR1	-0.40(9)	BuQUDR3	-0.27(11)
BuQUDR5	0.27(9)	BuCUBI1	1.06(29)	BuCUBI3	1.17(27)
BuCUBI7	-0.94(24)	BuQUR 1	-0.31(21)	BuQUR 2	-2.89(32)
BuQUR 3	-1.34(13)	BuQUR 4	-0.26(7)	BuQUR 5	0.00(6)
BuQUR 6	0.41(10)	BbEXPOC	4.47(-)	BbSPHER	0.1619(-)
BbLINR1	0.04(5)	BbLINR2	0.01(4)	BbQUDR1	-0.68(8)
BbQUDR2	-1.00(8)	BbQUDR3	-0.05(7)	BbQUDR5	-0.09(6)
BbCUBI1	0.69(26)	BbCUBI2	-0.85(27)	BbCUBI3	-0.56(21)
BbCUBI5	-0.17(17)	BbCUBI7	0.00(25)	BbCUBI8	-0.31(21)
BbQUR 1	-0.25(15)	BbQUR 2	0.60(14)	BbQUR 3	-0.32(9)
BbQUR 4	0.03(14)	BbQUR 5	-1.06(15)	BbQUR 6	0.45(7)
BbQUR 7	-0.17(15)	BbQUR 8	0.30(14)	BbQUR12	-0.95(9)
CbEXPOC	5.28(-)	CbSPHER	0.0277(-)	CbLINR1	-0.40(4)
CbLINR2	-0.97(5)	CbQUDR1	0.46(7)	CbQUDR2	0.26(8)
CbQUDR3	0.21(6)	CbQUDR5	-0.11(6)	CbCUBI1	3.52(22)
CbCUBI2	-1.41(25)	CbCUBI3	1.75(11)	CbCUBI5	1.83(18)
CbCUBI7	-2.95(21)	CbCUBI8	0.23(16)	CbQUR 1	0.07(10)
CbQUR 2	0.87(13)	CbQUR 3	0.55(9)	CbQUR 4	-0.22(12)
CbQUR 5	0.13(13)	CbQUR 6	0.15(5)	CbQUR 7	-0.31(11)
CbQUR 8	0.00(13)	CbQUR12	0.75(8)	HmEXPOC	5.45(-)
HmSPHER	0.0051(-)	HmLINR1	-0.634(19)	HmQUDR1	0.117(9)
HmQUDR5	-0.055(23)	HmCUBI1	0.120(29)	HmCUBI7	-0.06(3)
HbEXPOC	5.45(-)	HbSPHER	0.1144(-)	HbLINR1	1.13(4)
HbQUDR1	0.461(29)	HbQUDR5	-0.26(4)	HbCUBI1	-0.29(11)
HbCUBI7	0.24(11)	MuEXPOC	5.45(-)	MuSPHER	0.1067(-)
MuLINR1	1.09(13)	MuLINR2	1.61(14)	MuQUDR1	2.79(17)
MuQUDR2	0.54(14)	MuQUDR3	0.44(13)	MuQUDR5	-0.55(13)
MuCUBI1	0.92(32)	MuCUBI2	3.40(41)	MuCUBI3	0.52(27)
MuCUBI5	-1.52(26)	MuCUBI7	0.91(34)	MuCUBI8	-2.38(39)

Orienatations of the polar axes follow the sequence :
linear terms 100 010 001

quadratic terms	110	1-10	101	10-1	011	01-1
cubic terms	110	1-10	101	10-1	011	01-1
	111	1-1-1	-11-1	-1-11		
quartic terms	100	010	001	A11	1A1	11A
	-A11	1-A1	11-A	A-11	1A-1	-11A
	A1-1	-1A1	1-1A			

The parameter 'A' is the constant $\sqrt{2} - 1$.

The bond distances involving hydrogen atoms bonded to C are all too short (for example the mean C-H on the phenyl ring is 0.672Å). In contrast the B-H bonds are too long with B-H (terminal) 1.399Å. Such short distances are not realistic and the deformation density in C-H (and B-H) bonds should not be given even a qualitative interpretation. The bond distances in $[B_3H_8]^-$ confirm that the bridged B-B connectivities are *shorter* than the unbridged one. This anomalous behaviour is the subject of Chapter 5. The bond distances in BTMA are unexceptional. The conformation of the BTMA ion, defined by the torsion C_{methyl}-N-C7-C6, is the prevalent one in a compilation of BTMA geometries prepared from a search of the Cambridge Crystallographic Database.

4.4.3. Static Deformation Density Maps

The maps were prepared by direct summation using the multipolar functions rather than Fourier methods. Contributions from symmetry generated molecules are therefore absent.

4.4.3.1. The Benzyltrimethylammonium Cation

Figs 4.4.3.1(a) shows the static deformation density in the plane of the phenyl ring. Fig 4.4.3.1(b) similarly shows a plane perpendicular to the ring containing the N-C7-C6 bonds. The respective esd's for the deformation density are plotted in Figs 4.4.3.1(c) and (d). The deformation peak heights are particularly large, consequently the contours are in intervals of $0.1 e\text{Å}^{-3}$. In the aromatic ring there are six peaks ($0.7 e\text{Å}^{-3}$), each centred on the midpoint of a

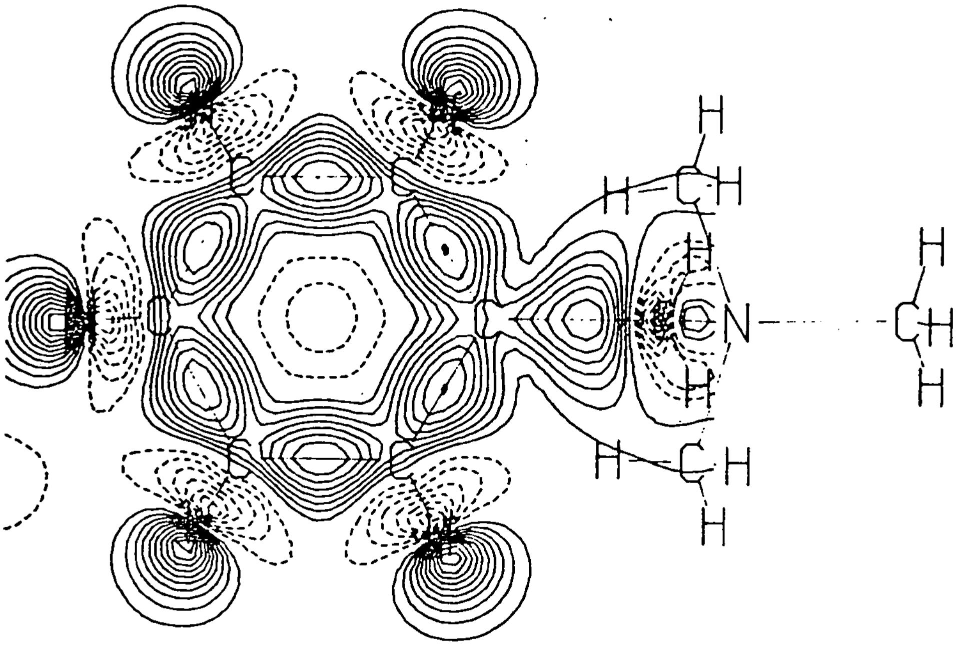

FIGURE 4.4.3.1(A)

Static Deformation Density
in the plane of the phenyl ring.

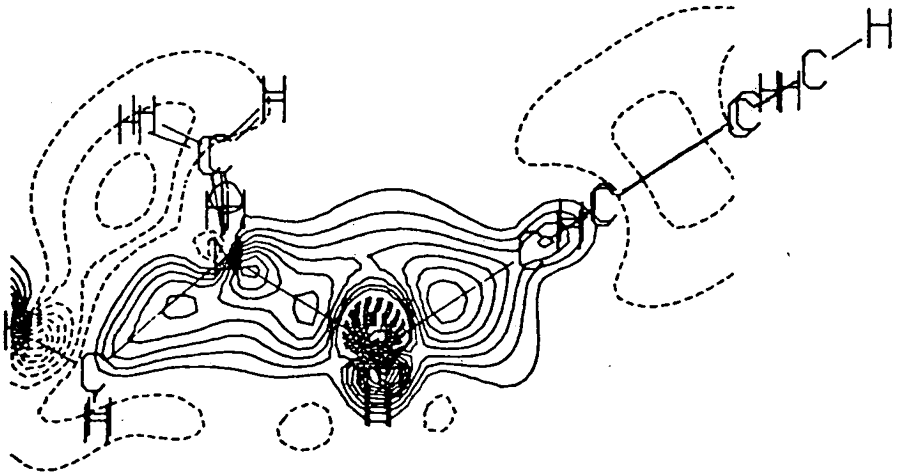

FIGURE 4.4.3.1(B)

Static Deformation Density
in the N-C7-C6 plane.

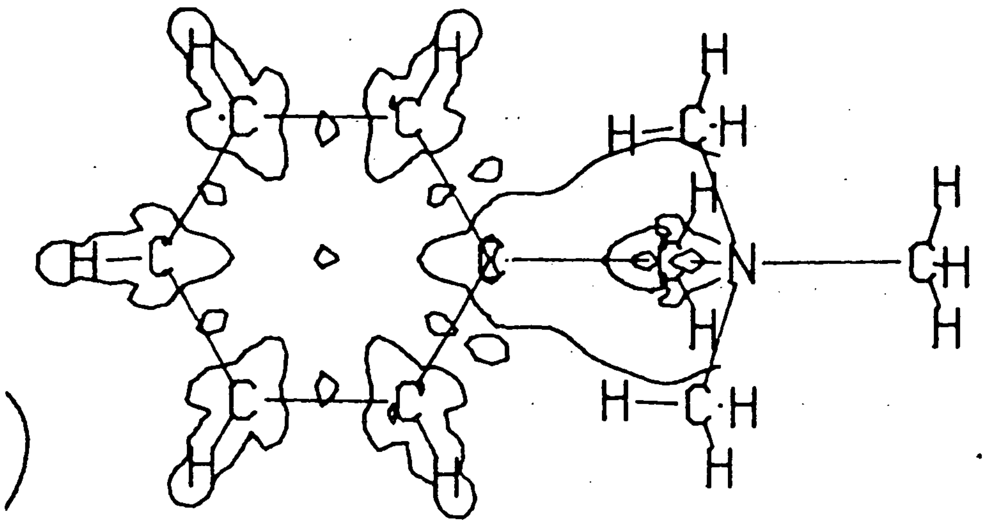

FIGURE 4.4.3.1(C)

ESD of Static Deformation Density
in the plane of the phenyl ring.

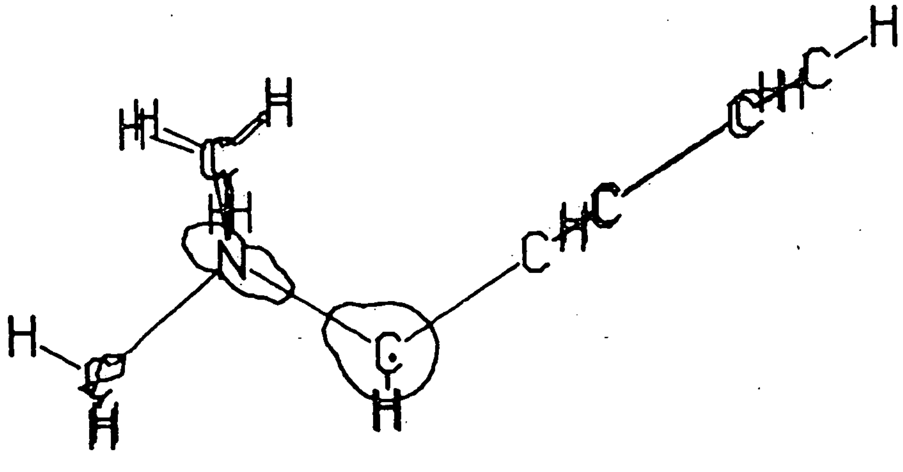

FIGURE 4.4.3.1(D)

ESD of Static Deformation Density
in the N-C7-C6 plane.

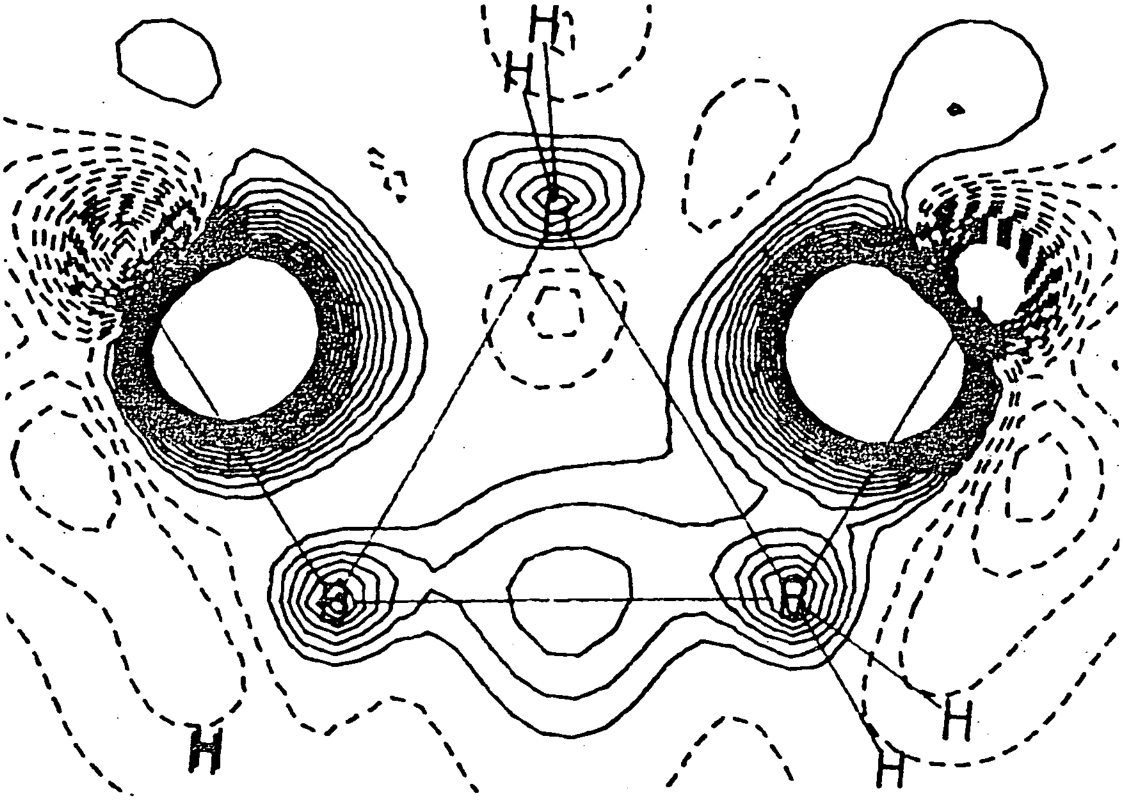

FIGURE 4.4.3.2(A)

Static Deformation Density
in the B1-B2-B3 plane.

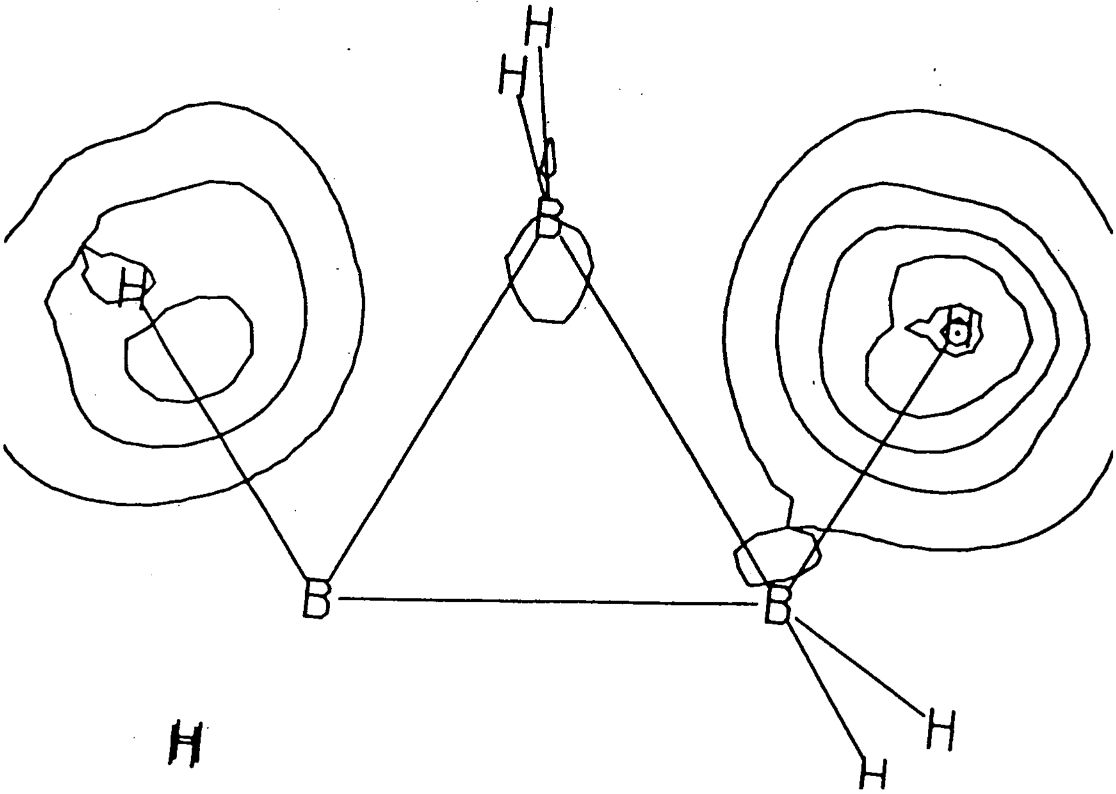

FIGURE 4.4.3.2(B)

ESD of Static Deformation Density
in the B1-B2-B3 plane.

C-C bond. The peak height on C6-C7 is similar (0.70eÅ^{-3}) but N-C8 is smaller (0.5eÅ^{-3}). On either side of the ring centre is a diffuse electron deficient zone (-0.20eÅ^{-3}).

4.4.3.2. The $[B_3H_8]^-$ Anion

Figure 4.4.3.2(a) shows the static deformation density in the plane of the three borons. Contours are in intervals of 0.1eÅ^{-3}. The zero contour is again omitted. The esd for this plane is shown in Fig 4.4.3.2(b)

The deformation in the plane is dominated by functions based on the bridging hydrogen atoms. This feature is unreliable as shown by the esd and almost vanishes after thermal smearing. Of much greater importance is the strong peak on the midpoint of the B2-B3 vector. Curiously the peak profile is almost circular. Between the apical boron and the triangle centre is a small region of electron deficiency (-0.20eÅ^{-3}).

4.4.4. Dynamic Deformation Density Maps

These maps were prepared by Fourier transform and calculated structure factors for which S_{max} was limited to 1.7Å^{-1} (7145 reflections). Figure 4.4.4(a) and (b) for the cation are analagous to figs 4.4.3.1(a) and (b). Figure 4.4.4(c) for the anion is analagous to Figure 4.4.3.2(a).

4.4.5. Residual Density Maps

The residual density associated with the dynamic deformation densities in the previous section are shown in Figures 4.4.5(a) to (c). They were calculated using observed and calculated structure factors with S <1.7Å^{-1} (3767 reflections).

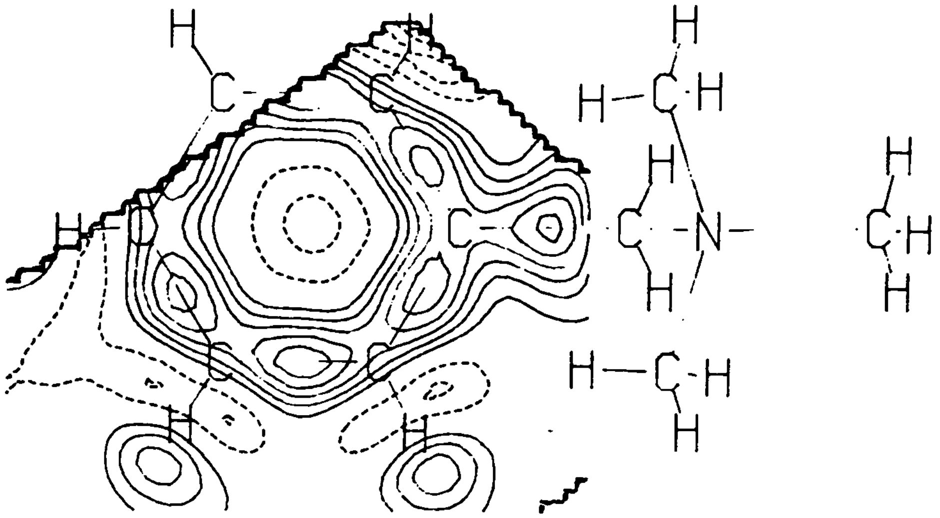

FIGURE 4.4.4(A)

Dynamic Deformation Density
in the plane of the phenyl ring.

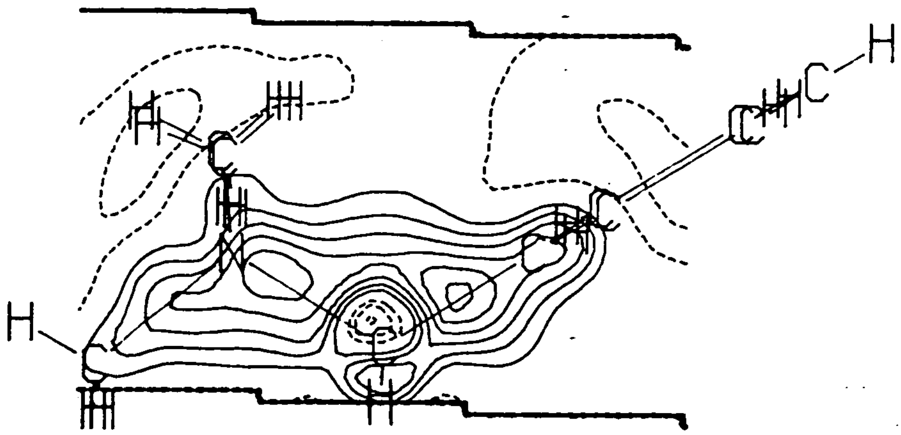

FIGURE 4.4.4(B)

Dynamic Deformation Density
in the N-C7-C6 plane.

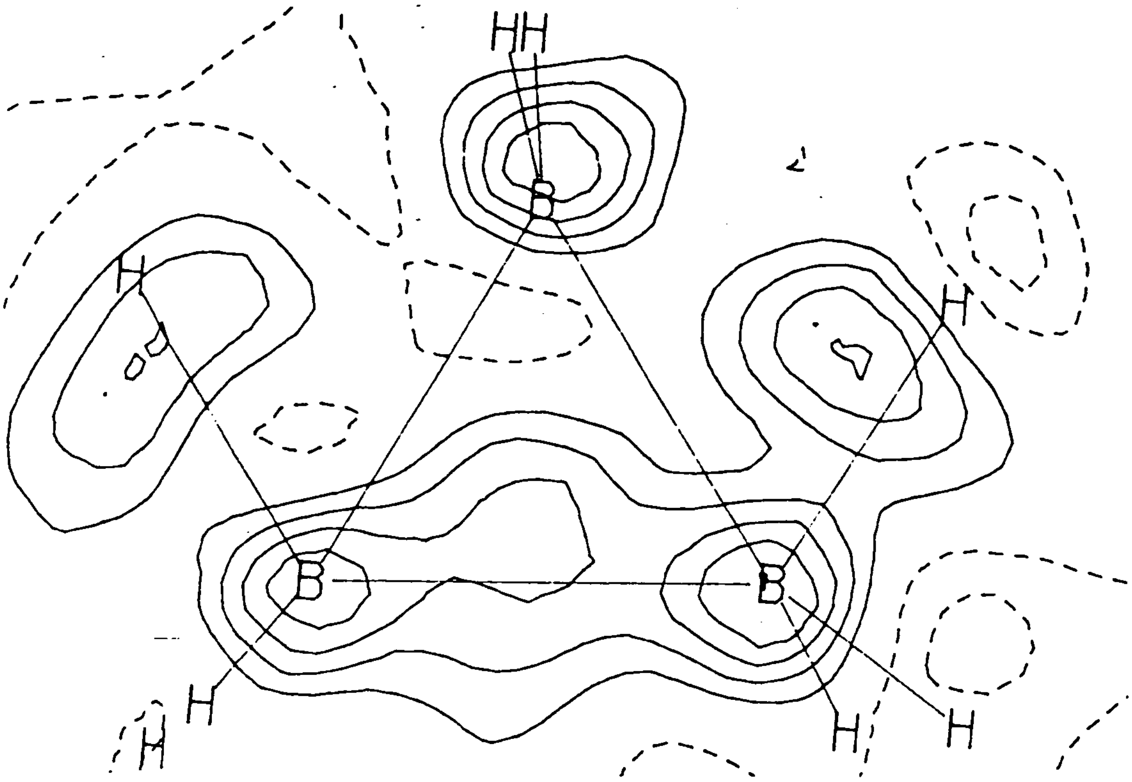

FIGURE 4.4.4(C)

Dynamic Deformation Density
in the B1-B2-B3 plane.

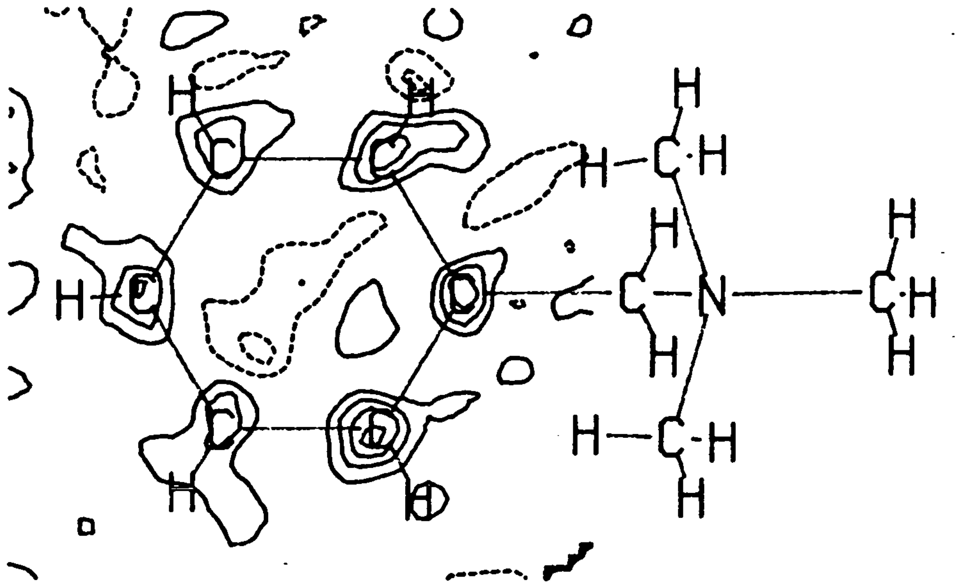

FIGURE 4.4.5(A)

Residual Density
in the plane of the phenyl ring.

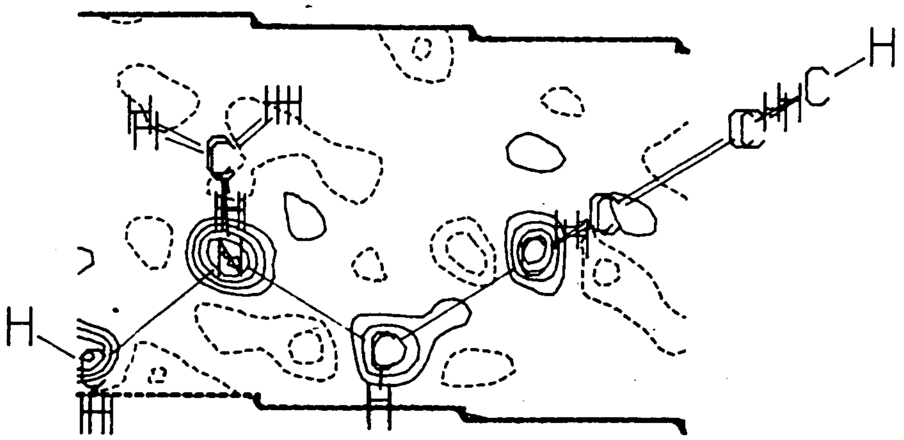

FIGURE 4.4.5(B)

Residual Density
in the N-C7-C6 plane.

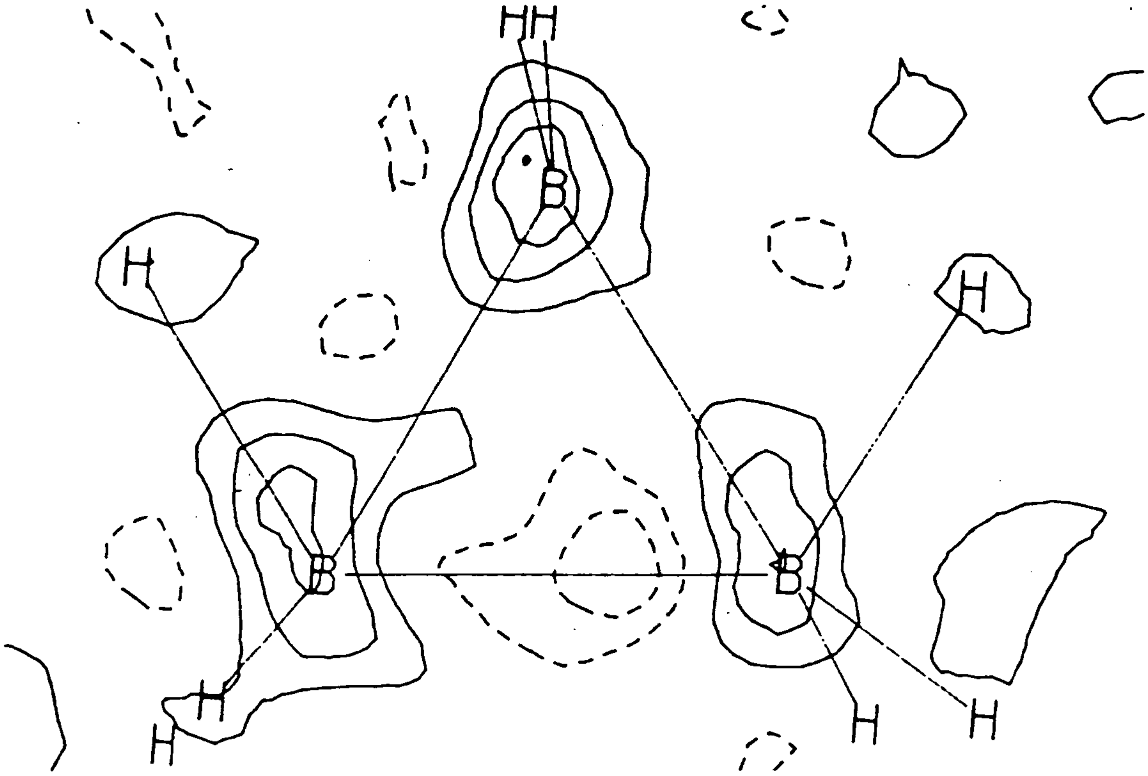

FIGURE 4.4.5(C)

Residual Density
in the B1-B2-B3 plane.

4.4.6. Charges and moments

Charges obtained by interpretation of the refined deformation coefficients are given in column 1 of table 4.4.6 . Charges obtained by application of the stockholder partitioning formula and numerical integration over a cube of edge 6Å centred on each atom and with divisions of 0.1Å are given in column 2. The stockholder recipe charges are averaged over atoms constrained with the same deformation functions.

TABLE 4.4.6

	1	2
N	-0.196	-0.207
C_{ar}	0.483	0.001(26)
C_{Me}	2.089	0.197(15)
C_{bz}	-3.382	-0.316
H_C	-0.367	-0.005(11)
B_{un}	4.735	-0.317
B_{bas}	4.600	-0.65(17)
H_{μ}	-3.136	0.061(9)
H_B	-1.231	-0.003(25)

The charges in column 1 have no utility other than to indicate which atoms in the refinement have even multipole functions with large coefficients. There would seem to be a tendency for the best fit of the deformation density to be obtained by adjacent atoms having even functions of opposite sign.

The charges in column 2 are chemically sensible - although these values produce a formula charge of $[BTMA]^{-0.38}$ $[B_3H_8]^{-1.52}$ (because of rounding error in the numerical integration) they still indicate the anion and cation. The charge distribution within the ions is plausible. Within the BTMA ion the bulk of the positive charge is localised on the three methyl groups attached to the quaternary nitrogen atom. The difference in the electronegativity between N and C is sufficient for N to acquire a small negative charge within the cation. The difference in charge between the N and C of the methyls (0.40) is similar to that between N and C1 in $[Et_3NH]^+$ (0.48) (see Chapter 3).

Within the $[B_3H_8]^-$ ion the charge distribution among the borons is such that the unique boron has fewer associated electrons. This observation is consistent with the type (I) topology (see section 4.1). The forbidden type (II) topology with the unique boron forming 5 bonds would predict the reverse.

The first moments interpreted from the multipolar coefficients are, like the charges, chemically ridiculous. First moments were calculated for the 38 independent atoms in the structure using numerical integration and the stockholder partitioning formula but these give no extra insight. Furthermore, after averaging over atoms constrained to have similar deformation functions most terms had values smaller than twice the estimated standard deviation. Consequently no meaningful interpretation can be given to the results for the 9 deformation types used. The second moments were similarly calculated for the 38 atoms in the structure. However, after averaging those atoms which were constrained to have similar deformation functions the number of second moment terms with values greater than twice the standard deviation was again too small to justify an interpretation. The large standard deviations in the integrated moments (for each of the nine deformation types employed in the refinement) are attributable to the different chemical environment of each of the 38 atoms.

The problem is least serious for the methyl carbons- which although crystallographically independent do have very similar chemical environments. The problem is most serious for the carbon atoms in the phenyl ring and if more powerful computer processing were available these carbons would have been refined using two or possibly even three or four deformation types.

4.5. Theoretical Deformation density Maps

4.5.1. Models for $[C_6H_5CH_2NMe_3]^+[B_3H_8]^-$

Each ion was modelled in isolation. The geometry for the BTMA cation was based on preliminary *X*-ray diffraction results but idealised to a C_s point symmetry with the phenyl ring exactly hexagonal and planar. Torsions were idealised to 0° ,120° or 180° as appropriate and chemically equivalent bond angles were averaged. Idealised bond distances for C-H (1.08Å) were also used. Unique bonds and angles for the model are:

Bond distances
C6-C7 1.498Å, C7-N 1.507Å, N-C8/9/10 1.490Å
Bond Angles
H-C8-N etc 108., H71-C7-C6 110., N-C7-C6 114
Bond Torsions
H71-C7-C6-C1 150., all others staggered.

The atom labelling is the same as for the crystallographic refinement (indicated in Figure 4.3).

The geometry for the $[B_3H_8]^-$ anion was also obtained by idealising the geometry from preliminary *X*-ray diffraction results. This experimental geometry model (EXPT) was supplemented by another from geometry optimisation at the split valence 4-31G level (SVOPT).

Parameters defining both models are listed in listed in Appendix V.

4.5.2. The $[C_6H_5CH_2NMe_3]^+$ Cation

For this large model the calculation was done at the 4-31G level only. Figures 4.5.2(a) and (b) show the deformation density in the plane of the phenyl ring and in the perpendicular plane containing N-C7-C6 (mirror plane).

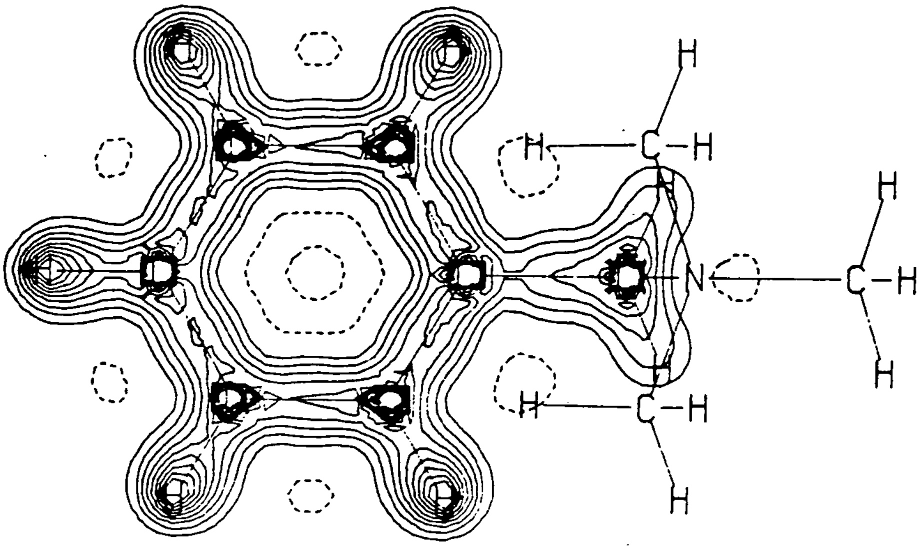

FIGURE 4.5.2(A)

Theoretical Deformation Density
in the plane of the phenyl ring.

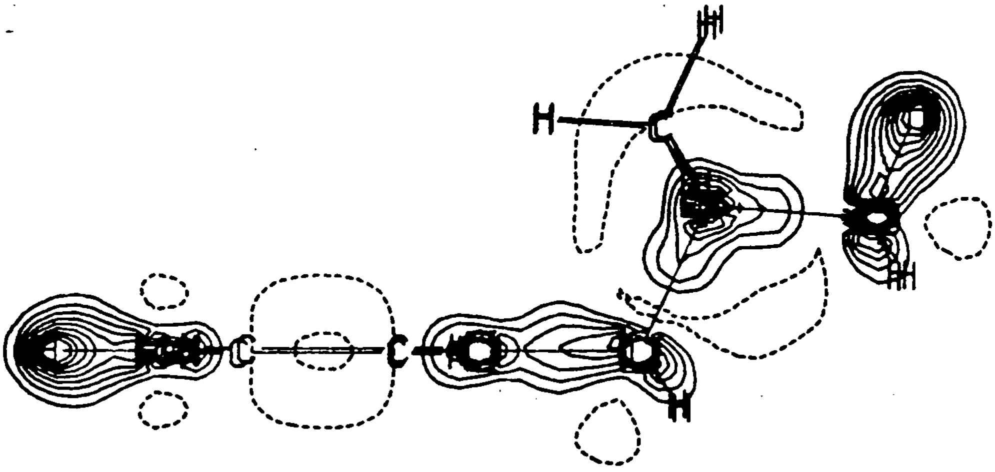

FIGURE 4.5.2(B)

Theoretical Deformation Density
in the N-C7-C6 plane.

The deformation density in the phenyl ring is in the form of cylinders parallel to the C–C bonds (rather than ellipsoids) with an elliptical cross section. There is, in the plane of the ring, a narrow strip like maximum of 0.5eÅ^{-3}. The peak on the N–C7 vector is smaller at 0.4eÅ^{-3} but the deformation along the C7–N vector is smaller and remarkably asymmetric. (This feature has also been seen in theoretical calculations on N–C in $[HNMe_3]^+$ and $[HNEt_3]^+$ see Chapter 3). The N–C8/C9/C10 bond deformation densities are all similar to each other and N–C7 with only a small surplus of 0.3eÅ^{-3} near the nitrogen atom which rapidly decays to -0.1eÅ^{-3} near the carbon.

4.5.3. The $[B_3H_8]^-$ Anion

This small model was examined at two levels of calculation (4-31G and TZV) and at two geometries (EXPT and SVOPT). The deformation densities in each of the mirror planes of these models of C_{2v} point symmetry are presented in Figures 4.5.3(a) (EXPT) and (b) (SVOPT) for the 4-31G level and similarly in Figures 4.5.3(c) and (d) for the TZV basis.

The EXPT and SVOPT geometries lead to strikingly different deformation densities. One is *not* a slight distortion of the other. They represent two different electron density topologies. This is the probable reason for the failure to adequately reproduce the experimental geometry at the 4-31G level.

The difference between the use of the 4-31G basis and the more flexible TZV basis is less profound than the difference caused by a change in geometry. The SVOPT geometry is calculated (in the TZV basis) to be more stable than the EXPT geometry.

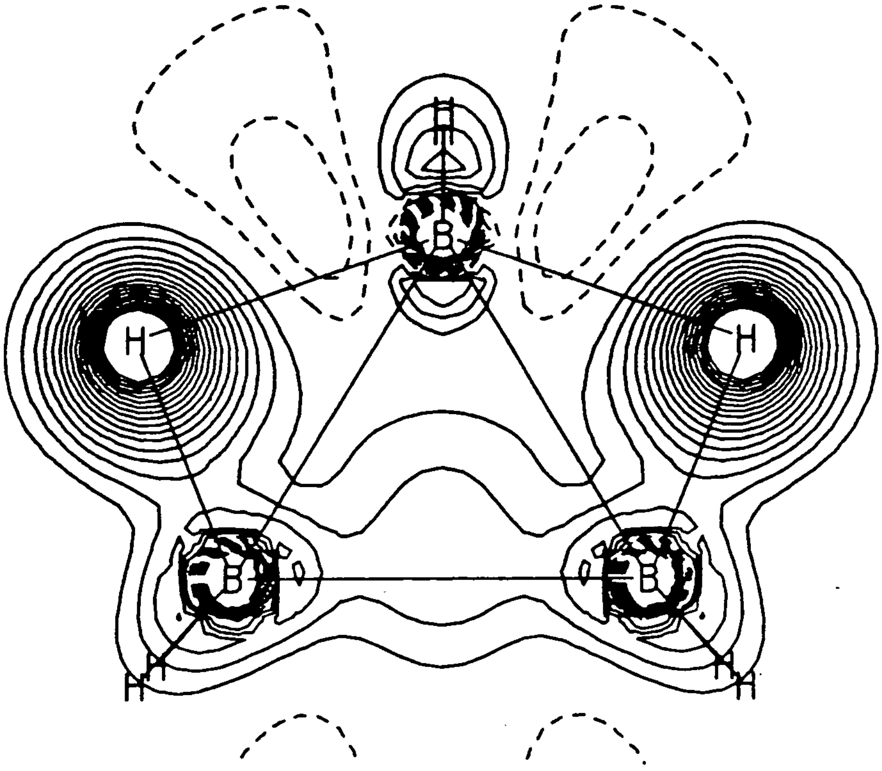

FIGURE 4.5.3(A)

Theoretical Deformation Density
in the B1-B2-B3 plane, EXPT geometry, 4-31G basis.

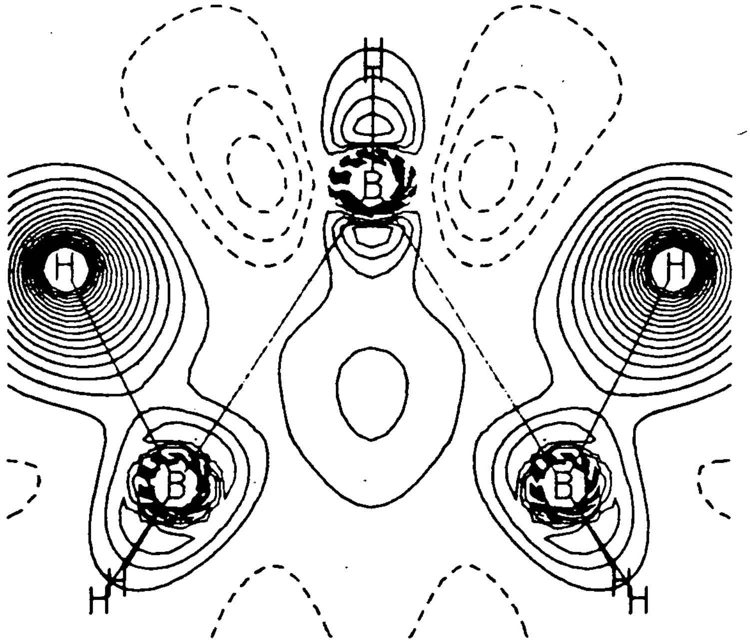

FIGURE 4.5.3(B)

Theoretical Deformation Density
in the B1-B2-B3 plane, SVOPT geometry, 4-31G basis.

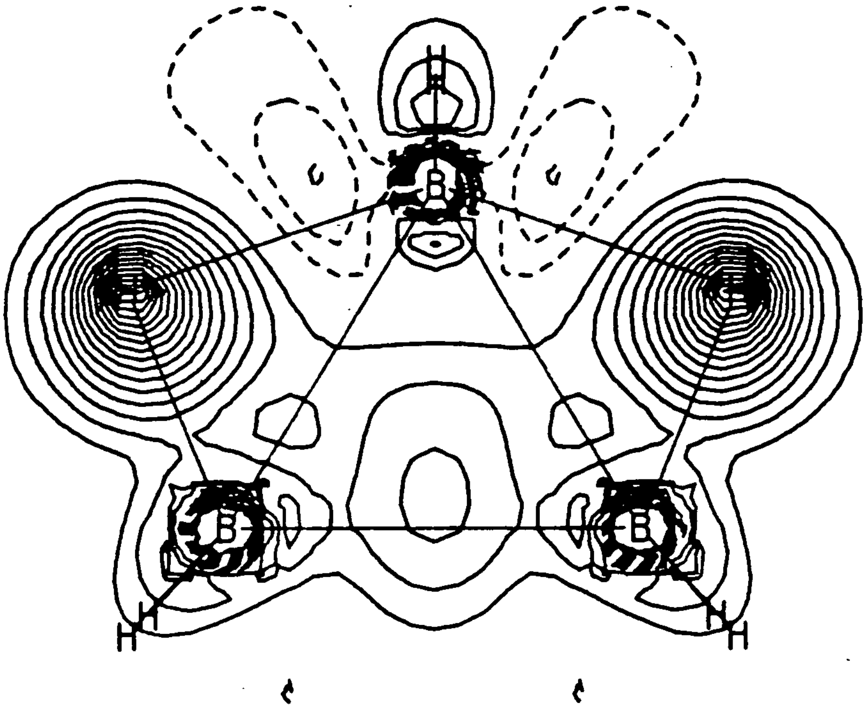

FIGURE 4.5.3(C)

Theoretical Deformation Density
in the B1-B2-B3 plane, EXPT geometry, TZV basis.

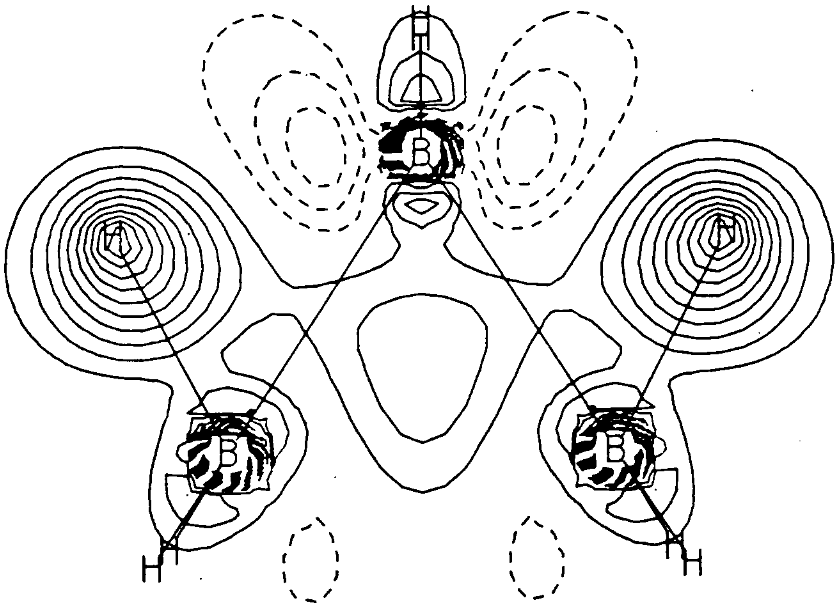

FIGURE 4.5.3(D)

Theoretical Deformation Density
in the B1-B2-B3 plane, SVOPT geometry, TZV basis.

4.6. Discussion : Theory and Experiment

4.6.1. BTMA Charge Distribution

The deformation density in BTMA, particularly in the phenyl ring, refined rapidly and smoothly to give a large feature in the deformation map ($0.7e\text{Å}^{-3}$ to good precision (esd *ca* $0.02e\text{Å}^{-3}$). This is, as explained below, *not* accidental. Non-random peaks in phenyl rings are so common, even in data sets of only routine quality and resolution, that it is worth explaining this phenomenon.

The first systematic investigation of residual peaks in aromatic rings was early (1966) in the study of deformation electron density [114]. By averaging residual density maps using non-crystallographic point symmetry and further averaging over several structures definite systematic features were observed, if only to low resolution.

The phenyl ring is extraordinarily rigid and invariable and the geometry is known to good precision and accuracy from neutron diffraction measurements. This has led to the use of rigid group refinement. In such circumstances the positions of atoms are not subject to an asphericity shift and, where the thermal motion is described by motion of the group, thermal parameters cannot be distorted to absorb the deformation electron density. This alone, however, is not responsible for the observation of bond peaks. Omission or relaxation of these restraints still leaves residual peaks which can be interpreted after averaging. Consideration of the Laplacian of the electron density, or more precisely its negative ($-\nabla^2\rho=-d^2\rho/dx^2\ -d^2\rho/dy^2\ -d^2\rho/dz^2$) is useful [115, 116]. This function is large and positive for regions of space which have a much higher electron density than the immediate environment. It measures the degree of localisation (not the magnitude) of electron density.

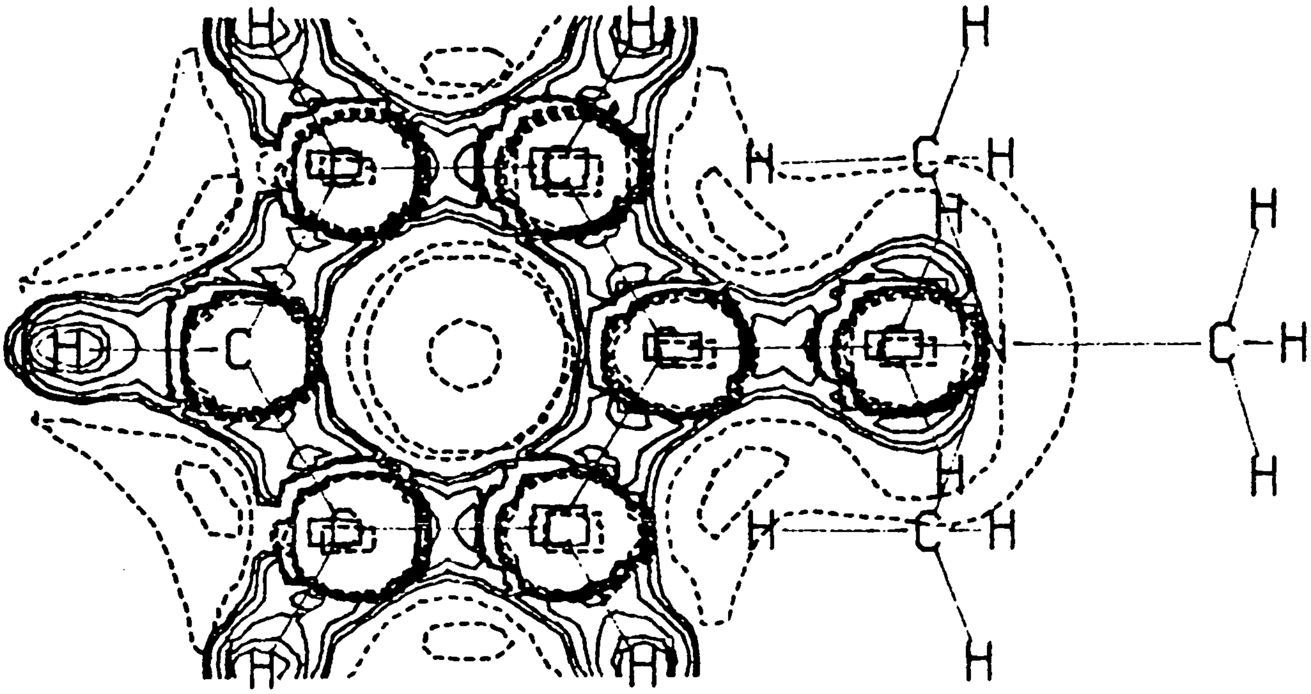

FIGURE 4.6.1(A)

Negative Laplacian of Electron Density
for phenyl ring plane.

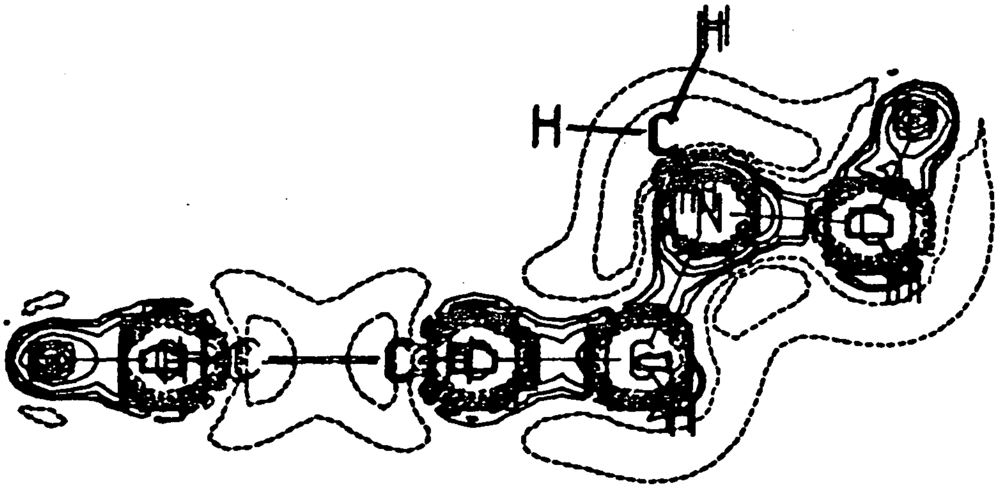

FIGURE 4.6.1(B)

Negative Laplacian of Electron Density
for the N-C7-C6 plane.

Figures 4.6.1(a) and (b) show the negative Laplacian for two planes in BTMA. On phenyl ring C-C bonds it reaches the extraordinary value of 0.8au (cf C6-C7 0.4au, C7-N 0.2au, N-C8 0.2au and also N-C 0.2au, C-C 0.4au in $[Et_3NH]^+$, B-B 0.1au in $[B_{12}H_{12}]^{2-}$ and B-B 0.2au in $[B_3H_8]^-$). This large value of 0.8au means that the C-C interatomic electron density is intensely localised and, in the nature of Fourier transforms, this results in a modification of the *X*-ray diffraction pattern (relative to that calculated using the free-atom model) extending out to a high value of $\sin(\theta)/\lambda$. Therefore, information on the deformation density is contained in a large number of structure factors - not merely the low-angle data. This results in the poor ability of positional or temperature factor parameters to mask the deformation. The utility of the Laplacian function in estimating the ease with which deformation electron density of a compound can be studied has so far not been exploited. In particular, this function could prove useful in determining the feasibility of studies of transition metal compounds where the interesting valence density is the product of diffuse d-orbitals.

Another application of the Laplacian is to clearly identify chemically bonded atoms. The deformation density alone is not always the most useful indicator. Between bound atoms (ie atoms closer than the sum of their Van der Waals radii) there can be a deficit of electron density along a substantial fraction of the interatomic vector (as in C7-N in BTMA above or the example of $Cr_2(OOCH_3)_4.2H_2O$ [117]). This presents a conceptual problem (the negative results are genuine) because the bond in dihydrogen has previously been taken as the archetypal sigma bond and there is electron density accumulation on the internuclear axis in dihydrogen. In fact the bond in dihydrogen is not typical because it has no p-orbitals. Several papers have been published affirming the authenticity of some negative or zero internuclear deformation densities and the resulting insight into the electron redistribution associated with chemical bonding. The function $-\nabla^2\rho$ is useful because, even when the deformation density is negative, a positive peak in $-\nabla^2\rho$ is found between bonded atoms - even if it is not on the internuclear axis.

A comparison of the experimental and calculated deformation densities shows some inconsistencies. These are :

- Aromatic C-C peaks are curved in the plane of the ring but calculated to be almost straight edged.
- These ring peaks are larger in the *X*-ray diffraction result (0.70(2)eÅ^{-3}) than calculated (0.5eÅ^{-3}).
- The calculated electron deficiency at the C7 end of the N-C7 vector (-0.1eÅ^{-3}) is replaced by a definite density surplus in the *X*-ray diffraction result (0.60(5)eÅ^{-3}).
- The calculated surplus at the N end of the N-C_{methyl} vector (0.30eÅ^{-3}) is underestimated relative to the *X*-ray diffraction result (0.50(5)eÅ^{-3}).

The interpretation of these differences depends on their significance and origin. Examination of the esd maps suggest that all four inconsistencies are significant. The possible origins for the differences are :

- The multipole expansion is not sufficiently flexible.
- A hole in reciprocal space data points at low angle (see Chapter 3).
- the basis set used for the calculation is too small.

The first can be tested by looking for non-random residual peaks in the final difference Fourier maps. Examination of these maps shows a scattering of sharp but small (0.10eÅ^{-3}) peaks with larger (0.20eÅ^{-3}) sharp peaks at the atomic positions. The random nature of the diffuse peaks is hard to prove but, for example, averaging of the map for the residual density in the plane of the

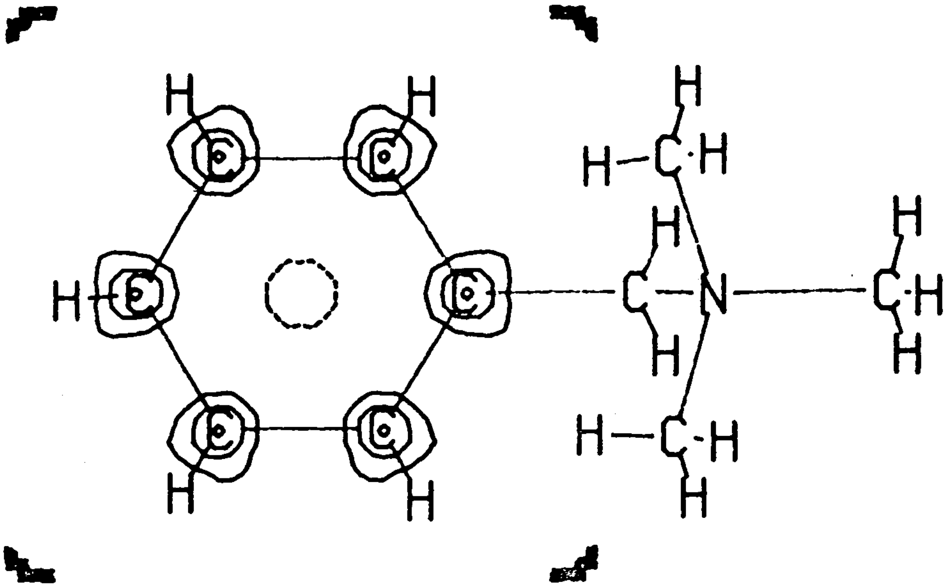

FIGURE 4.6.1(C)

Residual Density
in phenyl ring plane after averaging.

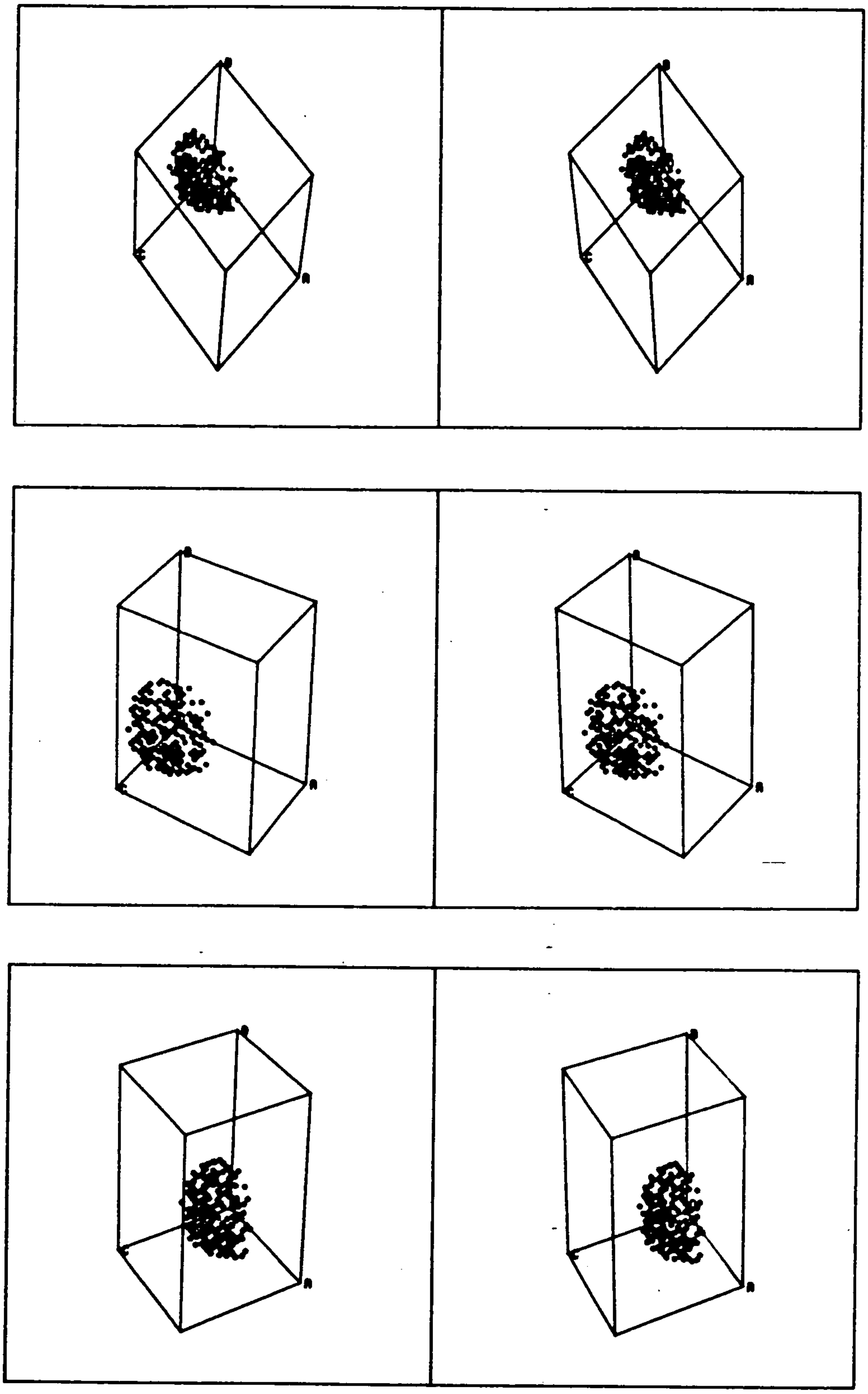

FIGURE 4.6.1(D)

Distribution of Data in Reciprocal Space.

phenyl ring using hexagonal symmetry about the ring centre produces a map (Fig 4.6.1(c)) without systematic residual features in the bond region, only peaks at the atom positions where the deformation density is ill-defined anyway.

The second source of error can be dismissed by examining Fig 4.6.1(d) which is a stereo pair of the distribution in a hemisphere of reciprocal space of low angle data points (including those equivalent by symmetry). There is no sizeable gap.

Assessment of the error in the calculated deformation density depends on the estimation of the limit of the deformation density as the basis is extended towards the Hartree-Fock limit. This is impractical for a whole BTMA model but small portions can be further examined.

Unfortunately the most interesting inconsistency (the profile of the N-C deformation) is difficult to examine. The most obvious model $[NMe_4]^+$ is too large to be suitable. However $[H_3NMe]^+$ is a practical size. A calculation at the TZV (*not* TZVP) level shows minimal changes with respect to 4-31G (see chapter 3). There is only a trend towards more circular bond peaks. This trend may explain the contrast in the curvature of deformation density contours in the phenyl ring. Benzene is too large a model for this trend to be verified by calculation at the TZV level.

4.6.2. $[B_3H_8]^-$ Charge Distribution

The static deformation density map gives no support for a contribution from the topologically forbidden form (II) (see Fig 4.1(a)), but the map can be interpreted in terms of form (I). The basal bond peak is underestimated in the calculation (4-31G : 0.14eÅ^{-3}) relative to the *X*-ray diffraction result (0.32eÅ^{-3}).

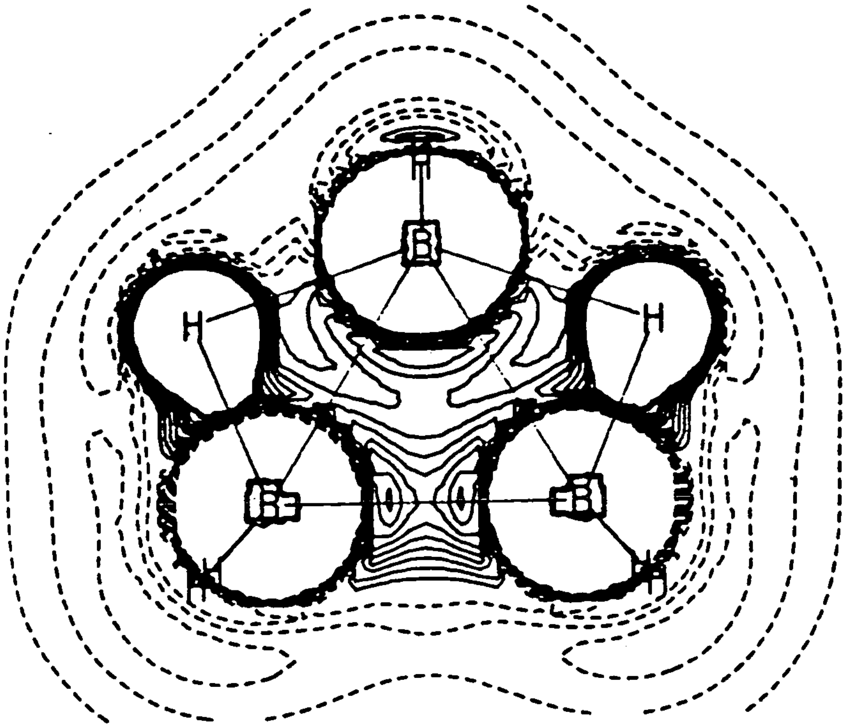

FIGURE 4.6.2(A)

Negative Laplacian of Electron Density
for B1-B2-B3 plane, EXPT geometry, 4-31G basis

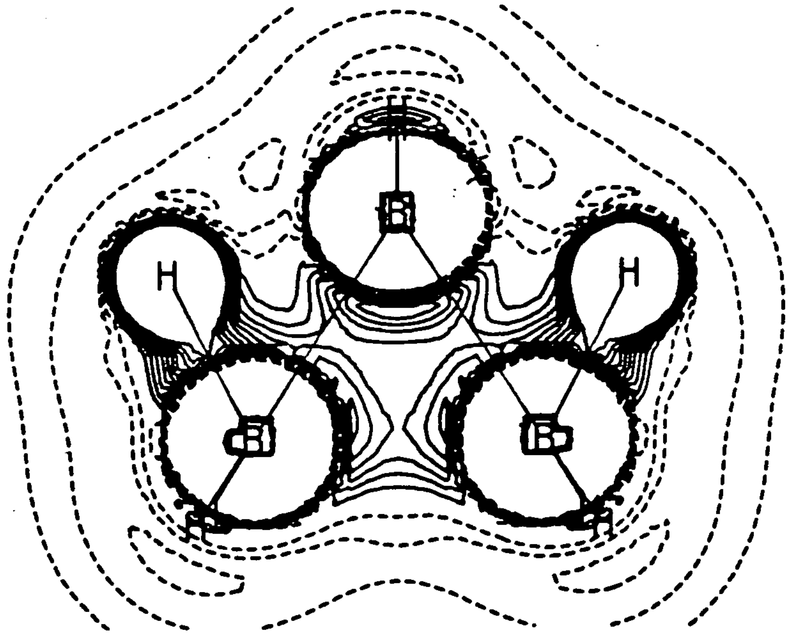

FIGURE 4.6.2(B)

Negative Laplacian of Electron Density
for the B1-B2-B3 plane, SVOPT geometry, 4-31G basis.

The calculation is however extremely sensitive to the geometry. For example there is a switch to another topology - more similar to (II) - if the geometry is optimised at the 4-31G level. This latter form has very little surplus deformation density on the basal (B2-B3) vector.

Inspection of the negative Laplacian of electron density makes the contrast in topology more clearly visible (see Figures 4.6.2(a),(b)). This shows the domination of the 2c-2e B2-B3 bond in the expt geometry with a type (II) topology. The distinction in topologies is proven by the different number and form of 'bond critical points' [115, 116].

In conclusion the poor agreement between the *X*-ray diffraction and calculated maps is probably attributable to an excess weight assigned to (II)-type topology in the calculation. This result casts doubt on the importance of (II) and therefore suggests that the invocation of (II) as an explanation for the observation of H-bridging leading to B-B shortening in $[B_3H_8]^-$ is unfounded. An alternative explanation is given in Chapter 5 and in a recent paper by the author and A.J.Welch [119].

Chapter 5

The Effect of Edge-bridging Hydrogen Atoms on the Lengths of B-B and Metal-Metal Bonds in Cluster Compounds

5.1. Introduction

A charge deformation density analysis on the salt benzyltrimethylammonium octahydrotriborate $[PhCH_2NMe_3]^+[B_3H_8]^-$ re-affirmed the finding of a much earlier XRD study on another $[B_3H_8]^-$ salt, which was that the bridged B-B lengths are shorter than the un-bridged one (see Chapter 4). This shortening of an H-bridged bond is extremely rare and may be unique.

The explanation previously proposed - that the shortening is attributable to a contribution of a topologically forbidden canonical form - has been shown, by a deformation density study (Chapter 4), to be unfounded. An alternative rationalisation of the shortening has been proposed in a recent paper by the author and A.J.Welch [119]. The paper forms Appendix VII. The same arguments are not entirely repeated in this chapter. Instead, the method employed is justified and demonstrated (with reference to the examples of Appendix VII). Finally, the merits of this approach to rationalising the effect of edge-bridging hydrogen atoms on the lengths of bonds are assessed.

5.2. The Problem Addressed

To determine the effect of edge-bridging hydrogen on the bond lengths of B-B (or M-M) bonds in cluster compounds it is necessary to have two measurements. These are the bridged bond length and, for reference, the length of the same bond in the absence of a bridging hydrogen. This strict requirement is necessary because, for example, in an asymmetric molecule with an H-bridged bond the length of the bond is dependent on factors other than the presence or absence of the bridging hydrogen(s). The problem addressed is therefore to be one of rationalisation of the relative bond lengths of two bonds whose only difference is the presence or absence of bridging hydrogens. There are several compounds where such bond lengths have been determined simultaneously in an XRD study. These are:

$[B_3H_8]^-$	119,105
$[B_{11}H_{13}]^-$	120
$[H_2Os_4(CO)_{12}]^{2-}$	121
$[HRe_3(CO)_{12}]^{2-}$	122
$[H_2Re_3(CO)_{12}]^-$	123

The hydrogens were not directly located in the transition metal compounds but were confidently assigned positions from the dispositions of the carbonyl ligands.

5.3. Rationalisation via FMO Occupation

The rationalisation of the bond lengths in the five structures listed above depends on the the fragmentation of each complex into bridging proton(s) and the complementary anion eg.

$$[B_3H_8]^- \Rightarrow [B_3H_6]^{3-} + [H...H]^{2+}$$

The anion is then idealised to have a geometry where all chemically similar bonds have equivalent lengths. In the above example a model of $[B_3H_6]^{3-}$ has point symmetry D_{3h} and similarly $[Os_4(CO)_{12}]^{4-}$ would have point symmetry T_d. The Molecular Orbitals (MO's) for the original anion and its constituent protonated and deprotonated fragments are then calculated using the empirical Extended Huckel MO (EHMO) theory. The deprotonated anion fragment MO's (FMO's) include degenerate sets. The occupation of the members of a set are necessarily equal. There is (by symmetry) no unbalanced force to distort the anion from its point group symmetry. When the anion and bridging proton(s) are brought together the interaction of members of the formerly degenerate sets with the (empty) proton s-orbitals are NOT equal - some may have exactly zero overlap, others not. Since the resulting wavefunction contains orbitals which are linear combinations of (occupied) anion FMO's with (unoccupied) FMO's of the proton(s) then the occupation of the anion FMO's in the molecule is modified. This process is neatly expressed in terms of the density matrix.

The wavefunction for a polyatomic molecule with a basis set of N orbitals can always be expressed as a density matrix. The density matrix is a square symmetric matrix of NxN elements D_{ij} where D_{ij} is defined as

$$D_{ij} = \sum n_\alpha C_{i\alpha} C_{j\alpha}$$

where the summation is over all orbitals "α" with occupation n_α where each molecular orbital is defined in terms of atomic orbitals ϕ_i

$$\psi_a = \sum C_{i\alpha} \phi_i$$

When two fragments interact the resulting wavefunction can be expressed as a larger density matrix : (n+m) x (n+m). This molecular density matrix can therefore be considered as made up of 3 parts as shown below.

- the anion density matrix (n x n)
- the bridging hydrogen(s) density matrix (m x m)
- the overlap density matrix (n x m)

If, in addition, the fragment components are calculated for each fragment in isolation the difference between the fragment density matrices (FDM's) will contain all the information about changes to be expected in that fragment upon molecule formation. This might initially appear a complex source of such information - an nxn symmetric matrix each element of which is a difference between corresponding elements of two matrices - but if the density matrices are expressed in an FMO basis set the FDM's are diagonal and Δ(FDM) is simply a set of n numbers. A numerical example is given below for the system $[B_3H_8]^-$/ $[B_3H_6]^{3-}$/ $[H...H]^{2+}$ with a geometry corresponding to asymmetric bridging (σ=0.6, see Appendix VI). FMO's are presented in order of increasing energy with degenerate FMO's grouped in brackets.

```
[B3H6]3- isolated 2.00{ 2.00 2.00} 2.00{ 2.00 2.00} 2.00{ 2.00 2.00}
[B3H6] in [B3H8]- 1.85{ 1.73 1.99} 2.00{ 2.00 2.00} 2.00{ 1.15 1.14}
Δ                -0.15{-0.27-0.01} 0.00{ 0.00 0.00} 0.00{-0.85-0.86}

[H...H]2+ isolated 0.00 0.00
[H...H] in [B3H8]- 0.98 1.06
Δ                  0.98 1.06
```

As expected only a small proportion of the elements of the FDM's change appreciably. Interatomic forces are now created and inspection of the wavefunctions of those members of degenerate sets (where one component is preferentially de-occupied) gives the direction of those forces. For example, de-occupation of a previously occupied FMO which is bonding between a pair of atoms will cause a lengthening of that bond. Conversely the partial occupation of a previously unoccupied FMO which is bonding between a pair of atoms leads to a shortening of that bond. Application of these arguments explains the lengthening upon symmetric edge-bridging in $[B_3H_8]^-$ (predicted), $H_2Re_3(CO)_{12}$ and $HRe_3(CO)_{12}$. The changes in the FDM can, however, be dependent on the whether or not the hydrogens bridge symmetrically. In the case of $[B_3H_8]^-$ the asymmetrisation of the hydrogen bridges (such that B-μH to the unique B is longer) gives a ranking by occupation of the 2E′ of $[B_3H_6]^{3-}$ which is the reverse of the order when the hydrogens bridge symmetrically. This dependence on fine geometry is a property more easily investigated by FMO and FDM's than by other approaches (see below).

5.4. Advantages of using FMO Occupations and FDM's

The above rationalisation of the changes in bond length upon molecule formation can be achieved using the same EHMO calculations but interpreting the results by other, more familiar matrices such as the energy matrix

$$E_{ii} = \sum N_\alpha C^2_{i\alpha} H_{ii}$$

$$E_{ij} = \sum N_\alpha C_{i\alpha} C_{j\alpha} H_{ij}$$

This energy matrix can be further reduced to a matrix whose elements are now related to inter-atomic energy interactions. The advantage of FMO occupation changes are:

- the interacting orbitals of each of the fragments are readily identifiable.
- having identified the active FMO's the dependence of the interaction on the position of the fragments relative to each other can be quickly estimated.

For example the ΔFDM shows that in $[B_3H_8]^-$/ $[B_3H_6]^{3-}$/ $[H...H]^{2+}$ it is the 2E' which are important in the distortion of the triangle. Having identified the 2E' the dependence of the distortion on the H atom coordinates can be estimated without resorting to a tedious evaluation of the molecular wavefunction for each possible coordinate of the hydrogens. Instead it is sufficient to estimate the component of the 2E' which will have the dominant interaction with the hydrogen orbital(s). In EHMO this interaction H_{ij} is defined to be dependent on the average atomic energy $(H_{ii}+H_{jj})$ and the overlap function S_{ij} according to :

$$H_{ij} = 0.5\ K\ S_{ij}\ (H_{ii}+H_{jj})$$

where K is the Huckel constant (usually 1.75). The competing components are

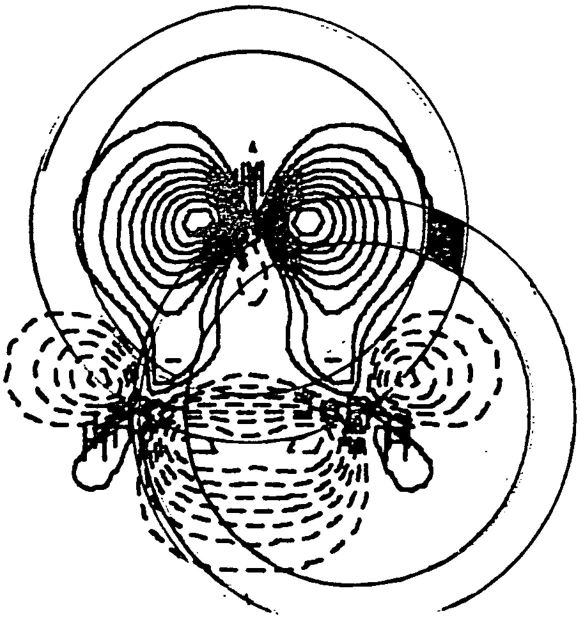

FIGURE 5.4(A)

Δρ for $[B_3H_6]^{3-}$

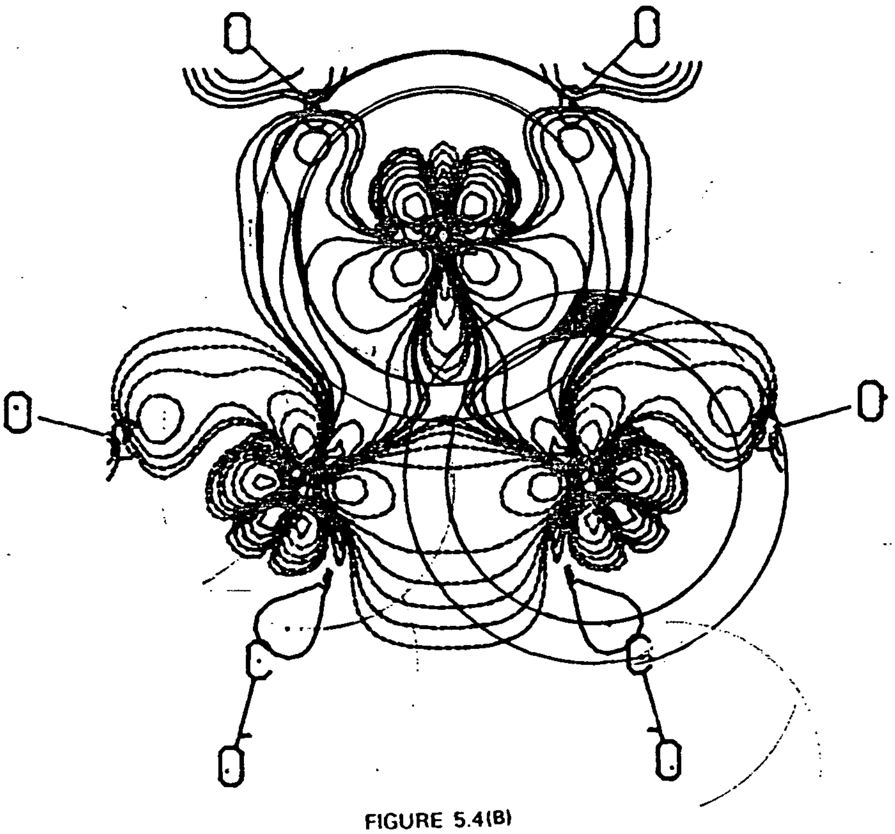

FIGURE 5.4(B)

Δρ for $[Re_3(CO)_{12}]^{3-}$

necessarily at the same energy and in the case of [H...H] the Σ_u^+ and Σ_g^+ are at similar energies if H...H is long (> 2Å). The estimation of the dominant interaction can then be approximated by the function

$$\Delta\rho = (\Psi_{2E'a})^2-(\Psi_{2E'b})^2$$

This function is mapped, in the plane of the triangle, in Figure 5.4(a). The overlap would be even better approximated by the convolution of $\Delta\rho$ with the Gaussian function $\exp(-\alpha r^2)$ (α = 2.6 au^{-2}) since the H 1s orbitals are of finite size. Nevertheless $\Delta\rho$ shows the expected domains of bridged bond shortening (dashed contours) and bridged bond lengthening (solid contours). The black diamond on the figure indicates the domain where B-H is between 1.4 and 1.7Å.

Although $[Re_3(CO)_{12}]^{3-}$ and $[B_3H_6]^{3-}$ are composed of isolobal vertices, the dibridged structure $[H_2Re_3(CO)_{12}]^-$ has bridged Re-Re bonds longer. The corresponding $\Delta\rho$ function for an idealised model of $[Re_3(CO)_{12}]^{3-}$/ $[H_2Re_3(CO)_{12}]^-$ / $[H...H]^{2+}$ is presented in Figure 5.4(b). This shows there are again two domains but the domain for bridge bond shortening (dashed contours) is largely excluded by the van der Waals radii (C 1.7Å, O 1.5Å) and bond restrictions (1.6Å< H-Re <1.9Å) indicated by the black diamond on the Figure. The bridging hydrogens are constrained to be near symmetric positions and hence, unlike in $[B_3H_8]^-$, bridged bonds are lengthened.

5.5. LMO Approximations : FDM's for Low Symmetry Species

At the beginning of this chapter the problem addressed was defined as the rationalisation of the structures of a very small class of compounds - those where in a single structural determination there were bonds whose only difference was the presence or absence of a bridging hydrogen. The methods used to solve this problem and the conclusions from the solution can be adapted to the more general case.

In $[Re_3(CO)_{12}]^{3-}$ and $[B_3H_6]^{3-}$ the orthogonalisation of the wavefunction into fragment molecular orbitals conveniently produces a set of degenerate orbitals where one of the three connectivities is strongly bound by one member of the set but not by the others. In these examples bond length changes are correlated with just a pair of elements from the ΔFDM. This need not be the case for $[Os_4(CO)_{12}]^{4-}$ or 1,6-$C_2B_4H_6$. For these species the bond lengths are correlated with several elements of the FDM and the orthogonalisation of the wavefunction is, for these high symmetry anions, not unique. It is more convenient to transform the FDM using a basis set of localised molecular orbitals (LMO's). After this transformation predicted changes in bond length upon protonation would, as for $[Re_3(CO)_{12}]^{3-}$ and $[B_3H_6]^{3-}$, be correlated to only a few elements of the ΔFDM. In the absence of a LMO transformation program the localisation can be improved by a small perturbation of the geometry eg for $[Os_4(CO)_{12}]^{4-}$ from point symmetry T_d to D_{2d}.

The recognition that bond length changes can be rationalised by an inequality in occupations of formerly degenerate LMO's permits an extension of this method to low symmetry species. This is described below. The first step is, as before, to idealise the geometry such that similar bonds (bridged or not) are made equal in length. The second step is, using this model species, a calculation of the wavefunction for the parent molecule and its component proton(s) and deprotonated form. Next the FDM's are transformed to an LMO basis. Now chemically similar (but distinguishable) bonds in the deprotonated fragment will each be correlated to a single FDM diagonal element. The change in the occupation of each of these diagonal elements upon protonation will be an indicator of the degree to which each of the bonds will lengthen or shorten as a result of protonation. By plotting the difference density function

$$\Delta\rho = (\Psi_x)^2-(\Psi_y)^2$$

for pairs of LMO's centred on bonds x and y the domains within which x is lengthened relative to y can be quickly explored. The ultimate test of this new approach will be to identify the second compound for which a bridging hydrogen causes bond shortening. It may even be possible to modify an existing cluster compound by, for example, substituting ligands in such a way as to force -by van der Waals contacts- a bridging hydrogen into a domain where the previous effect on the bridged bond is cancelled or inverted.

Chapter 6

Hydride Location in Transition Metal Clusters

6.1. The Need for Empirical Methods

The location of hydrides in transition metal compounds by *X*-ray diffraction (XRD) is difficult because not only is the contribution to *X*-ray scattering from the hydride a very small fraction of the total scattering but the hydride is of the order of 2Å from a heavy metal atom and to resolve this requires data of at least medium resolution - but unfortunately hydrogen only weakly scatters at such angles. Consequently the least-squares refinement of hydrogen coordinates is rarely attempted in these circumstances as the minimisation of $|F_o-kF_c|$ is insensitive to the change in hydrogen coordinates. The problem can be overcome by using neutron diffraction where the scattering power of elements is approximately proportional to $Z^{1/3}$ rather than Z (Z is the atomic number). Disadvantages to using neutron diffraction are that the intensity measurements are typically of lower precision, the crystal size required is much larger and the expense of using a neutron source is considerable.

The observation that where hydrides have been located the metal-metal bond, if bridged, is usually lengthened led to the practice of assigning hydride positions using only XRD determined metal-metal bond lengths. Moreover, this method is flawed by the assumption that there are no other origins for a small change from the mean bond length - such as the pattern of ligands around the metal. This method could be used only to assign the topology of the hydride and not it's coordinates with respect to the other atoms.

6.2. The "HYDEX" Computer program by A.G. Orpen

This program was designed to estimate the coordinates of the hydride ligands. The approach adopted by Orpen [124] was to take the non-hydride atom coordinates as found by XRD (supplemented with calculated hydrogen coordinates on the non-hydride ligands if necessary) and optimise the coordinate(s) of the hydride(s) (from an initial guess) using a potential energy function of the form:

$$M = \sum_i V(r_i) + \sum_k |(R_k - R)/S|^2$$

where V(r) is the potential energy attributable to non-bonded contacts within approximately 3.5Å and is of the form :

$$V(r) = a.e^{-br}.r^{-d} - c.r^{-6}$$

where a, b, c, and d are numerical constants dependent on the atom type of the second atom in the H...X contact. These constants were taken from work on earlier empirical molecular mechanics work[125]. The second summation term in M is a penalty function which operates on all M-H bonds. The number, k, and length, R_k of these bonds must be specified in the input to Orpen's program. This penalty function limits the domain for hydride coordinates to the intersection of the surface of k spheres of radius R_k. The reproduction of neutron determined hydride coordinates was found by Orpen to be good for 17 of 18 test cases. The case where the fit was poor was $Rh_3H_3\{P(OMe)_3\}_6$. Orpen identified the source of this failure to be that, in this compound unlike the others, there was not a close packed arrangement of ligands with only one gap-site for the hydride. The potential function M is dominated by the repulsive V-terms and the hydride site can therefore only be well defined if there is a dense arrangement of ligands excluding the hydride probe from anywhere else. In view of this defect Orpen did not apply the program to polyhydride complexes such as $[Re_2H_8L_4]$, $[OsH_4L_3]$, $[MoH_2(C_5H_5)_2]$ or $[TaH_3(C_5H_5)_2]$.

This chapter describes a successful attempt to devise a method for identifying hydride sites even for an open transition metal-ligand framework. A potential energy function is again employed but it is based on the use of EHMO calculations together with classical electrostatics. Such a potential has the advantage of the appearance, when the hydride is in a chemically plausable bonding site, of a large favourable energy term. Consequently it is *not* necessary to specify the topology of the hydride nor the M-H bond lengths.

6.3. Anderson's EHMO Method : ASED

EHMO calculations have been widely used for the rationalisation of conformations of molecules and ions. The method is successful because the sum of one-electron energies for occupied orbitals as calculated by this semi-empirical method is sensitive to the angular overlap of the orbitals of the atoms which make up the molecule. The radial coordinates of pairs of atoms also influence the energy but cannot be used to refine bond lengths because in simple EHMO methodology no terms for the electrostatic repulsion between positive nuclei are included in the energy calculation. Without these terms the result of refining bond lengths is a set of very short distances at which inter-atomic orbital overlaps have been maximised. A modification of the EHMO method with a sensible interatomic distance dependence was first proposed by A.B.Anderson and R.Hoffmann in 1974 [126]. This was the basis of what was in subsequent papers called the ASED method: Atom Superposition /Electron Delocalisation.

For a homonuclear diatomic the exact potential energy as a function of internuclear distance R can be considered as two *exact* terms $W_\beta(R)$ and

$W_{NPF}(R)$. Of these terms $W_\beta(R)$ is dependent only on the elements involved and their separation. $W_\beta(R)$ is always positive, and is the electrostatic potential energy of the interaction of nucleus α, charge Z_α, with the 'free-atom', spherically symmetric neutral atom β. Analytical formulae can be used to evaluate $W_\beta(R)$. The other term, $W_{NPF}(R)$ is specific to a given molecule and represents the electrostatic potential energy due to the interaction of nucleus α with the "non-perfectly following" (NPF) electron density - which is another name for the charge deformation density :

$$\rho_{NPF} = \rho_{mol} - \sum \rho_{atom}$$

This second term is extremely difficult to evaluate numerically but must be negative (bonding) for bound molecules. Fortunately, when a molecule is near its equilibrium separation $W_{NPF}(R)$ can be replaced, to within a constant, by $W_{EH}(R)$ which is the sum of occupied orbital energies from an EHMO calculation. The potential is now:

$$W^*(R) = W_\beta(R) + W_{EH}(R)$$

which, although no longer exact or on a correct absolute energy scale, should still be a minimum for a molecule at its equilibrium geometry.

In the extension to heteronuclear diatomics the W_β term could be evaluated using the nuclei of either atom and the net neutral density of the other. The convention adopted by Anderson and Hoffmann was to use the neutral density of the more electronegative atom. The further extension to polyatomics simply requires the pairwise summation of the $W_\beta(R)$ terms.

The W_β function is dependent on the valence orbital exponent of the neutral atom or more precisely γ which is twice the orbital exponent and describes the decay of the electron density. Equations A1 and A2 of A&H's paper give W_β in atomic units for an l-shell (2s2p) and M-shell (3s3p) atom respectively. The function for hydrogen is *not* published but is obviously important to hydride location and is derived below.

Derivation of Wβ for a K-shell atom.

The force is given by Coulomb's law :

$$F_{ENC} = Z_\alpha Z_{ENC}/r^2$$

where Z_{ENC} is the effective nuclear charge of atom β as seen by nucleus α.

$$Z_{ENC} = Z_\beta - \int_0^r 4\pi r^2 \rho_\beta(r)dr$$

For a hydrogen atom the Slater orbital is of the form

$$\phi = \sqrt{(\zeta^3/\pi)}\ e^{-\zeta r}$$

where $\sqrt{(\zeta^3/\pi)}$ is a tabulated normalisation factor.

$$\Rightarrow \rho_b(r) = \phi^2 = (\zeta^3/\pi)\ e^{-2\zeta r}$$

substituting $\gamma = 2\zeta$

$$\Rightarrow \rho_b(r) = (\gamma^3/8\pi)\ e^{-\gamma r}$$

$$\Rightarrow Z_{ENC} = Z_\beta - \int_0^r 4\pi r^2.(\gamma^3/8\pi)e^{-\gamma r}dr$$

$$\Rightarrow Z_{ENC} = Z_\beta - \int_0^r (\gamma^3/2).r^2 e^{-\gamma r}dr$$

For a neutral atom :

$$Z_\beta = \int_0^\infty (\gamma^3/2).r^2 e^{-\gamma r}dr$$

And using this substitution :

$$\Rightarrow Z_{ENC} = \int_r^\infty (\gamma^3/2).r^2e^{-\gamma r}dr$$

$$Z_{ENC} = (\gamma^3/2)\ [(-1/\gamma)e^{-\gamma r}r^2 + \int_r^\infty(1/\gamma)e^{-\gamma r}.2r]_r^\infty$$

$$Z_{ENC} = (\gamma^3/2)\ [(-1/\gamma)e^{-\gamma r}r^2 - (1/\gamma^2)e^{-\gamma r}.2r - (2/\gamma^3)e^{-\gamma r}]_r^\infty$$

$$Z_{ENC} = (\gamma^3/2)\ e^{-\gamma r}(r^2/2 + 2r/\gamma^2 + 2/\gamma^3)$$

The force per unit Z_α is now given by:

$$F_{ENC}(R) = Z_{ENC}(R)/R^2$$

$$F_{ENC}(R) = (\gamma^3/2)e^{-\gamma R}[\ 1/\gamma + 2/(R\gamma^2) + 2/(R^2\gamma^3)]$$

⇒ Potential energy :

$$W_\beta(R) = -\int_\infty^R F_{ENC}(R)dR$$

$$W_\beta(R) = -\int_\infty^R (\gamma^2/2 + \gamma/R + 1/R^2)\ e^{-\gamma R}dR$$

$$W_\beta(R) = \int_R^\infty e^{-\gamma R}.(\gamma^2/2).dR + \int_R^\infty e^{-\gamma R}.(\gamma/R).dR + \int_R^\infty e^{-\gamma R}(1/R^2).dR$$

$$W_\beta(R) = (\gamma/2).e^{-\gamma R} + ((1/R).e^{-\gamma R} - \int_R^\infty e^{-\gamma R}/R^2.dR) + \int_R^\infty e^{-\gamma R}/R^2.dR$$

$$W_\beta(R) = e^{-\gamma R}[\gamma/2 + 1/R]$$

The units of the above equation are atomic ie R is measured in bohr (1 bohr = 0.529..Å), γ is in bohr^{-1} and W_β is in hartrees (1 hartree = 27.2117 eV). A typical value for γ for hydrogen is between 2.0 and 2.6 bohr^{-1}. This formula generates the W_β curve in Figure 1 of A&H's paper.

6.4. Hydride Location using the ASED Method

6.4.1. Implementation of the Formula

The foundation computer program was the widely available EHMO program ICON[127]. This was incorporated together with a simple routine to evaluate the W_β function in a new program CCCP (Cluster Coordinate Convergence Program) which utilises the numerical analysis method of simplex minimisation as present in a NAG library function. The simplex method is slow but robust and is preferred to finite gradient analysis which is confused by the appearance of discontinuities which are generated by the iteration to a finite tolerance in calculation of interatomic overlaps.

The minimised geometry is slightly dependent on two parameters used to describe the hydride atom viz the Coulson potential COULH and the exponent ZETA. Using the $HMn(CO)_5$ structure alone as a guide suitable values for these terms were found to be either −12.6eV /0.85au^{-1} or −14.6eV /1.0au^{-1}. In view of the assumed polarity of $M^{\delta+}$-$H^{\delta-}$ the former parameters were adopted and fixed.

6.4.2. Examples

Neutron test cases

a) $HMn(CO)_5$[128] This model served as a means of tuning the exponent of the probe hydride and the potential H_{ii}. Using values of 0.85 and −12.6 an Mn-H bond length of 1.61Å was obtained. This is within 0.01Å of the distance determined in the neutron diffraction study.

b) $(\mu_2H)_2Os_3(CO)_{10}$

		Neutron[129]	
		Os2	Os3
Neutron	H1	1.840	1.843
	H2	1.845	1.852
CCCP	H1	1.733	1.725
	H2	1.741	1.836

c) $(\mu_2H)_3Rh_3(PH_3)_6$ a model for $(\mu H)_3Rh_3(P(OMe)_3)_6$

		Neutron[130]		
		Rh1	Rh2	Rh3
Neutron	H1	1.838	-	1.748
	H2	1.733	1.731	-
	H3	-	1.752	1.784
CCCP	H1	1.732	-	1.721
	H2	1.621	1.623	-
	H3	-	1.691	1.726

d) $(\mu_2H)_2(\mu_2CH_2)Os_3(CO)_{10}$

		Neutron[131]				
		Os1	Os2	Os3	H3	H4
Neutron	H3	1.883	-	1.755	-	-
	H4	1.834	1.808	-		
CCCP	H3	1.760	-	1.672	0.21	-
	H4	1.767	1.769	-	-	0.10

e) $H_2Mo(C_5H_5)_2$ This compound has exact two-fold symmetry.

		Neutron[132]	
		Mo	H
Neutron	H	1.684	2.063
CCCP	H	1.546	0.151

f) $[HRu_6(CO)_{18}]^-$

Neutron[133]						
Ru1	Ru2	Ru3	Ru4	Ru5	Ru6	H

Neutron	H	2.035	2.031	2.055	2.038	2.034	2.026	-
CCCP	H	2.045	2.017	2.028	2.059	2.049	2.018	

g) $[HOs_6(CO)_{18}]^-$

		Neutron[134]		
		Os1	Os2	Os3
Neutron	H	-No coordinates available-		
CCCP	H	1.715	1.964	1.742

h) $[HCo_6(CO)_{15}]^-$

		Neutron[135]						
		Co1	Co2	Co3	Co4	Co5	Co6	H
Neutron	H	1.811	1.855	1.872	1.804	1.799	1.801	-
CCCP	H	1.929	1.923	1.759	1.748	1.808	1.790	0.132

j) $H_3Ta(C_5H_5)_2$

		Neutron[136]			
		Ta	H11	H12	H13
Neutron	H11	1.769			
	H12	1.774			
	H13	1.776			
CCCP	H11	1.582	0.238	-	-
	H12	1.684	-	0.179	-
	H13	1.582	-	-	0.195

X-ray Diffraction Examples

i) $(\mu_2H)_2Os_3(CO)_9PH_3$

		X-ray[137]		
		Os1	Os2	Os3
CCCP	H	1.855	1.710	2.918
CCCP	H'	1.814	1.707	2.925

k) $(\mu_2H)HOs_3(CO)_{10}PH_3$ a model for $(\mu H)_2Os_3(CO)_9(PPh_3)$

		X-ray[138]			
		Os1	Os2	μH	H
X-ray	H	-	1.517	-	-
X-ray	μH	1.741	1.996	-	-
CCCP	H	-	1.569	0.131	-
CCCP	μH	1.645	1.720	-	0.339

l) $H_2Fe[(MeC)_2B_4H_4]_2$ This compound has exact two-fold symmetry.

		X-ray[139]	
		Fe	B
CCCP	H	1.543	1.4397

m) $(\mu_2H)Fe_3(CO)_9SC_6H_{11}$

		X-ray[140]			
		Fe1	Fe2	Fe3	μH
X-ray	μH	-	1.609	1.862	-
CCCP	μH	2.944	1.670	1.679	0.391

n) $(\mu_3H)_4Co_4(C_5H_5)_4$ This model was too complex (12 dimensional minimisation) to be exhaustively minimised. After 106 iterations starting from the diffraction determined hydride coordinates the program had produced the result below as the most stable.

		X-ray[141]			
		Co1	Co2	Co3	Co4
CCCP	H	-	1.642	1.638	1.617
	H2	1.709	-	1.698	1.673
	H3	1.641	1.646	-	1.620
	H4	1.626	1.632	1.642	-

		X-ray			
		H1	H2	H3	H4
CCCP	H	0	-	-	-

H2	-	0.126	-	-
H3	-	-	0.014	-
H4	-	-	-	0

6.5. Assessment of Results

The results are very encouraging. Although at first sight the absolute error in the coordinates, where neutron coordinates are available, is large (0.10-0.30Å) all true solutions are paralleled by at least local minima in the energy function. More important is the conclusion that relationships in the lengths of M-H bonds are reproduced by the CCCP program. For example in $H_3Rh_3(P(OMe)_3)_6$ the Rh-H bonds are in order of increasing length Rh2-H2 RH2-H1 RH2-H3 RH3-H6 RH3-H3 RH1-H1 The full range spans 0.10Å. The order given by CCCP is identical except for an interchange of the first two - which differ by only 0.02Å. The ability of the ASED method employed by the CCCP program to reproduce the asymmetry of most μ_2H bridges is further proven by an example ($[H_2Os_3(CO)_{10}CH_2]$) where the asymmetry has been determined by neutron diffraction to be very large : one μ_2H binds symmetrically (Δ=0.03Å) the other asymmetrically (Δ=0.13Å). The CCCP program gives differences of 0.00Å and 0.09Å respectively. This is the first advantage of CCCP over the HYDEX program.

The second advantage is that CCCP can be successfully used to identify clusters with interstitial hydrides. In the ions $[HRu_6(CO)_{18}]^-$ and $[HCo_6(CO)_{15}]^-$ the interstitial site is certainly a local minimum. In contrast for the ion $[HOs_6(CO)_{18}]^-$ the correct solution of a μ_3H capping an octahedral face is found very rapidly - even if the starting point is the interstitial site.

The third advantage of CCCP is demonstrated by the success of the program in finding a solution for compounds where the non-hydrogen framework around the metal atom is sparse. For example $[MoH_2(C_5H_5)_2]$, $[TaH_3(C_5H_5)_2]$ and $H_2Fe[(MeC)_2B_4H_4]_2$ as well as the previously discussed $H_3Rh_3(P(OMe)_3)_6$.

6.6. Proposed Improvements to the Program

The CCCP test program has confirmed the utility of combining Anderson's W_β function with EHMO to predict hydride atom positions. There are many more *X*-ray diffraction determined structures where the hydride position could be predicted using CCCP and many more neutron diffraction determined structures where the accuracy of CCCP could be tested. This has not yet been attempted. Before this task can be begun the CCCP must first be rewritten in order that it makes efficient use of computer resources. This rewriting should recognise that there is a large degree of repetition in calculating the wavefunction for a model in which only one or a few atoms have changed position. This task is left to others.

The minimisation method employed could be further improved by a combination of grid point evaluation, finite iteration, clustering and exhaustive simplex searching. Such an approach would be more reliable in producing the global minimum as the solution. Briefly the method is to begin with a series of regularly spaced points spanning the whole plausable domain. For a finite number of steps each grid point in turn is optimised using short steps. After all of the grid points have been processed the result is a set of points some of which are isolated but in which others form tracks in the variable coordinate space each converging on a local minimum. Cluster analysis identifies these tracks. Filtering (such as retaining only the best 50% of points) further sharpens these tracks to highlight the local minima. Lengthy iterations at each of these minima give precise function values for each. The final step is to rank these function values to determine the global minimum.

1. "Electron Distributions and the Chemical Bond", P.Coppens and M.B.Hall (Eds.), Plenum Press, New York (1982), 479 pages. Proceedings of a symposium on Electron Distributions and the Chemical Bond for the national meeting of the American Chemical Society held March 28-April 2, 1981 in Atlanta, Georgia.

2. *Israeli Journal Of Chemistry*, (1977), **16**. 29 articles by numerous authors, 229 pages.

3. "Proceedings of NATO Advanced Study Institute on Electronic and Magnetic Distributions in Molecules and Crystals, Arles", Plenum Press, New York.

4. "*X*-ray Analysis and the Structure of Molecules" J.D.Dunitz, Cornell Univ. Press Ltd., (1979). Chapter 8: 'Electron Density Distributions in Molecules', pp391-497.

5. ref 1 : 'Concepts of Charge Density Analysis, the Experimental Approach ', P.Coppens, pp61-92.

6. K.Angermund, K.Claus, R.Goddard and C.Kruger, *Angew.Chem.(Int.ed)*, (1985), **24**(4), 237-356.

7. P.Coppens, *Angew.Chem.(Int.Ed)*, (1977), **16**, 32.

8. F.Wudl, D.Nalewajek, J.M.Troup and M.W.Extine, *Science*, (1983) **222**, 415.

9. J.D.Dunitz, *Science*, (1985), **228**, 353-354.

10. International Tables For Crystallography, Volume IV, (1974), Kynoch Press, Birmingham, England.

11. R.F.Stewart, *J.Chem.Phys.*, (1970), **53**, 2070.

12. P.Coppens, T.N.Guru-Row, P.Leung, E.D.Stevens, P.J.Becker and Y.W.Yang, *Acta Crystallogr.*, (1979), **A35**, 63. or see ref 5 pp 66-67.

13. P.Coppens, D.Pautler and J.F.Griffin, *J.Amer.Chem.Soc.*, (1971), **93**, (5), 1051-1058.

14. P.Coppens, W.F.Cooper and F.K.Larsen, *Science*, (1972), **176**, 165-166.

15. C.A.Coulson, "Valence", Oxford Univ.Press, Oxford, (1961).

16. R.F.Stewart, *J.Chem.Phys.*, (1969), **51**, 4569.

17. B.Dawson, *Proc.Roy.Soc.(London)*, (1967), **A298**, 63.

18. see ref 2, F.L.Hirshfeld, pp226.

19. V.H.Smith, 'Concepts of Charge Density Analysis: The Theoretical Approach', ref 1, pp3-59.

20. R.F.Stewart, *J.Chem.Phys.*, (1969), **51**, 4569-4577.

21. C.A.Frishberg, L.J.Masa, M.J.Goldberg, ref 1, pp101-110; C.A.Frishberg and L.J.Masa, *Phys.Rev.B(Condensed Matter)*, (1981), **24**, (12), 7018-7024; *idem*, *Acta Crystallogr.*, (1982), **A38**, (1), 98-102; L.J.Masa, M.J.Goldberg, C.A.Frishberg, R.F.Boehme and S.J.LaPlaca, *Phys.Rev.Lett*, (1985), **55**, (6), 622-625.

22. H.Moissan and P.Williams, *C.R.Acad.Sci.*, (1897), **125**, 629.

23. I.R.Epstein and W.N.Lipscomb, *Inorg. Chem.*, (1971), **10**, (9), 1921-1928.

24. J.L.Boone, *J.Amer.Chem.Soc.*, (1964), **86**, 5036-5036.

25. R.Schaeffer, Q.Johnson and G.S.Smith, *Inorg. Chem.*, (1965), **4**, (6), 917-8.

26. P.Coppens, *Isr.J.Chem*, (1977), **16**, 144-148.

27. G.M.Sheldrick, (1976), SHELX76. Program for Crystal structure determination. Univ.Cambridge, England.

28. M.vonStackelberg and F.Neumann, *Zeit.Phys.Chem.*, (1932), **19**, 314-320.

29. F.L.Hirshfeld, *Isr.J.Chem.*, (1977), **16**, 226-229.

30. V.Schomaker, Program & Abstracts, Amer.Cryst.Assoc.Summer Meet., San Diego, (1982), Ca., 15-19 Aug, p21.

31. W.C.Hamilton, *Acta Crystallogr.*, (1965), **18**, 502-510.

32. F.L.Hirshfeld, *Acta Crystallogr.*, (1976), **A32**, 239-244.

33. R.E.Rosenfield, K.N.Trueblood and J.D.Dunitz, *Acta Crystallogr.*, (1978), **A34**, 828-829.

34. M.Aono, M.Ishii, S.Muranaka and S.Kawai, *Solid State Commun.*, (1976), **20**, 437-440.

35. Ya.I.Dutchak, Ya.I.Fedyshin, Yu.B.Paderno, D.I.Vadets and *Izv.Ucheb.Zaved.Fiz.*, (1973), **1**, 154-156. = *Soviet Physics Journal*, (1973), **16**, 133-136.

36. B.Rees, *Acta Crystallogr.*, (1976), **A32**, 483-488.

37. F.L.Hirshfeld, *Isr.J.Chem.*, (1977), **16**, 198-201.

38. "General Chemistry : An Introduction to Descriptive Chemistry and Modern Chemical Theory", L.Pauling. Published by W.H.Freeman, San Francisco, (1953)pp236.

39. F.L.Hirshfeld, *Theor.Chim.Acta*, (1977), **44**, 129-138.

40. S.Vega, *Isr.J.Chem.*, (1977), **16**, 213-219.

41. D.Schwarzenbach and N.Thong, *Acta Crystallogr.*, (1979), **A35**, 652-658.

42. R.F.Stewart, *Chem.Phys.Lett.*, (1977), **49**(2), 281-284.

43. N.Thong and D.Schwarzenbach, *Acta Crystallogr.*, (1979), **A35**, 658-664.

44. J.Lewis and D.Schwarzenbach, *Acta Crystallogr.*, (1981), **A37**, 507-510.

45. M.Aono and S.Kawai, *J.Phys.Chem.Solids*, (1979), **40**, 797-802.

46. R.E.J.Sears, *J.Chem.Phys.*, (1982), **76**, (11), 5651-5652.

47. T.Kushida, N.Laurance and A.H.Silver, *Bull.Amer.Chem.Soc.*, (1962), **7**, 226.

48. N.F.Ramsay, "Nuclear Moments", Wiley, New York (1953).

49. G.F.Mitchell 'TENSOR' a computer program to evaluate the electric field gradient from deformation density structure factors, Edinburgh, (1986).

50. G.F.Mitchell 'TENSNEB', a computer program to evaluate the electric field gradient due to promolecular charge density, Edinburgh, (1986).

51. V.R.Saunders, *Faraday Symp.Chem.Soc.*, (1984), **19**, 79-84.

52. G.F.Mitchell, 'MOSCOW', a computer program for the display of wavefunctions, electron density, deformation electron density, and Laplacian of electron density, Edinburgh(1986).

53. R.B.Helmholdt and A.Vos, *Acta Crystallogr.*, (1977), **A33**, 456-465.

54. H-L.Hase, H.Reitz and A.Schweig, *Chem.Phys.Lett.*, (1976), **39**, 157-159.

55. D.J.Fuller and D.L.Kepert, *Inorganic Chemistry*, (1982), **21**, 163-167.

56. C.E.Housecroft and K.Wade, *Inorganic Chemistry*, (1983), **22**, 1391-1393.

57. D.J.Fuller and D.L.Kepert, *Polyhedron*, (1983), **2**, 749-759.

58. PG.Perkins, J.J.P.Stewart and D.R.Armstrong , *J.Chem.Soc. Dalton Trans.*,(1975), **8**, 627-632.

59. PG.Perkins, D.R.Armstrong and A.Breeze, *J.Physics C*, (1975), **8**, 3558.

60. G.Moss in 'Electron Distributions and the Chemical Bond', (ref. 1) pp383-411.

61. I.G.Czismadia, "Theory and Practice of MO Calculations", Elsevier, (1976), pp257.

62. D.Schwarzenbach, J.Lewis in 'Electron Distributions and the Chemical Bond' (ref. 1) pp 413-429.

63. H.C.Longuet-Higgins and M.deV.Roberts, *Proc.Roy.Soc.*, (1954), **224**, 336.

64. S.Flodmark, *Arkiv fur Fysik*, (1959), **14**, 513-550.

65. J.Etourneau, J-P.Mercurio, R.Naslain and P.Hagenmuller, *J.Solid State Chem.*, (1976), **2**, 332-342.

66. V.G.Aleshin, T.Ya.Kosolapova, V.V.Nemoshkalenko, T.I.Serebryakova and N.G.Chudinov, *J.Less Common Metals*, (1979), **67**(1), 173-177.

67. M.Aono, S.Kawai, S.Kono, M.Okusawa, T.Sagawa and T.Takehana, *J.Phys.Chem.*, (1976), **37**, 215-219.

68. M.Yamazaki, *J.Phys. Soc. Japan*, (1957), **12**, 1.

69. G.Shoham, D.Schomburg and W.N.Lipscomb, *Cryst.Struct.Commun.*, (1980), **9**, 429.

70. K.A.Solntsev, N.T.Kuznetsov and V.I.Ponomarev, *Dokl.Akad.Nauk SSSR*, (1976), **228**, (4), 853.

71. S.I.Uspenskaya, K.A.Solntsev and N.T.Kuznetsov, *Zhurnal Strukturnoii Khimii*, (1975), **16**, (3), 482-484.

72. K.A.Solntsev, N.T.Kuznetsov and V.I.Ponomarev, *Izvest.Akad.Nauk SSSR Ser. Neorg. Materialy*, (1972), **12**, (6), 1044-1047.

73. K.A.Solntsev, N.T.Kuznetsov, N.V. Raneev and V.E.Zavodnik, *Dokl.Akad.Nauk SSSR*, (1977), **232**, (6), 1366.

74. Z.Cai, K.Pan and L.Zhang, *Jiegou Huaxue*, (1984), **3**, (3),

231-234.

75. K.A.Solntsev, N.T.Kuznetsov, V.K.Trunov, O.G.Karpinsky, G.S.Klimchuk, S.I.Uspenskaya and Yu.V.Oboznenko, *Zhurnal Neorg.Khim.*, (1977), **22**, 3200-7.

76. F.L.Hirshfeld and H.Hope, *Acta Crystallogr.*, (1980), **B36**, 406-415.

77. M.Harel and F.L.Hirshfeld, *Acta Crystallogr.*, (1975), **B31**, 162-172.

78. E.D.Stevens and H.Hope, *Acta Crystallogr.*, (1977), **A33**, 723-729.

79. E.D.Stevens and H.Hope, *Acta Crystallogr.*, (1977), **A31**, 494-498.

80. H.G.Miller and E.L.Muetterties, *Inorganic Syntheses*, (1967), **10**, 81.

81. F.R.Scholer and L.J.Todd in *Preparative Inorganic Chemistry*, W.L.Jolly (Ed.), Wiley-Interscience (Publ.), (1971), *7*, chapter 1: "Polyhedral Boranes and Heteroatom Boranes", pp13-14.

82. G.F.Mitchell and A.J.Welch, *Acta Crystallogr.*, (1986), **C42**, 101-103.

83. A.E.Dwight and C.W.Kimball, *Acta Crystallogr.*, (1974), **B30**, 2791.

84. K.Kitihama, H.Kiriyama and Y.Baba, *Bull.Chem.Soc.Japan*, (1979), **52**, 324.

85. Y.Higama, L.G.Butler and T.L.Brown, *J.Magn.Reson.*, (1975), **60**, 472-480.

86. R.Brill, H.Dietrich and H.Dierks, *Acta Crystallogr.*, (1971), **B27**, 2003.

87. A.J.Leffler, *J.Chem.Phys.*, (1984), **81**, (6), 2574.

88. R.K.Bohn and M.D.Bohn, *Inorg.Chem.*, (1971), **10**, 350.

89. L.V.Vilkov, V.S.Mastryukov, A.F.Zhigach and V.N.Siryatskaya, *Zhurnal Struktur.Khim.*, (1966), **7**, 5.

90. *idem*, *ibid*, (1969), **10**, 136.

91. K.-R.Tsai, P.M.Harris and E.N.Lasettre, *J.Phys.Chem*, (1956), **60**, 338-344.

92. S.Huzinaga (Ed.) "Gaussian Basis Sets for Molecular Calculations", Elsevier, (1976), Amsterdam.

93. R.A.Beaudet and R.L.Poynter, *J.Chem.Phys.*, (1965), **43**, 2166.

94. E.A.McNeil and F.R.Scholer, *J.Mol.Struct.*, (1975), **27**, 151-159.

95. T.Ito and I.Higashi, *Acta Crystallogr.*, (1983), **B39**, 239-243.

96. T.Ito, I.Higashi and T.Sakurai, *J.Solid State Chem.*, (1979), **28**, 171-184.

97. R.Brill, H.Dietrich and H.Dierks, *Acta Crystallogr.*, (1971), **B27**, 2003.

98. H.Dietrich and C.Scheringer, *Acta Crystallogr.*, (1978), **B34**, 54-63.

99. E.A.Laws, R.M.Stevens and W.N.Lipscomb, *J.Amer.Chem.Soc.*, (1972), **94**, 4467-4474.

100. J.Evans, *J.Chem.Soc. Dalton Trans.*, (1978), 25.

101. P.Brint, E.F.Healey, T.R.Spalding and T.Whelan, *J.Chem.Soc. Dalton Trans.*, (1981), 2515.

102. M.A.Cavenaugh, T.P.Fehlner, R.Stramel, M.E.O'Neil and K.Wade, *Polyhedron*, (1985), **4**, 687-695.

103. I.Yu.Kuznetsov, D.M.Vinitskii, K.A.Solntsev, N.T.Kuznetsov and L.A.Butman, *Dokl.Akad.Nauk SSSR*, (1985), **287**, (4), 873-7.

104. C.R.Peters and C.E.Nordmann, *J.Amer.Chem.Soc.*, (1960), **82**, 5758.

105. F.Zhuji, P.Kezhen, L.Jiaxi, Z.Guomin and Z.Hong, *J.Struct.Chem.*, (1982), **1**, 57-2.

106. I.M.Pepperburg, D.A.Dixon, W.N.Lipscomb and T.A.Halgren, *Inorg.Chem.*, (1978), **17**, 587.

107. T.A.Halgren, L.D.Brown, D.A.Klier and W.N.Lipscomb, *J.Amer.Chem.Soc.*, (1977), **99**, 6793.

108. S.J.Andrews and A.J.Welch, *Inorg.Chim.Acta*, (1984), **88**, 153-160.

109. J.C.Calabrese, D.F.Davies, S.J.Hildebrandt and J.H.Morris, *J.Amer.Chem.Soc.*, (1976), **98**, (4), 5489.

110. S.J.Lippard and K.M.Melmed, *Inorg. Chem.*, (1969), **8**, 2755.

111. Yu.Wang, M.J.Chen and C.H.Wu, *Acta Crystallogr.*, (1988), **B44**, 179-182.

112. Y.Wang, K.Angermund, K.Goddard and C.Kruger,

J.Amer.Chem.Soc., (1987), **109**, 587-589.

113. E.Amberger and E. Gut, *Chem.Ber.*, (1968), **101**, 1200.

114. A.M.O'Connell, A.I.M.Rae and E.N.Maslen, *Acta Crystallogr.*, (1966), **21**, 208.

115. R.F.W.Bader, P.J.MacDougall and C.D.H.Lau, *J.Amer.Chem.Soc.*, (1984), **106**, 1594- 1605.

116. D.Cremer and E.Krafka, *J.Amer.Chem.Soc.*, (1985), **107**, 3800-3810.

117. M.Benard, P.Coppens and J.Muller, *J.Solid State Comm.*, (1976), **19**, 29.

118. J.D.Dunitz and P.Seiler, *J.Amer.Chem.Soc.*, (1983), **105**, 7056-7058.

119. G.F.Mitchell and A.J.Welch, *J.Chem.Soc Dalton Trans.*, (1987), 1017-1025 (Appendix VI).

120. C.J.Fritchie, *Inorg.Chem*, (1967), **6**, 1199.

121. B.F.G.Johnson, J.Lewis, P.R.Raithby, G.M.Sheldrick and G.Suss, *J.Organomet.Chem.*, (1978), **162**, 179.

122. M.R.Churchill in "Transition Metal Hydrides", ed R.Bau, Adv. Chem.Ser., American Chemical Society, (1978), **167**, pp38-39.

123. M.R.Churchill, P.H.Bird. H.D.Kaesz, R.Bau and B.Fontal, *J.Amer.Chem.Soc.*, (1968), **90**, 7135.

124. A.G.Orpen, *J.Chem.Soc. Dalton Trans.*, (1980), 2509-2516.

125. N.Pavel, C.Quagliata and N.Scarcelli, *Z.Krist.*, (1976), **144**, 64.

126. A.B.Anderson and R.Hoffmann *J.Chem.Phys*, (1974), **60**, 4271-4273.

127. J.Howell, A.Rossi, D.Wallace, K.Haraki and R.Hoffmann, "ICON", Quantum Chemistry Program Exchange, University of Indiana, (1977), No. 344.

128. S.J.LaPlaca, W.C.Hamilton, J.A.Ibers and A.Davison, *Inorg.Chem.*, (1969), **8**, 1928.

129. A.G.Orpen, A.V.Rivera, E.G.Bryan, D.Pippard, G.M.Sheldrick and K.D.Rouse, *J.Chem.Soc. Chem.Comm.*, (1978), 723; R.W.Broach and J.H.Williams, *Inorg. Chem.*, (1979), **18**, 314.

130. R.K.Brown, J.M.Williams, A.J.Sivak and E.L.Muetterties, *Inorg.Chem*, (1980), **19**, 370.

131. A.J.Shultz, J.M.Williams, R.B.Calvert, J.R.Shapley and G.D.Stucky, *Inorg.Chem*, (1979), **18**, 319.

132. A.J.Shultz, K.L.Stearley, J.M.Williams, R.Mink and G.D.Stucky, *Inorg.Chem.*, (1977), **16**, 3303.

133. a) C.R.Eady, P.F.Jackson, B.F.G.Johnson, J.lewis, M.C.Malatesta, M. McPartlin and W.J.H.Nelson, *J.Chem.Soc. Dalton.Trans.*, (1980), 383. b) P.F.Jackson, B.F.G.Johnson, J.Lewis, P.R.Raithby, M.McPartlin, W.J.H.Nelson, K.D.Rouse, J.Allibon and S.A.Mason, *J.Chem.Soc., Chem.Comm.*, (1980), 295. c) C.R.Eady, B.F.G.Johnson, J.Lewis, M.C.Malatesta, P.Machin and M.McPartlin, *idem*, , (1976), 945.

134. M.McPartlin, C.R.Eady, B.F.G.Johnson and J.Lewis, *J.Chem.Soc. Chem.Comm*, (1976), 883.

135. a) D.W.Hart, R.G.Teller, C.Y.Wei, R.Bau, G.Longoni, S.Campanella, P.Chini and T.F.Koetzle, *Angew.Chem.Int.Edn.* (1979), **18**, 80. b) D.W.Hart, R.G.Teller, C.-Y.Wei, R.Bau, G.Longoni, S.Campanella, P.Chini and T.F.Koetzle, *J.Amer.Chem.Soc.*, (1981), **103**, 1458.

136. R.D.Wilson, T.F.Koetzle, D.W.Hart, A.Kvick, D.L.Tipton and R.Bau, *J.Amer.Chem.Soc.*, (1977), **99**, 1775.

137. R.E.Benfield, B.F.G.Johnson, J.Lewis, P.R.Raithby, C.Zuccaro and K.Henrick, *Acta Crystallogr., Sect.B*, (1979), **35**, 2210.

138. M.R.Churchill and B.G.DeBoer, *Inorg.Chem.*, (1977), **16**, 2397.

139. J.R.Pipal and R.N.Grimes, *Inorg.Chem.*, (1979), **18**, 263.

140. A.Winter, L.Zsolnai and G.Huttner, *Chem.Ber.*, (1982), **115**, 1286.

141. G.Huttner and H.Lorenz, *Chem.Ber.*, (1975), **108**, 973.

Apppendix II Glossary

Items marked † are taken from reference 1.

Asphericity shift† The difference between the atomic positions derived by least-squares refinement of *X*-ray data using the free-atom model and the unbiased position from, for example, neutron diffraction or refinement of very high order *X*-ray data.

Deformation density† The difference between the total electron density and the promolecule or procrystal density. Sometimes this is referred to as the "non-perfectly following density".

Dynamic <Deformation> Density† The <deformation> charge density smeared by the vibrational motions of the atoms in the crystal.

High-order data† The *X*-ray diffraction data measured above a value of $\sin\theta/\lambda$ at which the contribution of valence electron scattering is estimated to be small.

Hirshfeld refinement† Least-squares refinement of all structural parameters, exponents and population parameters of Hirshfeld-type $r^n\cos^n\theta_k\exp(-\varepsilon r)$ functions on all atoms.

Kappa parameter† A factor multiplying the radial coordinate of the atomic valence density, allowing expansion or contraction of the valence shell with variation of atomic charge.

Kappa refinement† Least-sqares refinement of all structural parameters, kappa, and spherical valence shell population parameters on all atoms.

Multipole Deformation Map† The difference between the total charge density calculated using the multipole model parameters and the charge density calculated from Hartree-Fock atomic *X*-ray form factors and multipole model positional and thermal parameters.

Multipole refinement† Least-sqares refinement of all structural parameters, kappa, spherical valence shell population parameters, and multipole population parameters on all atoms.

Procrystal density† - as for promolecule density but the superposition of spherical free atoms at their position s in the crystal.

Promolecule density† The charge density prior to the formation of bonds ie the superposition of the spherical free-atoms each centred at its position in the molecule.

Pseudoatom† All the charge density described by functions centred at the position of the nucleus.

Pseudomolecule† All the charge dnsity attributed to the pseudoatoms which constitute the molecule.

Residual Map† The difference between the total charge density and the charge density calculated with the scattering factors and paramaters of a least-sqares refinement, ie the remnant of the density not decribed by the refinement model.

Static <Deformation> Density† The <deformation> charge density of an atom, promolecule or molecule at rest.

Stockholder formula/concept† A way of partitioning the charge density such that each atom is assigned a fraction of the charge at a point in the crystal proportional to its contribution to the procrystal density at that point.

Valence density† The difference between the total electron density and the the superposition of free-atom atomic core densities.

X–N Map† The difference between the experimental total charge density and the charge density calculated from Hartree-Fock atomic *X*-ray form factors and neutron-diffraction determined positional and thermal parameters.

X–X Map† The difference between the experimental total charge density and the charge density calculated from Hartree-Fock atomic *X*-ray form factors and high order *X*-ray diffraction determined positional and thermal parameters.

Apppendix III Parameters used in *Ab-initio* Calculations

The program employed the General and Molecular Electronic Structure System (GAMESS).

MAXCYC maximum number of SCF cycles.
the default of 50 was used.

THRESHOLD : The maximum difference in density matrix elements below which convergence is assumed. The default of 10^{-5} was used.

LEVEL : The defaults of an occupied-virtual shifter of 1.0 applied for 5 iterations followed by a occupied-virtual shifter of 0.3 were used.

Apppendix IV Model Coordinates for Chapter 2

Model I

```
   (B6H5.)2  4- CHG , 4(X++)
   Net model charge = 0

z-matrix construction :
B
B    1   RBB
B    2   RBB   1   90.0
B    3   RBB   2   90.0   1    0.0   0
B    2   RBB   1   60.0   3   60.0  -1
B    4   RBB   1   60.0   3   60.0  -1
H    2   RBH   3  135.0   4  180.0   0
H    3   RBH   2  135.0   1  180.0   0
H    4   RBH   3  135.0   2  180.0   0
H    5   RBH   1  135.0   6  180.0   0
H    6   RBH   1  135.0   5  180.0   0
B    1   ROO   2  135.0   3  180.0   0
B   12   RBB   1  135.0   9    0.0   0
B   13   RBB  12   90.0   1  180.0   0
B   14   RBB  13   90.0  12    0.0   0
B   15   RBB  14   60.0  12   60.0  -1
B   13   RBB  14   60.0  12   60.0  -1
H   13   RBH  12  135.0   1    0.0   0
H   14   RBH  13  135.0  12  180.0   0
H   15   RBH  14  135.0  13  180.0   0
H   16   RBH  15  135.0  17  180.0   0
H   17   RBH  15  135.0  16  180.0   0
VARIABLES
RBB   1.7500
RBH   1.167183
ROO   1.6668
COORDINATES FOR POINT CHARGES
BQCA -2.0536056  2.0711  0.875          2.0
BQCA -2.0536056 -2.0711  0.875          2.0
BQCA  0.875      2.0711 -2.0536056      2.0
BQCA  0.875     -2.0711 -2.0536056      2.0
```

Model II

```
   (B6H5.)2  4- CHG , EXTENDED XTAL FIELD 24(X++),22(X--)
   Net model charge = 0

z-matrix construction :
-as for model I above

Variables :
-as for model I above

COORDINATES for point charges :
BQCA -2.0536056  2.0711  0.875          2.0
```

```
BQCA -2.0536056 -2.0711  0.875          2.0
BQCA  0.875      2.0711 -2.0536056      2.0
BQCA  0.875     -2.0711 -2.0536056      2.0
BQCA  3.804350   2.0711  0.875          2.0
BQCA  3.804350  -2.0711  0.875          2.0
BQCA  0.875      2.0711  3.804350       2.0
BQCA  0.875     -2.0711  3.804350       2.0
BQCA -2.0536056  2.0711 -4.9829554      2.0
BQCA -2.0536056 -2.0711 -4.9829554      2.0
BQCA -4.9829554  2.0711 -2.0536056      2.0
BQCA -4.9829554 -2.0711 -2.0536056      2.0
BQCA -4.9829554  2.0711  3.804350       2.0
BQCA -4.9829554 -2.0711  3.804350       2.0
BQCA  3.804350   2.0711 -4.9829554      2.0
BQCA  3.804350  -2.0711 -4.9829554      2.0
BQCA -2.0536056  6.2133  0.875          2.0
BQCA -2.0536056 -6.2133  0.875          2.0
BQCA  0.875      6.2133 -2.0536056      2.0
BQCA  0.875     -6.2133 -2.0536056      2.0
BQCA -4.9829554  6.2133  3.804350       2.0
BQCA -4.9829554 -6.2133  3.804350       2.0
BQCA  3.804350   6.2133 -4.9829554      2.0
BQCA  3.804350  -6.2133 -4.9829554      2.0
BQOX  0.875      4.1422  0.875         -2.0
BQOX  0.875     -4.1422  0.875         -2.0
BQOX -2.0536056  4.1422 -2.0536056     -2.0
BQOX -2.0536056 -4.1422 -2.0536056     -2.0
BQOX  3.804350   4.1422 -2.0536056     -2.0
BQOX  3.804350  -4.1422 -2.0536056     -2.0
BQOX -2.0536056  4.1422  3.804350      -2.0
BQOX -2.0536056 -4.1422  3.804350      -2.0
BQOX  0.875      4.1422 -4.9829554     -2.0
BQOX  0.875     -4.1422 -4.9829554     -2.0
BQOX -4.9829554  4.1422  0.875         -2.0
BQOX -4.9829554 -4.1422  0.875         -2.0
BQOX  3.804350   4.1422  3.804350      -2.0
BQOX  3.804350  -4.1422  3.804350      -2.0
BQOX -4.9829554  4.1422 -4.9829554     -2.0
BQOX -4.9829554 -4.1422 -4.9829554     -2.0
BQOX  3.804350   0.0000 -2.0536056     -2.0
BQOX -2.0536056  0.0000  3.804350      -2.0
BQOX  0.875      0.0000 -4.9829554     -2.0
BQOX -4.9829554  0.0000  0.875         -2.0
BQOX  3.804350   0.0000  3.804350      -2.0
BQOX -4.9829554  0.0000 -4.9829554     -2.0
```

Model III

```
   B6H6   EXTENDED XTAL FIELD 24(X++),23(X--)
   NET MODEL CHARGE = 00
z-matrix construction :

B
B     1   RBB
```

```
B      2    RBB    1    90.0
B      3    RBB    2    90.0    1     0.0    0
B      2    RBB    1    60.0    3    60.0   -1
B      4    RBB    1    60.0    3    60.0   -1
H      2    RBH    3   135.0    4   180.0    0
H      3    RBH    2   135.0    1   180.0    0
H      4    RBH    3   135.0    2   180.0    0
H      5    RBH    1   135.0    6   180.0    0
H      6    RBH    1   135.0    5   180.0    0
H      1    RBH    2   135.0    3   180.0    0
```

Coordinates of point charges:
-as for model II but with the extra point anion below

```
BQOX -2.0536056  0.0000   3.804350     -2.0
```

Parameters RBB and RBH as for Models I and II

Model IV

```
   B6H6   EXTENDED XTAL FIELD 24(X++),23(X--)
   NET MODEL CHARGE = 00
```

- as for Model III but with the following parameter values:

```
VARIABLES
RBB    1.690
RBH    1.167183
```

Apppendix V Models of $[B_3H_8]^-$ used in Chapter 4)

```
CHARGE -1
ZMAT ANGSTROM
B
B      1      R12
B      1      R12     2     A312
H      1      R14     2     A412     3      A412    1
H      1      R14     3     A412     2      A412    1
H      2      R62     3     A623     1      T6231
H      3      R62     2     A623     1      T6231
H      2      R62     3     A623     7       0.0
H      3      R62     2     A623     6       0.0
H      1      RMU     2     AM12     3       180.
H      1      RMU     3     AM12     2       180.
Values of Variables for the EXPT geometry
R12   1.782
R14   1.08
R62   1.14
RMU   1.415
A312  61.2
A412  114.
A623  109.47
AM12  40.2
T6231 114.
END
Values of Variables for the SVOPT (OPTIMISED) geometry
R12   1.810
R14   1.20
R62   1.20
RMU   1.577
A312  64.1
A412  117.
A623  106.3
AM12  42.7
T6231 118.
END
```

Apppendix VI Reprint of Acta Cryst. Paper

Acta Cryst. (1986). C42, 101–103

The Structure of Tetramethylammonium Undecahydro(triethylamine)-[I_h-(1551)-Δ^{20}-*closo*]dodecaborate(1−)*

By Gary F. Mitchell and Alan J. Welch

Department of Chemistry, University of Edinburgh, Edinburgh EH9 3JJ, Scotland

(*Received* 16 *July* 1985; *accepted* 27 *September* 1985)

Abstract. $C_4H_{12}N^+.C_6H_{26}B_{12}N^-$, $M_r = 316{\cdot}15$, monoclinic, $P2_1/c$, $a = 10{\cdot}620\,(4)$, $b = 14{\cdot}558\,(5)$, $c = 13{\cdot}244\,(4)$ Å, $\beta = 90{\cdot}40\,(3)°$, $U = 2047{\cdot}6$ Å^3, $Z = 4$ ion pairs, $D_x = 1{\cdot}025$ Mg m^{-3}, Mo $K\alpha$, $\lambda = 0{\cdot}71093$ Å, $\mu = 0{\cdot}047$ mm^{-1}, $F(000) = 688$, $T = 295$ K, final $R = 0{\cdot}0695$ for 965 observed reflections. $[NMe_4][Et_3NB_{12}H_{11}]$ forms as well separated ion pairs. In the anion the B_{12} fragment is not significantly distorted from an icosahedral geometry, and the B—N bond length, 1·632 (11) Å, compares favourably with that found in the previously studied potassium salt. The B_{12} framework is less distorted than that in the potassium salt.

Introduction. There has recently been some controversy concerning the relative importance of radial (cross-polyhedral) *versus* tangential B—B bonding in the series of *closo*-borane dianions $[B_nH_n]^{2-}$ (Fuller & Keppert, 1984; Housecroft & Wade, 1983). One potential method of quantifying the electron densities associated with these two kinds of interaction is through a series of deformation density studies.

In attempting to synthesize $[NMe_4]_2[B_{12}H_{12}]$ for this purpose we have serendipitously isolated a small amount of the compound $[NMe_4][Et_3NB_{12}H_{11}]$, characterized by the single-crystal X-ray diffraction study described herein. Shortly after completion of this work we became aware that the synthesis of $[NMe_4][Et_3NB_{12}H_{11}]$ had previously been reported, as had a crystallographic study of the potassium salt (Agafonov, Butman, Solntsev, Vinokurov, Zhukova & Kuznetsov, 1982).

Experimental. To the solid product of an attempted synthesis of $[HNEt_3]_2[B_{12}H_{12}]$, prepared according to Miller & Muetterties (1967) but at somewhat reduced temperature (448 K), was added, dropwise, 0·2*M* NaOH with constant boiling. The resulting solution was cooled to room temperature, and an excess of aqueous $[NMe_4]Cl$ was added. On cooling to 276 K colourless crystals were deposited, which were collected, washed with cold water and recrystallized by slow evaporation of a solution in 2-methoxyethanol:water, 1:1. Clear colourless blocks, 0·03 × 0·02 × 0·02 cm, mounted on a glass fibre; preliminary Weissenberg photography; CAD-4 diffractometer; lattice parameters from 25 centred reflections, $9 < \theta < 12°$; graphite-monochromated Mo $K\alpha$; for data collection $\theta_{max} = 20°$; ω–2θ scan in 96 steps; ω-scan width $(0{\cdot}8 + 0{\cdot}35\tan\theta)°$, rapid prescan, following which reflections with $I \geq 0{\cdot}33\sigma(I)$ remeasured such that final net intensity had $I \geq 50\sigma(I)$, subject to a maximum measuring time of 100 s; no significant crystal movement or decay; 2039 data measured (h 0→10, k 0→14, l −12→12) over *ca* 53 h. X-ray exposure yielding 1902 unique data on merging ($R_{int} = 0{\cdot}0361$); for structure solution and refinement 967 amplitudes used $[F \geq 2{\cdot}0\sigma(F)]$; automatic direct methods (Sheldrick, 1984) and iterative refinement/ΔF syntheses (Sheldrick, 1976); full-matrix least squares (F); $w^{-1} = [\sigma^2(F) + 0{\cdot}00268(F)^2]$; anisotropic thermal parameters for all non-H atoms; borane H atoms located from ΔF synthesis and positionally refined; methylene H atoms set in idealized positions, allowed to ride on respective C atoms; methyl functions treated as rigid groups allowed full rotation about C atom pivots, with chemical sense of resulting C—C—H angles checked; all

---

* Nomenclature according to Casey, Evans & Powell (1983).

0108-2701/86/010101-03$01.50

Table 1. *Fractional coordinates of refined atoms with standard deviations*

$$U_{eq} = \tfrac{1}{3}\sum_i\sum_j U_{ij}a_i^*a_j^*\mathbf{a}_i.\mathbf{a}_j.$$

	x	y	z	U_{eq}(Å^2)
N(1)	0·7542 (6)	0·4135 (4)	0·1496 (5)	0·0459
C(11)	0·8688 (7)	0·3897 (5)	0·0908 (6)	0·0523
C(12)	0·6439 (7)	0·3615 (6)	0·1070 (8)	0·0710
C(13)	0·7290 (8)	0·5138 (5)	0·1430 (7)	0·0663
C(14)	0·7758 (8)	0·3870 (6)	0·2573 (6)	0·0659
N(2)	0·7255 (6)	0·6456 (4)	0·5476 (4)	0·0397
C(21)	0·5905 (8)	0·6685 (6)	0·5202 (7)	0·0617
C(22)	0·5177 (9)	0·7229 (6)	0·5992 (7)	0·0759
C(31)	0·7824 (8)	0·6085 (5)	0·4500 (6)	0·0538
C(32)	0·7816 (9)	0·6743 (7)	0·3600 (7)	0·0780
C(41)	0·7928 (8)	0·7132 (5)	0·5779 (6)	0·0548
C(42)	0·9350 (8)	0·7334 (7)	0·5682 (8)	0·0851
B(1)	0·7354 (8)	0·5666 (6)	0·6348 (7)	0·0374
B(2)	0·6013 (9)	0·5059 (6)	0·6781 (8)	0·0453
B(3)	0·6846 (8)	0·5815 (7)	0·7593 (7)	0·0427
B(4)	0·8459 (9)	0·5710 (7)	0·7343 (8)	0·0519
B(5)	0·8659 (9)	0·4905 (7)	0·6388 (8)	0·0498
B(6)	0·7129 (9)	0·4502 (6)	0·6019 (7)	0·0469
B(7)	0·6313 (9)	0·4754 (7)	0·8047 (8)	0·0466
B(8)	0·7819 (9)	0·5157 (6)	0·8395 (8)	0·0493
B(9)	0·8924 (8)	0·4588 (6)	0·7653 (8)	0·0478
B(10)	0·8121 (9)	0·3824 (6)	0·6832 (8)	0·0534
B(11)	0·6486 (10)	0·3952 (7)	0·7072 (8)	0·0537
B(12)	0·7587 (8)	0·3976 (7)	0·8085 (8)	0·0504
H(2B)	0·500 (5)	0·522 (4)	0·645 (4)	
H(3B)	0·649 (5)	0·648 (4)	0·785 (4)	
H(4B)	0·905 (5)	0·635 (4)	0·747 (4)	
H(5B)	0·933 (5)	0·497 (4)	0·584 (5)	
H(6B)	0·686 (5)	0·423 (4)	0·532 (5)	
H(7B)	0·567 (5)	0·470 (4)	0·868 (4)	
H(8B)	0·815 (5)	0·539 (4)	0·917 (4)	
H(9B)	0·998 (5)	0·442 (4)	0·792 (4)	
H(10B)	0·870 (5)	0·319 (4)	0·660 (4)	
H(11B)	0·584 (5)	0·338 (4)	0·710 (4)	
H(12B)	0·765 (5)	0·349 (4)	0·868 (4)	

C–H distances 1·08 Å; $U_H{}^* = 0·03828$ Å^2 (BH), 0·10191 Å^2 (NMe_4), 0·07802 Å^2 ($C\underline{H}_2CH_3$) and 0·11726 Å^2 ($CH_2C\underline{H}_3$); max. Δ/σ in final cycle 0·056; max. peak and min. trough in final ΔF synthesis 0·2131 and −0·2304 e Å^{-3}; goodness-of-fit parameter 0·985; neutral-atom scattering factors for C, N, B and H inlaid in *SHELX*76; computer programs: *SHELX*76 (Sheldrick, 1976), *SHELX*84 (Sheldrick, 1984), *CALC* (Gould & Taylor, 1983) and *ORTEP*II (Johnson, 1976).

Discussion. Table 1 lists fractional coordinates of refined atoms, and Fig. 1 illustrates a perspective view of the zwitterionic anion $[Et_3NB_{12}H_{11}]^-$. In Table 2 are contained interatomic distances.†

The crystallographic analysis reveals the species to be the salt $[NMe_4][Et_3NB_{12}H_{11}]$. It is probable that the $[Et_3NB_{12}H_{11}]^-$ ion is formed (as its $[HNEt_3]^+$ salt) as a minor impurity in the preparation of $[HNEt_3]_2[B_{12}H_{12}]$ from $B_{10}H_{14}$ and Et_3NBH_3, since a temperature of only 448 K was used and it has been suggested (Agafonov *et al.*, 1982) that the predissociation of Et_3NBH_3 is incomplete below 463 K.

Distances and angles within the $[Et_3NB_{12}H_{11}]^-$ anion studied herein are in broad agreement with those reported for the potassium salt. Thus, there is no systematic variation in B–B lengths involving the boron atom, B(1), that carries the NEt_3 substituent compared with those that do not. The B–N bond lengths in the K^+ and $[NMe_4]^+$ salts are identical, 1·646 (13) and 1·635 (12) Å (two independent ion pairs in the asymmetric unit) *versus* 1·632 (11) Å respectively. All these distances are marginally longer than that, 1·600 (4) Å, in *arachno*-9-Et_3N-6-SB_9H_{11} (Hilty & Rudolph, 1979), probably a consequence of the greater coordination number of B in the icosahedron. Moreover, the

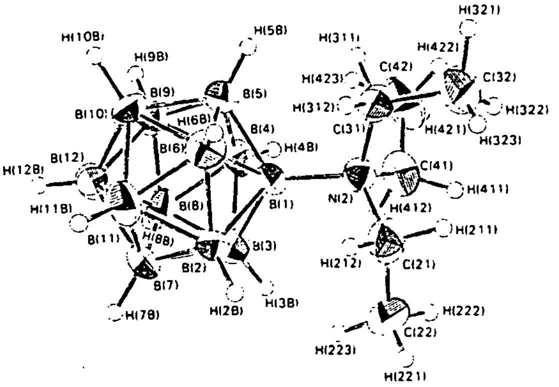

Fig. 1. View of the $[Et_3NB_{12}H_{11}]^-$ anion as its NMe_4^+ salt. Thermal ellipsoids are drawn at the 50% level, except for H atoms (radius 0·1 Å).

Table 2. *Interatomic distances* (Å)

N(1) C(11)	1·490 (10)	B(4)–B(8)	1·751 (14)
N(1) C(12)	1·502 (11)	B(4) B(9)	1·754 (14)
N(1) C(13)	1·488 (11)	B(4)–H(4B)	1·13 (6)
N(1) C(14)	1·494 (11)	B(5)–B(6)	1·793 (14)
N(2) C(21)	1·515 (10)	B(5) B(9)	1·759 (14)
N(2) C(31)	1·529 (10)	B(5) B(10)	1·776 (14)
N(2) C(41)	1·515 (10)	B(5)–H(5B)	1·03 (6)
N(2) B(1)	1·632 (11)	B(6) B(10)	1·796 (14)
C(21) C(22)	1·527 (12)	B(6)–B(11)	1·750 (14)
C(31) C(32)	1·530 (12)	B(6)–H(6B)	1·04 (6)
C(41) C(42)	1·516 (12)	B(7)–B(8)	1·762 (14)
B(1) B(2)	1·775 (13)	B(7)–B(11)	1·750 (14)
B(1) B(3)	1·752 (13)	B(7)–B(12)	1·765 (14)
B(1) B(4)	1·759 (13)	B(7)–H(7B)	1·09 (6)
B(1) B(5)	1·774 (13)	B(8)–B(9)	1·745 (14)
B(1) B(6)	1·766 (13)	B(8)–B(12)	1·784 (14)
B(2) B(3)	1·771 (13)	B(8)–H(8B)	1·13 (6)
B(2) B(6)	1·760 (14)	B(9)–B(10)	1·771 (14)
B(2) B(7)	1·760 (13)	B(9) B(12)	1·774 (14)
B(2) B(11)	1·730 (14)	B(9) H(9B)	1·20 (6)
B(2) H(2B)	1·18 (6)	B(10) B(11)	1·777 (14)
B(3) B(4)	1·754 (14)	B(10) B(12)	1·772 (14)
B(3) B(7)	1·753 (13)	B(10) H(10B)	1·15 (6)
B(3) B(8)	1·760 (14)	B(11) B(12)	1·774 (14)
B(3) H(3B)	1·10 (6)	B(12) H(12B)	1·05 (6)
B(4) B(5)	1·738 (14)		

---

* The isotropic temperature factor defined as exp $\{-8\pi^2U(\sin^2\theta)/\lambda^2\}$.

† Lists of structure factors, anisotropic thermal parameters, calculated H-atom coordinates, interbond angles and a packing diagram have been deposited with the British Library Lending Division as Supplementary Publication No. SUP 42536 (13 pp.). Copies may be obtained through The Executive Secretary, International Union of Crystallography, 5 Abbey Square, Chester CH1 2HU, England.

conformation of the pendant NEt_1 function in the $[NMe_4]^+$ salt, defined by the three B(1)–N(2)–C(*i*1)–C(*i*2) torsion angles, 73·4 (9), 176·2 (9) and 81·9 (10)° (i = 1–3), closely corresponds to one of the two distinct conformations observed in the K^+ salt.

There is, however, slight indication that the icosahedral B_{12} framework of the $[NMe_4]^+$ salt is somewhat less distorted. Thus, the range of B–B connectivity lengths determined herein is 1·738 (14)–1·796 (14) Å, *c.f.* 1·74–1·83 Å for the K^+ salt. This may be a consequence of the weaker polarizing power of the quarternary ammonium cation *versus* the group I*A* cation, and is consistent with less observed distortion in $[HNEt_3]_2[B_{12}H_{12}]$ (Shoham, Schomburg & Lipscomb, 1980) than in $Ca[B_{12}H_{12}]$ (Solntsev, Kuznetsov & Ponomarev, 1976).

The $[NMe_4]^+$ cation has effective T_d point symmetry, and the conformation about each N–C bond is close to staggered. There are no serious contacts within or between ions, and a crystal packing diagram, as seen along the *a* axis, has been deposited.

We thank the SERC for support.

References

AGAFONOV, A. V., BUTMAN, L. A., SOLNTSEV, K. A., VINOKUROV, A. A., ZHUKOVA, N. A. & KUZNETSOV, N. T. (1982). *Zh. Neorg. Khim.* **27**, 63–70.

CASEY, J. B., EVANS, W. J. & POWELL, W. H. (1983). *Inorg. Chem.* **22**, 2228–2235.

FULLER, D. J. & KEPPERT, D. L. (1984). *Inorg. Chem.* **23**, 3273–3274.

GOULD, R. O. & TAYLOR, P. (1983). *CALC*. Program for crystallographic calculations. Univ. of Edinburgh, Scotland.

HILTY, T. & RUDOLPH, R. W. (1979). *Inorg. Chem.* **18**, 1106–1108.

HOUSECROFT, C. E. & WADE, K. (1983). *Inorg. Chem.* **22**, 1391–1393.

JOHNSON, C. K. (1976). *ORTEP*II. Report ORNL-5138. Oak Ridge National Laboratory, Tennessee.

MILLER, H. C. & MUETTERTIES, E. L. (1967). *Inorg. Synth.* **10**, 88–91.

SHELDRICK, G. M. (1976). *SHELX*76. Program for crystal structure determination. Univ. of Cambridge, England.

SHELDRICK, G. M. (1984). *SHELX*84. Program for crystal structure determination. Univ. of Göttingen, Federal Republic of Germany.

SHOHAM, G., SCHOMBURG, D. & LIPSCOMB, W. N. (1980). *Cryst. Struct. Commun.* **9**, 429–434.

SOLNTSEV, K. A., KUZNETSOV, N. T. & PONOMAREV, V. I. (1976). *Izv. Akad. Nauk SSSR, Ser. Neorg. Mater.* **12**, 1044–1047.

Apppendix VII Reprint of Dalton Paper

J. CHEM SOC DALTON TRANS 1987

Extended Hückel Molecular Orbital Study of the Effects of Edge-bridging Hydrogen Atoms on the Lengths of Boron–Boron and Metal–Metal Bonds in Cluster Compounds, and the Crystal Structure of Benzyltrimethylammonium Octahydrotriborate(1−)†

Gary F. Mitchell and Alan J. Welch*
Department of Chemistry, University of Edinburgh, Edinburgh EH9 3JJ

The origin of the lengthening of B–B and M–M (M = transition metal) connectivities in borane and transition-metal cluster compounds as a consequence of edge H-bridging is traced, *via* EHMO–FMO calculations on $[B_{11}H_{13}]^{2-}$, $[Os_4H_2(CO)_{12}]^{2-}$, $[Re_3H(CO)_{12}]^{2-}$ and $[Re_3H_2(CO)_{12}]^-$, to asymmetry in the occupation of formerly degenerate orbitals of the cluster upon protonation. The unusual relative shortening of the bridged B–B connectivities in $[B_3H_8]^-$ is confirmed by an accurate, low-temperature crystallographic study of the ion as its $[PhCH_2NMe_3]^+$ salt. Crystals are monoclinic, space group $P2_1/c$ with four ion pairs in a cell of dimensions a = 11.225(4), b = 9.483(3), c = 13.218(4) Å, β = 111.70(3)°; R = 0.0569 for 2 903 data measured at 185 K. EHMO–FMO calculations show that the B–B edge shortening in $[B_3H_8]^-$ is strongly correlated with the asymmetric nature of the H-bridges, and that these two distortions are mutually self-regulating. A combined EHMO–FMO and MNDO study of the B–B edge protonation of 1,6-$C_2B_4H_6$ suggests that the edge shortening which has previously been predicted may be incorrect.

It is widely held that the effect of a hydrogen bridge is to cause lengthening (by *ca.* 0.1—0.15 Å) of a B–B or M–M (M = transition metal) connectivity in a polyhedral borane or transition-metal cluster compound.[1–3,‡] This principle is now so well established that it has become fairly standard practice in *X*-ray crystallographic studies of such species to make use of the lengthening to assume H-atom positions when they are not directly located.[5]

Surprisingly, no theoretical explanation of the cause of this lengthening has, to our knowledge, ever been offered. One simplistic approach would be to invoke polarisation of the electron density in a three-centre B–H–B or M–H–M bond towards the H atom, but this explanation fails to account for the known structures of apparent anomalies such as $[B_3H_8]^-$,[6] in which H-bridging is associated with *shortening* of the appropriate bond.

The structure of $[B_3H_8]^-$ is particularly interesting in that, in addition to the μ-H atoms residing on short B–B connectivities, the B–μ-H bond lengths are unusually asymmetric. Although both these features of the structure have been reproduced by high-level geometry-optimised molecular orbital (m.o.) calculations,[7] no rationalisation has been advanced.

In this paper we use the results of extended Hückel molecular orbital (EHMO) calculations to identify the cause of the general lengthening of B–B and M–M connectivities in clusters as a consequence of H-bridging. We also identify the asymmetry of the H-bridges in $[B_3H_8]^-$ as the origin of the unusual shortening of the bridged B–B bonds. Moreover, since the structure of $[B_3H_8]^-$ was determined many years ago[6] we have confirmed the important features of the structure by an accurate, low-temperature crystallographic study of the ion as a different salt. Finally, we have critically reinvestigated [*via* EHMO and modified neglect of diatomic overlap (MNDO) calculations] the B–B edge protonation of *closo*-1,6-$C_2B_4H_6$. Here an earlier MNDO study[8] had predicted shortening of the protonated edge, and this unusual result had been explained by polarisation arguments.

Experimental

Syntheses.—A number of salts of $[B_3H_8]^-$ were prepared by the general method of reaction of $Tl[B_3H_8]$[9] with the chloride or bromide of an appropriate cation. In a typical reaction $[PhCH_2NMe_3]Br$ (0.6334 g, 2.75 mmol) in MeOH–H_2O (3:1, 10 cm^3) was added with stirring to $Tl[B_3H_8]$ (0.6739 g, 2.75 mmol) in the same solvent mixture (10 cm^3). The precipitate of TlBr was filtered off and the filtrate evaporated *in vacuo* to afford $[PhCH_2NMe_3][B_3H_8]$ (**1**) as a colourless solid in almost quantitative yield (Found: C, 62.8; H, 12.65; N, 7.30. $C_{10}H_{24}B_3N$ requires C, 63.0; H, 12.7; N, 7.35%).

The compounds $[NEt_4][B_3H_8]$ (**2**), $[NPr_4][B_3H_8]$ (**3**), and $[N(PPh_3)_2][B_3H_8]$ (**4**), were prepared similarly.

X-Ray Crystallography.—Numerous crystallisations of (**1**)—(**4**) and of commercially-supplied $[NMe_4][B_3H_8]$ (**5**) were attempted. Although diffraction data were collected from the best samples of all species, those from (**2**)—(**5**) could not be either solved or satisfactorily refined because of poor crystal quality and/or disorder that could not be adequately modelled. Preliminary data for these salts are given in Table 1.

In contrast, (**1**) forms as diffraction-quality crystals by slow evaporation of a CH_2Cl_2 solution. A single crystal (0.4 × 0.4 × 0.3 mm) was mounted on a glass fibre with low-temperature epoxy-resin adhesive and, after preliminary Weissenberg photography, slowly cooled to 185 K on an Enraf-Nonius CAD4 diffractometer fitted with a ULT-1 attachment.

Crystal data. $C_{10}H_{24}B_3N$, M = 190.7, monoclinic, a = 11.225(4), b = 9.483(3), c = 13.218(4) Å, β = 111.70(3)°, U = 1 307.4 Å^3 by the least-squares refinement of 25 centred reflections, $14 < \theta < 15°$, λ = 0.710 69 Å, T = 185 K, space

---

† *Supplementary data available* (No. SUP 56667, 7 pp.): atomic co-ordinates used in EHMO calculations, MNDO-optimised co-ordinates, unit-cell packing diagram. See Instructions for Authors, *J. Chem. Soc., Dalton Trans.*, 1987, Issue 1, pp. xvii—xx.

‡ However, there are exceptions: in $[Fe_3H(CO)_9(SC_3H_7)]$ the face-capping SC_3H_7 group restrains the metal triangle to be essentially equatorial.[4]

Table 1. Preliminary crystallographic data* for (2)—(5)

	(2)	**(3)**	**(4)**	**(4)·xCH$_2$Cl$_2$**	**(5)**
Source of crystals	Cooling EtOH solution	Diffusion of hexane into CH$_2$Cl$_2$ solution	Diffusion of Et$_2$O into MeCN solution	Diffusion of Et$_2$O into CH$_2$Cl$_2$ solution	Cooling MeOH solution
Lattice	Tetragonal I	Monoclinic P	Monoclinic P	Monoclinic P	Tetragonal P
a/Å	9.340(16)	8.205(3)	15.291(3)	13.591(2)	8.704(7)
b/Å	9.340(16)	16.011(4)	14.452(3)	28.390(5)	8.704(7)
c/Å	7.540(4)	13.975(2)	16.023(3)	18.208(3)	6.390(3)
β	90	101.87(4)	110.875(13)	93.412(14)	90
U/Å^3	658	1 797	3 308	7 013	485
Space group	N.d.	$P2_1/n$	Pn or $P2/n$	$P2_1/n$	N.d.
Z	2	4	4	8	2
D_c/g cm^{-3}	0.862	0.838	1.162	1.10 (x = 0), 1.26 (x = 1)	0.786
Reason for abandoning	No single space group allows the symmetry of the anion to be less than 4 or $\bar{4}$	Severe disorder in the propyl groups	Disorder of the anion even in the lower symmetry space group	Impossible satisfactorily to model disorder in the solvate molecules	Very poor crystal quality

* Mo-K_α radiation. N.d. = Not determined.

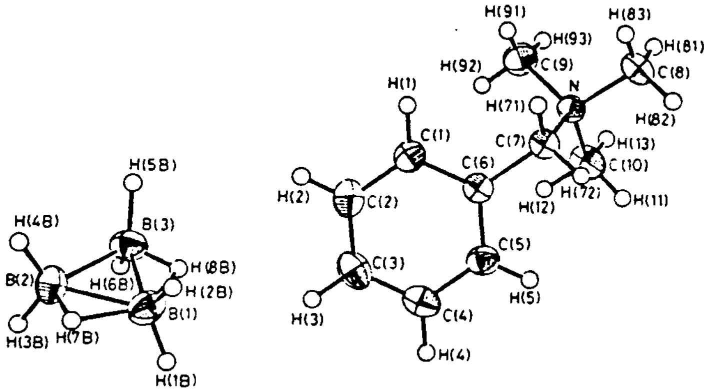

Figure 1. Molecular structure and numbering scheme in [PhCH$_2$NMe$_3$][B$_3$H$_8$] (1). Thermal ellipsoids are drawn at the 50% probability level, except for H atoms which have an artificial radius of 0.1 Å for clarity

group $P2_1/c$, Z = 4, D_c = 0.970 g cm^{-3}, μ(Mo-K_α) = 0.49 cm^{-1}, F(000) = 424.

Data collection and processing. ω/2θ scans in 96 steps with ω scan width (0.8 + 0.35 tan θ)°. Variable scan speeds dependent upon initial prescan. Graphite-monochromated Mo-K_α X-radiation. 4 183 reflections measured (1 < θ < 30°, +h +k +l and −h +k +l), 3 791 unique data, R_{merge} = 0.0256; 2 903 data with $F_o > 2.0\sigma(F_o)$ retained. No detectable crystal decay or movement throughout the data collection period.

Structure solution and refinement. Solved by direct methods (C and N atoms) and iterative full-matrix least-squares refinement and ΔF syntheses (B and H atoms). All non-H atoms allowed anisotropic thermal motion. Hydrogen atoms freely refined with individual isotropic thermal parameters. Weighting scheme, $w^{-1} = [\sigma^2(F_o) + 0.001\ 128\ F_o^2]$; R = 0.0569, R' = 0.0773, S = 1.396;* data: variables ratio 13:1. Maximum residue and minimum trough in final ΔF map 0.25 and −0.20 e Å^{-3}. Coefficients for analytical approximations to the atomic scattering factor curves were those inlaid in SHELX 76.[10] Computer programs used: CADABS,[11] SHELX 84,[12] SHELX 76, CALC,[13] and ORTEP-II.[14] Co-ordinates of refined atoms are listed in Table 2.

Molecular Orbital Calculations.—For EMHO calculations, locally modified version of ICON8-FMO[15] using the weighted H_{ij} formula[16] and orbital exponents and H_{ii} values listed in Table 3. Orthogonalised Å co-ordinates of each of the models used are in SUP 56667. For MNDO calculations the package was used as supplied.[17] Orbital plotting *via* ORBIT[18] and a locally modified version of PSI 77.[19]

Results and Discussion

Crystal Structure of [PhCH$_2$NMe$_3$][B$_3$H$_8$] (1).—A perspective view of an ion pair of (1) is shown in Figure 1 which also shows the atomic numbering scheme adopted. Bond lengths and angles in the [B$_3$H$_8$]$^-$ anion only are given in Table 4.

The species crystallises as well separated ion pairs with no significant inter-ion contacts. A unit-cell packing diagram is given in SUP 56667. The cation has effective C_s molecular symmetry and staggered conformations about all N–C bonds. Dimensions within the cation are unexceptional.

The [B$_3$H$_8$]$^-$ anion of (1) is characterised by the presence of two bridging hydrogen atoms, H(7B) and H(8B), lying within 0.1 Å of the plane of the B$_3$ triangle. The anion has approximate

---

* $R = \Sigma|F_o - F_c|/\Sigma|F_o|$; $R' = [\Sigma w(|F_o| - |F_c|)^2/\Sigma w|F_o|^2]^{\frac{1}{2}}$; $S = [\Sigma w(|F_o| - |F_c|)^2/(n.o - n.v)]^{\frac{1}{2}}$ (n.o = no. of observations, n.v = no. of variables).

Table 2. Fractional co-ordinates of refined atoms in [$PhCH_2NMe_3$][B_3H_8] (1)

Atom	x	y	z
N	0.807 40(10)	0.166 91(11)	0.522 21(9)
C(1)	0.593 86(13)	0.200 43(14)	0.645 96(12)
C(2)	0.512 68(14)	0.134 78(17)	0.688 59(13)
C(3)	0.555 24(16)	0.022 60(16)	0.759 39(14)
C(4)	0.679 77(16)	−0.025 49(16)	0.787 65(13)
C(5)	0.761 58(14)	0.039 26(15)	0.744 45(11)
C(6)	0.719 76(12)	0.152 57(13)	0.673 48(10)
C(7)	0.809 75(13)	0.224 97(15)	0.630 02(11)
C(8)	0.903 85(16)	0.247 43(19)	0.491 13(14)
C(9)	0.678 64(16)	0.186 50(22)	0.435 85(13)
C(10)	0.842 35(18)	0.014 40(16)	0.532 26(15)
B(1)	0.299 78(16)	0.129 04(21)	0.897 78(15)
B(2)	0.133 79(17)	0.141 23(20)	0.868 06(16)
B(3)	0.192 44(19)	0.090 97(19)	0.763 21(14)
H(1)	0.565 8(14)	0.278 1(17)	0.595 3(13)
H(2)	0.425 1(19)	0.166 2(19)	0.667 7(15)
H(3)	0.499 5(16)	−0.017 3(19)	0.792 8(14)
H(4)	0.707 9(16)	−0.111 3(20)	0.835 7(15)
H(5)	0.847 0(17)	0.008 0(19)	0.761 4(15)
H(71)	0.791 3(15)	0.318 4(19)	0.615 9(13)
H(72)	0.895 3(18)	0.212 8(19)	0.682 8(15)
H(81)	0.902 3(18)	0.217 6(21)	0.424 7(18)
H(82)	0.984 7(18)	0.228 8(19)	0.542 2(15)
H(83)	0.878 3(16)	0.344 0(20)	0.486 4(14)
H(91)	0.660 1(18)	0.286 6(22)	0.445 4(15)
H(92)	0.620 4(16)	0.129 6(20)	0.453 9(14)
H(93)	0.684 4(20)	0.143(3)	0.366 2(18)
H(11)	0.930 8(19)	0.000 3(21)	0.594 6(18)
H(12)	0.777 6(18)	−0.036 4(22)	0.557 4(17)
H(13)	0.845 8(20)	−0.013 0(24)	0.466 6(20)
H(1B)	0.350 1(17)	0.038 9(20)	0.943 8(15)
H(2B)	0.355 5(21)	0.221(3)	0.911 2(19)
H(3B)	0.085 0(17)	0.052 4(21)	0.890 6(15)
H(4B)	0.081 0(19)	0.238 3(24)	0.847 1(18)
H(5B)	0.164 1(17)	0.168 6(20)	0.689 8(15)
H(6B)	0.155 2(22)	−0.020(3)	0.737 2(21)
H(7B)	0.214 6(22)	0.168 4(23)	0.945 9(19)
H(8B)	0.291(3)	0.082(3)	0.797 9(23)

Table 3. Parameters used in EHMO calculations

Orbital	H_{ii}/eV	ζ_1	ζ_2	c_1	c_2
H(1s)	−13.60	1.30			
B(2s)	−15.20	1.30			
B(2p)	−8.50	1.30			
C(2s)	−21.40	1.625			
C(2p)	−11.40	1.625			
O(2s)	−32.30	2.275			
O(2p)	−14.80	2.275			
Os(5d)	−12.42	5.650	2.417	0.6680	0.5885
Os(6s)	−10.36	2.450			
Os(6p)	−5.23	2.286			
Re(5d)	−12.66	5.343	2.277	0.6662	0.5910
Re(6s)	−9.36	2.398			
Re(6p)	−5.96	2.372			

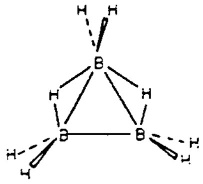

(I)

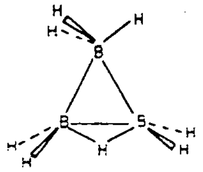

(II)

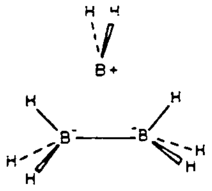

(III)

C_{2v} symmetry about the unique boron B(1). The important results of the structure determination in the context of our interest in the effects of H-bridging are that (*i*) the H-bridges are markedly asymmetric, and (*ii*) the bridged B–B bonds, B(1)–B(2) 1.760(3) and B(1)–B(3) 1.778(3) Å, are both substantially shorter than the unbridged one, B(2)–B(3) 1.804(3) Å.

The C_{2v} arrangement (I) of $[B_3H_8]^-$ has been shown by geometry-optimised *ab initio* m.o. calculations[7] to be only *ca.* 4 kJ mol^{-1} more stable than an alternative monobridged C_s form (II), and the equivalence of all eight hydrogen atoms in solution, at least on the n.m.r. time-scale, is well documented.[20] Such a small energy difference is well within the normal range of intermolecular forces in the solid state, and thus, whilst an earlier[6] crystallographic study of $[B_3H_8]^-$ as its $[H_2B(NH_3)_2]^+$ salt also indicated the dibridged C_{2v} structure, the monobridged form may yet be characterised by *X*-ray diffraction.

The structures of a number of derivatives of $[B_3H_8]^-$ have been determined in this laboratory and elsewhere. Examples exist of mono-[21,22] and di-bridged[23] forms and, in addition, some structures are found to be best described as intermediate, having one full and one partial hydrogen bridge.[24–26] Boron–boron bond lengths for these derivatives are given in Table 5. The pattern which clearly emerges from this compilation is one of H-bridging being associated with the shortest B–B connectivity, and this is fully consistent with the optimised structures for $[B_3H_8]^-$ in mono- and di-bridged forms of McKee and Lipscomb.[7]

In (1) H(7B) and H(8B) each bridge their respective B–B connectivities asymmetrically, being 1.38 and 1.36 Å from B(1), and 1.12 and 1.03 Å from B(2) and B(3), *cf.* 1.05—1.17 Å for the six terminal B–H bond lengths. To accommodate the relatively short B(2,3)–H(7B,8B) bonds the H atoms terminal to B(2) and B(3) are bent towards each other, resulting in narrower H(3—6)–B(2,3)–B(3,2) angles than H(1,2)–B(1)–B(2,3) angles. This affords the extreme view of the $[B_3H_8]^-$ anion as (III), an adduct between eclipsed $[B_2H_6]^{2-}$ and angular $[BH_2]^+$, the latter approaching along one of the C_2 axes of the former to make only two short B–H contacts. Although this simple description is in accord with the relative charges calculated[27] for the two kinds of boron atom it does not easily lead to an understanding of the relative lengths of bridged *versus* unbridged B–B bonds.

Therefore we have adopted an alternative method of fragmenting the $[B_3H_8]^-$ ion to understand the effects of H-bridging, and have used the same approach for other bridged borane and transition-metal clusters, as described in the following section.

Molecular Orbital Calculations.—To rationalise the consequences of H-bridging on B–B and M–M lengths one must

Table 4. Bond lengths (Å) and angles (°) in the $[B_3H_8]^-$ anion of (I)

B(1)-B(2)	1.760(3)	B(1)-H(7B)	1.382(24)	B(2)-H(3B)	1.104(20)	B(3)-H(5B)	1.165(20)
B(1)-B(3)	1.778(3)	B(1)-H(8B)	1.36(3)	B(2)-H(4B)	1.075(23)	B(3)-H(6B)	1.14(3)
B(1)-H(1B)	1.080(19)	B(2)-B(3)	1.804(3)	B(2)-H(7B)	1.121(24)	B(3)-H(8B)	1.03(3)
B(1)-H(2B)	1.048(24)						

B(2)-B(1)-B(3)	61.32(11)	H(1B)-B(1)-H(7B)	105.2(14)	B(3)-B(2)-H(3B)	111.3(10)	B(1)-B(3)-H(8B)	49.9(16)
B(2)-B(1)-H(1B)	117.9(10)	H(1B)-B(1)-H(8B)	96.9(16)	B(3)-B(2)-H(4B)	110.6(12)	B(2)-B(3)-H(5B)	114.1(10)
B(2)-B(1)-H(2B)	119.9(13)	H(2B)-B(1)-H(7B)	99.7(17)	B(3)-B(2)-H(7B)	111.4(13)	B(2)-B(3)-H(6B)	106.2(13)
B(2)-B(1)-H(7B)	39.6(10)	H(2B)-B(1)-H(8B)	105.2(18)	H(3B)-B(2)-H(4B)	116.2(16)	B(2)-B(3)-H(8B)	108.5(16)
B(2)-B(1)-H(8B)	96.6(12)	H(7B)-B(1)-H(8B)	136.2(16)	H(3B)-B(2)-H(7B)	103.9(16)	H(5B)-B(3)-H(6B)	112.2(16)
B(3)-B(1)-H(1B)	115.0(10)	B(1)-B(2)-B(3)	59.82(11)	H(4B)-B(2)-H(7B)	102.8(17)	H(5B)-B(3)-H(8B)	109.9(19)
B(3)-B(1)-H(2B)	118.7(13)	B(1)-B(2)-H(3B)	118.6(10)	B(1)-B(3)-B(2)	58.85(11)	H(6B)-B(3)-H(8B)	105.5(21)
B(3)-B(1)-H(7B)	100.8(10)	B(1)-B(2)-H(4B)	123.5(12)	B(1)-B(3)-H(5B)	125.5(10)	B(1)-H(7B)-B(2)	88.7(16)
B(3)-B(1)-H(8B)	35.4(12)	B(1)-B(2)-H(7B)	51.7(12)	B(1)-B(3)-H(6B)	121.8(13)	B(1)-H(8B)-B(3)	94.7(21)
H(1B)-B(1)-H(2B)	114.0(17)						

Table 5. Boron boron distances (Å) in $[B_3H_8]^-$ and its derivatives $[B_3H_7X]^-$

X	Bridged B-B	Intermediate B-B	Unbridged B-B	Ref.
CO[a]	1.75(1)		1.83(1), 1.86(1)	21
$NCBH_3$	1.718(7)		1.833(7), 1.840(7)	22
NCB_3H_7 or CNB_3H_7	1.710(10)		1.804(10), 1.813(9)	22
	1.715(10)		1.815(10), 1.833(11)	
$NCAgCNB_3H_7$[b]	1.75(3)		1.801(21), 1.829(24)	22
	1.687(24)	1.815(23)	1.809(12)	
NH_3	1.744(5)	1.803(6)	1.820(6)	24
NCS	1.760(5)	1.793(6)	1.807(5)	25
NCSe	1.763(8)	1.788(8)	1.794(8)	25
CH_2PPh_3	1.766(9)	1.793(9)	1.816(9)	26
H	1.77		1.80	6
H	1.760(3), 1.778(3)		1.804(3)	c
Cl_2[d]	1.754(16), 1.763(16)		1.804(13)	23

[a] Mean of two independent molecules. [b] One $\{B_3H_7\}$ fragment is monobridged, the other intermediate. [c] This work. [d] Disubstituted derivative [*trans*-1,2-Cl_2-B_3H_6]$^-$, bridged bonds are B(1)-B(3) and B(2)-B(3).

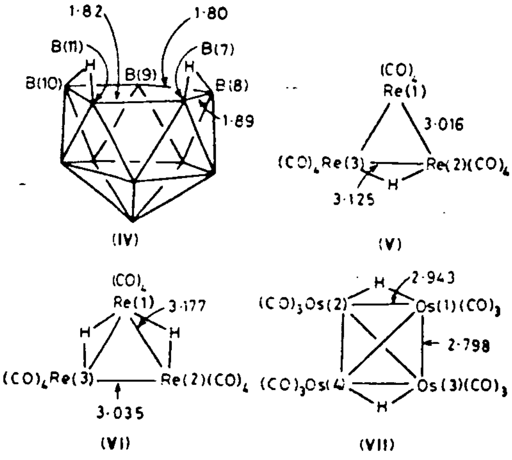

Figure 2. Some examples of clusters in which H-bridging is associated with a lengthening of the bridged bond (distances in Å)

consider molecules in which the presence or absence of H-bridges represents the only difference between otherwise equivalent connectivities. Thus, although the bridged connectivity of (II) is shorter than the unbridged connectivities, this species is not a strictly valid example of a structure in which H-bridging can be said to be associated with a difference in edge length. $[B_3H_8]^-$ in the C_{2v} form (I) is a suitable candidate, whose *X*-ray structure, confirmed above, shows that H-bridging is associated with *shortening* of the bridged B–B bonds.

In contrast, $[B_{11}H_{13}]^{2-}$ (IV) displays[28] *lengthening* of the bridged connectivities relative to otherwise equivalent ones (Figure 2). Many transition-metal cluster compounds also have edge-bridging H atoms whose effect seems to be a lengthening of the bridged bond, and Figure 2 shows line diagrams and important bond lengths (averaged over equivalent connectivities where appropriate) for some typical examples. Hydrogen atoms were not located in crystallographic studies of $[Re_3H(CO)_{12}]^{2-}$ (V),[29] $[Re_3H_2(CO)_{12}]^-$ (VI),[30] and $[Os_4H_2(CO)_{12}]^{2-}$ (VII),[31] but analysis of the disposition of the carbonyl ligands allowed confident prediction of the H-atom location(s) in each case. These molecules are suitable for this study since, again, bridged and unbridged bonds are otherwise chemically equivalent.

In all cases we have approached the problem by considering the perturbation of a high-symmetry anion as a consequence of protonation. For example, in the case of (I) we have doubly edge-protonated the D_{3h} species $[B_3H_6]^{3-}$ and traced the origins of its subsequent deformation. This approach is particularly rewarding in a comparison of (I) with (VI), since the anions $[B_3H_6]^{3-}$ and $[Re_3(CO)_{12}]^{3-}$ are composed of isolobal-isoelectronic C_{2v} $\{BH_2\}^-$ and C_{4v} $\{Re(CO)_4\}^-$ fragments, yet double protonation of the former trianion results in B–B bond shortening whilst similar protonation of the latter trianion results in Re–Re bond lengthening.

Finally, we have re-examined the B–B edge protonation of

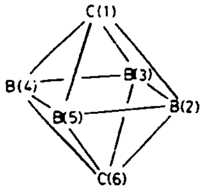

(VIII)

closo-1,6-$C_2B_4H_6$ (**VIII**) at the (geometry-optimised) MNDO level of calculation. This system is less attractive than those discussed above in that no experimental proof of the effect of protonation is available to check the validity of the theoretical arguments. It nevertheless aroused our interest since DeKock and Jasperse[8] report that symmetric H-bridging is predicted to result, unusually, in a contraction of the bridged B–B edge.

$$[B_{11}H_{11}]^{4-}\ (C_{5v}) + 2H^+ \longrightarrow [B_{11}H_{13}]^{2-}\ (C_s) \quad (1)$$

The orbitals of the $\{B_{11}H_{11}\}$ fragment have been described previously.[32] A partial interaction diagram for equation (1) is shown in Figure 3. For the sake of clarity constructions are only drawn if the coefficient of the fragment molecular orbital (f.m.o.) in the m.o. is >0.3. Interfragment overlap integrals >0.2 are $<5E_1\ \Sigma_u^+> 0.4958$, $<5A_1\ \Sigma_g^+> 0.2741$, $<2E_1\ \Sigma_u^+> 0.2634$, $<2A_1\ \Sigma_g^+> 0.3596$, $<1E_1\ \Sigma_u^+> 0.2951$, and $<1A_1\ \Sigma_g^+> 0.3099$.

On passing from C_{5v} $[B_{11}H_{11}]^{4-}$ to C_s $[B_{11}H_{13}]^{2-}$ the f.m.o.s of the cage which are of A_1 symmetry interact with the Σ_g^+ combination of the $[H\cdots H]^{2+}$ fragment. The degeneracies of the E_1 pairs of $[B_{11}H_{11}]^{4-}$ are lifted with that component having a nodal plane close to the protons being effectively unaltered in the dianion. The other component interacts with Σ_u^+ to afford A'' m.o.s. The E_2 orbitals of $[B_{11}H_{11}]^{4-}$ effectively have zero net overlap with the $[H\cdots H]^{2+}$ group orbitals since the protons are close to one of their nodal planes. Figure 3 clearly shows a three-orbital interaction with components of $5E_1$ and $3E_1$ mixing with Σ_u^+ to give the occupied m.o.s $6A''$ and $5A''$ in $[B_{11}H_{13}]^{2-}$. The strongly antibonding combination $10A''$ is high lying and unoccupied. The $5E_1$ and, to a lesser extent, the $3E_1$ orbital of $[B_{11}H_{11}]^{4-}$ are localised on, and are outpointing from, the pentagonal polyhedral face.[32]

Examination of the cage f.m.o. occupations in the dianion reveals the essential reason for the relative lengthening of the bridged connectivities B(7)–B(8) and B(10)–B(11). Occupations of all the previously filled orbitals are >1.8 e except for $6A_1$ (1.45 e) and one component of $5E_1$ (1.15 e). Deoccupation of the former would not be expected to reduce the symmetry of the $\{B_{11}\}$ fragment in the dianion. In contrast, asymmetric occupation of a formally equally occupied E_1 pair must lead to a molecular Jahn-Teller distortion. The orbitals $5E_1$, the highest occupied molecular orbitals (h.o.m.o.s) of $[B_{11}H_{11}]^{4-}$, are drawn in Figure 4. The component, (*b*), which becomes preferentially deoccupied in $[B_{11}H_{13}]^{2-}$ is π-bonding along B(7)–B(8) and B(10)–B(11), and π-antibonding between B(7)–B(11) and B(8)···B(10). The effect of its deoccupation will clearly be to lengthen the former pair of connectivities relative to the latter pair, and this is in full accord with the structure of (**IV**) determined crystallographically.[28]

$$[Os_4(CO)_{12}]^{4-}\ (T_d) + 2H^+ \longrightarrow [Os_4H_2(CO)_{12}]^{2-}\ (D_{2d}) \quad (2)$$

Interaction diagrams for the protonations (2)–(4) are very crowded due to intense concentrations of f.m.o.s and m.o.s arising from the *d* orbitals of the transition-metal atoms, and are therefore largely uninformative for the present purposes. However, an understanding of the observed lengthening of the bridged Os–Os bonds relative to unbridged ones in (**VII**) is afforded, again, by following the occupations of the f.m.o.s of the tetra-anion as it is protonated.

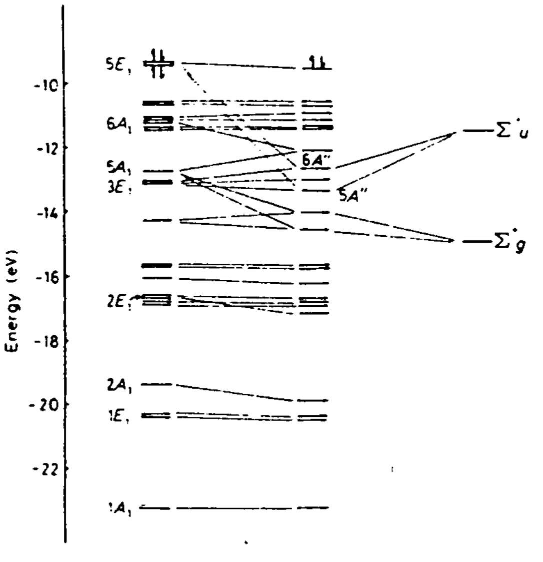

Figure 3. Interaction diagram for the double protonation of $[B_{11}H_{11}]^{4-}$. Only filled orbitals of this and the product $[B_{11}H_{13}]^{2-}$ are shown (eV ≈ 1.60×10^{-19} J)

Upon simultaneous Os(1)–Os(2) and Os(3)–Os(4) edge protonation the f.m.o.s of $[Os_4(CO)_{12}]^{4-}$ that are deoccupied by >0.2 e are one component each of $6E$ (occupation 1.79 e), $12T_2$ (1.02 e), and $7E$ (second h.o.m.o., 1.27 e). All these fragment orbitals have >70% metal character.

Views of the tetra-anion f.m.o.s for which deoccupation is the most marked are presented in Figure 5. (*a*) is the active component of $7E$ and (*c*), that of $12T_2$. Both are strongly σ-bonding along the Os(1)–Os(2) and Os(3)–Os(4) edges, and consequently their deoccupation would be expected to result in the bridged-bond lengthening that is observed.[31] In contrast, point-group symmetry demands that the other component of $7E$, Figure 5(*b*), and other components of $12T_2$, be noded at $\mu_{1,2}$-H and $\mu_{3,4}$-H positions, and must therefore remain fully occupied in the protonated complex.

$$[Re_3(CO)_{12}]^{3-}\ (D_{3h}) + H^+ \longrightarrow [Re_3H(CO)_{12}]^{2-}\ (C_{2v}) \quad (3)$$

A single μ-H atom can only interact by symmetry with those f.m.o.s of $[Re_3(CO)_{12}]^{3-}$ that are of A_1 symmetry and those components of E' pairs that are not noded through the H-atom position.

EHMO calculations show that the only filled f.m.o. of the trianion whose occupation changes by >0.2 e on protonation of the Re(2)–Re(3) edge is the appropriate component, Figure 6(*a*), of $15E'$, the occupation decreasing to 1.30 e. The $15E'$ orbitals, which lie only slightly below $10A_1$ {the h.o.m.o. of $[Re_3(CO)_{12}]^{3-}$}, are plotted in Figure 6, with (*a*) relevant to (**V**). The component in Figure 6(*a*) is strongly σ-bonding between Re(2)

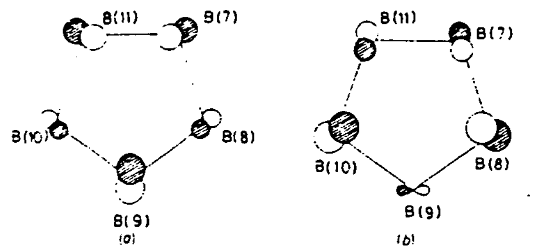

Figure 4. Components of the $5E_1$ set of $[B_{11}H_{11}]^{4-}$, viewed from a point directly above the open polyhedral face. Only B atoms in the open face, and no H atoms, are shown

Table 6. Variation of the $\langle 2E'(a)|\Sigma_g^+\rangle$ and $\langle 2E'(b)|\Sigma_u^+\rangle$ overlap integrals with shift (σ) of the μ-H atoms in $[B_3H_8]^-$

σ/Å	0.00	0.20	0.40	0.60
$\langle 2E'(a)\|\Sigma_g^+\rangle$	0.3923	0.4511	0.4903	0.5056
$\langle 2E'(b)\|\Sigma_u^+\rangle$	0.7127	0.6558	0.5764	0.4770

and Re(3), and therefore single protonation of $[Re_3(CO)_{12}]^{3-}$ results in the lengthening of the bridged bond that is observed crystallographically.[29]

$$[Re_3(CO)_{12}]^{3-}\,(D_{3h}) + 2H^+ \longrightarrow [Re_3H_2(CO)_{12}]^-\,(C_{2v}) \qquad (4)$$

The only orbitals of $[Re_3(CO)_{12}]^{3-}$ that undergo a substantial change in occupation upon double protonation [Re(1)–Re(2) and Re(1)–Re(3) edges] are $10A_1'$ (h.o.m.o., 2.00 e ⟶ 1.60 e) and $15E'$ (second h.o.m.o., 2 × 2.00 e ⟶ 1.63 e and 1.01 e). Again, reduction in fragment symmetry will only result from the latter uneven occupation. This time the component of $15E'$ which becomes the less occupied is Figure 6(*b*). This orbital is σ-bonding in character along the Re(1)–Re(2) and Re(1)–Re(3) bonds, and is π-antibonding between Re(2) and Re(3). Consequently, the effect of protonation of the Re(1)–Re(2) and Re(1)–Re(3) edges will be to cause their lengthening relative to the unbridged Re(2)–Re(3), as determined by the crystallographic study[31] of (**VI**).

$$[B_3H_6]^{3-}\,(D_{3h}) + 2H^+ \longrightarrow [B_3H_8]^-\,(C_{2v}) \qquad (5)$$

A partial interaction diagram for this system, in which the μ-H atoms *symmetrically* bridge the B(1)–B(2) and B(1)–B(3) connectivities, is given in Figure 7. Again f.m.o.s and m.o.s are linked only if the coefficient of the former in the latter is >0.3. The interfragment overlap integrals are $\langle 2E'\,\Sigma_g^+\rangle$ 0.3923, $\langle 2E'\,\Sigma_u^+\rangle$ 0.7127, $\langle 2A_1'\,\Sigma_g^+\rangle$ 0.1704, $\langle 1E'\,\Sigma_g^+\rangle$ 0.1903, $\langle 1E'\,\Sigma_u^+\rangle$ 0.3458, and $\langle 1A_1'\,\Sigma_g^+\rangle$ 0.5559.

On passing from D_{3h} $[B_3H_6]^{3-}$ to C_{2v} $[B_3H_8]^-$ [equation (5)] there is substantial mixing of the $2E'$ and $2A_1'$ f.m.o.s to afford $6A_1'$, $5A_1'$, and $3A_1''$ m.o.s, the last two also involving large components of the symmetric and antisymmetric $[H \cdots H]^{2+}$ group orbitals respectively. The $2E'$ f.m.o.s are sketched in Figure 8. Note their resemblance to $15E'$ of $[Re_3(CO)_{12}]^{3-}$ (Figure 6).

Inspection of the occupancies of the f.m.o.s of $[B_3H_6]^{3-}$ in $[B_3H_8]^-$ reveals that *symmetric* H-bridging causes both components of $2E'$ to be substantially deoccupied, component (*a*) falling to 1.30 e, and (*b*) to 0.94 e. Clearly, the consequence of this asymmetric occupation would be to cause the bridged connectivities to *lengthen* relative to the unbridged one, as in the related species $[Re_3H_2(CO)_{12}]^-$. This is in disagreement with the observed asymmetry in the B–B lengths determined in the above crystallographic study.

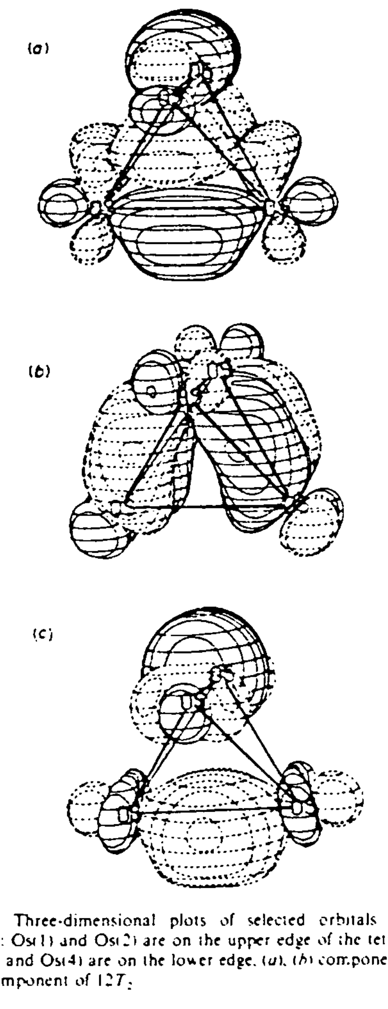

Figure 5. Three-dimensional plots of selected orbitals of $[Os_4(CO)_{12}]^{4+}$: Os(1) and Os(2) are on the upper edge of the tetrahedron, and Os(3) and Os(4) are on the lower edge. (*a*), (*b*) components of $7E$; (*c*) one component of $12T_2$

However, a fundamental difference between the *X*-ray-determined structure and the theoretical model used above is that in the former the μ-H atoms clearly *do not* symmetrically bridge the B–B edges. From the form of the $2E'$ orbitals in Figure 8 it is apparent that movement of the μ-H atoms parallel to the bridged edges, towards B(2) and B(3), will result in increasing interaction between Σ_g^+ and $2E'(a)$ at the expense of the Σ_u^+ $2E'(b)$ interaction. This is confirmed by the relevant overlap integrals in Table 6, where σ is the shift of the μ-H atoms from their symmetric positions.

Increasing interaction of the (filled) $2E'(a)$ orbital of $[B_3H_6]^{3-}$ with the (empty) Σ_g^+ group orbital of $[H \cdots H]^{2+}$ leads to the decreasing occupation of the former in the molecule, and a switch in the relative occupations of components (*a*) and (*b*) would lead naturally to bridged bond *shortening* compared to the unbridged bond. Figure 9 plots the f.m.o. occupation of $2E'$ of $[B_3H_6]^{3-}$ in $[B_3H_8]^-$ *versus* σ. The switch occurs at σ *ca.* 0.6 Å, which corresponds to B(1)–μ-H = 1.74 and B(2),B(3)–μ-H = 0.94 Å. Although the discrepancy in B–μ-H lengths here is obviously greater than that actually observed, the

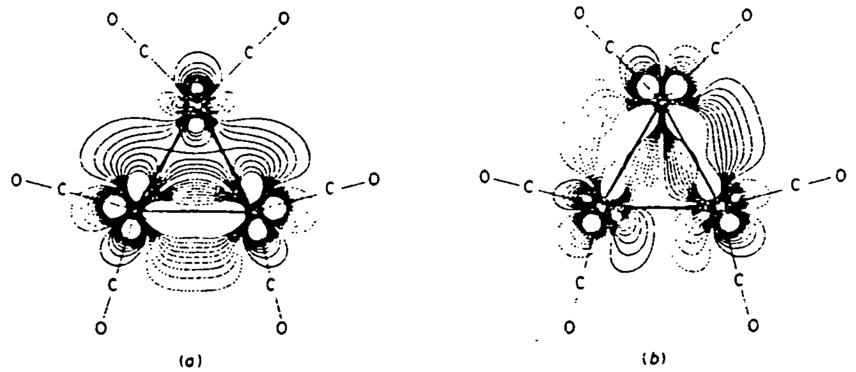

Figure 6. Two-dimensional (Re$_3$ plane) plots of the 15E' orbitals of [Re$_3$(CO)$_{12}$]$^{3-}$ Re(1) is the upper apex of the triangle and Re(2) and Re(3) are the basal atoms

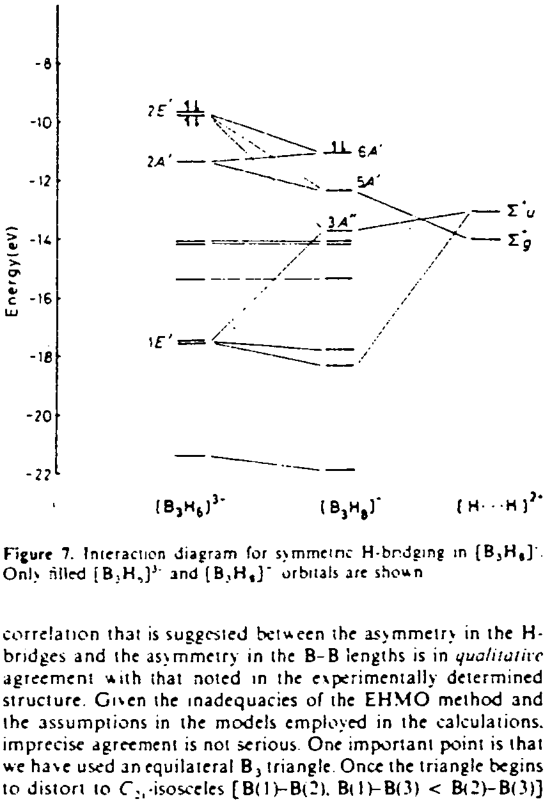

Figure 7. Interaction diagram for symmetric H-bridging in [B$_3$H$_8$]$^-$. Only filled [B$_3$H$_6$]$^{3-}$ and [B$_3$H$_8$]$^-$ orbitals are shown

correlation that is suggested between the asymmetry in the H-bridges and the asymmetry in the B–B lengths is in *qualitative* agreement with that noted in the experimentally determined structure. Given the inadequacies of the EHMO method and the assumptions in the models employed in the calculations, imprecise agreement is not serious. One important point is that we have used an equilateral B$_3$ triangle. Once the triangle begins to distort to C_{2v}-isosceles [B(1)–B(2), B(1)–B(3) < B(2)–B(3)] the B_1 f.m.o. derived from 2E'(a) lies at higher energy than the B_2 orbital derived from 2E'(b) and would therefore have reduced overlap with Σ_g^+, reducing the driving force towards further asymmetry in the H-bridges. Thus, not only are the two notable asymmetries in [B$_3$H$_8$]$^-$ (B–B connectivities and the position of the μ-H atoms) highly correlated, but they are also mutually self-regulating.

Finally, we note that shifting the μ-H atoms to σ = 0.6 Å in [B$_3$H$_8$]$^-$ also results in a difference in occupation between the components of 1E' of [B$_3$H$_6$]$^{3-}$. These are essentially B–H$_{\text{terminal}}$ bonding orbitals, and are sketched in Figure 10. Component (b), antibonding between the {B(2)H$_2$} and {B(3)H$_2$} fragments, becomes partially deoccupied (1.73 e) at σ = 0.6 Å [*cf.* component (a), 1.99 e]. This specific deoccupation of 1E'(b) will tend to oppose the relative shortening of the B(1)–B(2) and B(1)–B(3) bonds upon μ-H shift, but its effect in this sense will be relatively small. It does, however, nicely account for the bending towards each other of the H atoms terminal to B(2) and B(3) that is observed in the crystallographic study.

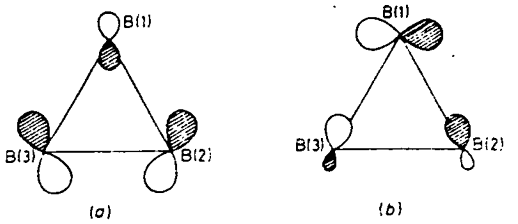

Figure 8. The 2E' orbitals of [B$_3$H$_6$]$^{3-}$, with H atoms omitted

$$1,6\text{-}C_2B_4H_6\,(D_{4h}) + H^+ \longrightarrow [C_2B_4H_7]^+\,(C_{2v}) \quad (6)$$

DeKock and Jasperse[8] have carried out a theoretical study of this edge protonation. They report, using geometry-optimised MNDO calculations, that $\mu_{2,3}$ protonation of 1,6-C$_2$B$_4$H$_6$ [equation (6)] results in a structure in which the bridged B–B connectivity (1.66 Å) is shorter than the adjacent [B(3)–B(4) and B(2)–B(5), 1.84 Å] and opposite [B(4)–B(5), 1.91 Å] edges, and they discuss this unusual result in terms of the specific interaction between H$^+$ and the h.o.m.o. of 1,6-C$_2$B$_4$H$_6$ (B_{1g}, bonding with respect to all B–B edges).

EHMO-FMO calculations on [C$_2$B$_4$H$_7$]$^+$ show that the only f.m.o.s of C$_2$B$_4$H$_6$ whose occupancy changes by >0.05 e on B(2)–B(3) edge protonation are 1B_{1g} (the h.o.m.o., occupancy 1.01 e) and component (a) of 1E_u (occupancy 1.87 e).

The 1E_u(a) orbital is sketched in Figure 11(a). It is composed of B(2s) and H(1s) character, being net B–B non-bonding but bonding with respect to all B–H$_{\text{terminal}}$ interactions. Importantly it is bonding between B(2) and B(3). However, it's deoccupation in the protonated complex is small compared to typical deoccupations noted above, and we would therefore expect a *slight lengthening* of B(2)–B(3) [and B(4)–B(5)] upon edge protonation. Since this is the opposite prediction to that of

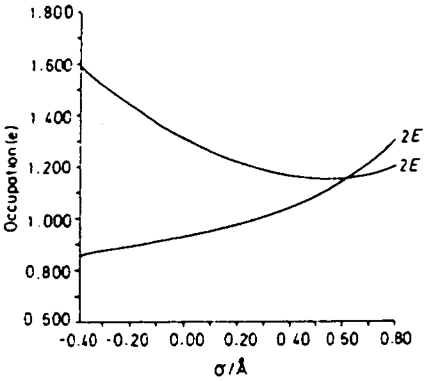

Figure 9. Changes in the occupation of the 2E' orbitals of $[B_3H_6]^{3-}$ in $[B_3H_8]^-$ as a function of σ, the shift of the μ-H atoms of the latter

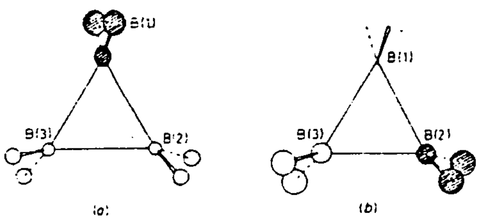

Figure 10. The 1E' orbitals of $[B_3H_6]^{3-}$

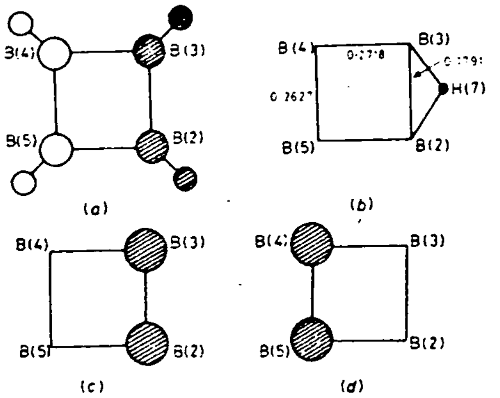

Figure 11. (a) Component $1E_u(a)$ orbital of $C_2B_4H_6$, (b) reduced overlap populations in $[C_2B_4H_7]^+$ [the μ-H atom bridges the B(2)–B(3) bond]; (c), (d) linear combinations of $1E_u(a)$ and $2A_{1g}$ of $C_2B_4H_6$

DeKock and Jasperse[5] we have reinvestigated both $C_2B_4H_6$ and $[C_2B_4H_7]^+$ *via* MNDO calculations. Note that in our calculations C_{2v} symmetry only was imposed on both species.

Optimised orthogonalised Å co-ordinates for both species are in SUP 56667. We agree with DeKock and Jasperse that the apparent equilibrium geometry of the protonated form is asymmetric, with B(2)–B(3) < B(3)–B(4), B(2)–B(5) < B(4)–B(5), and we reproduce their bond lengths almost exactly. However, the geometry-optimised calculation on $C_2B_4H_6$ (omitted from the work of DeKock and Jasperse[5]) affords an equilibrium geometry which is similarly asymmetric, but more so. Specifically, in this species B(2)–B(3) = 1.52, B(3)–B(4), B(2)–B(5) = 1.84, and B(4)–B(5) = 1.90 Å.

The compound 1,6-$C_2B_4H_6$ is known[33] to have a D_{4h} (pseudo-octahedral) geometry. Clearly the MNDO-optimised structure in which only C_{2v} symmetry is imposed is incorrect, the reasons for this are well documented.[34–36] Unfortunately DeKock and Jasperse have compared the C_{2v}-optimised structure of $[C_2B_4H_7]^+$ with a D_{4h}-optimised structure of $C_2B_4H_6$. Given the inadequacies of the MNDO method for molecules with multicentre bonding a comparison between optimised structures so derived is clearly inappropriate since the structural 'changes' in $[C_2B_4H_7]^+$ are largely attributable to the decreased symmetry constraints. However, it is still valid to compare the structures of neutral and protonated analogues optimised by MNDO *in the same point group*. In this case the only real structural change is a *lengthening* (0.14 Å) of the protonated B–B edge.

Reduced overlap populations in $[C_2B_4H_7]^+$ calculated by the EHMO method are shown in Figure 11(*b*). They are clearly consistent with B(2)–B(3) being the longest B–B connectivity in the protonated form. In C_{2v} $[C_2B_4H_7]^+$, B(2)–B(3) is no longer symmetry-equivalent to B(4)–B(5), but this is not reflected in the simple depopulation analysis reported above, which suggests only a rectangular and not a trapezoidal distortion of the B_4 square.

The overlap populations of $[C_2B_4H_7]^+$ are best understood by constructing localised orbitals from the m.o.s of $C_2B_4H_6$. On passing from D_{4h} $C_2B_4H_6$ to C_{2v} $[C_2B_4H_7]^+$, $1E_u(a)$ and $2A_{1g}$ of the former mix to produce in-phase and out-of-phase (A_1) combinations, Figure 11(*c*) and (*d*) respectively, of which only the former is substantially deoccupied upon B(2)–B(3) edge protonation.

Conclusions

Structures are known for a number of clusters in which H-bridging is the only difference between otherwise chemically equivalent connectivities. In all of these except $[B_3H_8]^-$, H-bridging is symmetric and is associated with relative lengthening of the bridged bond. We have shown that this results from an unequal occupation of degenerate orbitals* of the deprotonated form upon protonation.

In $[B_3H_8]^-$ the H-bridges are markedly asymmetric. Asymmetric double protonation causes a reversal in the deoccupations of the 2E' orbitals of $[B_3H_6]^{3-}$ relative to that if the bridges were symmetric. The reversal results in bridged bond shortening.

The vast majority of clusters containing H-bridges unfortunately do not contain connectivities whose only difference is the presence or absence of the bridge, and so lack a suitable built-in reference. In such cases it is clear that one cannot be certain that any observed differences in the lengths of bridged and unbridged bonds are largely due to the H-bridge. Consequently the value of the assignment of μ-H atom positions on

---

* In some cases, *e.g.* $[Re_3(CO)_{12}]^{3-}$, the active components of the degenerate sets of f.m.o.s are already sufficiently localised for the effects of protonation to be obvious. In others the canonical m.o.s *are not* adequately localised on the bonds to be contrasted, and in these cases it is necessary to construct linear combinations of the former. Thus for deprotonated molecules such as $[Os_3H(CH_2)(CO)_{10}]^-$,[37] in which the point group is non-degenerate, this procedure is required to produce the necessary degeneracy and localisation. In cases like $C_2B_4H_6$ partial distinction between bridged and unbridged bonds can be made immediately, but the construction of linear combinations is then needed to contrast, *e.g.* the B(2)–B(3) and B(4)–B(5) connectivities.

the basis of relative lengths alone is doubtful in clusters of this type. It is nevertheless still reasonable to attempt to answer the question of the influence of H-bridging on the length of a B-B or M-M bond in such molecules. A precise answer depends, however, on a rather more precise question, since there are in principle three ways of 'adding' a symmetric μ-H function to such a bond. (*i*) Addition of H^- must cause a localised two-centre, two-electron B-B or M-M bonding f.m.o. to become partially deoccupied in forming a bonding three-centre, two-electron interaction, and would therefore result in bond lengthening. (*ii*) Addition of H converts a two-centre, one-electron bond into a three-centre, two-electron bond. Its effect on bond length is expected to be small. (*iii*) Addition of H^- will partially occupy an orbital of the cluster that was previously B-B or M-M bonding but empty. This must cause bond shortening.

In chemical reactions μ-H atoms are invariably added to, or abstracted from, clusters as protons. Therefore the only comparison that is feasible (in cases where otherwise chemically equivalent bridged and unbridged connectivities do not exist) is that between B-B or M-M bond lengths in protonated and deprotonated analogues, assuming no gross structural changes.[38] In such cases the available evidence is that symmetric μ-H^- addition causes the bridged bond to lengthen.

Acknowledgements

We thank the S.E.R.C. for a postgraduate studentship (to G. F. M.) and Dr. J. H. Morris for crystals of the CH_2Cl_2 solvate of $[N(PPh_3)_2][B_3H_8]$.

References

1 M. R. Churchill, B. G. DeBoer, and F. J. Rotella, *Inorg. Chem.*, 1976, **15**, 1843.

2 P. R. Raithby, in 'Transition Metal Clusters,' ed. B. F. G. Johnson, Wiley, Chichester, 1980, pp. 5—192.

3 L. Barton, *Top. Curr. Chem.*, 1982, **100**, 169.

4 R. Bau, B. Don, R. Greatrex, R. J. Haines, R. A. Love, and R. D. Wilson, *Inorg. Chem.*, 1975, **14**, 3021.

5 See, for example, P. D. Boyle, B. J. Johnson, A. Buehler, and L. H. Pignolet, *Inorg. Chem.*, 1986, **25**, 7.

6 C. R. Peters and C. E. Nordman, *J. Am. Chem. Soc.*, 1960, **82**, 5758.

7 M. L. McKee and W. N. Lipscomb, *Inorg. Chem.*, 1982, **21**, 2846.

8 R. L. DeKock and C. P. Jasperse, *Inorg. Chem.*, 1983, **22**, 3843.

9 E. Amberger and E. Gut, *Chem. Ber.*, 1968, **101**, 1200.

10 G. M. Sheldrick, SHELX 76, University of Cambridge, 1976.

11 R. O. Gould, CADABS, University of Edinburgh, 1985.

12 G. M. Sheldrick, SHELX 84, University of Gottingen, Federal Republic of Germany, 1984.

13 R. O. Gould and P. Taylor, CALC, University of Edinburgh, 1986.

14 C. K. Johnson, ORTEP-II, Report ORNL-5138, Oak Ridge National Laboratory, Tennessee, U.S.A., 1976.

15 J. Howell, A. Rossi, D. Wallace, K. Haraki, and R. Hoffmann, ICON, Quantum Chemistry Program Exchange, University of Indiana, 1977, no. 344.

16 J. H. Ammeter, H-B. Burgi, J. C. Thibeault, and R. Hoffmann, *J. Am. Chem. Soc.*, 1982, **100**, 3686.

17 W. Thiel, MNDO, Quantum Chemistry Program Exchange, University of Indiana, 1977, no. 353.

18 G. F. Mitchell, ORBIT, University of Edinburgh, 1983.

19 W. L. Jorgensen, PSI 77, Quantum Chemistry Program Exchange, University of Indiana, 1977, no. 340.

20 W. C. Phillips, H. C. Miller, and E. L. Muetterties, *J. Am. Chem. Soc.*, 1959, **81**, 4496.

21 J. D. Glore, J. W. Rathke, and R. Schaeffer, *Inorg. Chem.*, 1973, **12**, 2175.

22 S. J. Andrews and A. J. Welch, *Inorg. Chim. Acta*, 1985, **105**, 89.

23 M. Arunchaiya, J. H. Morris, S. J. Andrews, D. A. Welch, and A. J. Welch, *J. Chem. Soc., Dalton Trans.*, 1984, 2525.

24 C. E. Nordman and C. Reimann, *J. Am. Chem. Soc.*, 1959, **81**, 3538.

25 S. J. Andrews and A. J. Welch, *Inorg. Chim. Acta*, 1984, **88**, 153.

26 S. J. Andrews and A. J. Welch, *Acta Crystallogr., Sect. C*, 1985, **41**, 1496.

27 L. D. Brown and W. N. Lipscomb, *Inorg. Chem.*, 1977, **16**, 1.

28 C. J. Fritchie, *Inorg. Chem.*, 1967, **6**, 1199.

29 M. R. Churchill, in 'Transition Metal Hydrides,' ed. R. Bau, Adv. Chem. Ser., American Chemical Society, 1978, vol. 167, pp. 38—39.

30 M. R. Churchill, P. H. Bird, H. D. Kaesz, R. Bau, and B. Fontal, *J. Am. Chem. Soc.*, 1968, **90**, 7135.

31 B. F. G. Johnson, J. Lewis, P. R. Raithby, G. M. Sheldrick, and G. Suss, *J. Organomet. Chem.*, 1978, **162**, 179.

32 D. M. P. Mingos, *J. Chem. Soc., Dalton Trans.*, 1977, 602.

33 E. A. McNeill, K. L. Gallaher, F. R. Scholer, and S. H. Bauer, *Inorg. Chem.*, 1973, **12**, 2108.

34 M. J. S. Dewar and M. L. McKee, *J. Am. Chem. Soc.*, 1977, **99**, 5231.

35 M. J. S. Dewar and M. L. McKee, *Inorg. Chem.*, 1978, **17**, 1569.

36 M. J. S. Dewar and M. L. McKee, *Inorg. Chem.*, 1980, **19**, 2662.

37 A. J. Schultz, J. M. Williams, R. B. Calvert, J. R. Shapley, and G. D. Stucky, *Inorg. Chem.*, 1979, **18**, 319.

38 M. McPartlin, C. R. Eady, B. F. G. Johnson, and J. Lewis, *J. Chem. Soc., Chem. Commun.*, 1976, 883.

Received 23rd June 1986; *Paper* 6/1258

LECTURE COURSES AND MEETINGS ATTENDED

"Non-crystallographic Least-Squares" J.Tellinghausen

"Numerical Methods" K.P.Lawley

"Powder Diffraction" A.J.Blake, R.O.Gould, B.Lowe

"Diffraction Studies of DNA Fragments and Introduction to the Cambridge Crystallographic Database" T.Brown, O.Kennard, F.H.Allen, S.R.Bellard, D.G.Watson

"Microcomputers in the Laboratory" A.G.Rowley, Mr.A.King

"VSEPR Theory" C.Glidewell

Crystallography Group Meetings

Inorganic Chemistry Group Meetings

Intraboron Meeting, Durham

European Crystallographic Meeting, Turin (1985)

Scottish Universities Summer School in Physics - "Synchrotron Radiation", Aberdeen (1985)

British Crystallographic Association Winter School on Crystallography, Aston (1987)